MICRODISCHARGE-BASED PRESSURE CONTROLLING DEVICES AND THEIR APPLICATIONS TO CHEMICAL SENSING IN HARSH ENVIRONMENTS

by

Scott Andrew Wright

A dissertation submitted in partial fulfillment
of the requirements for the degree of
Doctor of Philosophy
(Electrical Engineering)
in The University of Michigan
2009

Doctoral Committee:

Professor Yogesh B. Gianchandani, Chair
Professor Brian E. Gilchrist
Professor Khalil Najafi
Associate Professor John E. Foster
Associate Professor Euisik Yoon

© Scott Andrew Wright

All rights reserved

2009

To Mom and Ray.

ACKNOWLEDGEMENTS

First of all I would like to thank my family. My parents Chris and Ray King, and Tina and Jim Wright, my sister Amanda Wilson, my grandparents Lucille and Stan Davis, and Elizabeth and Larry Wright, and my great-uncle Sumner Davis. These individuals have supported me throughout my life and academic career, for which I am eternally grateful.

I would like to thank my advisor, Yogesh Gianchandani. He has dedicated countless hours not only to our academic progress, but to teaching me as an individual to perform and publish research. I would like to thank the professors at the University of Michigan, including Professor Kensall Wise and my thesis committee: Professors Khalil Najafi, Brian Gilchrist, Euisik Yoon, and John Foster for all of their help and guidance.

I would like to thank the WIMS, SSEL, and LNF staff including: Brendan Casey, Dennis Schweiger, Robert Gordenker, Sandrine Martin, Ed Tang, and Trasa Burkhardt.

I would like to thank my group members, lab mates, and friends at the University of Michigan and in Ann Arbor. They have always been there for me, providing help and making my time at Michigan enjoyable. This group includes: Allan Evans, Christine Eun, Mark Richardson, Jong Park, Bhaskar Mitra, Angelo Gaitas, Naveen Gupta, Scott Green, Tao Li, Weibin Zhu, Richard Fung, Amar Basu, Karthik Visvanathan, Kabir Udeshi, Senol Mutlu, Ken Takahata, Tzeno Galchev, Niloufar Ghafouri, Amir Borna, Erkan Aktakka, Ali Besharatian, Andy Gross, Seow Yuen Yee, Jeff Gregory, Jae Yoong Cho, Sang Won Yoon, Sang-Hyun Lee, Jay Mitchell, Hanseup Kim, Sang Woo Lee, Andrew Kuo, Neil Welch, Ruba Borno, Tushar Bansal, Gayatri Perlin, Razi Haque, Angelique Johnson, Emine Cagin, Kim Khalsa, Shahrzad Naraghi, Becki Veeneman, Awlok Josan, Kiran Pandey, Kwan Tan, Mark Ferriss, Jeff Siddiqui, Danese Joiner, Elizabeth Hansson, Jamey Lister, Marc Siciliano, Carl Grant, Charles Doriean, and Michael McCorquodale.

I am grateful for all of you.

TABLE OF CONTENTS

DEDICATION ii

ACKNOWLEDGEMENTS iii

LIST OF FIGURES vii

LIST OF TABLES xiv

LIST OF APPENDICIES xv

ABSTRACT xvii

CHAPTER 1 INTRODUCTION 1

1.1 Electrical Breakdown in Gases 2

1.2 Uses of Macroscale Plasmas 8

1.3 Microdischarges 11

1.3.1 Calculated Steady State Parameters 14

1.3.2 Microdischarge Modeling 16

1.4 Types of Microdischarges 17

1.4.1 Dielectric Barrier Discharge 17

1.4.2 Microhollow Cathode Discharge 18

1.4.3 Inductively Coupled Microplasma 19

1.4.4 Planar Discharge 20

1.4.5 Parallel Plate Discharge 21

1.5 Microdischarge Devices 21

1.5.1 Display Technology 21

1.5.2 Microdischarges for Chemical Analysis 22

1.5.3 Other Microdischarge Devices 23

1.6 Microdischarge-Based Microtransducers 23

1.6.1 Vacuum Generation Using Microdischarges 24

1.6.2 Pressure Sensing Using Microdischarges 26

1.6.3 Chemical Sensing Microsystem 29

1.7 Organization of Thesis 32

CHAPTER 2 VACUUM GENERATION USING MICRODISCHARGES 34
2.1 Background 35
2.2 Device Concept and Operation 40
2.3 Theoretical Considerations 44
2.4 Design and Fabrication 57
2.5 Experimental and Modeling Results 60
2.5.1 Removing Air from Microelectronic Packages 60
2.5.2 Pressure Reduction Behavior 64
2.5.3 Operating Micro-SIPs at Lower Pressures 67
2.5.4 Relationship between Discharge Gap Spacing, Pressure, and Air Removal Rate 67
2.5.5 Removal Rates of Various Gases 69
2.5.6 Removal Rate of Water Vapor 72
2.5.7 Pulsed Discharge Operation 74
2.5.8 Thermally Assisted Discharges 76
2.6 X-Ray Photoelectron Spectroscopy Results 77
CHAPTER 3 PRESSURE SENSING USING MICRODISCHARGES 79
3.1 Background 79
3.2 Device Concept and Operation 83
3.2.1 Pulsed Discharges 86
3.2.2 Current Pulse Operation and Simulation 87
3.3 Design and Fabrication 91
3.4 Experimental Results 94
3.5 Discussion of Results 104
CHAPTER 4 CHEMICAL SENSING MICROSYSTEM 106
4.1 Background 107
4.2 Detrimental Effect of Contaminant Nitrogen in Spectral Chemical Sensing 116
4.2.1 Background 116
4.2.2 Resulting Spectra in SF_6 117
4.3 Using Micro-SIPs for Gas Purification 122
4.3.1 Concept, Operation, and Design of Gas Purifying Micro-SIPs 122
4.3.2 Results and Discussion 124
4.4 Harsh Environment Chemical Sensor 126
4.4.1 System Concept 126
4.4.2 System Optical Emission Sensor 127
4.4.3 System Bidirectional Micromachined Valves 129
4.4.4 System Operation and Fabrication 130

4.4.5 Results and Discussion 132

CHAPTER 5 CONCLUSION........ 134

5.1 Dissertation Summary........ 134
5.2 Suggestions for Future Work 137
5.2.1 Utilizing Micro-SIPs to Reach High Vacuum (10^{-6} Torr) 137
5.2.2 Harsh Environment Chemical Sensor Packaging 141
5.2.3 Selective Growth of Doped Nanowires Using Microdischarges 142

APPENDICES 143

BIBLIOGRAPHY 192

LIST OF FIGURES

Figure 1.1: Paschen curves for discharges created between copper parallel plate electrodes in various gases.. 4

Figure 1.2: Paschen curves for parallel and planar electrodes with 500 µm spacing [Wil03b].. 12

Figure 1.3: Schematic diagrams of the (a) volume discharge and (b) surface discharge DBD.. 18

Figure 1.4: Schematic diagram of the microhollow cathode discharge configuration. ... 19

Figure 1.5: Schematic diagram of typical planar electrodes and planar microdischarge. 20

Figure 1.6: Schematic diagram of typical parallel plate electrodes and microdischarge.. 21

Figure 1.7: Plot of required device operating temperature vs. fabrication complexity for several pressure reducing devices. (See table for the list of abbreviations and references.)... 26

Figure 1.8: Plot of maximum operating temperature vs. fabrication steps for various high temperature pressure sensors. (See table for the list of abbreviations and references.) 29

Figure 1.9: Plot of operating temperature range vs. number of detectable chemical species for various high temperature gas sensors. (See table for the list of abbreviations and references.) 32

Figure 2.1: Illustration of NEG isolation from micromachined device in a microscale package. 37

Figure 2.2: Plot of required device operating temperature vs. fabrication complexity for several pressure reducing devices. (See table for the list of abbreviations and references.)... 40

Figure 2.3: Schematic of a commercial package, commercial pressure sensor, micro-SIP, power, and readout circuitry. R_{B1} and R_{B2} are ballast resistors of varied resistance which limit the current flowing between the anode and cathode. 40

Figure 2.4: Schematics of micro-SIP electrodes: (a) basic design, top view, (b) heated cathode design, top view, and (c) side view. 41

Figure 2.5: Modeled electric field strengths normal to a version 2 micro-SIP surface at a height of 50 µm above the electrodes. 56

Figure 2.6: (a) Version 2 chip with a single anode and eight cathodes. (b) Version 3 chip with a single anode and two cathodes, each having 15 discharge gaps. (c) Version 4 chip with high current density. (d) Version 5 chip with low current density. 58

Figure 2.7: A commercial package after opening, with two commercial pressure sensors and three different micro-SIP versions. 60

Figure 2.8: Pressure drop in a 6.33 cm^3 package over time. Fifteen consecutive 10 minute discharges drop the pressure 168 Torr. The pressure remains stable over periods of 10 hours of micro-SIP inactivity and returns to atmospheric pressure when the package is opened. 62

Figure 2.9: Pressure drop, shown in Fig. 2.8, as a function of cumulative energy supplied to the discharge with an initial pressure of 760 Torr. The upper and lower trend lines, respectively, show the pressure readings when the discharge is interrupted (causing spikes as the pressure stabilizes without an increase in energy) and when the discharge remains on. The corresponding number of gas molecules removed at room temperature, and the fraction of the package volume evacuated, are noted on the second *Y* axis.. 63

Figure 2.10: Pressure drop in a 4.0 cm^3 package over 30 minutes of micro-SIP operation, starting at an initial pressure of 31 Torr.. 63

Figure 2.11: Micro-SIP electrodes displaying remains of a cathode after reactive sputtering, illustrating areas of complete titanium sputtering. 66

Figure 2.12: (a) Experimentally measured (over 20 min.) and (b) theoretically determined pressure reduction rates in air as a function of discharge gap spacing and pressure. The micro-SIPs have between 35 µm and 150 µm discharge gaps, are operated with 1,500 V, have initial pressures between 100 Torr and 725 Torr, and are operated in a 4 cm^3 package... 69

Figure 2.13: Spectrum of the micro-SIP electrode pair discharge in air indicating the dissociation of oxygen and ionization of titanium and nitrogen............................... 70

Figure 2.14: Change in pressure in environments of pure oxygen, nitrogen, helium, and air. The micro-SIPs have 100 µm discharge gaps, are operated with 1,000 V, have initial pressures of 200 Torr, and are operated in a 4 cm^3 package. This shows that the mixed gas air environment is removed at a rate between oxygen and nitrogen as expected, based on the different chemisorptions rates of the gases. Helium is not removed as it is an inert gas and does not bond with titanium. 72

Figure 2.15: Schematic of the glass package, micro-SIP, and external equipment used to introduce and measure humidity removal.. 73

Figure 2.16: Experimentally measured change in humidity using a micro-SIP. The micro-SIP has a 100 μm discharge gap, is operated with 1,000 V, has an initial pressure of 400 Torr, and is operated in a 4.0 cm^3 glass package. A mechanical pump is used for comparison, starting at the same initial pressure and relative humidity. The micro-SIP removes more relative humidity than the mechanical pump when both reduced the pressure by 10 Torr. The heating and cooling transients are caused by the discharge induced heat from the micro-SIP. They are absent in the mechanical pump measurements due to the absence of a heat increase.................... 74

Figure 2.17: Pulses of 1,000 V are applied at a frequency of 1 Hz. (a) Pressure reduction rate as a function of pulse duration, averaged over 20 minutes of gas removal. The longer pulse durations reduce pressure faster. The error bars indicate a standard deviation of removal rate. (b) Relative energy required to remove an arbitrary unit of pressure with different pulse durations, normalized to a DC discharge. Pulses are five times more energy efficient, but require a longer duration of time.................... 75

Figure 2.18: Average pressure reduction rate comparison using micro-SIPs with thin-film heaters as cathodes. In the "hot" trials, the cathodes are heated through the application of the indicated average power, while in the "cold" trials; identical micro-SIPs with cathode heaters are not heated. The calculated average cathode temperatures are indicated. The heaters are all 50 μm in width and 1 mm or 2 mm in length. The micro-SIPs are operated with 1,000 V at initial pressures of 100 Torr and 200 Torr in a 1 cm^3 package. 77

Figure 3.1: Plot of maximum operating temperature vs. fabrication steps for various high temperature pressure sensors. (See table for the list of abbreviations and references.) 83

Figure 3.2: Schematic of (a) a Bulk Foil sensor with electrodes above a quartz chip, illustrating placement, and the microdischarge chamber during operation, and (b) a Planar sensor with microdischarge. 85

Figure 3.3: Diagram of a microdischarge between a single anode and two cathodes in a Bulk Foil structure. 86

Figure 3.4: Circuit model for discharge. The pulse power source is represented by the discharging of the capacitor, *C,* that is switched on at time $t = 0$. The current pulse is represented as a series combination of an inductance, *L*, and resistance, *R* along the current path. R_s is a shunt resistance, which allows a small amount of secondary current to flow during the main current pulse. 88

Figure 3.5: Modeled (a) and experimentally measured (b) current pulses in cathodes 1 and 2 in a pressure sensor with electrodes spaced 50 μm apart, 1 mm in diameter, and 125 μm thick at 200 Torr. The modeled pulses are referred to as M_1 and M_2... 89

Figure 3.6: Fabrication processes for Bulk and Planar sensors....................................... 92

Figure 3.7: Bulk Foil sensors with (a) electrodes spaced 100 µm apart, 50 µm thick and (b) electrodes spaced 50 µm apart, 125 µm thick. Planar sensors with (c) three circular cathodes spaced 50 µm apart, 300 µm in width and (d) five straight cathodes spaced 50 µm apart, 50 µm in width. 94

Figure 3.8: Pulse generating and readout circuitry used for sensor operation. 95

Figure 3.9: Oscilloscope trace of the voltage pulses used for pressure measurements. The voltage was measured across 100 Ω resistors and used to calculate the current, with V_1 as the voltage in cathode 1 and V_2 as the voltage in cathode 2. 96

Figure 3.10: Measured current pulse peak values. (a) Sum of the pulse currents in two Bulk Foil cathodes as a function of pressure and temperature. The empirical curves for each temperature are indicated by the solid lines. (b) Temperature trend for equation terms C_1 and C_2 in the peak current equation. 97

Figure 3.11: Percentage of total current in the cathodes at 1,000˚C in a Bulk Foil sensor with electrodes spaced 50 µm apart, 1 mm in diameter, and 125 µm thick. 98

Figure 3.12: Differential current output determined from the percentage of total current in Bulk Foil sensors with electrodes (a) spaced 50 µm apart and (b) spaced 100 µm apart, 1 mm in diameter, and 125 µm thick. Each data point is the average of 100 measurements. The two empirical curves per temperature are indicated by the solid lines. 99

Figure 3.13: The average sensitivities in both the low and high pressure ranges for the Bulk Foil sensors in Fig. 3.12(a) and (b) as functions of temperature. 100

Figure 3.14: Percentage of total current and differential current output in Planar sensors with (a) electrodes spaced 50 µm apart, 300 µm in width and (b) electrodes spaced 50 µm apart, 50 µm in width. Each data point is the average of 100 measurements. 103

Figure 4.1: Plot of operating temperature range vs. number of detectable chemical species for various high temperature gas sensors. (See table for the list of abbreviations and references.) 113

Figure 4.2: (a) Plot of sensitivity vs. speed of detection for various kinds of chemical sensors (see table for the list of abbreviations and references). Each of the publications mentioned represent the best results of the various classes of devices. (b) Plot of selectivity vs. number of detectable chemical species for gases and organic compounds. L, M, and H represent a low, medium, and high number of chemicals [Mit08c]. 114

Figure 4.3: Microplasma emission spectra in air and SF_6 at 3 Torr. All figures use the same arbitrary unit scale for the intensity. (a) SF_6 environment with 800 V and 500

μA. (b) SF_6 environment with 1,000 V and 2.7 mA after the spectrum produced in air has been subtracted out. (c) Air environment with 500 V and 500 μA. (d) Average normalized difference between SF_6 and air emission spectra recorded between 400 mTorr and 10 Torr. 119

Figure 4.4: Emission spectra in (a) air and (b) SF_6 between 400 nm and 510 nm where the molecular emission band produced by SF_6 has been observed. Three consecutive measurements are averaged in each environment. 121

Figure 4.5: Gas-purifying micro-SIPs. A DC voltage is applied to selectively remove nitrogen and oxygen. 124

Figure 4.6: Percentage of contaminants (nitrogen and oxygen) in a helium sample during gas purification, showing the thorough removal of the unwanted gases. 125

Figure 4.7: Spectra of the pump discharge in 99.25% helium with air contamination at 200 Torr (a) before purification and (b) after purification. Small amounts of nitrogen cause intense emission lines compared to helium at time = 0, demonstrating the necessity of nitrogen removal. 126

Figure 4.8: Schematic of the entire harsh environment chemical sensing system........ 127

Figure 4.9: Microdischarge optical emission sensor (chemical detector) used to detect carbon and other vapors through recorded spectra. (a) Schematic. (b) Photograph. 128

Figure 4.10: Microvalve concept: The valve consists of ceramic-PZT-Si-glass structure. A PZT stack actuator moves the silicon plate to open or close the valve. Micro-groove patterns are fabricated on the silicon plate to increase the flow area [Par08]. 130

Figure 4.11: System before sealing in ceramic package next to a U.S. penny. 131

Figure 4.12: Ratio of carbon to nitrogen emission line intensity during gas purification at 200°C, based on their strongest emission lines. 132

Figure 4.13: Spectra of acetone sample backfilled with helium during gas purification at 200°C. (a) Spectrum recorded before purification, showing strong nitrogen emissions and low C_2 emissions. (b) Spectrum recorded after purification, showing diminished nitrogen and increased CN and C_2 emissions. 133

Figure 5.1: Schematic of a micro-SIP and accompanying magnet in a sealed package with outlet ports. 139

Figure 5.2: Schematic of harsh environment chemical sensor package with semi-permeable membrane and integrated fiber optic cable. 142

Figure A1.1: Radii of microdischarges as a function of pressure and temperature........ 147

Figure A1.2: Predicted electric field strength in a microdischarge-based pressure sensor with 50-µm gaps and 125-µm-thick electrodes. 158

Figure A2.1: The atomic composition of used anodes, cathodes, and fresh unused titanium electrodes. These are the only five elements found in the electrode surfaces. Broad spectra are examined and at least three spectra are averaged for each data point. 161

Figure A2.2: The distribution of oxygen, titanium and nitrogen based on the atomic composition of used anodes, cathodes, and fresh unused electrodes. Narrow, focused spectra are examined and at least three spectra are averaged for each data point. The figure only considers the concentration of these three elements in the sample. 161

Figure A2.3: The atomic concentration of titanium and nitrogen in anodes and cathodes of micro-SIPs which had been operated at different initial pressures. 162

Figure A2.4: The atomic concentration of oxygen in anodes and cathodes of micro-SIPs which had been operated at different initial pressures.. 162

Figure A3.1: Schematic diagram of a thermionic cathode with heating circuit. 165

Figure A3.2: Emission current as a function of cathode temperature with two materials. 167

Figure A3.3: Emission current as a function of applied anode-cathode potential difference. 169

Figure A4.1: Emission spectrum of pure SF_6 produced in a RIE chamber. An excitation frequency of 13.56 MHz is used. Three consecutive measurements are averaged. 175

Figure A4.2: Schematic of electrodes and system set-up. 177

Figure A5.1: Emission spectra produced in SF_6 with different applied power. The stronger intensities are produced by applying 1,000 V and the weaker intensities are produced by applying 800 V... 180

Figure A5.2: Emission spectra produced in SF_6 at different pressures. The stronger intensities are produced at 5 Torr and the weaker intensities are produced at 10 Torr. 181

Figure A6.1: Layout with liquid tin in a ceramic crucible next to the substrate with a tungsten anode. 185

Figure A6.2: Nanowires, approximately 50 nm in diameter and 10 µm in length. 186

Figure A6.3: Gold particle at the tip of a nanowire, with additional particles in the background. The particle is measured as 55.7 nm in diameter.............................. 187

Figure A6.4: Silicon substrate showing regions with and without nanowire growth.... 187

Figure A6.5: Region of low nanowire growth, demonstrating sparse nanowire formation. 188

Figure A6.6: Resulting substrate exposed to a microdischarge with a high power density. 190

LIST OF TABLES

Table 1.1: Minimum breakdown voltage and *pd* value at which it occurs in various gases [Cob58]. 5

Table 1.2: DC glow microdischarge operating parameters in a microdischarge-based pressure sensor. 15

Table 2.1: Calculated parameters for a micro-SIP with 50-µm discharge gaps and 1,500 V applied at a pressure of 100 Torr. 57

Table 3.1: Typical performance of four different sensor designs with the highest performance in each category in bold. 101

Table A1.1: DC glow microdischarge operating parameters in a microdischarge-based pressure sensor, calculated over the range of 10-2,000 Torr and 23-1,000ºC. 146

Table A1.2: DC sheath operating parameters in a microdischarge-based pressure sensor, calculated over the range of 10-2,000 Torr and 23-1,000ºC. 148

Table A6.1: Parameters varied to determine the optimum environment for nanowire growth. 189

LIST OF APPENDICIES

APPENDIX 1 CALCULATING MICRODISCHARGE PARAMETERS 144

A1.1 Microdischarge Parameters in a Pressure Sensor 145
A1.2 Breakdown Voltage.. 148
A1.3 Primary Discharge... 149
A1.4 Cathode Sheath 154
A1.5 Other Current Generating Mechanisms 157

APPENDIX 2 X-RAY PHOTOELECTRON SPECTROSCOPY RESULTS 159

A2.1 Measurement Description 159
A2.2 Electrode Composition Results 160

APPENDIX 3 CONSIDERATIONS FOR A MICROSCALE ION GAUGE............... 164

A3.1 Macroscale Ion Gauges 164
A3.2 Hot Cathode Ionization Gauges 165
A3.3 Cold Cathode Ionization Gauges 166
A3.4 Microscale Hot Cathode Ion Gauges 166
A3.5 Microscale Cold Cathode Ion Gauges 169
A3.6 Operating Pressure Range 171
A3.7 Conclusion 172

APPENDIX 4 MICROPLASMA SF_6 EMISSION LINE DETECTION 173

A4.1 SF_6 Emission Spectrum Characterization 173
A4.2 Experimental Setup 176

APPENDIX 5 SF_6 MICROPLASMA CHARACTERISTICS 179

APPENDIX 6 INVESTIGATION INTO THE GROWTH OF DOPED NANOWIRES USING MICRODISCHARGES 182

A6.1 Introduction.. 182
A6.2 Setup.. 184

A6.3 Results 186
A6.4 Conclusions 190

ABSTRACT

MICRODISCHARGE-BASED PRESSURE CONTROLLING DEVICES AND THEIR APPLICATIONS TO CHEMICAL SENSING IN HARSH ENVIRONMENTS

by

Scott Andrew Wright

Chair: Yogesh B. Gianchandani

Microdischarges offer an alternative and often advantageous sensing and actuation method that has not been significantly exploited in microtransducers. This thesis explores the capabilities of microdischarges to address problems such as cavity pressure control, cavity pressure detection, and purity control of fill gases, which are relevant to microsystems. Microdischarge-based transducers have been developed for these purposes. One interesting aspect of microdischarge-based transducers is the wide latitude of operating temperatures, as they are advantageous for room and high temperature operation.

On-chip sputter-ion pumps control the pressure and gas purity in cavities. They consist of thin-film titanium electrodes patterned on glass substrates. Microdischarges sputter the cathodes, resulting in the selective chemisorption of titanium-reactive gases. Using DC discharges, these devices have reduced the pressure by 168 Torr in an air-filled, hermetically sealed, 6.33 cm^3 package. Starting at 200 Torr, the pressure reduction

rate of air is 7.2 Torr/h; oxygen 11.5 Torr/h, and nitrogen 3.4 Torr/h. Relative humidity is reduced at 6%/h. The pumps do not remove helium, purifying gas environments by selectively removing contaminating nitrogen and oxygen. A theoretical model outlining the dependency of gas removal rates on microdischarge parameters is presented.

Microdischarge-based pressure sensors operate by correlating the measured change in spatial current distribution of pulsed DC microdischarges with pressure. One sensor version uses three-dimensional arrays of horizontal bulk metal electrodes embedded in quartz substrates with electrode diameters of 1-2 mm and 50-100 μm inter-electrode spacing. These devices have been operated over 10-2,000 Torr, at temperatures as high as 1,000˚C. The maximum measured sensitivity is 5,420 ppm/Torr, while the minimum temperature coefficient of sensitivity is -550 ppm/K. Sensors of a second version use planar electrodes, with 0.13 mm^2 active areas.

To explore the utility of pressure controlling devices, these transducers are combined with an optical emission sensor to create a high temperature gas phase chemical detection microsystem. The microdischarge-based pressure sensor determines the sample and backfilling gas pressure while the microscale-sputter-ion pump purifies the gas environment. The contaminating nitrogen concentration has been reduced by 56.5x relative to helium and the spectral detection limit has been improved by 8x for carbon at 200°C.

CHAPTER 1

INTRODUCTION

The utility derived from macroscale plasmas combined with current microfabrication techniques has allowed for the development of microscale devices which use microdischarges for operation. Microdischarge is the term applied to a small, localized plasma region which, due to its size, demonstrate characteristics different from those of plasma regions created on a larger scale [Wil03a, Kus05, Foe06]. Microplasma is another term used to describe a microdischarge, but is typically used to describe a low pressure glow discharge as opposed to the more general category.

Microdischarge-based transducers offer many advantages over their macroscale counterparts, some result directly from the characteristics of microdischarges. One advantageous characteristic is the ability to operate at pressures higher than atmosphere. Additionally, microdischarge-based devices consume less power, which combined with their small size, light weight, and low gas volume requirement, provides for the possibility of use in portable, battery-operated microinstruments. Portable instruments allow for real-time analysis in the field, without bringing samples to a laboratory. Additionally, microdischarge-based devices may be embedded within other instruments and numerous devices may be operated in parallel, due to their small size. One potential instance of this is the use of microdischarge-based chemical sensors as detectors for gas

chromatography (GC) systems. Finally, if microdischarge-based devices are microfabricated they can be mass-produced, making individual devices cheap.

A few forms of microdischarges have been utilized in microscale devices in the past, but this thesis presents the use of DC and pulsed DC microdischarges for pressure control, primarily in sealed packages or microsystems, which includes pressure sensing and actuation.

Section 1.1 presents a qualitative review of electrical breakdown and various discharge types. Section 1.2 presents a discussion of the uses of macroscale plasmas in semiconductor processing and high vacuum pumps. Section 1.3 presents the operation of microdischarges and the differences between them and their macroscale counterparts. Section 1.4 presents several different microdischarge modes of operation. Section 1.5 presents various devices that use microdischarges. Section 1.6 presents the motivation behind the development of, and contributions derived from, microscale-sputter-ion pumps, high temperature microdischarge-based pressure sensors, and high temperature chemical sensors. This section also contains brief comparisons to other technologies. Section 1.7 presents the organization of this thesis.

1.1 Electrical Breakdown in Gases

Plasmas are characterized by charged ions and negatively charged electrons in background neutral environments. They are created when energy is applied to a non-conducting material, typically a neutral gas, causing the ionization of gas molecules and the generation of free electrons. To form a plasma the neutral gas "breaks down" as the ions and electrons undergo a multiplication process in which the gain from ionization

exceeds the net loss from processes such as diffusion, recombination, and attachment. The initiation of this breakdown allows current to flow through though the plasma regions, via the movement of the charged particles. Breakdown induces atomic transitions, resulting in emissions which can often be visually observed. Breakdown can occur through the application of high frequency and/or DC voltages, but this thesis focus on the creation of DC plasmas and DC breakdown will thus be primarily discussed. Faraday was the first to outline the properties of ionized gas [Far1839, Far1844, Far1855] and the word plasma was later used by Langmuir and Tonks [Lan29]. For a more detailed description of macroscale gas discharge physics, the reader is referred to [Cob58], [Lie94], and [Rai97].

When an external DC field is applied between electrodes in a gas environment, electrons are drawn from the lower potential cathode electrode(s) to the higher potential anode electrode(s). If the applied voltage is low, carrier multiplication is insufficient to produce a self-sustained discharge and random current bursts occur. When the external field is greater than the "breakdown voltage", breakdown occurs and a self-sustained DC discharge is created which does not require an external ionizing source. In this discharge the electrons collide with gas molecules and produce positive ions, which subsequently drift to the cathode. Upon cathode impact, the energetic ions eject high energy "secondary electrons" from the cathode, which sustain DC discharges by ionizing additional neutral molecules. This "avalanche breakdown" process continues until an appreciable level of ionization is reached (typically an ionization of above 10^{-8} ions/atoms [Rai97]). A positively charged "sheath" region at the cathode with high electric fields is formed with a high density of ions.

The breakdown voltage is a function of the product of pressure (p) and electrode spacing (d) according to Paschen's law and is estimated as [Cob58]

$$V_{BD} = \frac{Bpd}{\ln\left[\frac{Apd}{\ln(1/\gamma)}\right]}, \qquad (1.1)$$

where A and B are gas dependent constants and γ is the second Townsend ionization coefficient. The relationships between the breakdown voltages and the pd products are described by Paschen curves, which are shown in Fig. 1.1 for discharges between copper parallel plate electrodes in various gas environments.

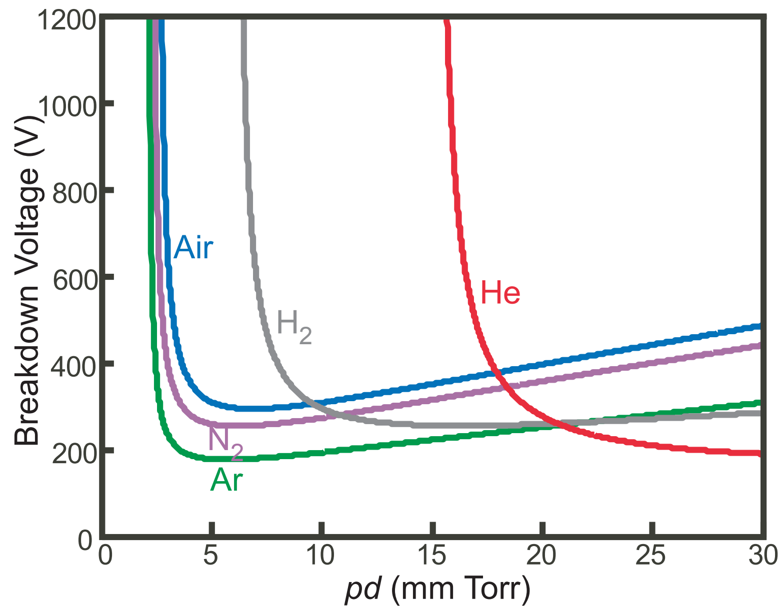

Figure 1.1: Paschen curves for discharges created between copper parallel plate electrodes in various gases.

The breakdown voltage reaches a minimum for a given optimal value of the product pd as shown in each Paschen curve. The minimum occurs at a pressure where the electron mean free path is similar to the distance between electrodes. At lower pd values, the breakdown voltage increases as the electrons undergo fewer collisions and

thus have a smaller chance of producing an ionizing collision. At higher *pd* values, the breakdown voltage also increases as the mean free path length decreases, which decreases the energy gained by the ions between collisions. Both instances necessitate a higher electric field to initiate avalanche breakdown. The minimum breakdown voltage can be calculated as

$$V_{BD\min} = 2.718\frac{B}{A}\ln\frac{1}{\gamma}. \tag{1.2}$$

Table 1.1 presents the minimum breakdown voltage and the corresponding *pd* value at which it is achieved in various gas environments. Discharges preferentially form at a distance between electrodes which minimizes the *pd* product for a given pressure.

Table 1.1: Minimum breakdown voltage and *pd* value at which it occurs in various gases [Cob58].

Gas	V_{BDmin}	*pd* cm·Torr
Air	327	0.567
Ar	137	0.9
H_2	273	1.15
He	156	4.0
CO_2	420	0.51
N_2	251	0.67
N_2O	418	0.5
O_2	450	0.7
Na (vapor)	335	0.04
SO_2	457	0.33
H_2S	414	0.6

DC discharges typically take the steady state form of glow or arc discharges. Glow discharges occur at lower pressures with lower current densities while higher current densities, which can be caused by a high ambient pressure, result in arc

discharges. The discharges are sometimes initiated by high current arcs, before a glow or arc discharge is formed. These discharge types and sparks will be discussed individually.

Applying a voltage greater than the breakdown voltage creates a transition from the Townsend, or "dark" discharge to a glow discharge. The glow discharge has a high level of ionization, which results in an inhomogeneous electric field concentrated over the cathode. After the initial formation of the glow discharge, it requires a lower applied voltage to be sustained. The discharge is accompanied by a bright optical emission, caused by atoms and ions excited to higher energy states through collisions with energetic electrons. These photons created by atomic energy level transitions can then induce secondary electrons through photoemission when they impinge upon the cathode, especially when using low work function electrodes. The glow discharge is a non-equilibrium or "low temperature" plasma, with the average electron temperature much higher than the average ion temperature. The ion temperature is almost in thermal equilibrium with the ambient gas environment. The cathode temperature does not significantly change, allowing the glow discharge to be categorized as cold-cathode discharge. The discharge is also referred to as a weakly ionized discharge as the plasma density is only a small fraction of the neutral gas density

Glow discharges are classified as normal or abnormal discharges. The normal discharge has a constant current density at the cathode. When the power to the discharge is varied, only the area over which the glow exists varies, while the current density is constant throughout the glow. After the entire cathode is enveloped within the glow, the current density increases. This is known as the abnormal or anomalous glow discharge, and requires relatively large increases in the applied voltage to cause small increases in

the current density. As the current density increases, it is accompanied by a decrease in cathode sheath thickness, leading to a higher electric field and voltage drop in the sheath, which increases the positive ion energy. The increased energy of the incoming positive ions raises the temperature of the cathode, assuming the cathode is not cooled, causing increased "thermionic emission". Thermionic emission is the flow of charge carriers, typically electrons, from a surface resulting when the thermal vibrational energy overcomes the electrostatic forces restraining the carriers. A positive feedback can occur, which can lead to the formation of an arc discharge.

A high current density results in an arc discharge, characterized by a high current and low voltage. The arc voltage is low as the source of electrons is thermionic emission supplied by a localized region of high current density (and high temperature) on the cathode. This thermionic emission reduces the need for considerable field amplification necessary in the glow discharge. When low boiling point metals are used, such as copper, iron, and silver, the arc is anchored on localized hotspots on the cathode surface, which can reach temperatures of 2,000–4,000 K. However, these high temperatures cause rapid cathode erosion which in turn, cause the arc hotspots to shift rapidly. When refractory materials (such as carbon or tungsten) are used, the arc is seen to be anchored in a fixed location. The arc is referred to as a thermal or equilibrium plasma in which the electrons, ions, and gas molecules are in thermal equilibrium, which is in contrast to the glow discharge. This high gas temperature, high ionization rate, and high rate of exciting collisions causes the arc discharge to have a much more intense emission compared to the glow discharge. An arc discharge typically begins as a glow discharge, which degenerate into an arc discharge as a result of thermal instabilities and high current densities.

In the spark discharge, breakdown is initiated through the Streamer mechanism. This mechanism is fundamentally different from the Townsend mechanism, which characterizes arc and glow discharges. The spark discharge consists of a single transient avalanche trail, instead of a steady state discharge, and requires a large voltage. In an electron avalanche, the number of electrons and ions increases exponentially with distance. If the discharge gap is large, a single avalanche can result in an appreciable level of ionization. Consequently, the path of a single avalanche can create an advancing "spark channel", which glows brightly due to the large number of highly energetic electrons. When the avalanche reaches the anode, a spark channel full of positive ions remains (the positive ions are assumed to be stationary for the duration of the avalanche). Additional avalanches are initiated near the spark channel from photoemission from the initial avalanche. The electrons from these are pulled into the positive ion filled spark channel. Since there is no source of electrons to sustain it, the spark discharge is a transient discharge. Lightening is a typical example of such a discharge.

1.2 Uses of Macroscale Plasmas

In conventional macroscale plasmas, DC discharges are infrequently used as high frequency methods of initiating discharges, such as RF, permit the use of dielectric elements, which prevent electrodes sputtering. Plasmas are used for a variety of purposes on the macroscale including IC fabrication and pressure reduction. Inert plasmas are used in the sputter deposition of thin films and in the removal of films from wafers. Chemically reactive plasmas are used in the deposition of silicon and dielectrics, as well as in the chemical etching of various thin films. Several different types of plasma

systems are used to implement these semiconductor fabrication techniques. Parallel plate reactors are commonly used for etching and operate through the application of a RF voltage to two electrodes, one of which is attached to a capacitor [Lie94]. Electrons are accelerated towards the electrode coupled to the capacitor faster than ions, causing a negative bias on this electrode which influences ion directionality. Inductively coupled plasmas (ICPs) use an external RF coil to inductively heat the plasma and increase ionization. This increases the plasma density and etch rate without increasing substrate damage relative to a parallel plate reactor [Lie94]. Electron-cyclotron reactors (ECRs) use a magnetic field, which cause particles to move in circular trajectories, heating the plasma. All of these macroscale plasmas are created in relatively large chambers, as opposed to being created in localized regions of the wafers undergoing processing.

In addition to the various plasmas used for IC fabrication, macroscale plasmas are used for pressure reduction in the general class of ion pumps. Titanium sublimation pumps (TSPs), orbitron pumps, and sputter-ion pumps (SIPs) operate in high and ultrahigh vacuum environments using titanium to getter gas molecules [Sch99, Wel01, Wel03]. TSPs function by subliming a hot filament of titanium onto the inner walls of a chamber where it chemisorbs impinging reactive gases. Orbitron pumps use electron injectors to introduce electrons into an electrostatic field between two concentric cylinders. The central cylinder is the anode, while the outer cylinder or wall serves as the cathode. The electrons are injected with angular momenta and energies causing them to miss the central anode and orbit it with long path lengths, on the order of several hundred meters. Several variations have been developed. Diode pumps utilize the electrons to heat and sublime bulk titanium partially surrounding the anode, and to ionize gas

molecules. The sublimed titanium coats the cathode, and the reactive gas ions are absorbed and thus removed [Dou65]. Triode pumps use titanium on a separate cathode which is sputtered by impinging ions. This coats the internal surfaces of the pump, absorbing the impinging ions [Bil67, Den67]. Today, orbitron pumps function in a manner similar to the triode pumps. The cavity wall (the cathode) is composed of titanium into which ions are accelerated and entrapped. A titanium source is also sputtered by electrons to replenish the cathode surfaces during pump operation.

Macroscale-SIPs operate through the creation of Penning discharges in externally applied magnetic fields which are imposed axially to the discharges, crossing the electric field, which cause electrons to move in long spiral paths during which they ionize gas molecules. The ions are then accelerated toward the cathodes, both diffusing into it and sputter fresh titanium onto the surrounding walls and anode. Gas molecules chemically combine with this titanium to form solid compounds, removing the gas from the environment and reducing the pressure. The gas diffusing into the cathode is eventually reemitted, except for hydrogen which diffuses into the cathode bulk. Titanium is traditionally used as it is chemically reactive with most gases including nitrogen and oxygen [Hol59, Den67, Col94, Sch99, Mat01, Wel03]. Heavy nonreactive gases can also be confined as they are buried by the deposited materials [Hol59, Sch99, Mat01, Wel03]. To improve trapping of nonreactive gases, noble diode pumps utilize tantalum and triode pumps utilize more complex geometries. These pumps traditionally have pumping rates of 0.3-2 liters/second and can operate between 400 and 40,000 hours, depending on the pressure [Sch99]. The pumping speed increases with pressure as the number of ions bombarding the cathode increases more than linearly:

$$I = kp^n \; , \tag{1.3}$$

where I is the ion current, k is a constant, p is the pressure, and n is between 1.05-1.2.

Macroscale-sputter-ion pumps approximately 3 cm in length and 0.3 kg in weight are commercially available, but these devices are significantly larger than the pumps described in this thesis [Rut99, Var08].

1.3 MICRODISCHARGES

Microdischarges demonstrate characteristics different from those of plasma regions created on a larger scale. Macroscale plasmas tend to be unstable and susceptible to arcs at higher pressures, including atmospheric pressure, which limits their use. Microdischarges however, can exist at high pressures due to the small distance between electrodes. Paschen's law, Section 1.1, describes this favorable so-called *pd* scaling which allows microdischarges to be formed with relatively low applied voltages at high pressures between closely spaced electrodes. Lower applied voltages reduce the current densities in the sheath region, which reduces instabilities and arc formation.

In certain microdischarges multiple path lengths are simultaneously available between electrodes, which makes the discharge gap a variable and permits a low breakdown voltage to be sustained, even as the pressure changes from the value that favors the minimum electrode spacing [Wil03b]. This is shown in Fig. 1.2, which compares the conventional Paschen curve for parallel plate electrodes and the measured breakdown voltage for planar electrodes spaced 500 μm apart at their nearest edges. The coplanar electrodes are 1 μm thick Al on 20 μm polyimide patterned on a silicon wafer.

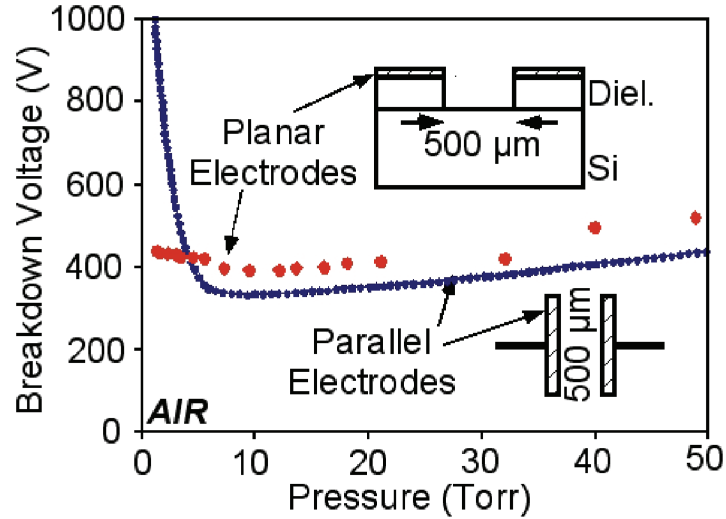

Figure 1.2: Paschen curves for parallel and planar electrodes with 500 µm spacing [Wil03b].

In addition to functioning at high pressures, microdischarges experience much higher power densities, voltage gradients, and electric field strengths in their space charge or sheath region compared to their macroscale counterparts when similar voltages are applied [Wil03a, Ede05, Kus05, Foe06, Cho07]. This allows ions to gain signification energy to induce secondary electron emission and sputtering at pressures exceeding atmosphere. Most of the voltage drop in microdischarges is across the sheath, where the electrons are accelerated to high energies due to the strong electric field. In microdischarges, the width of the sheath and the size of the microdischarge can be similar [Kus05]. They can also be on the same scale as the Debye length, which is the characteristic length scale in a plasma and the distance scale over which significant charge densities can exist. This can impact the ability of the discharge to utilize the full electrode geometry. Power densities of tens of kW-cm^{-3} to $\geq$ 1 MW-cm^{-3} are achieved in microdischarges [Ede05, Kus05, Foe06]. Power densities of this magnitude are only

achieved on the macroscale by using pulsed biases. These variations from typical macroscale behavior are due to small electrode sizes and discharge spacing.

A benefit of microdischarges is that they can exist as unbounded discharges, where their size is determined by the electrode spacing, electrode shape, pressure, and temperature as opposed to the volume of the spatial cavity in which they are generated.

DC microdischarges resemble normal or abnormal glow discharges, as they are driven by high energy secondary electron emission with glow regions self-localized over the cathodes. They resemble weakly ionized or low temperature plasma discharges as the ions and neutral gas molecules in the discharge are near the ambient temperature and in thermal equilibrium. Emission and absorption spectroscopic experiments reveal gas temperatures only 100-150 K above the ambient [Ede05]. Despite the high collision rate at pressures as high as atmosphere, the electrons are in non-equilibrium, as they have much higher temperatures. In these weakly ionized plasmas, electron-electron and electron-ion collisions can be ignored compared to electron-neutral collisions. In addition the positive column, typically observed in macroscale plasmas, can be absent. At higher operating pressures, microdischarges transition into high-temperature arcs or microarcs.

Unlike traditional glow discharges, microdischarges additionally have a large number of high energy “runaway electrons” with energies in excess of 100 eV at 1.2 Torr [Wil03a, Kus05]. These electrons are referred to as “beam” electrons, which are secondary electrons that are accelerated through the sheath without collisions while attaining high energies. These electrons primarily drive microdischarges. Their high energy creates a non-Maxwellian electron energy distribution in microdischarges

between the lower energy "bulk" electrons and the higher energy beam electrons [Wil03a, Ede05, Cho07, Hon08]. (The distribution function in macroscale discharges is typically assumed to be Maxwellian.) The bulk electrons have been found to have temperatures of 5.5-6.0 eV near the cathode and 2-3 eV between the electrodes, near the center of the discharge.

1.3.1 Calculated Steady State Parameters

To describe steady state DC microdischarges, the ionization frequency and other parameters are calculated both in the discharge and in the sheath, which is situated at the cathode. The parameters describing a DC, glow microdischarge in a microdischarge-based pressure sensor (Chapter 3) under steady-state operation at 10 Torr and 23ºC are shown in Table 1.2 to serve as a typical example. The microdischarge is created between two planar parallel electrodes with an applied voltage of 1,000 V. The parallel electrodes are spaced 50 μm apart. The microdischarge radius is measured along the axis parallel to the electrodes. As the pressure is increased, the microdischarge does change from a normal glow discharge to an abnormal glow discharge however, these discharge mechanisms are similar, and similar analysis can be applied for the different regions of operation unless the microdischarge transitions to a microarc [Cob58]. The plasma density is found to be 8.5×10^{13} cm^{-3} at 10 Torr, which is similar to the modeling results of an argon microdischarge at 50 Torr with an estimated density of 2×10^{13} cm^{-3} [Kus05]. See Appendix 1 for a detailed description of the parameters and derivations used to describe steady state microdischarges, when operating as glow discharges.

Several parameters in the sheath and discharge can be compared to yield insight concerning planar microdischarge operation. The ion density is slightly lower at the

sheath boundary, n_s, than in the discharge, n_o, 7.4 x 10^{13} cm^{-3} vs. 8.5 x 10^{13} cm^{-3}, due to the ion density decrease in the "presheath", which is situated between the discharge and the sheath. The ion velocity is higher at the sheath boundary, u_s, 2,800 m/s vs. 700 m/s, due to higher electric field in the sheath causing ion acceleration. However, as previously mentioned, microdischarges have been found to have higher electric field strengths in the sheath than predicted by traditional macroscale models [Mit08c].

Table 1.2: DC glow microdischarge operating parameters in a microdischarge-based pressure sensor.

Parameter	Symbol	Units	Value at 23ºC and 10 Torr
Plasma Density	n_o	cm^{-3}	8.5 x 10^{13}
Debye Length	λ_{De}	µm	1.4
Electron Temperature	T_e	eV	3
Electron Mobility	μ_e	m^2/ V · s	3.5
Electron Velocity	v_e	m/s	1.2 x 10^6
Ion Temperature	T_i	eV	0.056
Ion Mobility	μ_i	m^2/ V · s	2.9 x 10^{-2}
Ion Velocity	v_i	m/s	700
Ionization Rate	v_{iz}	Hz	4 x 10^7
Ion Diffusion Step Between Collisions	L_i	µm	3.7
Radius	R	µm	114
Electric Field Strength	E	V/cm	340
Sheath Parameters			
Density at Sheath Boundary	n_s	cm^{-3}	7.4 x 10^{13}
Ion Velocity at Sheath Boundary	u_s	m/s	2,800
Current Density	J_o	A/cm^2	3.3 x 10^8

The ambient pressure and temperature affect microdischarges as well. As the pressure increases, and as the temperature decreases, discharges become exponentially

more confined. The radius is decreased and the sheath is reduced in thickness. This results in an increase in electric field strength, both in the discharge and in the sheath. The current in a DC discharge is given by

$$I_{discharge} = 2\pi e n_0 \left(\frac{R^2}{\chi_{01}} \right) J_1(\chi_{01}) \mu_e E . \qquad (1.4)$$

1.3.2 Microdischarge Modeling

Several modeling techniques are used to model steady state microdischarges, most of which concentrate on cylindrically symmetric structures with a central hole through a metal-dielectric-metal sandwich stack [Foe06]. Modeling microdischarges is complex due to the differences between macroscale plasmas and microdischarges. In particular, considering the non-Maxwellian electron energy distribution function, which is not considered in Section 1.3.1, improves model accuracy. Fluid models exist which solve continuity, flux, and energy equations for separate species in the microdischarges [Boe05]. A 2-D fluid model has been developed by Kushner which takes into account both low energy bulk and high energy beam electrons and their position at various time steps [Kus05]. The model uses a Monte Carlo simulation to track the beam electrons. While more difficult, Monte Carlo simulations account for non-local plasma kinetics, collisionless heating, and non-equilibrium characteristics, which are pertinent to microdischarge operation. These are not considered in fluid models. Additional 1-D Monte Carlo models for steady state microdischarges have been developed [Cho07, Hon08]. Kushner found the ion density to be 2×10^{13} cm^{-3} at 50 Torr and 1.8×10^{14} cm^{-3} at 65 Torr in an argon microdischarge, while densities up to 5×10^{16} cm^{-3} have been reported [Mos03]. The development of a 3-D Monte Carlo simulation would be useful,

given the multiple path lengths and spatially varying non-uniform fields in microdischarges. A microdischarge model considering multiple cathodes with varied spacing would also be useful.

1.4 TYPES OF MICRODISCHARGES

Different structures are used to create microdischarges, which leads to the creation of discharges with varied characteristics and applications. They are optimized for different purposes and are fabricated using different techniques. Among the various forms of discharges created are the dielectric barrier discharge (DBD), microhollow cathode discharge (MHCD) or microstructure electrode discharge (MSE), inductively coupled microplasma (ICP), planar discharge, and parallel plate discharge. A review paper detailing these and other microdischarges as well as their behavior is presented by Foest *et al.* [Foe06].

1.4.1 Dielectric Barrier Discharge

The dielectric barrier discharge (DBD) is a microdischarge which has at least one dielectric layer in contact with the discharge, as opposed to the discharge being formed on the electrodes. It typically has an applied high voltage signal at frequencies from a few Hz to MHz. The DBD is a highly transient, low-temperature, non-equilibrium discharge formed from electrons of high mean energy, which exist over a broad range of pressures [Gib00, Bec04]. The DBD is used in the treatment of surfaces, as a mercury-free radiation source, and in plasma chemistry. Two different configurations are used in the DBD. The "volume discharge" consists of two parallel electrodes separated by air and a dielectric while the "surface discharge" has an electrode on one side of a dielectric

and a metallic cover on the reverse side of the dielectric as shown in Fig. 1.3. Both variations can operate at atmospheric pressure and consist of arc-like discharge pulses that are approximately 10 ns in duration. The cylindrical dielectric barrier discharge (C-DBD) is created in a variation of the DBD configuration. It is formed in a cylindrical dielectric alumina tube surrounded by copper electrodes, essentially using two dielectric layers between the electrodes [Mas05]. A source of 13.56 MHz is used to create a stable discharge inside the tube, and the discharge is confined between electrodes along the length of the tube.

Figure 1.3: Schematic diagrams of the (a) volume discharge and (b) surface discharge DBD.

1.4.2 Microhollow Cathode Discharge

The microhollow cathode discharge (MHCD), or microstructure electrode discharge (MSE), is a microdischarge created in a circular metal-insulator-metal sandwich structure, which spatially confines the discharge as shown in Fig. 1.4. Traditionally, the term “hollow cathode” refers to a mode of operation in which the sustaining voltage drops as the current increases (hollow cathode mode) but the MHCD is commonly operated as a normal or abnormal glow discharge. However, it is referred to as a MHCD or microdischarge regardless of the mode of operation [Foe06]. Operation of an atmospheric pressure microdischarge in a cylindrical hollow cathode geometries was first reported by Schoenbach *et al.* [Sch96]. MHCDs have also been operated in two

dimensional arrays, in series, and in parallel [Pen00, Ede03]. The gas temperature, electric field distribution, and electron densities have been determined experimentally and through modeling [Kur04, Kus05, Wan05]. Research on the MHCD is motivated by uses in industrial applications including instantly activated reflectors and absorbers for electromagnetic radiation in industrial applications, surface treatments, thin film depositions, remediation and detoxification of gaseous pollutions, and gas lasers [Sta99, Mos03].

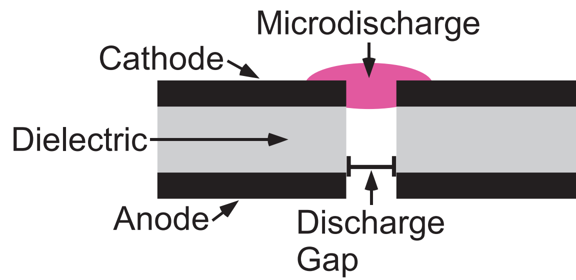

Figure 1.4: Schematic diagram of the microhollow cathode discharge configuration.

1.4.3 Inductively Coupled Microplasma

The microfabricated inductively coupled plasma (mICP) has been created using a microdischarge without contacting electrodes [Hop00]. A planar spiral inductor coil, 5 mm, 10 mm, or 15 mm in diameter is connected in series with a tuning and load capacitor to create a strong RF field. A gas is enclosed in glass at pressures of 0.1-10 Torr and when the LC circuit resonates near a specified frequency, previously 450 MHz, an electron current flows through the conductive plasma region to oppose the generated RF magnetic field from the coils. Operating frequencies other than 450 MHz have also been characterized [Iza02].

1.4.4 Planar Discharge

The planar discharge is created above thin-film electrodes, typically patterned on a dielectric or glass substrate as shown schematically in Fig. 1.5. The planar microdischarge is similar to the MHCD, but differs in that it is not confined in a circular hole. Rather, it expands between electrodes based on the applied voltage bias and pressure. However, it has been confined in microplasma chambers [Eij00] and in channels (70 μm x 500 μm) when necessary [Bes02]. This discharge is commonly created using DC biases at pressures as high as atmosphere. Devices utilizing the planar discharge can be fabricated using traditional IC microfabrication techniques, making the devices attractive from a fabrication standpoint. The planar discharge has been used as an optical emission sensor in air [Eij00, Bes02, Mit08b] and as a liquid sensor [Wil02, Que05]. The planar DC discharge has been modeled, indicating that there are high ion densities and strong electric fields, in the sheath, as in other microdischarges [Wil03a].

In the planar microdischarge, Paschen's curve is not applicable in the traditional sense as the breakdown voltage for fixed electrodes is relatively insensitive to pressure in the 1-20 Torr range, remaining at ~400 V in air. This behavior results from multiple path lengths, which are simultaneously available between electrodes in most microstructures, making the discharge gap a variable. This permits a low breakdown voltage to be sustained as the pressure is decreased, due to the increasing discharge path length.

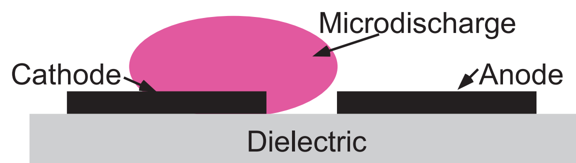

Figure 1.5: Schematic diagram of typical planar electrodes and planar microdischarge.

1.4.5 Parallel Plate Discharge

The parallel plate discharge is created between parallel bulk electrodes spaced by a dielectric layer or substrate as shown schematically in Fig. 1.6. The parallel plate microdischarge is similar to the MHCD and the planar discharge in that the discharge is not shielded by a dielectric layer. This microdischarge provides a constant electrode discharge gap spacing across the electrode surface. This uniformity allows DC operating parameters to be calculated without the high electric field regions encountered at the electrode edge in the planar discharge.

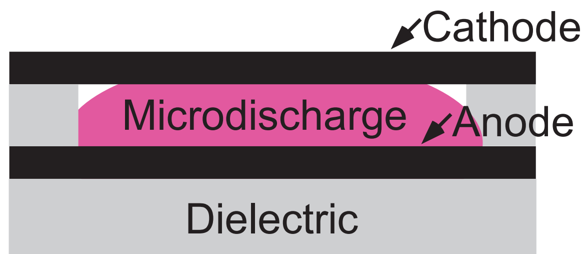

Figure 1.6: Schematic diagram of typical parallel plate electrodes and microdischarge.

1.5 MICRODISCHARGE DEVICES

1.5.1 Display Technology

Miniature plasma display technology has evolved throughout the years into a heavily researched and developed industry. In the 1950's, plasma based Nixie tubes were used to display numbers using multiple cathodes in the shape of numerical digits and a single mesh anode [Mcl60, Wes68]. Individual pixels were created by A.M. Skellet using small cavities in an aperture plate, surrounded by two glass plates [May56]. Voltage was applied to perpendicular anode and cathode lines to specify certain pixels. Unfortunately, energizing an individual bar initiated breakdown in neighboring pixels as

well. In 1963, Thompson added series resistors to hold each cavity at the specified voltage, allowing individual pixels to be turned on [Lea63]. In 1964, Bitzer placed electrodes on the outside of glass plates and cavities, creating the first AC plasma display with capacitive paths between electrodes [Bit66]. This technology required smaller drive voltages and individual pixels could hold a state for short periods of time. The first plasma display screen was commercialized using this technology in 1968 by Owens-Corning. Significant developments in modeling and in the technology have been made, and the technology is now recognized by the industry [Sob98, Got99]. Flat panel displays and UV sources for these displays have been created using arrays of microhollow cathode discharges [Shi99, Pos00]. Flexible arrays using microdischarges have also been developed [Par00].

1.5.2 Microdischarges for Chemical Analysis

All of the microdischarges described in Section 1.4 are used in microscale chemical analysis. Microscale spectral sensors have been developed using DBDs, MHCDs, planar discharges, ICPs, capacitively coupled plasmas (CCPs), micro-wave-induced plasmas, and discharges using liquid electrodes. A detailed description of microdischarge-based optical emission sensors used for gas characterization is presented in Chapter 4. Microdischarge-based optical emission sensors for the detection of water impurities have been developed using planar microdischarges [Jen02, Wil02, Que05, Mit08b]. Biochemicals were also detected at atmospheric pressure using fluorescence excited by microdischarges [Mit06a]. Review papers detailing microdischarge applications in chemical analysis are presented by Broekaert, Franzke *et al.*, and Karanassios [Bro02, Fra03, Kar04].

1.5.3 Other Microdischarge Devices

A variety of other devices and experiments utilize and encounter microdischarges [Wil03b]. Efforts have been made to use porous silicon as an LED like device by creating localized internal arcs [Koz96, Hua98]. Microdischarges are also created around imperfections in heavily biased PIN diodes [Vas90] and other semiconductor devices [Kim90, Kon90]. Furthermore, microplasma jets have been operated in torch systems [Rao92]. Laser-generated microplasmas have been created to study fusion grade inertial confinement plasmas [Erk95, Von95], and are used in numerous spectroscopy studies [Nan92, Sim93]. Finally, microdischarges have been used in the localized etching [Wil01a], and in the deposition of silicon [Wil07].

1.6 Microdischarge-Based Microtransducers

Microsystems have an inherent need for pressure control, both sensing and actuation, due to the high sensitivity of micromachined devices often enclosed in hermetically sealed environments. The enclosed environments provide for optimal device operation and for protection from external contamination, but the enclosed environments themselves require setting and measurement. Devices utilizing microdischarges are particularly attractive for pressure control as they typically only require two electrodes between which microdischarges are created. This allows them to be small, simple to fabricate, and inexpensive, allowing room, effort, and cost to be devoted to the primary packaged device. Additionally, microdischarge-based devices are well-suited for high temperature applications without requiring significant modifications.

The development of microtransducers, which utilize microdischarges, additionally furthers the knowledge concerning microdischarge operation. The development of a microdischarge-based pressure sensor involves developing an understanding of the changing microdischarge characteristics with pressure. Likewise, the development of a pressure controlling device requires the development of an understanding of microdischarge sputtering. The knowledge gained concerning microdischarges also helps define the similarities and differences between them and their macroscale counterparts.

1.6.1 Vacuum Generation Using Microdischarges

Vacuum-sealed cavities are essential for a variety of micromachined sensors and actuators. For example, resonating devices such as gyroscopes and frequency references utilize them to minimize damping; pressure sensors utilize them as references; and electrostatic actuators such as switches are packaged in them to minimize the likelihood of charge accumulation and corrosion. The absorption or removal of gas from these sealed cavities is used to lower the pressure below the initial sealing pressure or to maintain a desired pressure over extended time periods. This is necessary because as the cavity volume is scaled down, its internal pressure can be easily increased by even small amounts of parasitic leakage, such as outgassing from surfaces or diffusion of gases through the cavity walls. For example, with a 10 μTorr sealing pressure in a microscale package, the outgassing rate is 2×10^{-8} (Liter x Torr)/(cm x sec) [Mit06b]. Outgassing rates are also increased by heating, and removal of moisture and less reactive gases such as nitrogen can be particularly challenging.

There are several microscale options for gas absorption from sealed cavities including coatings and pumps. Options that eliminate moving parts are promising from

the viewpoints of longevity and field usability. Past efforts involving the application of coatings to the inside of sealed cavities include non-evaporable getters (NEGs), thin-film getters (e.g. Nanogetters^{TM}), and reactive sealing. While these technologies work on both the macroscopic and microscopic scales, they typically operate in the millitorr range and require activation temperatures of 200-550°C. Micromachined thermal molecular pumps without moving parts have been proposed and Knudsen pumps have also been developed. However, these typically require high temperatures as well [Hob00, McN05]. For devices that require pressure control near their maximum operating temperature (typically 100-150ºC), alternative or complementary means of controlling the pressure are needed.

One goal of this thesis is to describe a new method of reducing the pressure in large cavity packages, through the development of on-chip microscale-sputter-ion pumps (micro-SIPs). These devices utilize thin-film titanium electrodes, patterned on glass substrates and exposed to the cavity environment. Microdischarges between the electrodes sputter the cathodes, resulting in the selective chemisorption of oxygen, nitrogen, and other titanium-reactive gases. In this way they operate in the manner of macroscale-sputter-ion pumps.

Micro-SIPs are designed to provide several advantages over the previously described pressure controlling technologies. They are capable of reducing humidity and selectively removing titanium-reactive gases, while leaving non-reactive gases, without significantly increasing the ambient temperature. The duration of micro-SIP usage also gives users control over the amount of gas removed. Micro-SIPs may be operated when a package is sealed to initially lower the pressure, or operated after a long period of leakage to return the package to an initial pressure. In addition, micro-SIPs do not require heating

and do not significantly heat the environment they are operated in. They can be fabricated using a single mask. This technology can also potentially create millitorr or microtorr operating pressures in microscale packages as discussed in Chapter 5. The operation of these devices has previously been reported in journal form [Wri07b].

Two metrics can be used to compare these described gas removing technologies including the presented micro-SIPs. These metrics are the fabrication complexity and the required operating temperature of the device. The fabrication complexity is assessed by examining the number of steps required to make and incorporate the device into a package. Fig. 1.7 plots this comparison. A detailed comparison is presented in Chapter 2.

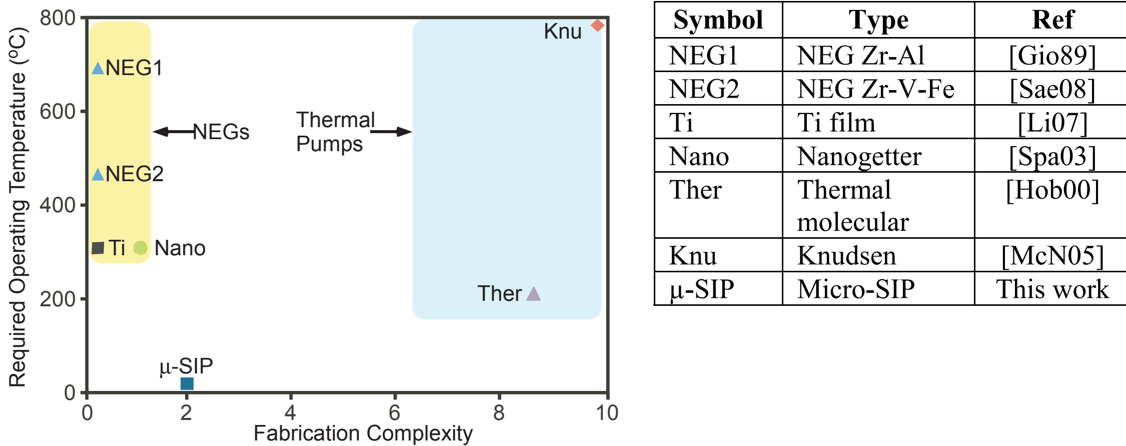

Symbol	Type	Ref
NEG1	NEG Zr-Al	[Gio89]
NEG2	NEG Zr-V-Fe	[Sae08]
Ti	Ti film	[Li07]
Nano	Nanogetter	[Spa03]
Ther	Thermal molecular	[Hob00]
Knu	Knudsen	[McN05]
µ-SIP	Micro-SIP	This work

Figure 1.7: Plot of required device operating temperature vs. fabrication complexity for several pressure reducing devices. (See table for the list of abbreviations and references.)

1.6.2 Pressure Sensing Using Microdischarges

Pressure sensors amenable to high temperatures have uses in numerous industrial sectors, and have additionally been used in gas turbine engines, coal boilers, furnaces, and machinery for oil/gas exploration. Macroscale fiber optic pressure sensors have been

developed, but microscale sensors are advantageous as they can be utilized in small volume cavities. These include combustion chambers, intake manifolds, and exhaust manifolds of internal combustion engines [Flo90, Moc91, Che04]. Their small size also allows attachment to gas turbine engines [Pul02]. Additionally, they can be inserted down boreholes in oil/gas exploration equipment [Stu82]. Some high temperature fiber optic pressure sensors have been reduced in size to several feet in length, including a fiber optic based sensor using cubic zirconia prisms which has an operating temperature of up to 1,000ºC [Pen05]. However, further miniaturization of high temperature sensors expands their use to new applications.

A variety of microscale pressure sensing solutions have been explored, including Fabry-Perot and other interferometers. These use an optically reflective cavity on the end of a fiber optic cable; the cavity size changes with pressure, causing measurable interference changes in reflected light. A thin diaphragm is typically used as the reflective surface. Operating temperatures up to 800˚C have been achieved with sapphire membranes. An interferometer-based sensor has also been fabricated inside a fiber optic cable. Another sensing technology uses Bragg gratings, which are photo inscribed into fibers, and used to trace wavelength shifts caused by pressure and temperature changes at temperatures exceeding 350˚C, and potentially over 1,500˚C. Piezoresistive pressure sensors with diaphragms made from silicon carbide, and more recently even silicon, have been reported to operate at 600ºC. Sapphire membranes are also used in this context.

A second goal of this thesis is to describe a new class of microdischarge-based pressure sensors which can be used in the described context. They operate by measuring

the change, with pressure, in the spatial current distribution of pulsed DC microdischarges.

These sensors are designed to provide several contributions to the field of microscale high temperature pressure sensing. These are the first microdischarge-based high temperature pressure sensors and they demonstrate comparable functionality to other technologies, and the potential of a microdischarge-based approach. They are designed to operate over a pressure range of 10-2,000 Torr at temperatures as high as 1,000˚C, and potentially down to cryogenic temperatures. Additionally, they are designed for high sensitivity and a low temperature coefficient of sensitivity. They are also designed to provide ease of fabrication, with as few as a single mask step, electrical transduction, and structural simplicity. The operation of and results from the sensors have previously been reported in journal form [Wri08].

Two metrics can be used to compare these described technologies including the presented microdischarge-based pressure sensors. These metrics are the required number of fabrication steps and the maximum operating temperature of these pressure sensors. Fig. 1.8 illustrates this comparison. A detailed comparison is presented in Chapter 3.

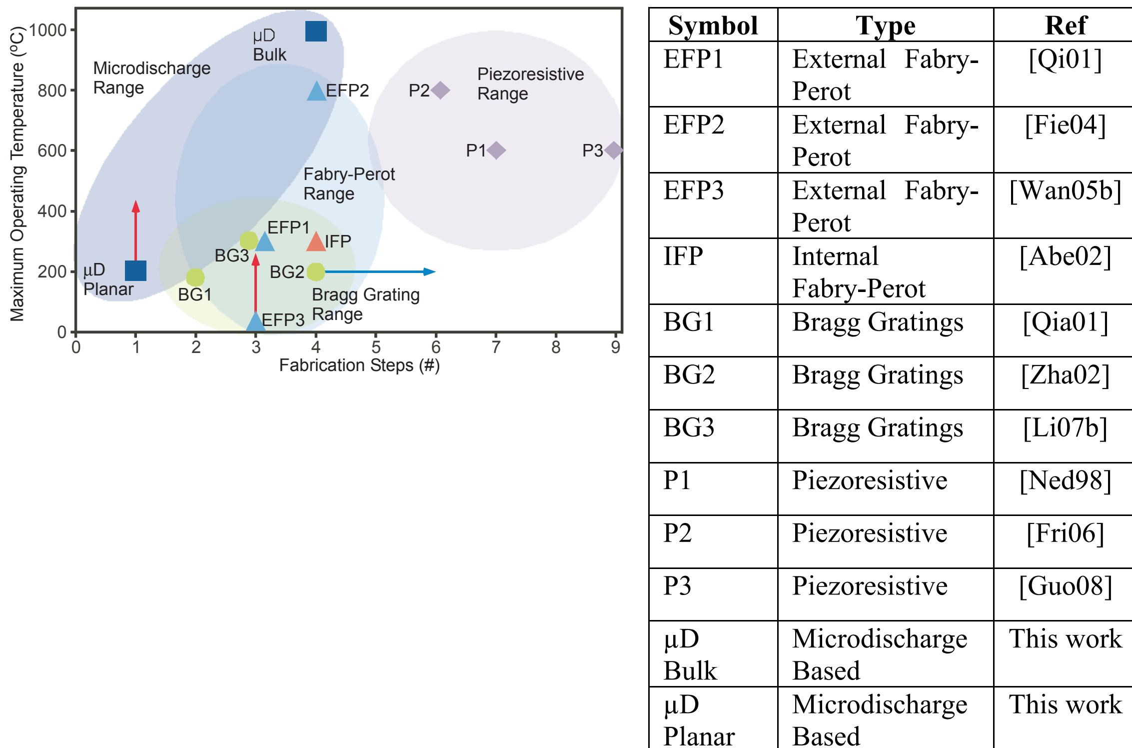

Symbol	Type	Ref
EFP1	External Fabry-Perot	[Qi01]
EFP2	External Fabry-Perot	[Fie04]
EFP3	External Fabry-Perot	[Wan05b]
IFP	Internal Fabry-Perot	[Abe02]
BG1	Bragg Gratings	[Qia01]
BG2	Bragg Gratings	[Zha02]
BG3	Bragg Gratings	[Li07b]
P1	Piezoresistive	[Ned98]
P2	Piezoresistive	[Fri06]
P3	Piezoresistive	[Guo08]
µD Bulk	Microdischarge Based	This work
µD Planar	Microdischarge Based	This work

Figure 1.8: Plot of maximum operating temperature vs. fabrication steps for various high temperature pressure sensors. (See table for the list of abbreviations and references.)

1.6.3 Chemical Sensing Microsystem

The detection of chemicals in harsh environments is important to numerous industries and researchers. In particular, the use of microscale harsh environment chemical sensors can potentially reduce the cost of drilling for petroleum exploration, field development, and long-term geological monitoring [Alb00]. During petroleum exploration and pumping, the flow of removed material is a combination of oil, water, and gases. Continuous down-hole analysis of gas during petroleum pumping is useful for the control of product quality, the detection of unwanted contaminants, and the optimization of product treatment downstream [Hun97]. Continuous chemical analysis is also useful during petroleum detection. The down-hole sensors for detection and monitoring must be able to withstand elevated temperatures and pressures. They also

must be able to detect carbon, sulfur-containing gases, and contaminant gases such as H_2S and CO_2 [Col95, Hun97]. Other high temperature applications also require chemical sensing and monitoring. For example, automobile emission control requires monitoring of the levels of nitric oxides (NO_x) and hydrocarbons (C_xH_y).

Numerous miniature high temperature chemical sensors have been developed, many of which utilize the changing properties of thin films in the presence of certain gases or chemicals. Chemiresistors, or resistor based chemical sensors, have a selective layer whose conductivity is modulated by interactions with analyte(s). Semi-conductive metal oxide chemiresistors are used extensively at high temperatures. Another sensor technology, metal insulator semiconductor sensors, operate by measuring capacitance changes caused by the concentration of certain gases and are fabricated from silicon carbide for high temperature operation. Another technology uses Schottky-barrier sensors to measure voltage bias shifts in the presence of chemicals, and uses nitrides as insulating layers for high temperature operation. Another commonly used senor technology is the ChemFET, which is essentially a field effect transistor, which measures the change in work function caused by the presence of certain gases. Finally, surface acoustic wave devices measure the change in resonant frequency of acoustic waves on the surface of piezoelectric materials with changing chemical concentrations.

A third goal of this thesis is to explore the integration of the developed devices in a microdischarge-based system, which detects chemicals in the context of the previously described high temperature chemical sensors. The system has three microdischarge-based devices in total: a pressure sensor, a gas purifier, and an optical emission sensor. The system operates by obtaining a gas sample while monitoring the pressure, purifying

the sample using a microscale-sputter-ion pump, and determining the chemical composition of the sample using an optical emission sensor at temperatures up to 200ºC.

This system is designed to provide several contributions to the field of microscale chemical sensing. The microdischarge-based optical emission sensors can detect numerous gases concurrently, while the previously discussed technologies typically focus on the detection of a single or several gases with high sensitivity. The system is designed to demonstrate the ability of micro-SIPs to be used for gas purity control and gas purification, in addition to pressure and humidity control for which they were originally designed. Additionally, this chemical detection system is designed to demonstrate the ability of the microdischarge-based devices to function concurrently. The system may be capable of operation at even higher temperatures, expanding its potential applications. This system has been previously described in [Wri07a].

Two metrics can be used to compare these described chemical detecting technologies including the microdischarge-based optical emission chemical sensing microsystem. These metrics are the number of chemicals detected by a single device and the device operating temperature range. Fig 1.9 plots this comparison. A detailed comparison of all of these technologies is presented in Chapter 4.

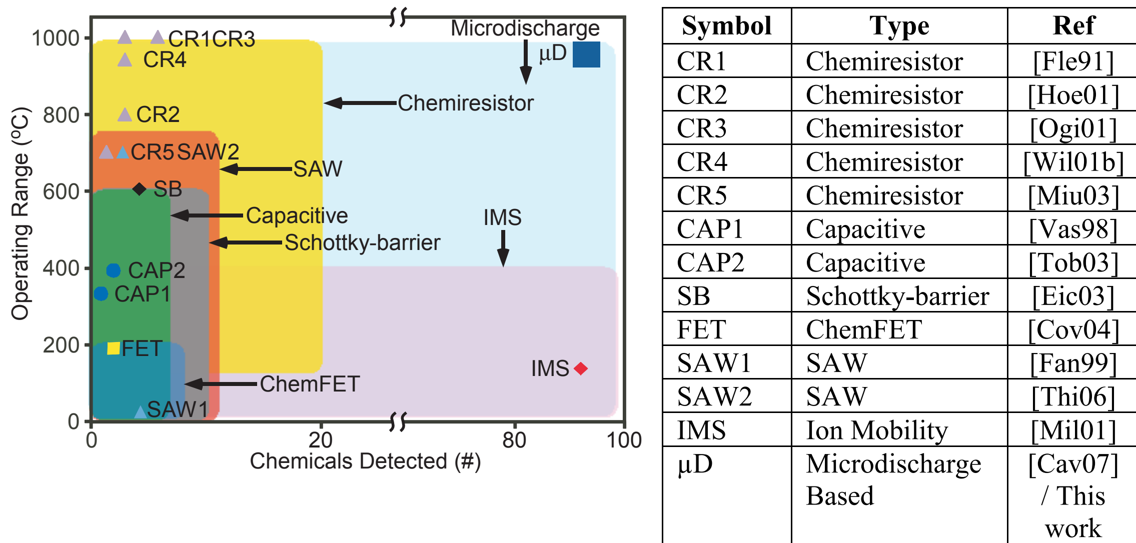

Symbol	Type	Ref
CR1	Chemiresistor	[Fle91]
CR2	Chemiresistor	[Hoe01]
CR3	Chemiresistor	[Ogi01]
CR4	Chemiresistor	[Wil01b]
CR5	Chemiresistor	[Miu03]
CAP1	Capacitive	[Vas98]
CAP2	Capacitive	[Tob03]
SB	Schottky-barrier	[Eic03]
FET	ChemFET	[Cov04]
SAW1	SAW	[Fan99]
SAW2	SAW	[Thi06]
IMS	Ion Mobility	[Mil01]
µD	Microdischarge Based	[Cav07] / This work

Figure 1.9: Plot of operating temperature range vs. number of detectable chemical species for various high temperature gas sensors. (See table for the list of abbreviations and references.)

1.7 Organization of Thesis

The thesis is organized as follows. This chapter presents microdischarges and their use in microscale devices. It also introduces and briefly compares the microdischarge-based devices discussed in this thesis to current technologies. Chapter 2 presents microscale-sputter-ion pumps and their use in the controlled reduction of cavity pressure and humidity. The influence of (1) the micro-SIP design, (2) the environment in which micro-SIPs are operated, (3) the mode of micro-SIP operation, and (4) microdischarge characteristics on micro-SIP pumping operation are investigated. A model estimating micro-SIP air removal rates is also presented. Chapter 3 presents microdischarge-based pressure sensors and their operation at temperatures of up to 1,000ºC and pressures up to 2,000 Torr. Chapter 4 presents an exploration of the use of these devices in a harsh environment microdischarge-based system which detects chemicals at temperatures of up to 200ºC. Chapter 5 concludes the thesis and presents

potential future work to continue the development of these high-temperature microdischarge-based devices.

CHAPTER 2

VACUUM GENERATION USING MICRODISCHARGES

This chapter discusses on-chip titanium microscale-sputter-ion pumps (micro-SIPs) and their use in the controlled reduction of pressure in large cavity packages. The influence of (1) the micro-SIP design, (2) the environment in which micro-SIPs are operated, (3) the mode of micro-SIP operation, and (4) microdischarge characteristics on micro-SIP pumping operation are investigated. Some of the microdischarge characteristics that impact micro-SIP performance are the Townsend ionization coefficients, ionization efficiencies of various gases, the composition of the exposed electrode pair surfaces, and the gas temperature. These are explored through examining micro-SIP operation with varied discharge gap spacing at varied pressures, the removal rates of various gases, humidity removal, the ability of pulsed micro-SIP operation to improve efficiency, and the effect of thermally assisted discharges.

Section 2.1 presents the relevance of micro-SIPs and a detailed comparison of other gas removal technologies. Section 2.2 presents the concept and operation of micro-SIPs. Section 2.3 presents a theoretical model used to determine gas removal rates. Section 2.4 presents several designs and the fabrication method used. Section 2.5 presents the results of various experiments. Section 2.6 presents the results of X-Ray photoelectron spectroscopy in determining electrode composition.

2.1 BACKGROUND

Vacuum-sealed cavities are essential for a variety of micromachined sensors and actuators. For example, resonating devices such as gyroscopes and frequency references utilize them to minimize damping; pressure sensors utilize them as references; and electrostatic actuators such as switches are packaged in them to minimize the likelihood of charge accumulation and corrosion. The absorption or removal of gas from these sealed cavities is used to lower the pressure below the initial sealing pressure or to maintain a desired pressure over extended time periods. This is necessary because as the cavity volume is scaled down, its internal pressure can be easily increased by even small amounts of parasitic leakage, such as outgassing from surfaces or diffusion of gases through the cavity walls. For example, with a 10 μTorr sealing pressure in a microscale package, the outgassing rate is 2×10^{-8} (Liter x Torr)/(cm x sec). This increased the pressure to 12 Torr from the initial sealing pressure [Mit06b]. Outgassing rates are also increased by heating. Removal of moisture and less reactive gases such as nitrogen can be particularly challenging. Two important metrics which determine the usefulness of pressure reduction devices for different applications are the ease with which the devices can be fabricated and the minimum temperature required by the devices for operation.

Numerous coatings and pumps have been suggested for use on the microscale to evacuate small cavities. Options for gas absorption or removal that eliminate moving parts are promising from the viewpoints of longevity and field usability, and can be compared. One of the simplest methods of removing gas from sealed packages is to use non-evaporable getters (NEGs). NEGs are typically included in hermetically sealed

environments in the form of strips or pellets. They remove gases through oxide formation, hydride formation, and surface chemisorptions. In this way, package pressure can be lowered below the sealing pressure. Reactive sealing using oxide, nitride, or polysilicon deposition provides another method of pressure reduction, but also requires heating [Guc88].

Macroscale metallic getters have been used for decades in cathode ray tubes, field emission flat panel displays, particle accelerators, semiconductor processing equipment, and other vacuum equipment. NEGs were first applied to MEMS devices in the mid 1990's in tablet or strip form, and typically consist of sintered metal particles. They are packaged on the inner surfaces of vacuum cavities or in separate micromachined cavities adjacent to the operating chips.

NEGs are formed from reactive metals and alloys. Pure metals of Ba, Al, Ti, Zr, V, and Fe are used as well as alloys such as Zr-Al and Zr-Fe-V. Unfortunately, a high-temperature activation step is required in vacuum, or in a hydrogen containing reducing ambient, to remove the NEGs' surface oxide layers so oxygen, nitrogen, and hydrocarbons can be chemisorbed. Hydrogen can be trapped at room temperature. This activation is performed by annealing an entire package containing the NEG, or by Joule heating the NEG strip. Standard getters, such as various SAES getter group's Zr-Fe-V NEGs, are activated at temperatures of 300-750˚C [Hal91, Hen94, Sae08]. NEGs have been shown to work at pressures between 10^{-5} Torr and 400 Torr. They also absorb different gases at different rates [Hen94]. A thin-film getter deposited in a cleanroom environment with much smaller particles than traditional NEGs has been developed and

named Nanogetters™, but still requires activation at temperatures of 300˚C or higher [Spa03].

Using NEGs in microscale packaging applications has several additional drawbacks in addition to requiring heating: 1) They must be deposited or attached to a micro-package, 2) NEGs saturate over time and do not return to their original state, even with reactivation [Hen94], and 3) the sintered metal particles can shift inside the package, interfering with the MEMS devices. A packaging scheme, shown in Fig. 2.1, has been developed to minimize the number of particulates contaminating the packaged MEMS devices while allowing gas to pass between cavities, equalizing the pressure.

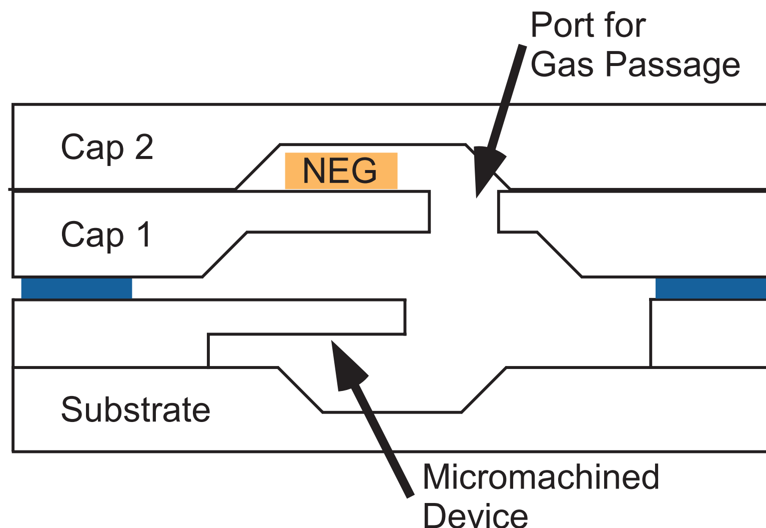

Figure 2.1: Illustration of NEG isolation from micromachined device in a microscale package.

Thin-film titanium has been used as a NEG without microdischarges or sputtering. However, the titanium film requires heating to temperatures of 300˚C to begin absorbing gases and the heating process causes outgassing [Li07]. When removing N_2, CO, or O_2, the pressure increase is larger than the obtainable pressure decrease

resulting from the titanium NEG operation, even when heated to 500˚C. This indicates a separate outgassing step is necessary. Titanium film also chemisorbs fewer molecules than an alloy of Zr-V-Fe [Gio89].

Various thermal molecular pumps without moving parts have been developed and could potentially be applied to reduce package pressure. They use temperature differences and micromachined structures to operate. Unfortunately, they require liquid nitrogen [Hob00] or temperatures of up to 1,100˚C [McN05].

Microscale orbitron pumps have previously been proposed. A chip-scale pump was proposed and the electron motion has been simulated but the pump does not appear to have been fabricated to date [Koo05]. A miniature ring orbitron ion pump was also proposed but never developed [Wil99, Wil08].

Another option for the controlled reduction of pressure in large cavity microscale packages are on-chip microscale-sputter-ion pumps (micro-SIPs). These devices utilize thin-film titanium electrodes patterned on glass substrates and exposed to the cavity environment. Micro-SIPs operate in the manner of macroscale-sputter-ion pumps: they utilize microdischarges between thin-film titanium electrodes on a microchip to sputter a cathode and chemisorb gases through reactive sputtering. The amount of air removed is controlled through the duration of the applied voltages that energize the created microdischarges. The use of microdischarges in sputter-ion pumps is appealing because the discharges are very localized (to <500 μm) and allow air removal at room temperature and atmospheric pressure without significantly increasing the ambient temperature. In addition, micro-SIPs have no moving parts, increasing durability.

Several devices have used sputtering caused by microdischarges. This sputtering has previously been used to synthesize thin films through cluster-beam deposition [Bar99]. It has also been used in a microscale pump, which utilizes an electron-generating cathode to impart motion to air for the purpose of cooling electronics, as opposed to removing pressure from a sealed cavity [Go06].

Various pressure reduction methods without moving parts are compared in Fig. 2.2, showing the fabrication complexity and temperature difference necessary for device operation. The fabrication complexity is assessed by examining the number of steps required to make and incorporate the device in a package. While all of the devices can reduce the pressure in cavities without moving parts, some applications cannot be heated to the temperatures required to activate NEGs or operate pumps. For example, devices using piezoelectric materials cannot be heated as a common piezoelectric material, lead zirconate titanate (PZT), undergoes phase transitions negatively affecting the Young's modulus and mechanical losses at 250ºC [Bou05]. The Curie temperature of various PZT composites, indicating further phase transitions, is between 250ºC and 350ºC [Pie08]. This makes micro-SIPs an attractive alternate or a complementary means of controlling pressure. In addition, an ability to reduce pressure without heating is advantageous as outgassing occurs during the heating process, increasing pressure. Micro-SIP pressure reduction can be closely controlled by regulating the power to reach desired pressures.

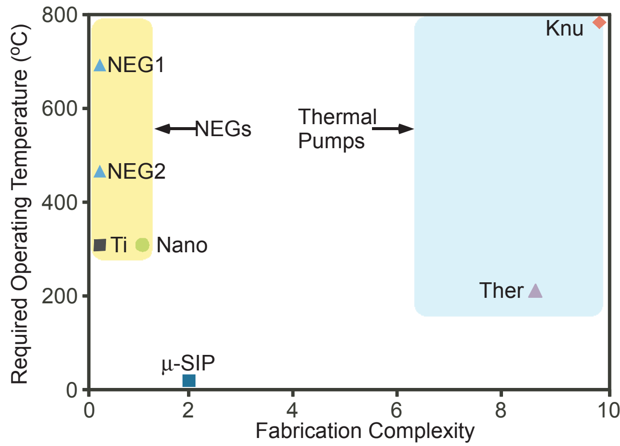

Symbol	Type	Ref
NEG1	NEG Zr-Al	[Gio89]
NEG2	NEG Zr-V-Fe	[Sae08]
Ti	Ti film	[Li07]
Nano	Nanogetter	[Spa03]
Ther	Thermal molecular	[Hob00]
Knu	Knudsen	[McN05]
μ-SIP	Micro-SIP	This work

Figure 2.2: Plot of required device operating temperature vs. fabrication complexity for several pressure reducing devices. (See table for the list of abbreviations and references.)

2.2 Device Concept and Operation

The microchips that constitute micro-SIPs consist of one or more planar thin-film titanium anode-cathode pairs patterned on glass substrates separated by discharge gaps. They can be enclosed in hermetically sealed industry-standard packages and operated to remove air and humidity, as shown in Fig. 2.3.

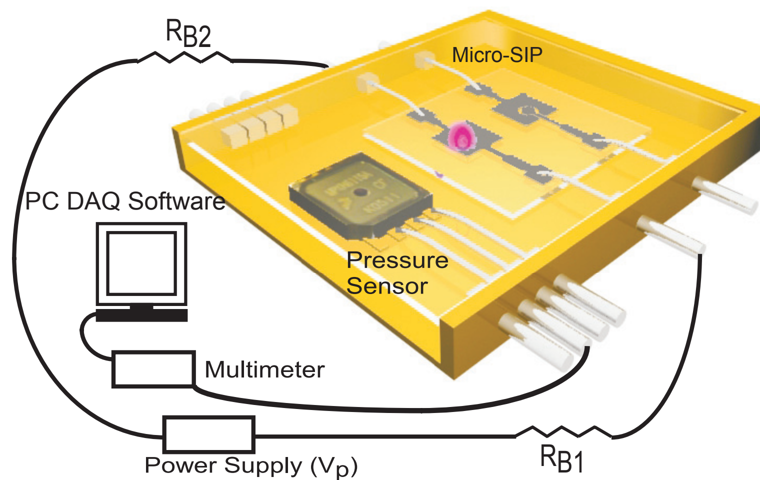

Figure 2.3: Schematic of a commercial package, commercial pressure sensor, micro-SIP, power, and readout circuitry. R_{B1} and R_{B2} are ballast resistors of varied resistance which limit the current flowing between the anode and cathode.

Microdischarges are created by applying voltages across the micro-SIP electrode pairs, and the cathodes are sputtered while chemisorbing select gases. Schematics displaying basic micro-SIP features are shown in Fig. 2.4. The micro-SIPs are designed with circular discharge gaps for uniform sputtering and with large cathodes to increase the amount of available titanium. Increasing the voltage differences between micro-SIP electrodes increases the proportion of beam electrons with energies above 100 eV [Kus05]. For this reason, relatively high voltages of 1,000 V to 1,500 V are applied to operate the micro-SIPs. Power is applied through cavity leads (or, alternatively, by adjacent circuits that are copackaged with the micro-SIPs). Given that typical microelectronic devices operate with low voltages (< 15 V), separate circuits and isolation are required to provide the high voltages required to operate micro-SIPs. Typically, 20 μm of polyimide provides sufficient insulation for this [Wil01a]. External ballast resistors are used in series with the electrodes to limit the current and provide control over discharge energy.

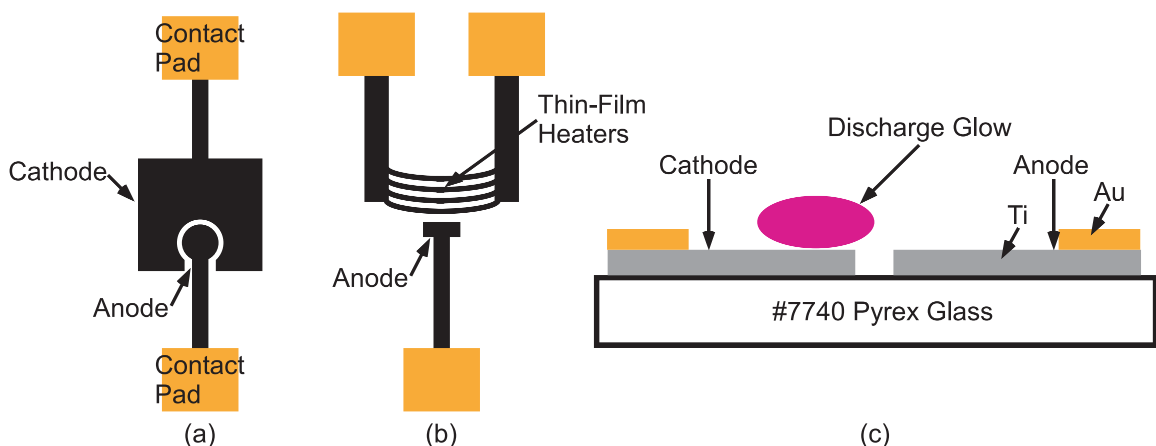

Figure 2.4: Schematics of micro-SIP electrodes: (a) basic design, top view, (b) heated cathode design, top view, and (c) side view.

Because of the high collision rate encountered at the operating pressures of the micro-SIPs, the discharges are considered low temperature plasmas and the ions and neutral gas species in the discharges are almost in thermal equilibrium with the ambient environment as discussed in Chapter 1, Section 1.1. This results in only very small temperature increases inside the packages during operation of $< 2.5^{o}C$, as experimentally determined by measuring the increase resulting from heating during micro-SIP operation. However, the electrons are at much higher temperatures in the microdischarges.

The sputtered ions from micro-SIPs should not affect surrounding micromachined devices at higher pressures due to their low mean free path. At lower pressures, micro-SIPs can be enclosed in separate wells to block sputtered ions, a concept similar to the walls used in macroscale-SIPs to block ions from sensitive structures. Additionally, ions are implanted within the titanium cathodes due to their high energy, which can reach 100 eV, as in macroscale SIPs. This potentially allows micro-SIPs to remove non-reactive gases with modified cathode geometries to contain implanted ions so they are not re-released when the cathode is significantly sputtered.

Micro-SIPs function in a manner similar to traditional SIPs, operating by reactively sputtering titanium targets, but there are several differences as well. Macroscale-SIPs create plasma regions between the anodes and cathodes while using external magnets to spatially confine the carriers. In contrast, microdischarges do not require magnetic confinement, as past work shows that discharges between narrowly spaced electrodes can be spatially confined in a very effective manner by controlling the powering scheme [Wil01a, Wil04, Wil07]. In addition, stable microdischarges can be created and reactive sputtering can occur at pressures as high as atmospheric pressure

through the creation of very localized microdischarges, without creating unstable arc discharges [Mit08b]. Having a small distance (*d*) between electrodes at a relatively high pressure (*p*), atmospheric, allows the product *pd* to be similar to the macroscale case, resulting in low breakdown voltages and in lower current densities as discussed in Chapter 1, Section 1.3. At 760 Torr, the minimum breakdown voltage in air is achieved with an ~8 μm gap. This causes the breakdown voltages at high pressures, when using very small gaps, to be similar to those found in large volume, low-pressure plasmas. A discharge gap distance less than 1 mm is required to approach the minima in Paschen's curves for almost all gases at atmospheric pressure [Foe06].

Titanium has been shown to getter CO, CO_2, H_2, N_2, and O_2 with high efficiency in the more general category of getter-ion pumps [Den67]. It also reacts with water vapor to form oxides and liberate hydrogen in these getter-ion pumps [Hol59]. In macroscale titanium SIPs the deposited film layers, when removing air, have been shown to consist of 44% Ti, 40% N, 8% O, and 8% C [Ves05]. Titanium and nitrogen are known to be uniformly distributed throughout the thickness of the deposited layer as well. These data indicate that one titanium atom is able to getter approximately one atom from the surrounding air environment [Col94]. However, microscale discharges differ in some ways, which can potentially change this [Wil03a]. In particular, they are typically localized above the cathode, which can affect the redeposition pattern of sputtered molecules and, consequently, the final distribution of compounds. In addition, microdischarges have electrons and ions with extremely high energy, which can affect the binding of titanium with gas molecules. Titanium films have been shown to

chemisorb oxygen without microdischarges, but require temperatures of 300ºC to do so [Li07].

In summary, like their larger-scale counterparts, microscale titanium sputter-ion pumps operate by chemisorbing gases from the environment. The devices differ in their size, the need for magnetic confinement, and useful operating range because micro-SIPs present localized plasmas at atmospheric pressure.

2.3 Theoretical Considerations

The gas removal rates achieved by micro-SIPs depend on a number of design and operating parameters, such as electrode shape, spacing, material, discharge energy, and ambient pressure. The discharge and the Townsend ionization coefficients used to describe the discharge are initially discussed. In the context of this background information, the influence of the operating parameters on the discharge, ionization coefficients, and the pressure reduction rate is examined.

The discharges utilized in micro-SIPs primarily operate as normal glow discharges (Chapter 1, Section 1.1) with the unique characteristics of microdischarges (Chapter 1, Section 1.3). However, operating micro-SIPs with larger discharge gaps at higher pressures causes the microdischarges to transition to arc discharges or microarcs (Chapter 1, Section 1.1), reducing the micro-SIP effectiveness.

The first and second Townsend ionization coefficients characterize the rate of electron impact ionization and the behavior of microdischarges, as DC discharges are sustained by electron movement. They are influenced by the discharge gap spacing between electrodes and affect the gas removal rates of micro-SIPs. Additionally, the

breakdown conditions of DC discharges depend on these coefficients, which will be described. The first Townsend ionization coefficient, α, indicates the number of electron-ion pairs created by an electron per unit distance and is given as [Lie94]

$$\alpha = pA\exp\left(-\frac{Bp}{E}\right), \tag{2.1}$$

where p is the pressure, E is the electric field strength, and A and B are determined experimentally and found to be roughly constant over a range of fields and pressures for any given gas. In air, $A \approx 14.6$ and $B \approx 365$. The increase in the number of electrons over a distance dx is give by

$$dn = \alpha n dx, \tag{2.2}$$

where n is the number of electrons. Solving 2.2 gives

$$n(x) = n_t e^{\alpha x}, \tag{2.3}$$

where n_t is the total number of electrons leaving the cathode and $n(x)$ is the number of electron-ion pairs produced by n_t electrons as they travel across the electrode gap. This total number of electrons is a sum of the number of original electrons, n_o, leaving the cathode due to the field and the number of secondary electrons, n_s, ejected from the cathode due to ion impact. If $n_s(x)$ is the number of secondary electrons produced by the $n(x)$ electrons and s is the average number of secondary electrons produced by each primary electron-ion pair,

$$dn_s = sn(x)dx. \tag{2.4}$$

Combining equations 2.3 and 2.4 yields

$$n_s(x) = \frac{s}{\alpha} n_t (e^{\alpha x} - 1), \tag{2.5}$$

which can be used to determine the total number of secondary electrons produced as the primary electrons travel the distance, d, between electrodes by evaluating at $x = d$. By using this result and defining the second Townsend ionization coefficient, $\gamma = \frac{s}{\alpha}$, (also referred to as the secondary electron emission coefficient) which represents the fraction of primary ionizing collisions that result in additional secondary electron production,

$$n_t = \frac{n_o}{1-\gamma\left(e^{\alpha d}-1\right)}. \tag{2.6}$$

Substituting equation 2.6 into 2.3 gives

$$n(d) = \frac{n_o e^{\alpha d}}{1-\gamma\left(e^{\alpha d}-1\right)}. \tag{2.7}$$

Given that current is carried by electrons in a plasma, it can be expressed as:

$$i = \frac{i_o e^{\alpha d}}{1-\gamma\left(e^{\alpha d}-1\right)}. \tag{2.8}$$

Here i_o is the current at the cathode. As $e^{\alpha d} >> 1$, the expression becomes

$$i = \frac{i_o e^{\alpha d}}{1-\gamma e^{\alpha d}}. \tag{2.9}$$

From equation 2.9 it is apparent that the breakdown condition occurs when $\gamma e^{\alpha d} = 1$, or

$$\gamma = \frac{1}{e^{\alpha d}}. \tag{2.10}$$

The current is not infinite, but limited by the external ballast resistor used in series with the microdischarge. Thus, the ionization coefficients determine the microdischarge breakdown condition. The second Townsend ionization coefficient can be determined according to the procedure in [Gui03]. Briefly, Paschen's curve is determined for the given gas to obtain the breakdown voltages. The breakdown voltage is used to determine

the “reduced electric field”, or ratios of electric field strength to pressure (*E/p*), and α is determined as a function of this reduced electric field. Following this, γ is then determined as a function of α.

The first Townsend ionization coefficient however, requires additional modification. The attachment coefficient a represents the number of electrons which attach themselves to electronegative molecules per unit distance and reduces the effective first ionization coefficient $\alpha_{eff} = \alpha - a$. The reduced electric field determines if α is greater than a. If the reduced electric field does not surpass a threshold value, α will be less than a, and the multiplication of electrons is impossible. The reduced electric fields obtained in micro-SIPs between 100 Torr and 760 Torr, 22-1,071 V/(cm Torr), are similar to those obtained in macroscale plasmas due to the smaller discharge gap but higher operating pressures and are valid for sustained discharges, as they exceed the necessary threshold.

The ambient pressure has been shown to be a factor affecting microdischarges. Past reports have established through modeling that in microdischarges created in cylindrical metal-dielectric-metal sandwich structures in argon, with 200 µm discharge gaps and 100 µm thick electrodes, electron density surrounding the cathode increases monotonically between 50 Torr and 625 Torr due to more tightly confined secondary electrons [Kus05]. Ionization and the density of atoms in excited states have also been shown to increase approximately linearly with pressure in this range as a result of an increase in secondary electron peak power and an increase in current density. This indicates that increasing the pressure causes an increase in electron density, ionization, and secondary electron peak power, which theoretically contribute to an increase in

sputtering rates and the resulting micro-SIP air removal rates. However, this previously developed model did not explore sputtering in relation to microdischarges.

The theoretical increase in ionization and secondary electron production resulting from reduced discharge gap spacing causes cause micro-SIPs with smaller discharge gaps to function more effectively. Both ionization coefficients of nitrogen increase as the discharge gap is reduced from 150-35 μm. The first ionization coefficient increases from 305-872 ion pairs/cm, while the second ionization coefficient, γ, increases from 1.09×10^{-8}-4.99×10^{-6} with a 1,500 V operating voltage at 100 Torr without considering attachment. A larger γ indicates more secondary electrons, making an increase in γ beneficial to microdischarges and micro-SIP operation as the discharges are primarily driven by secondary electron emission. However, γ is much smaller than in traditional plasmas due to the relatively small discharge gap spacing in all micro-SIPs. The greater amount of ionization and electron emission obtained using smaller discharge gaps becomes increasingly important as the ionized nitrogen mean free path decreases with increasing pressure, from 0.48 μm at 100 Torr to 0.063 μm at 760 Torr, and the microdischarge becomes more confined. The micro-SIPs utilizing smaller discharge gaps additionally encounter lower breakdown voltages than the larger discharge gap micro-SIPs. This occurs as the *pd* products for all of the micro-SIPs, operating between 100 Torr and 760 Torr, is larger, to the right, of the Paschen curve minimum. Reducing the discharge gap, *d*, reduces the *pd* product and brings it closer to the ideal spacing at which the minimum breakdown voltage is obtained.

The characteristics of the discharges themselves also influence the gas removal rates of micro-SIPs. As the *pd* values of the microdischarges increase with increasing

pressure and discharge gap distance, the discharges transition from microdischarges operating as glow discharges to microarcs operating as arc discharges with different characteristics. During this glow to arc transformation, the discharges change from non-thermal to thermal discharges as the neutrals are heated and two primary discharge characteristics change: 1) The radius of the discharges are reduced and 2) The cathode is heated resulting in a transition from secondary electron emission to thermionic emission of electrons from the cathode [Sta05]. The reduced discharge radius diminishes the amount of titanium being sputtered. The reduction in secondary electrons reduces electron density and ionization as secondary electrons are the major source of ionization in microdischarges. These factors reduce the effectiveness of micro-SIPs, and occur when microdischarges transition to microarcs.

The gas removal rates of micro-SIPs are affected by the composition of the exposed electrode pair surfaces. When reactively sputtering at high pressures, the chemical reactions occur directly on the cathodes' surfaces [Mad02]. In addition, the chemically active cathodes can become saturated over time, reducing the removal rates. Removal rates are also reduced by redeposition and the buildup of insulating films, such as TiO_2, on the anode in a scenario termed the "disappearing-anode effect." This scenario can cause changes in the metal impedance and arcing characteristics. This is especially characteristic at higher pressures, where large amounts of redeposition are encountered due to a small mean free path [Ohr92]. Positive charge can build up on electrically insulating or "poisoned" portions of the cathode, which are cathode areas with a thick layer of dielectric compound, typically titanium nitride or titanium oxide for a titanium cathode. The positive charge buildup under DC operation resists sputtering and leads to

arc formation [Mat03]. Magnetron sputtering targets use discrete pulses that allow the targets to discharge any positive charge buildup on poisoned metal surfaces [Mat03], and this technique can be applied to microdischarges as well. Additionally, very short pulses of 10 ns have been shown to increase the electron density by a factor of 10 in microdischarges as well as more than double the mean electron energy [Mos03].

Another method for potentially improving the gas removal rates of micro-SIPs is to use heated cathodes to heat and impart energy to the ions directly above the cathode. This will create more energetic microdischarges with higher energy collisions, translating to higher energy ion impacts and improved "sputtering yield" (atoms sputtered/incident atom). This in turn will improve micro-SIP efficiency. Heating the cathodes using thin-film heaters differs from the heat induced by arc discharges as arc discharges heat localized hotspots to a much greater extent than the thin-film heaters. The heat generated by arc discharges cause the emission of thermionic electrons, while the heat generated by the heaters does not to a significant extent. Without localized heating, modeled argon microdischarges with similar currents to those used by micro-SIPs at 250 Torr heat the gas temperature in the discharge by 58ºC over ambient slightly outside of the sheath [Kus05]. The thin-film heaters are designed to be heated to 205ºC over ambient, heating the neutral gas and ions in close proximity to the cathode.

To predict the quantified gas removal rate of micro-SIPs, a model is reported here based on macroscale reactive sputtering models. Berg *et al.* [Ber87, Ber88] and Li and Hsieh [Li05] present a model which considers the pressure change in a macroscale system as a function of target erosion, gas injection, reactive gas gettering at all surfaces, etc. The model determines the fractional coverage of a metal target and substrate by a

compound film as they are sputtered by argon mixed with a reactive gas. The fractional surface coverage θ indicates the fraction of sites on the target surface occupied by the compound over the total number of target sites, while (1-θ) indicates the fraction of un-reacted metal sites. The change in the number of sites occupied by the compound on the target per unit time is expressed as

$$\frac{dN}{dt} = \alpha_m FA\left(1-\theta\right)a - \frac{JS_N}{e}A\theta + \alpha_m FS_N A\theta a\ , \qquad (2.11)$$

where F is the reactive gas flux, A is the target area, α_m is the sticking coefficient of the reactive gas molecules to the pure metal, a is the "stoichiometric number of compound formation" (ratio of compound molecules/reactive molecules), J is the ion current density, e is the unsigned charge of an electron, and S_N is the sputtering yield of the compound. The first term in equation 2.11 represents the reaction between the reactive gas molecules and the fresh metal portion of the target. The second term represents the reduction in compound fraction as a result of sputtering the compound off the metal. The third term represents the reaction between the reactive gas molecule and fresh metal sites which are uncovered when a compound molecule is sputtered [Yos88]. The reactive gas flux is determined using a Maxwellian distribution of molecular velocities as

$$F = \frac{p_p}{\sqrt{2\pi m k_B T}}\ , \qquad (2.12)$$

where p_p is the partial pressure of the reactive gas, m is the mass of the reactive gas molecule, k_B is the Boltzmann constant, and T is the temperature. In this model, all of the absorbed reactive gas molecules are assumed to contribute to the formation of compound molecules on the target surface.

The macroscale model developed by Berg *et al.* [Ber87, Ber88] describes reactive sputtering systems with low reactive gas partial pressures and requires adaptation to describe the high-pressure environments in which micro-SIPs are operated in this study. The primary difference between the two models is due to the high impingement rate of reactive gas molecules at high pressures, which impinge due to random motion without sputtering. These molecules can form native oxide layers, or other compound layers, covering the entire substrate surface. This leaves no fresh titanium to getter reactive molecules without sputtering. Theoretically, this can be confirmed by finding the critical pressure above which the target surface is completely covered by a compound. This critical pressure is determined by equating the rate at which the compound is removed by sputtering and the rate at which the compound is formed by reactive gas molecules impinging on the fresh metal sites, and solving for the pressure. The compound removal rate is the second term in equation 2.11 and the compound forming rate is the third term in equation 2.11. If the pressure is below the critical pressure, the compound is removed faster than it is formed (until a steady-state is reached as presented in the Berg model), while if the pressure is higher, compound eventually covers the target surface. The critical pressure is:

$$P_{\mathrm{crit}} = \left(\frac{S_N JA}{e}\right)\left(\frac{\left(2\pi m k_B T\right)^{1/2}}{\alpha S_N a A}\right). \qquad (2.13)$$

Using nitrogen as the reactive and sputtering gas, using a titanium cathode as the target, assuming stoichiometric TiN as the compound, and using other parameters determined from the micro-SIP design, the critical pressure is calculated as 1.98 Torr. Given that micro-SIPs are operated at pressures much higher than this, the entire surface

is covered during normal operation. Considering the use of pure nitrogen as a reactive gas and given that the entire surface is covered by TiN after the native oxide layer is removed, the removal of nitrogen gas only results from sputtering TiN molecules to expose fresh titanium atoms which will bond with the nitrogen. This indicates that the first term in equation 2.11 is irrelevant and the third term is the only relevant term indicating nitrogen removal from the environment and, consequently, pressure reduction. However, the process is now limited by the sputtering rate as opposed to the gas impingement rate, making the rate of nitrogen removal by the micro-SIPs (molecules/s) simply

$$R_{\text{pump}} = S_N \frac{J}{e} A\theta \,. \tag{2.14}$$

This does not need to consider the sticking coefficient as available sites will be filled much faster than the rate at which they are uncovered. TiN is considered to be sputtered as a molecule, as opposed to as titanium and nitrogen separately. As no fresh titanium is being sputtered from the cathode onto other portions of the substrate, all of the evacuated gas molecules are bound to the surface of the cathode, and not on other portions of the substrate.

The pressure reduction resulting from the removal of nitrogen from air is determined using the parameters below. By the ideal gas law, the change in pressure is

$$\frac{dp}{dt} = -\frac{k_B T}{V} S_N \frac{J}{e} A\theta \,. \tag{2.15}$$

Considering a micro-SIP with a 50-μm discharge gap and 1,500 V applied at a pressure of 100 Torr, 1.49 x 10^{14} molecules per second are sputtered and absorbed while the

pressure changes by 68.6 mTorr/minute. The rate at which nitrogen impinges on fresh titanium is

$$\frac{dN}{dt} = \alpha_m F S_N A \theta \qquad (2.16)$$

and is equal to 5.2×10^{19} molecules per second. This is almost five orders of magnitude faster than the rate at which the surface is sputtered, indicating that the assumption of a sputter rate limited equation is valid.

Several parameters are required to calculate the gas removal rate of micro-SIPs using the above equations, including the stoichiometric number, the sticking coefficients, the sputtering yields, the electric field strengths, and the current density. The stoichiometric number used is 2, as two titanium atoms can bond with a single N_2 molecule. The sticking coefficient of nitrogen molecules on pure titanium is 0.4 at 20ºC and the sticking coefficient of N atoms on TiN_x films is ~0.003 for nitrogen-rich TiN films [Yok05]. The sputtering yields, which are the number of atoms or molecules ejected from a target surface per incident ion, are calculated for nitrogen ions impinging on fresh titanium and TiN according to previously derived equations [Ohr92]. In a nitrogen DC discharge with higher current but lower current density, N_2^+ ions have average energies of 100 eV in the sheath, at the cathode [Kum93]. Higher applied voltages also decrease the number of collisions for ions in the sheath, causing a larger number of high-energy ions [Pet93]. Using an impinging ion energy of 100 eV, the sputtering yield of pure titanium is calculated as 0.14 while the combined yield of titanium and nitrogen from TiN is 0.24. A large number of ions have significantly less energy but are not considered in the calculation. The combined yield of titanium and nitrogen from TiN is typically larger than that of titanium from pure titanium, while the

yield of just titanium from TiN is smaller than that of titanium from pure titanium [Ran01]. Sputtering yields are typically very low at high pressures but are aided by the very localized microdischarges in micro-SIPs.

To determine the electric field strengths, field orientations, and electric field lines produced by the micro-SIP electrodes, COMSOL MULTIPHYSICS® finite element analysis (FEA) is used. A micro-SIP with 50-μm discharge gaps and an applied voltage of 1,500 V is examined. The analysis reveals uniform electric field strengths around the circular discharge gaps as shown in Fig. 2.5. Examining a three-dimensional image reveals an arc-like orientation of electric field lines, which indicates that the distance between electrodes, as experienced by the bombarding ions, is longer than the minimum planar discharge gap separation. The theoretical distance is approximately four times the planar discharge gap spacing, and this increase in distance is included in the micro-SIP model to more accurately describe the ion trajectories. The resulting predicted maximum electric field strength for this particular micro-SIP is 7.25×10^6 V/cm without the presence of a discharge, which is higher than traditional plasmas due to the small gap spacing. The creation of a discharge would increase the field strength at the cathode, in the sheath region, above this predicted value.

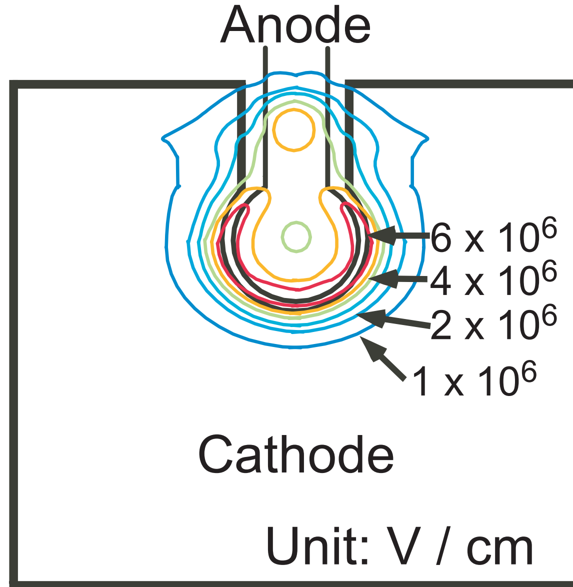

Figure 2.5: Modeled electric field strengths normal to a version 2 micro-SIP surface at a height of 50 μm above the electrodes.

The current density experienced by the ions is estimated as [Zhu98]

$$J = \left(\frac{p}{C}\right)\frac{I}{A}\frac{1}{e(1+\gamma)}, \tag{2.17}$$

where I is the discharge current, p is the pressure, and C is a correction factor. The ion current density is the total discharge current, as the current is carried by ions through the sheath to the cathode, over the discharge area. It is reduced by the secondary electrons as their negative charge repels ions, lowering the current density. The pressure correction factor *(p/C)* is included to account for the change in microdischarge current density with pressure. A summary of calculated parameters for the described micro-SIP is displayed in Table 2.1.

Table 2.1: Calculated parameters for a micro-SIP with 50-μm discharge gaps and 1,500 V applied at a pressure of 100 Torr.

Parameter	Value
First ionization coefficient α (cm^{-1})	761
Second ionization coefficient γ	2.47×10^{-7}
Current densities (A/cm^2)	3.4×10^{16}
E/p (V/(cm x Torr))	750
Sputtering rate and nitrogen consumed (molecules/s)	1.49×10^{14}
Nitrogen removal rate (mTorr/min)	68.6

2.4 DESIGN AND FABRICATION

Micro-SIPs with different electrode designs are used to examine the effect of electrode design on gas removal rates and device durability. To maintain controlled, progressive sputtering for extended durations of time, the cathodes are made larger than the anodes and designed to erode evenly along the discharge gap boundaries. FEA confirms that the circular design provides a uniform electric field over a large boundary of interaction between the micro-SIP anode/cathode pairs. In contrast, if any sharp corners are present, the discharges form at these locations preferentially. Three different micro-SIP designs for prolonged reactive sputtering are fabricated on separate chips, each with a 1 cm^2 footprint. Discharge gaps of 5-150 μm are designed and fabricated but discharge gaps less than approximately 35 μm tend to short due to microscale conductive coatings such as dust. The first micro-SIP design (version 1) has two single anode/cathode pairs and uses separate lead connections for each electrode, providing redundancy should one electrode be destroyed through the application of a large current or a bad connection. This design explores the use of a separate anode for each anode/cathode discharge gap and large cathodes. The second micro-SIP design (version 2) [Fig. 2.6(a)] has a single composite anode that operates with eight separate but

identical cathodes. As anodes are not significantly sputtered by the discharge, a common lead to them is sufficient. Each cathode can be activated individually or shunted off-chip with others. In this design, four times as much titanium is available for reactive sputtering as compared to version 1. The third micro-SIP design (version 3) [Fig. 2.6(b)] has a single anode and two cathodes. Each cathode has 15 discharge gaps, which maximize the amount of potentially sputtered titanium but version 3 does not allow the user as much control compared to the other versions. Versions 1, 2, and 3 micro-SIPs have 5.06 mm^2, 1.82 mm^2, and 33 mm^2 cathodes respectively and each provides a distinct operating advantage as previously described.

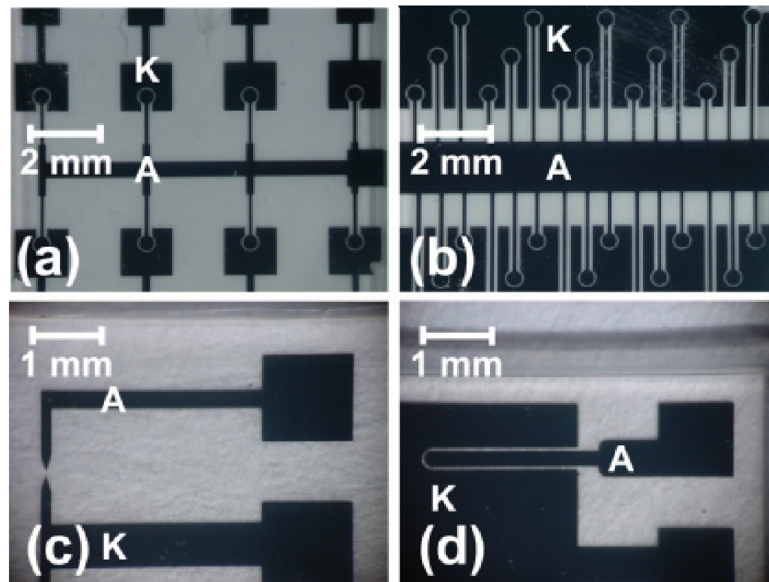

Figure 2.6: (a) Version 2 chip with a single anode and eight cathodes. (b) Version 3 chip with a single anode and two cathodes, each having 15 discharge gaps. (c) Version 4 chip with high current density. (d) Version 5 chip with low current density.

In addition to the devices described above, additional version 2 micro-SIPs with identical cathode areas of 1.82 mm^2 and discharge gap spacing of 35 μm, 50 μm, 75 μm, 100 μm, and 150 μm are fabricated to evaluate the relationship between gas removal rate

and discharge gap spacing. Despite the larger gaps, at atmospheric pressure the breakdown voltages of these micro-SIP electrode pairs is theoretically estimated to be between 500 V and 1,200 V.

To examine the effect of varied current densities on gas removal rates, micro-SIPs having both small and large discharge gap boundaries between electrodes are used. The micro-SIP design (version 4) [Fig. 2.6(c)] has pointed electrodes to confine the microdischarges and produce high current densities over the small cathode areas. Another micro-SIP design (version 5) [Fig. 2.6(d)] has extended discharge gap boundaries between electrodes, to disperse the microdischarges and reduce the current densities. While the electrodes in version 4 micro-SIPs only have a small point at which the discharge gap is minimized, the version 5 electrodes have discharge gap boundaries 4.6 mm in length. Both designs have minimum discharge gaps of 50 μm, to allow performance comparisons to version 1-3 micro-SIPs with 50-μm discharge gaps. These micro-SIPs are fabricated on chips with footprints of 25 mm^2, one-quarter the size of the chips with micro-SIPs designed for prolonged sputtering.

Micro-SIPs utilizing micro-heaters as cathodes are designed to increase the temperature of the microdischarges and a schematic diagram of the electrodes is shown in Fig. 2.4(b). Four micro-heaters, 50 μm in width, serve as the cathodes and when heated through the application of 3 V, reach temperatures of 232°C. These micro-SIPs are designed for rapid sputtering over short periods of time, due to the small volume of titanium available at the cathodes. They are fabricated on identical chips to the version 4 and 5 micro-SIPs.

All micro-SIPs were fabricated with two masks to simplify processing. A Ti film (1 µm thick) and a Au film (500 nm thick) were thermally evaporated onto #7740 Pyrex™ glass wafers (500 µm thick) without removing the wafers from vacuum. The contact pads were patterned on the gold layer using photolithography and etched using Transene GE-8148 gold etchant, which does not etch titanium. The electrodes were then patterned in the titanium layer using photolithography to produce the patterns shown in Figs. 2.6(a)- (d). Figure 2.7 illustrates the packaged devices.

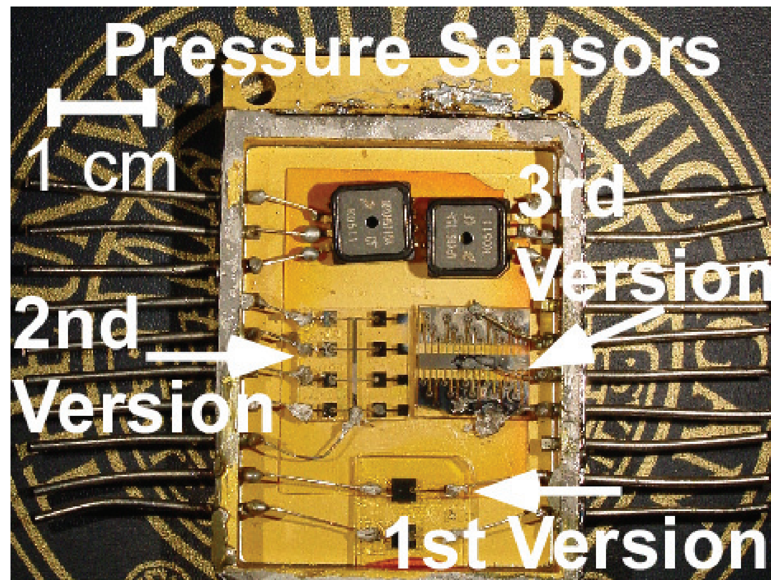

Figure 2.7: A commercial package after opening, with two commercial pressure sensors and three different micro-SIP versions.

2.5 Experimental and Modeling Results

2.5.1 Removing Air from Microelectronic Packages

Micro-SIPs were sealed in industry-standard packages and re-sealable packages with pressure sensors and operated with externally applied voltages while the pressure was monitored. Version 1-3 micro-SIPs were used. They were hermetically sealed in

metal flatpack packages, which are often used for power electronics, using solder bonding. The sealing was performed at the University of Michigan. One package was a 3.3 x 4.3 cm^2 (6.33 cm^3) gold plated nickel package from HCC Aegis (Catalog # 0J7H2), while the second was a 2.5 x 2.5 cm^2 (2.2 cm^3) steel package from Sinclair Manufacturing Co. (Product # SQ 1000-250-12-10GC). Stainless steel lids were used to seal the packages at 760 Torr. A third, re-sealable glass package, 2.5 cm in diameter (4 cm^3), was used to test the micro-SIPs at initial pressures lower than atmosphere. The initial package pressure was set by a two-stage rotary vane roughing pump (Oerlikon Leybold Vacuum Trivac D 16B), accompanying pressure controller (MKS® 600 Series), and external macroscale pressure transducer (MKS® Baratron® Capacitance Manometer model #627B23TDC1B). A needle valve was used to seal the re-sealable package while the micro-SIP(s) operated. Large tubing external to the package was used to avoid low conductance. The pressure was measured by two piezoresistive pressure sensors (Freescale MPXH6115A) for confirmation in the larger (6.33 cm^3) package and by one in the smaller (4 cm^3) and re-sealable package (4 cm^3). A multimeter and a computer interface were used to record the pressure sensor output voltages at programmable intervals while the current was also recorded.

The pressures in the packages were reduced through micro-SIP operation. Three micro-SIPs were sealed in the 6.33 cm^3 package at atmospheric pressure. In one test demonstrating a typical amount of air removal, 15 discharges 10 minutes in duration were applied to the micro-SIPs using four different electrode pairs, and the pressure was reduced by 168 Torr from the sealing pressure, as shown in Fig. 2.8. The pressure remained steady for periods of up to 10 hours between discharges, and the figure shows

that the pressure sensor correctly measured atmospheric pressure when the cavity was opened for inspection. Figure 2.9 displays the same pressure reduction and absorbed molecules as a function of the energy used for the discharges. The upper trend line represents the pressure drops measured with the discharge off, when no energy was being applied to the system. In the 2.2 cm^3 package, the pressure was reduced by 126 Torr through the application of extended discharges. The ambient temperatures in the packages never increased more than 2.2ºC during micro-SIP operation, as measured by the increase in package pressure due to heating of the ambient environment from the microdischarges.

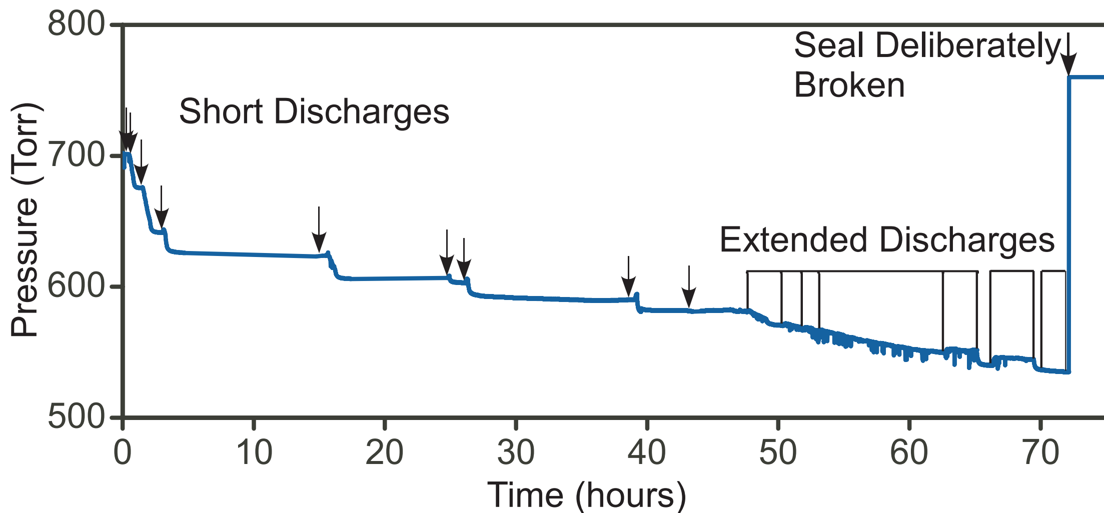

Figure 2.8: Pressure drop in a 6.33 cm^3 package over time. Fifteen consecutive 10 minute discharges drop the pressure 168 Torr. The pressure remains stable over periods of 10 hours of micro-SIP inactivity and returns to atmospheric pressure when the package is opened.

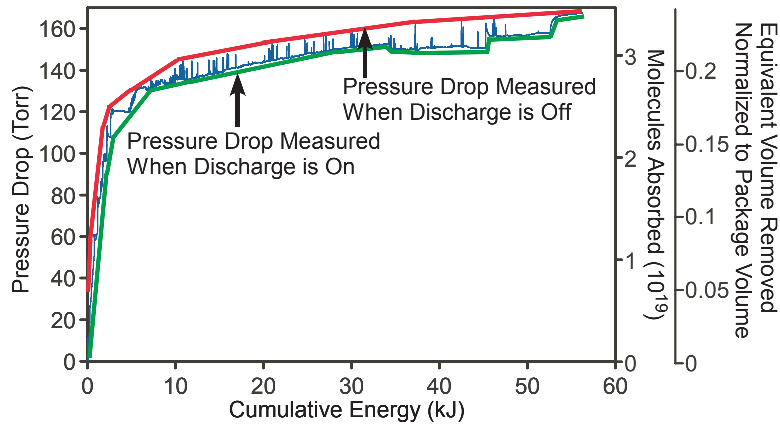

Figure 2.9: Pressure drop, shown in Fig. 2.8, as a function of cumulative energy supplied to the discharge with an initial pressure of 760 Torr. The upper and lower trend lines, respectively, show the pressure readings when the discharge is interrupted (causing spikes as the pressure stabilizes without an increase in energy) and when the discharge remains on. The corresponding number of gas molecules removed at room temperature, and the fraction of the package volume evacuated, are noted on the second *Y* axis.

A micro-SIP was operated with an initial pressure of 31 Torr in a 4 cm^3 package. It reduced the pressure by 4 Torr in 30 minutes, at an average rate of 133 mTorr/min, as shown in Fig. 2.10. Operating micro-SIPs at relatively low pressures (1-30 Torr) resulted in large amount of sputter redeposition. Testing micro-SIP operation at pressures below 30 Torr is addressed in the following sub-section.

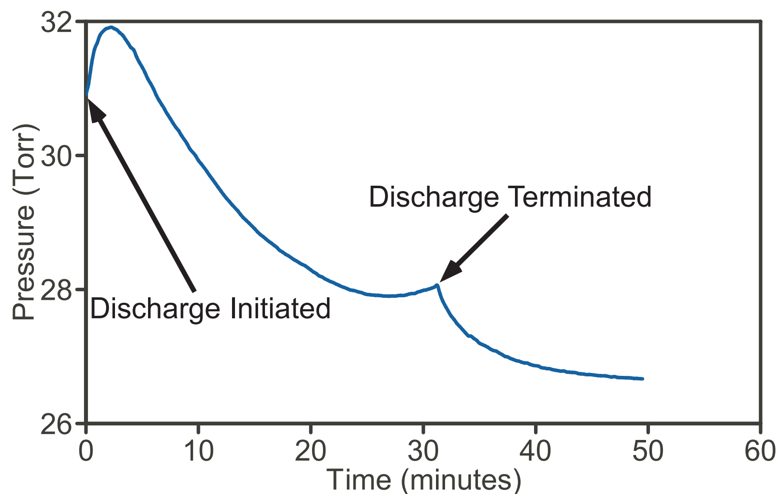

Figure 2.10: Pressure drop in a 4.0 cm^3 package over 30 minutes of micro-SIP operation, starting at an initial pressure of 31 Torr.

2.5.2 Pressure Reduction Behavior

The general behavior of the pressure change with time during the microdischarge induced sputtering, an example of which is displayed in Fig. 2.10, requires explanation. At the initiation of a DC microdischarge, the pressure in the sealed microscale cavities typically rose due to the heating of the ambient environment. The heating was found to raise the temperature by a maximum of 2.2ºC, by measuring the heat induced pressure increase, although the gas and ion temperature in the microdischarges increased by hundreds of degrees. As the compound was sputtered from the cathode, molecules were removed from the environment and the pressure began decline, eventually surpassing the initial pressure. Reactively sputtering for short periods, e.g. 10 minutes, resulted in pressure rises for approximately 3 of the 10 minutes before falling sharply.

When the micro-SIPs were operated for long periods of time, they demonstrated signs of saturation. For example, the initial discharge in Fig. 2.8 reduced the pressure at a rate of 678 mTorr/min, while the extended discharge utilized at a later time reduced the pressure at a rate of 27 mTorr/min. Additionally, shown in Fig. 2.10, the micro-SIPs demonstrated saturation after operating for periods of time as short as 30 minutes. This saturation was eventually evident in all examined micro-SIPs and at higher pressures ($> \approx 100$ Torr) appeared to be caused by a lack of cathode material after a great deal was sputtered off, and by saturation of the titanium in the cathode. At lower pressures, the saturation appeared to be caused by saturation of the titanium in the cathode and by buildup of insulating nitride and oxide films on the cathode. As the insulating films continued to be formed and re-deposited at the surface, the fresh titanium capable of chemisorbing additional gas was buried and became increasingly unreachable by the

impinging ions. Temporarily reversing the electrode bias or using AC driven discharges could have circumvented these restraints but was not examined. As this saturation occurred, the package leakage rate eventually surpassed the pumping rate, as shown in Fig. 2.10, at which point the discharge was terminated. The packages were increasingly susceptible to leakage at low pressures due to the pressure difference between the sealed and external environments and the low gas density which were compromised by small amounts of leakage.

The pressure continued to decline after microdischarge extinction due to two factors. The first involved the return of the packaged gas temperature to the original state, as the microdischarge did not continue to heat the environment. The second factor involved continued chemisorption by exposed titanium sites which had not formed compound at the time of discharge termination. This occurred to a greater extent at lower pressures as demonstrated in Fig. 2.10. After discharge extinction, the pressure continued to drop for up to 20 minutes and eventually stabilized, holding steady for hours between discharges as if the leakage rate was significantly low. Otherwise leakage caused the pressure to increase.

Discharges of different durations produced varied pressure responses. Reactively sputtering for short periods, e.g. 10 minutes, caused the pressure to rise and subsequent decline after the gas removal countered the heating effects. Reactively sputtering for extended durations, e.g. hours, resulted in steady pressure drops after initial rises due to temperature. To maintain discharges for hours, the applied voltages required increases with time due to the effective increase in discharge gap spacing as the proximal cathode regions were sputtered away.

The titanium regions of the cathodes were sputtered as intended, which was apparent upon opening the cavities, as shown in Fig. 2.11. A film was also evident on the substrates and anodes. Areas of the 1-μm-thick titanium were completely removed down to the substrate in the intended manner. As the titanium was sputtered from the initial discharge locations, the discharges occurred at different locations and thus sputtered the cathodes uniformly on all sides of the anodes. This uniform removal led to the concentric consumption of the cathodes over time. The anodes remained largely intact, showing no indication of sputtering, although some delamination and damage could potentially occur due to heating caused by localized hotspots and arcs.

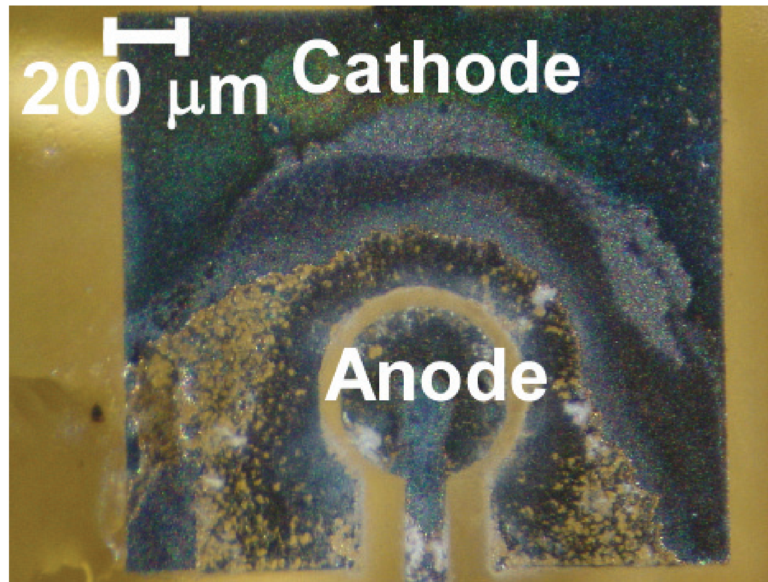

Figure 2.11: Micro-SIP electrodes displaying remains of a cathode after reactive sputtering, illustrating areas of complete titanium sputtering.

The device lifetime was dependent on microdischarge current density, which was a function of the applied voltage and pressure. Operating at 760 Torr with an applied 1,000 V, the micro-SIPs lasted on the order of an hour before significant titanium was removed and the devices became inoperative. At this point other cathodes were used. At

pressures below 300 Torr with an applied 1,000 V, the devices lasted for days and could potentially last longer at lower operating pressures.

2.5.3 Operating Micro-SIPs at Lower Pressures

Micro-SIP operation was examined at pressures as low as 1 Torr. Version 2 micro-SIPs were enclosed in a re-sealable glass package, 2.5 cm in diameter (4 cm^3), and operated with an applied voltage of 1,500 V. Freescale MPXM2102 pressure sensors, which operate between 0.1 Torr and 760 Torr, were used. However when the packages were sealed at lower pressures (1 Torr), they were compromised by leakage and outgassing, precluding micro-SIP evaluation at these initial pressures.

2.5.4 Relationship between Discharge Gap Spacing, Pressure, and Air Removal Rate

To determine the relationship between the micro-SIPs' gas removal rates, the initial ambient pressure, and the discharge gap spacing, micro-SIPs with varied discharge gaps were operated in air at different initial pressures. Version 2 micro-SIPs with identical designs and 1.82 mm^2 cathodes were used, having 35 μm, 50 μm, 75 μm, 100 μm, and 150 μm planar physical discharge gaps at pressures between 100 Torr and 725 Torr in a re-sealable glass package, 2.5 cm in diameter (4 cm^3). At these pressures all of the discharge gaps were much larger than the mean free path of gas molecules. The initial pressures inside the package were set using the procedure described in Section 2.5.1.

The air removal rate varied as a function of pressure, discharge gap spacing, and discharge characteristics. Figure 2.12 shows the experimental and theoretically determined pressure reduction rates as a function of starting pressure, p_S. The theoretical rates were determined using the calculated removal rate of nitrogen in air. The

theoretical model exhibits the same dependence of gas removal rate on pressure, but overestimates the removal rate of large discharge gap micro-SIPs and underestimates the rate of smaller discharge gap micro-SIPs. In micro-SIPs with smaller discharge gaps, 35 µm and 50 µm, higher initial pressures resulted in faster gas removal rates as a result of the increase in electron density, ionization, and secondary electron peak power at increasing pressures. At each examined pressure, micro-SIPs with smaller discharge gaps generally remove air faster than micro-SIPs with larger discharge gaps. This is consistent with the larger ionization coefficients, resulting increase in ionization, and resulting increase in secondary electron production associated with smaller discharge gap micro-SIPs. A change in micro-SIP discharge characteristics, from glow microdischarges to microarcs, was associated with a reduction in removal rate. As the starting pressure was increased for the micro-SIPs with larger discharge gaps, 75 µm and larger, the discharges became spatially confined and the discharges exhibited arcing characteristics. This corresponded to a decrease in pressure reduction rates. This decrease caused the maximum pressure reduction rate of these micro-SIPs to occur at pressures less than atmosphere. The coinciding change in discharge characteristics and pressure reduction rate suggests that a reduction in secondary electron production in the arc-like discharges reduced the pumping rate.

The high and low current density micro-SIPs proved to be unusable for extended durations of time. The very high localized current densities encountered in the version 4 micro-SIPs eroded the cathodes within 10 minutes at atmospheric pressure, making them unusable for long term operation. The low current density version 5 micro-SIP deposited the sputtered material between electrodes, shorting them together and halting gas removal

within 5 minutes of use. These results indicate that significantly increasing or decreasing the current density does not improve micro-SIP performance over that achieved with version 1-3 micro-SIPs.

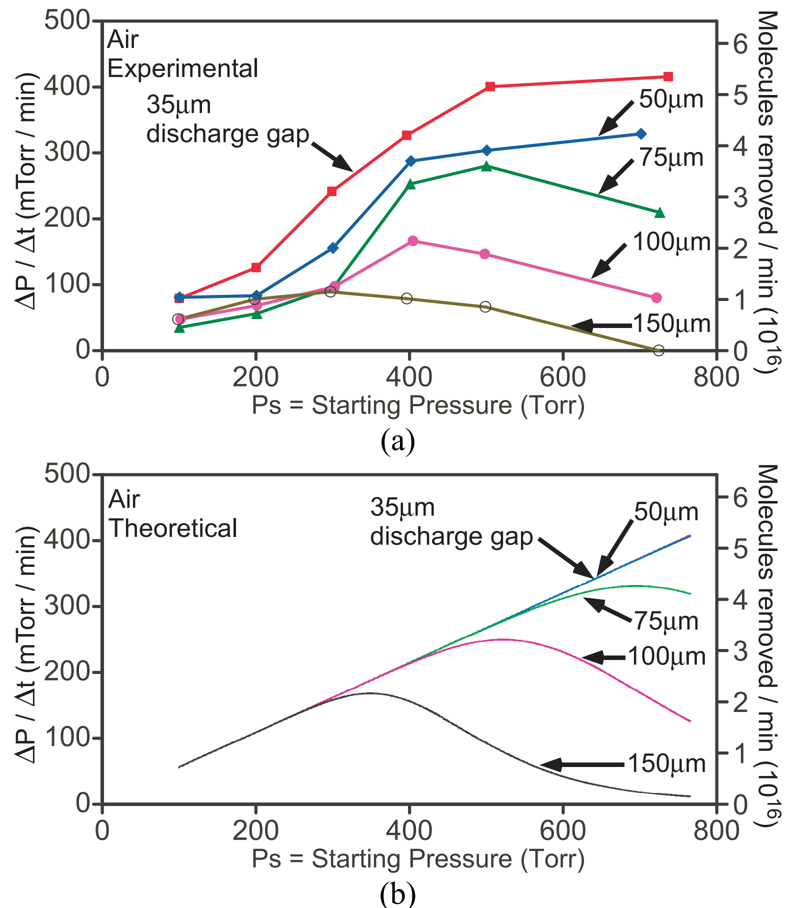

Figure 2.12: (a) Experimentally measured (over 20 min.) and (b) theoretically determined pressure reduction rates in air as a function of discharge gap spacing and pressure. The micro-SIPs have between 35 µm and 150 µm discharge gaps, are operated with 1,500 V, have initial pressures between 100 Torr and 725 Torr, and are operated in a 4 cm^3 package.

2.5.5 Removal Rates of Various Gases

Figure 2.13 shows the species being ionized and excited in an air environment at 760 Torr, as identified by examining the spectrum produced by the discharge [Pea63,

Har69]. In this mixed gas environment, the strongest emissions were produced by Ti^+, O^+, and N_2^+.

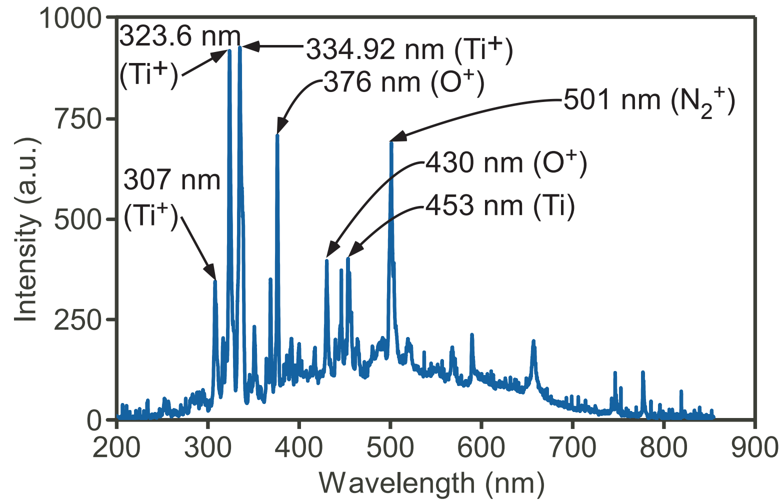

Figure 2.13: Spectrum of the micro-SIP electrode pair discharge in air indicating the dissociation of oxygen and ionization of titanium and nitrogen.

The gas selectivity of titanium micro-SIPs was examined by individually introducing pure nitrogen, oxygen, and helium (as an inert reference) into a previously evacuated package and measuring the removal rates at 200 Torr. The micro-SIPs were enclosed in a re-sealable glass package, 2.5 cm in diameter (4 cm^3). The gas concentration was set by MKS® Mass-Flo® Series Mass Flow Controllers (Model #'s 1479A13CR1BM and 1479A21CR1BM), accompanying pressure controller (MKS® 600 Series), and external macroscale pressure transducer (MKS® Baratron® Capacitance Manometer model #627B23TDC1B). The air initially in the package was removed by a two-stage rotary vane roughing pump (Oerlikon Leybold Vacuum Trivac D 16B). A needle valve was used to seal the re-sealable package while the micro-SIPs operated. The version 2 micro-SIP design with 1.82 mm^2 cathodes and 100 µm discharge gaps was used.

Figure 2.14 illustrates the partial pressure reduction in each environment; oxygen is removed faster than nitrogen, and helium is not noticeably removed. Helium is not removed as it is an inert gas and does not bond with titanium. In macroscale getter ion pumps, inert gases are implanted and retained using complex cathode geometries or tantalum (Chapter 1, Section 1.2). While inert gases might temporarily be implanted, they will later be released as they are not chemically bonded to titanium. Figure 2.14 indicates this as the helium pressure is initially reduced, followed by an increase. Averaging three trials, oxygen is found to be removed at 11.5 Torr/hr, nitrogen at 3.4 Torr/hr, and air at 7.2 Torr/hr. These reduction rates are significantly higher than those observed in macroscale SIPs. Oxygen is removed at over three times the rate of nitrogen, which corresponds to the ratio of chemisorption rates of these gases on titanium at room temperature [Hol59]. This suggests that in a mixed gas environment such as air, oxygen will be removed more rapidly than nitrogen as well. This was experimentally confirmed, as shown in Fig. 2.14.

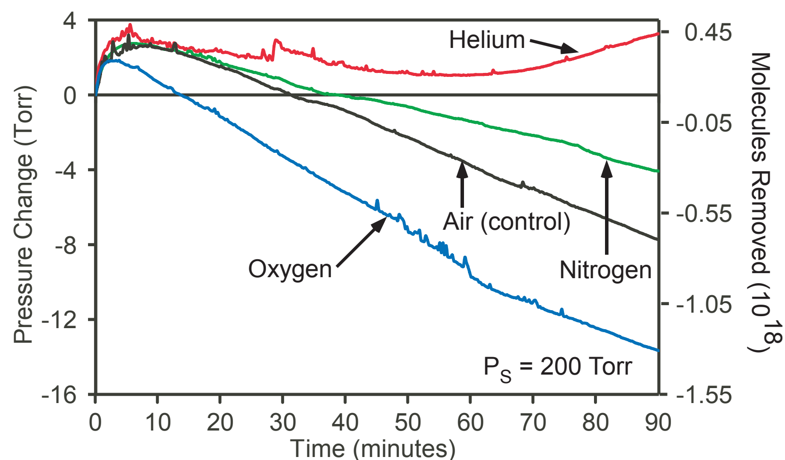

Figure 2.14: Change in pressure in environments of pure oxygen, nitrogen, helium, and air. The micro-SIPs have 100 µm discharge gaps, are operated with 1,000 V, have initial pressures of 200 Torr, and are operated in a 4 cm^3 package. This shows that the mixed gas air environment is removed at a rate between oxygen and nitrogen as expected, based on the different chemisorptions rates of the gases. Helium is not removed as it is an inert gas and does not bond with titanium.

2.5.6 Removal Rate of Water Vapor

The ability of micro-SIPs to remove water vapor was determined by introducing water vapor into sealed packages and measuring the relative humidity drop during micro-SIP operation with humidity sensors. A re-sealable glass package, 2.5 cm in diameter (4 cm^3), was used to test the micro-SIPs. Humidity was introduced through an Ace Glass 7533 Midget Impinger Bubbler. The initial package pressure was set by a two-stage rotary vane roughing pump (Oerlikon Leybold Vacuum Trivac D 16B), accompanying pressure controller (MKS® 600 Series), and external macroscale pressure transducer (MKS® Baratron® Capacitance Manometer model #627B23TDC1B). A needle valve was used to seal the re-sealable package while the micro-SIP(s) operated. Honeywell HIH4000 humidity sensors were used to monitor the humidity in the package. The set-up is shown in Fig. 2.15.

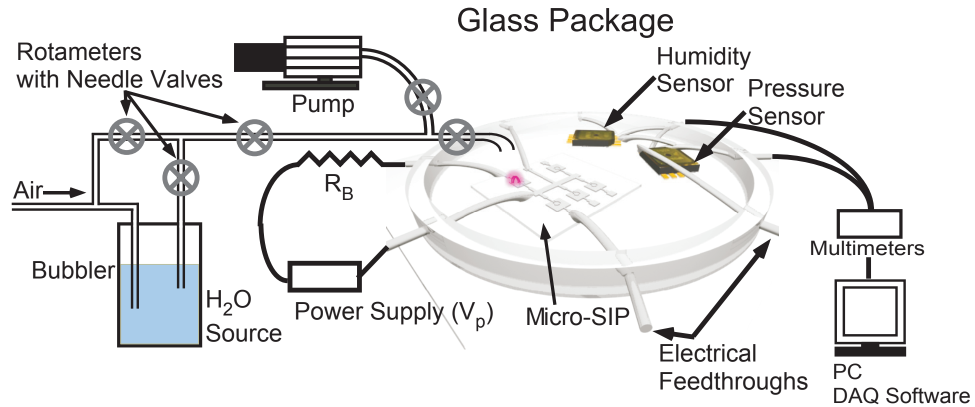

Figure 2.15: Schematic of the glass package, micro-SIP, and external equipment used to introduce and measure humidity removal.

Figure 2.16 shows the typical relative humidity and pressure drops observed using a version 2 micro-SIP with a 100 μm discharge gap at a starting pressure of 400 Torr. For comparison, it also shows the relative humidity drop when the rotary vane roughing pump was used to reduce the pressure by the same amount in the same package. A micro-SIP reduced relative humidity by 4% while reducing the pressure by 10 Torr in 45 minutes. Using the mechanical pump to reduce the pressure by 10 Torr, starting from the same initial pressure and relative humidity, reduced the relative humidity by only 0.1%. Initially, the micro-SIP removed humidity much faster than the mechanical pump over the same pressure drop, but this measurement was influenced by the temperature increase while the discharge was on, which caused a lower relative humidity reading. After the micro-SIP was turned off, the relative humidity rose and stabilized at a value lower than that obtained simply by removing the air with the mechanical pump. This indicates that micro-SIPs can operate effectively in the presence of water vapor and may offer an advantage to mechanical pumps in the suppression of humidity.

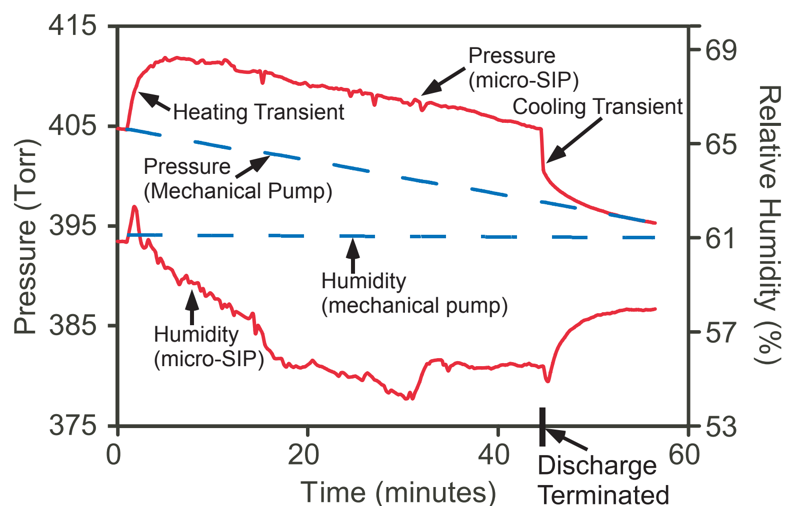

Figure 2.16: Experimentally measured change in humidity using a micro-SIP. The micro-SIP has a 100 µm discharge gap, is operated with 1,000 V, has an initial pressure of 400 Torr, and is operated in a 4.0 cm^3 glass package. A mechanical pump is used for comparison, starting at the same initial pressure and relative humidity. The micro-SIP removes more relative humidity than the mechanical pump when both reduced the pressure by 10 Torr. The heating and cooling transients are caused by the discharge induced heat from the micro-SIP. They are absent in the mechanical pump measurements due to the absence of a heat increase.

2.5.7 Pulsed Discharge Operation

To evaluate the removal rate improvements possible through the reduction of positive charge buildup on compounds covering the cathodes [Mat03], and possible energy efficiency improvements, pulsed discharges were applied to version 2 micro-SIPs with 50 µm discharge gaps at an initial pressure of 400 Torr in the re-sealable glass package, 2.5 cm in diameter (4 cm^3). Figure 2.17(a) shows the removal rates obtained when the current applied to the micro-SIPs was pulsed for periods between 25 ms and 500 ms, at a frequency of 1 Hz. The rate at which air was removed from the package was directly related to the duration of this applied current. Micro-SIPs operated using DC discharges removed air faster than pulsed discharges with duty cycles of 50% or less, showing that pulsing compromises evacuation rates. Figure 2.17(b), however, compares

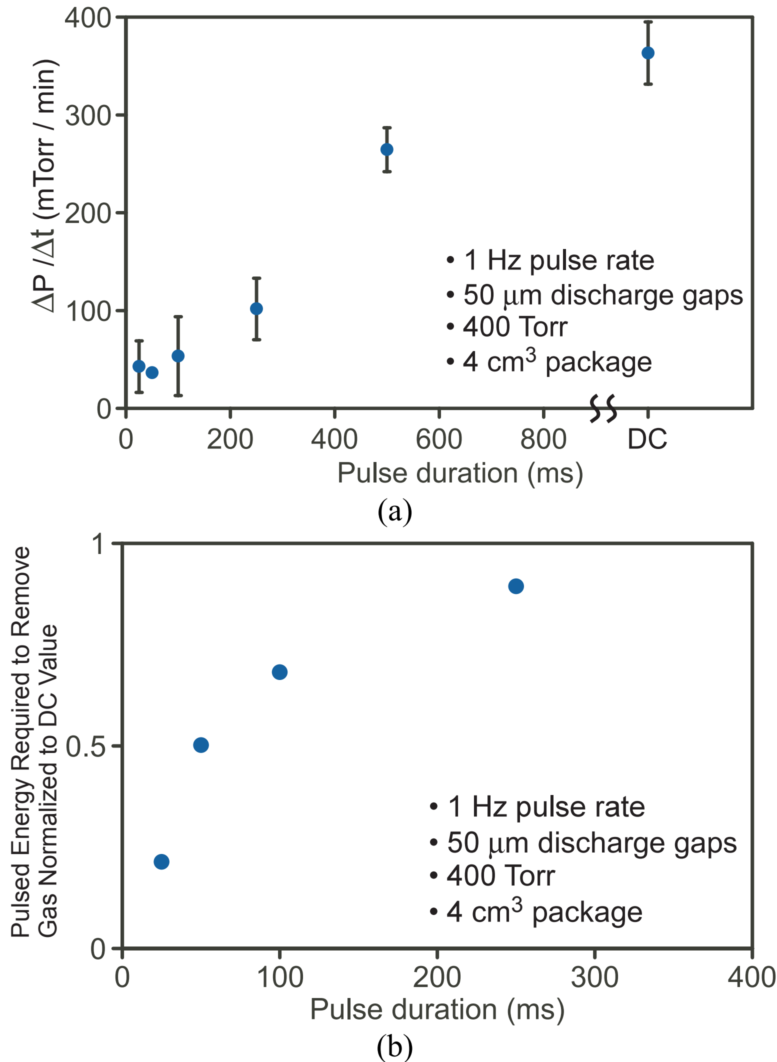

Figure 2.17: Pulses of 1,000 V are applied at a frequency of 1 Hz. (a) Pressure reduction rate as a function of pulse duration, averaged over 20 minutes of gas removal. The longer pulse durations reduce pressure faster. The error bars indicate a standard deviation of removal rate. (b) Relative energy required to remove an arbitrary unit of pressure with different pulse durations, normalized to a DC discharge. Pulses are five times more energy efficient, but require a longer duration of time.

the relative energy required by micro-SIPs using pulsed discharges of different durations to remove a fixed amount of air from a package. The energy required to remove this arbitrary amount of air with the different duration discharges is normalized to the amount of energy required by a DC discharge. This indicates that given the same amount of energy and enough time to apply this energy to pulsed discharges at a set frequency,

micro-SIPs using pulses of 25 ms in duration can remove almost five times as much air as micro-SIPs using DC discharges. This also indicates that shorter pulses are more energy efficient despite their slower removal rates as they are able to dissipate charge buildup on the electrodes. Pulsed discharges have also been shown to increased electrode lifetime as a result of shorter sputtering periods.

2.5.8 Thermally Assisted Discharges

To thermally assist the plasma and reactive sputtering, thin-film resistive heaters were designed to serve as titanium cathodes for some micro-SIPs as shown in Fig. 2.4(b), on Pyrex® substrates. These micro-SIPs were tested in the re-sealable glass package, 2.5 cm in diameter (4 cm^3) using the procedure described in Section 2.5.1. Four heaters, 50 μm in width, 1 μm in thickness, and 1 mm or 2 mm in length, were heated by applying a DC voltage drop of 3 V across them. The heaters had final calculated temperatures increases between 218°C and 232°C. These temperatures were calculated using the resistance of the heaters, the glass substrate thermal resistance, the applied voltage, and the temperature coefficient of resistivity (TCR) of the titanium heaters. When the heaters were turned on, they caused the temperature of the gas inside the cavity away from the discharges to rise between 15°C and 19°C. This was measured by recording the temperature induced pressure increase when the heaters were operated before micro-SIP operation. For comparison, the temperature was raised by a maximum of 2.2ºC during micro-SIP operation without heaters as cathodes. Identical micro-SIPs with inactive heaters as cathodes were examined for comparison; the results, comparing the removal rates of heated and unheated micro-SIPs at 100 Torr and 200 Torr, are shown in Fig.

2.18. Two different thin-film heater designs increased the air removal rate at 100 Torr by almost 2x but did not increase the air removal rate at 200 Torr.

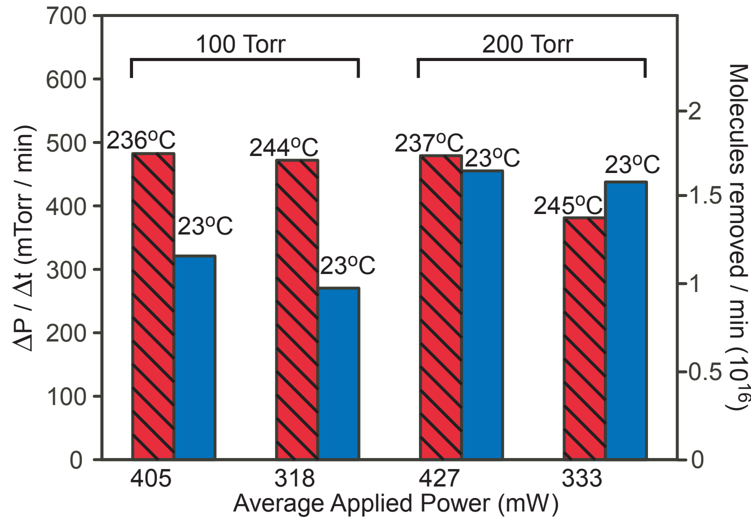

Figure 2.18: Average pressure reduction rate comparison using micro-SIPs with thin-film heaters as cathodes. In the "hot" trials, the cathodes are heated through the application of the indicated average power, while in the "cold" trials; identical micro-SIPs with cathode heaters are not heated. The calculated average cathode temperatures are indicated. The heaters are all 50 μm in width and 1 mm or 2 mm in length. The micro-SIPs are operated with 1,000 V at initial pressures of 100 Torr and 200 Torr in a 1 cm^3 package.

2.6 X-RAY PHOTOELECTRON SPECTROSCOPY RESULTS

In an effort to determine the extent to which specific gases were removed from air environments by micro-SIPs, the atomic composition of used and unused electrodes were examined by X-ray Photoelectron Spectroscopy. Micro-SIPs which had been used to remove air from sealed packages for one hour at 200 Torr, 500 Torr, and 725 Torr were examined. The used cathode surfaces were found to have atomic concentrations of 43.6% oxygen, 1.1% nitrogen, and 1.7% titanium through averaging four sample spectra. The anode surfaces were found to have similar atomic concentrations. Unused electrodes were also examined and the surfaces were found to consist of 41.3% oxygen and 2.3%

titanium by averaging the composition of five sample spectra. The remaining composition of all electrodes was found to be contaminant carbon and silicon from the substrates. While nitrogen was found in used electrodes, it could not be detected in unused electrodes. However, aside from this disparity, the measurable atomic concentrations gave little indication as to micro-SIP operation due to the oxidation of micro-SIP surfaces in air after sputtering had ceased. Additionally, the extent of implantation could not be determined. These results were similar to the results obtained by Li *et al.* [Li07] in which XPS samples of titanium films used to chemisorb oxygen were examined. Li found that carbon and oxygen were present, and attributed the measured film surface compositions to the layer of reactive molecules that covered the titanium films when exposed to air. See Appendix 2 for a detailed setup description and complete results.

CHAPTER 3

PRESSURE SENSING USING MICRODISCHARGES

This chapter discusses microdischarge-based pressure sensors, which operate by measuring the change, with pressure, in the spatial current distribution of pulsed DC microdischarges. These devices are well-suited for high temperature operation because of the inherently high temperatures of the ions and electrons in the microdischarges. Two sensor versions are described. The first type uses three-dimensional arrays of horizontal bulk metal electrodes embedded in quartz substrates while sensors of the second type use planar electrodes. Section 3.1 presents other high temperature pressure sensors and compares them to these sensors. Section 3.2 presents the operation of the microdischarge-based sensors in detail and a current pulse circuit model. Section 3.3 presents the fabrication processes and device designs. Section 3.4 presents the experimental results from both sensor geometries while Section 3.5 discusses factors influencing the sensor output.

3.1 BACKGROUND

Pressure sensors amenable to high temperatures have uses in numerous industrial sectors, and have additionally been used in gas turbine engines, coal boilers, furnaces, and machinery for oil/gas exploration. Macroscale fiber optic pressure sensors have been

developed, but microscale sensors are advantageous as they can be utilized in small volume cavities. These include combustion chambers, intake manifolds, and exhaust manifolds of internal combustion engines [Flo90, Moc91, Che04]. Their small size also allows attachment to gas turbine engines [Pul02]. Additionally, they can be inserted down boreholes in oil/gas exploration equipment [Stu82]. Some high temperature fiber optic pressure sensors have been reduced in size to several feet in length, including a fiber optic based sensor using cubic zirconia prisms which has an operating temperature of up to 1,000ºC [Pen05]. However, further miniaturization of high temperature sensors expands their use to new applications.

Micromachined pressure sensors capable of operating in high temperature environments have been fabricated and operate as interferometers on the ends of fiber optical cables, beginning in the late 1970's and early 1980's. Four types of interferometers have been constructed with fiber optic components: Mach Zehnder, Michelson, Sagnac, and Fabry-Perot. Fabry-Perot interferometers use an air gap as an optically reflective cavity. Light waves are sent through a fiber optic cable to this cavity, where pressure alters the cavity's size. This causes the reflected reference and sensing light waves to interfere constructively or destructively, based on path length differences, as they travel through the fiber optic to a sensing unit. This results in a measurable change in Fabry-Perot reflectance peaks. Fabry-Perot interferometers, external to the fiber optic cables, can use a thin-film diaphragm as a reflective surface at the end of the cavity [Wol91, Wan05b] or two optical fibers with an air gap between them [Qi01]. Operating temperatures up to 800˚C have been achieved with sapphire membranes [Fie04]. One Fabry-Perot sensor has been fabricated inside a fiber optic cable [Abe02].

To increase the operating range of these sensors, silicon carbide has been proposed as a diaphragm material with sapphire optics [Pul02].

Another sensing technology uses Bragg gratings, which are photo inscribed into fibers, and used to trace wavelength shifts caused by pressure and temperature changes [Qia01, Zha02]. They can use light-emitting diode (LED) sources and trace reflected wavelength shifts, caused by environmental changes, using spectrometers. These sensors can be used to measure temperature and pressure simultaneously in oil and gas pipelines. They have been used to measure pressure at 350˚C [Li07b]. Piezoresisitve pressure sensors with diaphragms made from silicon carbide [Ned98], and more recently even silicon [Guo08], have been reported to operate at 600ºC. Sapphire membranes have also been used in this context [Fri06].

Microdischarge-based pressure sensors present another method for high temperature pressure monitoring. These pressure sensors operate by measuring the change in spatial current distribution of microdischarges with pressure. The targeted pressure and temperature ranges are 10-2,000 Torr and 200-1,000˚C, as might be encountered in a variety of manufacturing applications. As gas pressure increases, the mean free path of ionized molecules is reduced and consequently, the breakdown and discharge characteristics are altered. Microdischarge-based pressure sensors are fundamentally different than ion gauges, which are not effective at atmospheric pressure because the small mean free path of the created ions, 20-65 nm, makes them difficult to detect at the collector [Ede90]. See Appendix 3 for a detailed discussion of the feasibility and limiting factors in developing microscale ion gauges.

Two metrics of importance for high temperature, micromachined pressure sensors are the temperature operating ranges and the fabrication complexity of the sensors. All micromachined harsh environment sensors have the advantage of smaller footprints and sizes compared to macroscale sensors, but can be further differentiated using these metrics. The various high temperature microfabricated sensors are compared in Fig. 3.1, showing the sensors' operating ranges and fabrication steps required for construction. The number of fabrication steps does not include packaging the sensor, and considers the deposition and patterning of one layer as a single step. The devices using interferometers external to the fiber optical cable were not tested at high temperatures but can potentially operate at them. The temperature range of sensors utilizing fiber optics is also often limited by the temperature range of the adhesives which attach the sensors to the fiber optical cables [Wol91, Kim95]. Piezoresistive sensors can operate at high temperatures, but require numerous fabrication steps. Microdischarge-based sensors are advantageous in regards to these metrics as they provide fabrication and structural simplicity, requiring as few as a single fabrication step, and the ability to operate at temperatures of 1,000˚C.

Microdischarge-based sensors offer several additional benefits. They utilize a simple structure without moving components, which increases durability. Additionally, they offer a direct electrical readout that simplifies packaging, unlike fiber optic based sensors which require a fiber optic cable and package feedthrough. Finally, the presented sensors benefit from a lack of complex and expensive electronics.

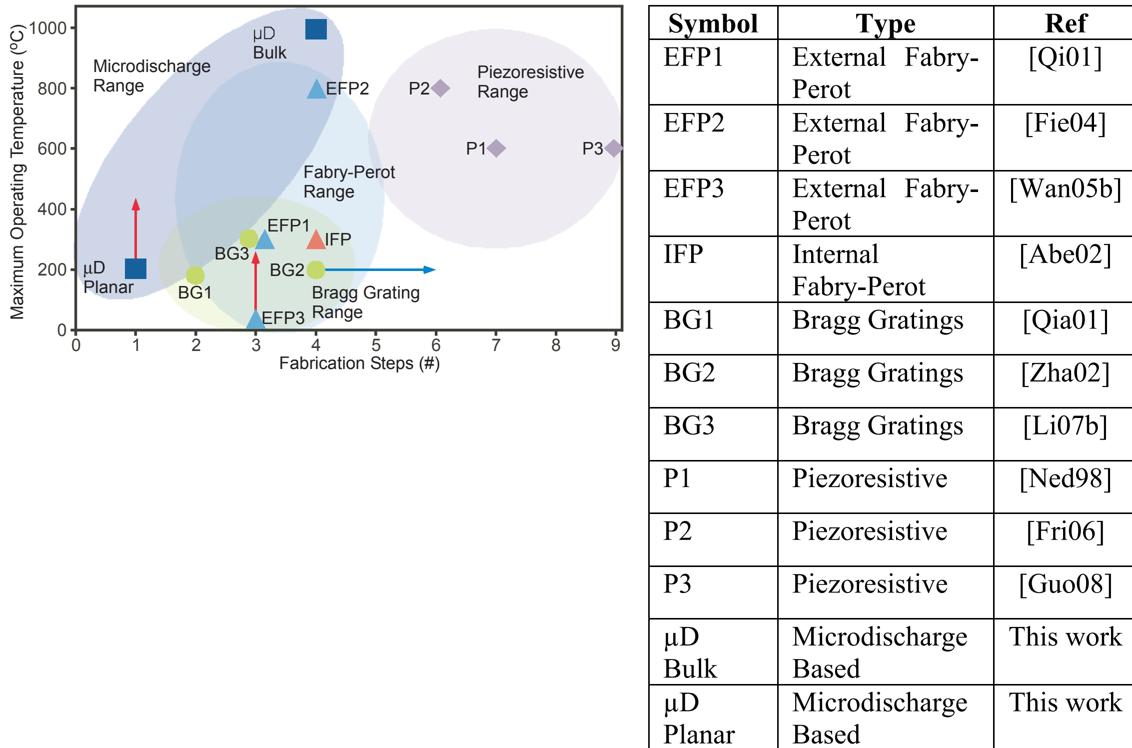

Symbol	Type	Ref
EFP1	External Fabry-Perot	[Qi01]
EFP2	External Fabry-Perot	[Fie04]
EFP3	External Fabry-Perot	[Wan05b]
IFP	Internal Fabry-Perot	[Abe02]
BG1	Bragg Gratings	[Qia01]
BG2	Bragg Gratings	[Zha02]
BG3	Bragg Gratings	[Li07b]
P1	Piezoresistive	[Ned98]
P2	Piezoresistive	[Fri06]
P3	Piezoresistive	[Guo08]
µD Bulk	Microdischarge Based	This work
µD Planar	Microdischarge Based	This work

Figure 3.1: Plot of maximum operating temperature vs. fabrication steps for various high temperature pressure sensors. (See table for the list of abbreviations and references.)

3.2 Device Concept and Operation

Devices utilizing microdischarges are well suited for high temperature operation as the bulk electrons have average thermal energies exceeding 3 eV (34,815 K) [Kus05, Mit08c] away from the cathode and small populations of very high energy beam electrons with thermal energies exceeding 400 eV near the cathode [Wil03a]. Ions have thermal energies exceeding 0.03 eV (621 K) in a 23ºC (296 K) ambient environment. These temperatures allow the species to be only minimally affected by a high or low temperature ambient, making it possible for microdischarge-based devices to operate at temperatures in excess of 1,000˚C and potentially down to cryogenic temperatures. The targeted performance range for this work is 200-1,000˚C, but some baseline studies at room temperature are included.

Two microdischarge-based microscale pressure sensor geometries are evaluated – the Bulk Foil, and the Planar. Both geometries use multiple cathodes and provide a differential current readout. (Multiple anodes may also be used; however, anode current shows excessive pressure dependence because of the high mobility of electrons that dominate it [Wil03a]. This high sensitivity results in relatively small dynamic ranges, thereby limiting the utility of multi-anode configurations.) The first geometry, Bulk Foil, uses bulk metal foils in a stress-relieved two-cathode stack within a quartz substrate, and the second, Planar, uses planar thin-film metal electrodes on a Pyrex® substrate. The Bulk Foil sensors are designed for very high temperature operation while the Planar sensors, which use thin-film metals, are designed for conventional microfabrication. While this effort focuses on the performance of these devices in a nitrogen ambient, with appropriate encapsulation, they may be used in corrosive or liquid ambients.

The Bulk Foil sensor structure consists of several electrodes suspended over a cavity in a quartz chip (Fig. 3.2). Each electrode has a single lead for electrical contact and between one and three additional supports, which maintain the suspended position of the electrode. A microdischarge chamber exists in the center of the chip, in a through-hole, as shown in Fig. 3.2(a). A single disk-shaped anode electrode serves as the bottom of the chamber while the center electrode is torus-shaped, allowing the discharges to exist between the bottom anode and both cathodes. The top cathode is disk-shaped as well, confining the discharges. The Planar sensor structure consists of several patterned electrodes on the substrate. A single circular planar anode is partially surrounded by concentric, C-shaped cathodes, and microdischarges are created above the electrodes as shown schematically in Fig. 3.2(b).

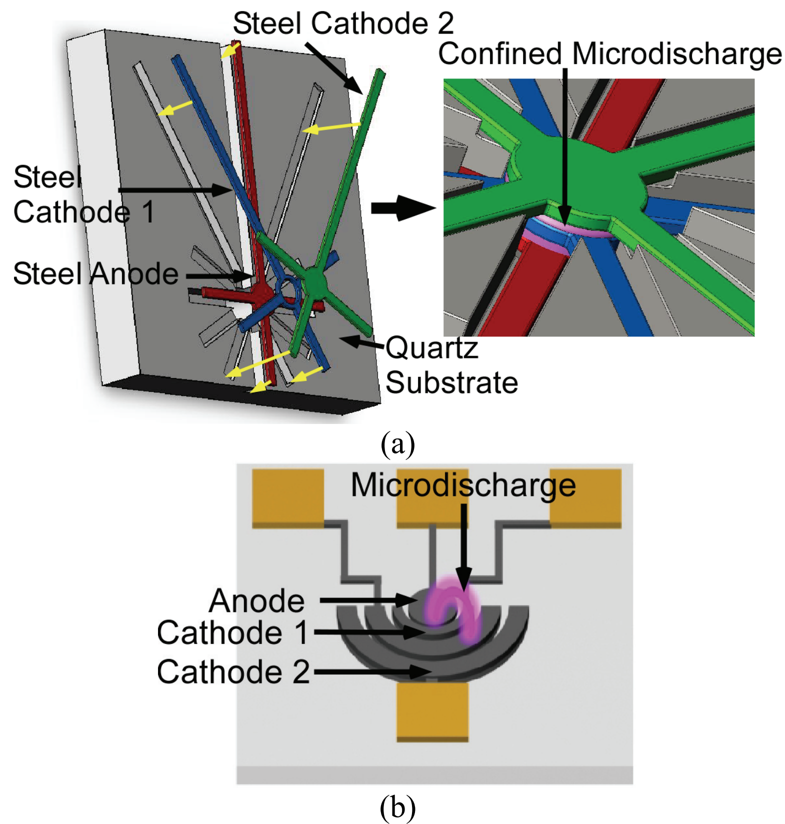

Figure 3.2: Schematic of (a) a Bulk Foil sensor with electrodes above a quartz chip, illustrating placement, and the microdischarge chamber during operation, and (b) a Planar sensor with microdischarge.

To determine the pressure, it is first necessary to separately determine the current in two of the cathodes. These current components are denoted as I_1 in the proximal cathode (cathode 1) and I_2 in the distal cathode (cathode 2). The differential current, expressed as a fraction of the total peak current, $(I_1 - I_2) / (I_1 + I_2)$, is treated as the sensor output. At low pressures, current favors the farthest cathodes, while at high pressures, the opposite occurs. An important benefit of using a differential output that is expressed as a fraction of the total is that the exact magnitudes are less important than fractional changes or discharge size.

The basic operation of a DC microdischarge in a Bulk Foil sensor is illustrated in Fig. 3.3, indicating electron and ion transport. The electrons are drawn towards the anode, whereas the positive ions are drawn to the two separate cathodes forming positively charged sheaths around them. Upon cathode impact, the energetic ions eject high energy secondary electrons from the cathodes, which sustain the microdischarges by ionizing additional neutral molecules and continuing the breakdown process. High energy ions are encountered in microdischarges at pressures higher than atmosphere as a result of the high power densities and voltage gradients encountered in the small gap spacing. The current in each cathode is composed of a combination of positive ions impacting the cathodes from the microdischarge and secondary electrons ejected from the cathodes upon ion impact. Further away from the cathodes, the current is carried primarily by the faster moving electrons.

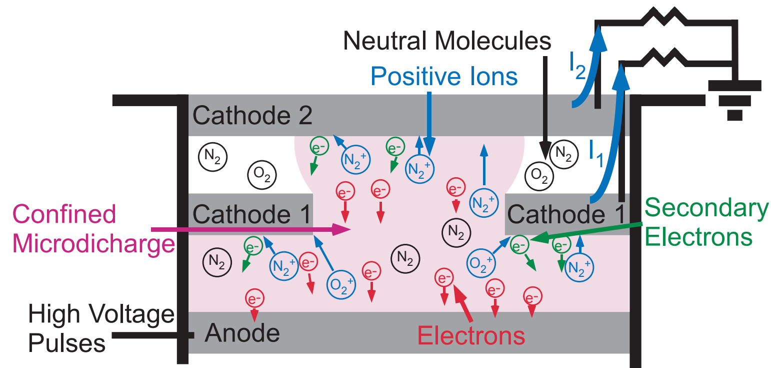

Figure 3.3: Diagram of a microdischarge between a single anode and two cathodes in a Bulk Foil structure.

3.2.1 Pulsed Discharges

Power consumption and parasitic heating in the pressure sensors are controlled by using pulsed DC microdischarges, as opposed to constant DC discharges. The use of

pulsed powering creates high current pulse arcs (40-100 ns in duration), which initiate the microdischarges as described by several authors [Sta05, Rah07, Cho08]. The current pulses are measured for operation as they provide greater sensitivity to pressure than the sustained DC current levels in the microdischarges. It will be shown in Section 3.4 that the magnitudes of the current pulses respond to pressure with greater sensitivity at low pressures than at high, and that this characteristic also appears in the differential output of the sensors. While steady state models exist for plasmas, the initial transient current pulses encountered during microdischarge initiation have not been modeled. Furthermore, the developed closed form microdischarge models are not viable for complex arrangements in which there are more than two electrodes. The steady state operating parameters of the microdischarges in a pressure sensor are presented in Appendix 1.

3.2.2 Current Pulse Operation and Simulation

The current pulses in cathodes 1 and 2 of microdischarge-based pressure sensors are roughly approximated by a circuit model, which predicts the pulse profile in time as a function of discharge voltage. The pulse power source is represented by the discharging of a capacitor, C, while the current pulse is represented as a series combination of an inductance, L, and resistance, R, as developed by Robiscoe *et al.* [Rob88a, Rob88b]. A large shunt resistance, R_s, is used to allow secondary current, I_s, to drain the capacitor, even if the pulse current, I, is zero. The pulse circuit model is shown in Fig. 3.4. As all of the circuit elements are passive, the relationships between voltage drops across the circuit elements result in a linear system of differential equations with constant

coefficients. The solutions to these systems are damped trigonometric oscillations if the circuit rings, or exponentially decaying voltage profiles if the circuit is overdamped.

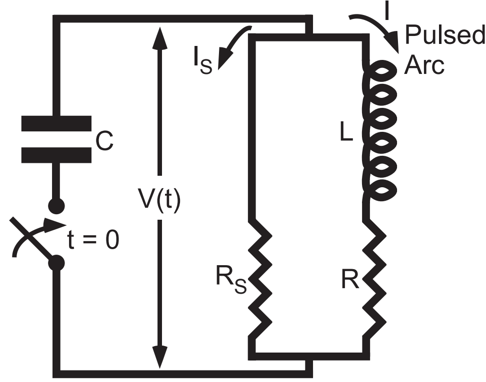

Figure 3.4: Circuit model for discharge. The pulse power source is represented by the discharging of the capacitor, *C,* that is switched on at time t = 0. The current pulse is represented as a series combination of an inductance, *L*, and resistance, *R* along the current path. R_s is a shunt resistance, which allows a small amount of secondary current to flow during the main current pulse.

The circuit elements in the model can be determined using experimentally obtained pulse values. The pulse rise time, pulse duration, peak current, and pulse energy are all functions of the circuit element values, and can thus be used to determine these values for the particular pulses encountered in cathodes 1 and 2 of the microdischarge-based pressure sensors. The pulse rise time is expressed as

$$t_r = (1+2\varepsilon)\frac{L}{R}\left(\ln\frac{1}{\varepsilon}-r\right), \tag{3.1}$$

where $\varepsilon = L/(CR^2)$ and $r = R/R_s$. The pulse duration is expressed as

$$t_p = \left[(1+\varepsilon)RC\right](1-r). \tag{3.2}$$

The pulse peak current is

$$Ip = \frac{V_0}{R}\left[1-\varepsilon\ln\left(\frac{1}{\varepsilon e}\right)-r\right], \tag{3.3}$$

where V_o is the initial applied voltage. The pulse energy is

$$Q = \frac{1}{2}\frac{CV_o^2/R}{(1+r)(1+\varepsilon r)}. \tag{3.4}$$

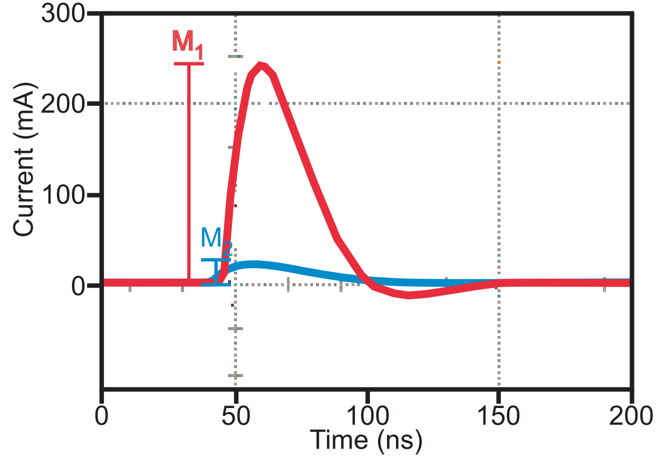

(a)

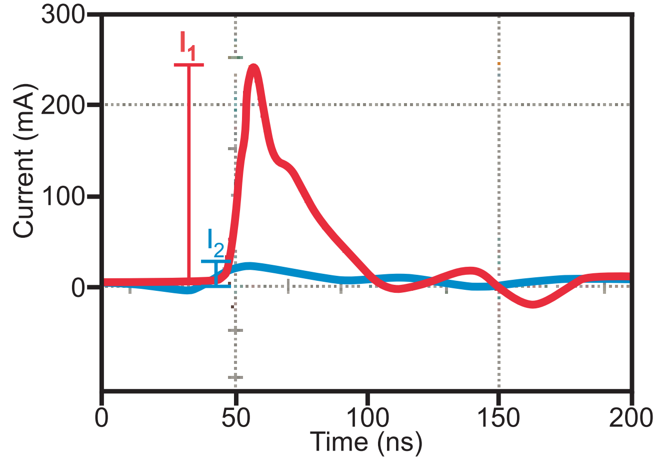

(b)

Figure 3.5: Modeled (a) and experimentally measured (b) current pulses in cathodes 1 and 2 in a pressure sensor with electrodes spaced 50 µm apart, 1 mm in diameter, and 125 µm thick at 200 Torr. The modeled pulses are referred to as M_1 and M_2.

Figure 3.5(a) shows the theoretical current pulses in cathodes 1 and 2 of a pressure sensor with electrodes spaced 50 µm apart, 1 mm in diameter, and 125 µm thick at a pressure of 200 Torr. For cathode 1, the pulse rise time is 10 ns, the pulse duration, measured from initiation to the I_p/e time, is 50 ns, and the peak current is 235 mA. For

cathode 2, the parameters are 20 ns, 40 ns, and 10.6 mA respectively. Using these parameters and equations 3.1-3.3, the values for *R*, *L*, and *C* are obtained numerically for each cathode. Further refinement is possible by fitting to experimental results. The circuit elements for cathode 1 in the described sensor are found to be 2.6 kΩ, 25 μH, and 6.8 pF respectively and 48 kΩ, 600 μH, and 0.6 pF for cathode 2. The shunt resistance is simulated as a large impedance, 100 kΩ. The predicted current pulses as a function of time are determined through modeling utilizing SPICE. Similar analysis can be applied to determine the circuit elements for various pressure sensor configurations.

In addition to the physical effects discussed above, it is worthwhile to consider other possible contributors to the electrode current. Thermionic emission current, for example, can be estimated by the Richardson-Dushman equation [Smi70]. This current component is estimated to contribute at least four orders of magnitude less current than the discharge current at 1,000˚C, although cathode spots could result in much higher localized temperatures. The flow of electrons from field emission is considered according to the Fowler-Nordheim equation. To contribute measurable current, the electric field strengths need to be on the order of 10^7 V/cm [Cob58]. The maximum field strength is predicted as 2.4 x 10^5 V/cm utilizing COMSOL Multiphysics®, although this considers a uniform electric field and the actual field strength may be much greater, especially in the sheath. Additionally, unwanted asperities can concentrate and increase electric field strength. These contributions are discussed in more detail in Appendix 1, Section A1.5.

3.3 DESIGN AND FABRICATION

The Bulk Foil sensors, which are intended for operation at temperatures up to 1,000ºC, use a quartz substrate. For the electrodes, #302 stainless steel is used for several reasons. Primarily, it is robust, inexpensive, easily machinable by micro-electro-discharge machining (μ-EDM) [Tak02, Tak04, Tak06, Ric08] and photochemical etching, and has a sufficient secondary emission coefficient (i.e. 0.04 secondary electrons per incident 50 eV Na^+ ion [Wal99]). Additionally, it is oxidation-resistant at high temperatures and can be heated to 1,420ºC before melting. Alternate refractory metals such as tungsten, molybdenum, and niobium oxidize at high temperatures in air, making them less desirable. Platinum, iridium, and platinum-rhodium are attractive options but are significantly more expensive than stainless steel.

The electrodes are lithographically patterned and etched from stainless steel foil, using photochemical machining (Fig. 3.6) [All03]. This process involves coating a thin sheet of metal with photoresist, exposing the resist, and spraying the sheet with a chemical etchant to dissolve the exposed metal. The exposed metal is completely removed, leaving through-holes in the sheet, and the resist is stripped (Fotofab, Chicago IL). Alternatively, electrodes have been fabricated using micro-electro-discharge machining.

Next, the electrodes are integrated into the substrate. An arrangement that accommodates the expansion mismatch between electrodes and substrate is necessary. Trenches of specified depths and a through-hole in the center are cut into the planar quartz substrate. Both mechanical and wet-etch processes can be used for this purpose. The electrodes are assembled into the trenches, with the circular portions located in the

through-hole. The different depths between the various trenches specify the discharge gap spacing, as the electrodes lie flush with the bottom of the trenches. Ceramic epoxy holds the electrode lead and support arms in place, without adhering to the stainless steel. This allows the leads and supports to expand separately from the quartz chip and the ceramic epoxy without buckling. High temperature-compatible wires are soldered to the electrodes and the solder is encased in ceramic. This ceramic keeps the solder in position so it maintains electrical contact, even at high temperatures.

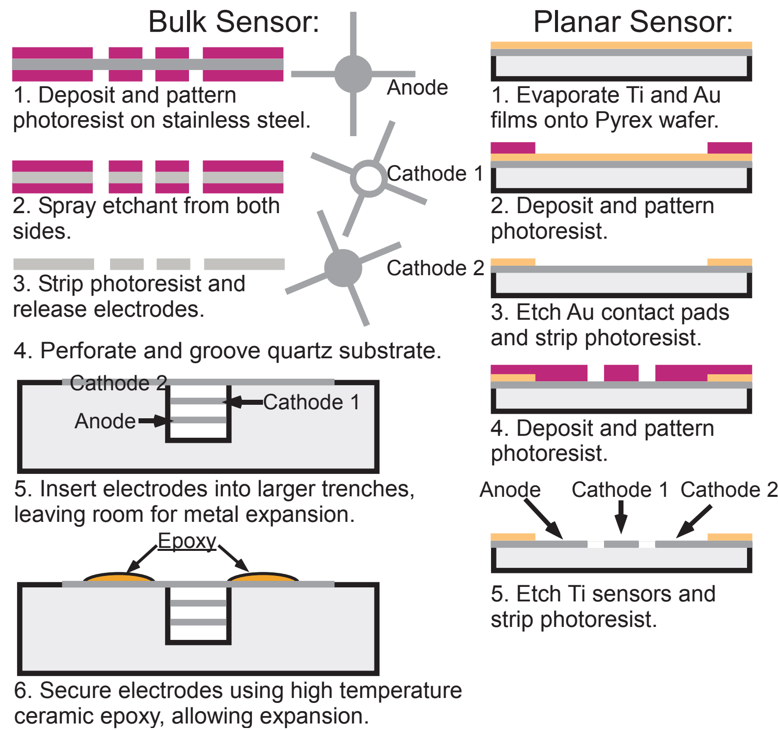

Figure 3.6: Fabrication processes for Bulk and Planar sensors.

The Planar sensors, which are intended for operation at temperatures up to 200ºC, are even easier to fabricate (Fig. 3.6). The substrates are #7740 Pyrex® glass wafers, which have a softening temperature of 820ºC. A Ti film (1 μm thick) and an Au film (500 nm thick) are thermally evaporated onto 500 μm thick glass wafers without

removing the wafers from vacuum. Thin-film titanium electrodes are used as they have previously been utilized to create sustained microdischarges [Wil01a]. The contact pads are patterned on the gold layer using photolithography and the film is removed using Transene GE-8148 gold etchant, which does not etch titanium. The electrodes are then patterned in the titanium layer using photolithography.

Sensor characteristics such as the sensitivity, pressure dynamic range, and temperature dynamic range depend on a variety of dimensional parameters, including inter-electrode spacing, electrode diameter, and the cathode thickness. (Cathode thickness effects sheath sizes as well as electrode spacing.) The anode/cathode spacing in these sensors is set to produce measurable results up to 1,000ºC. (The sensors are designed to function with an applied voltage of 1,000 V; altering the voltage results in different sensitivities.) A typical Bulk Foil design with electrodes spaced 100 μm apart, 3 mm in diameter, and 50 μm thick is shown in Fig. 3.7(a). These sensors have active areas of 7 mm^2 and are fabricated on 4 cm^2 chips. A typical Bulk Foil design with electrodes spaced 50 μm apart, 1-2 mm in diameter, and 125 μm thick is shown in Fig. 3.7(b). These sensors have active areas of 0.8-3 mm^2 and are fabricated on 1 cm^2 chips.

The Planar sensors have 3-7 cathodes, of which two are selected for the pressure measurement. The remaining are shunted to ground, and while they draw currents, they are not used in pressure measurement. The cathodes are spaced 5-100 μm apart and are 5-300 μm in width. The sensors have active areas of 0.13-3 mm^2 and are fabricated on 0.25 cm^2 chips. A typical Planar sensor design, with three circular cathodes, spaced 50 μm apart and 300 μm in width, is shown in Fig. 3.7(c), while a design with five straight cathodes spaced 50 μm apart and 50 μm in width, is shown in Fig. 3.7(d).

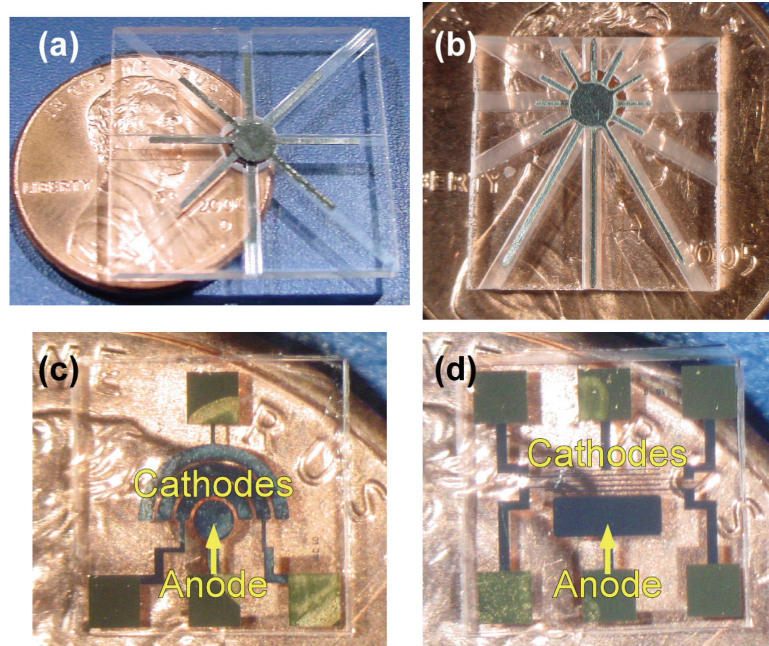

Figure 3.7: Bulk Foil sensors with (a) electrodes spaced 100 µm apart, 50 µm thick and (b) electrodes spaced 50 µm apart, 125 µm thick. Planar sensors with (c) three circular cathodes spaced 50 µm apart, 300 µm in width and (d) five straight cathodes spaced 50 µm apart, 50 µm in width.

3.4 Experimental Results

Bulk Foil pressure sensors were fabricated and tested at various temperatures up to 1,000ºC, measuring pressures between 10 Torr and 2,000 Torr. They were tested in a vacuum chamber with the pressure set by a two-stage rotary vane roughing pump (Oerlikon Leybold Vacuum Trivac D 16B) and accompanying pressure controller (MKS® 600 Series). Positive pressure was applied using compressed gas. The pressure sensors were calibrated against an external macroscale pressure transducer (MKS® Baratron® Capacitance Manometer model #627B23TDC1B). The temperature was set by testing the sensors on a silicon nitride igniter (Igniters Direct™ Glo-stix™), which was capable of producing surface temperatures of 1,500ºC. The igniter consisted of a thin-film tungsten heater insulated in planar silicon nitride structure. K-type thermocouples were

used to measure the temperature at the top and bottom surfaces of the pressure sensors at several locations to provide a temperature control feedback system. Pulses, 1-20 ms in duration, were applied at a rate of 2-10 Hz to the anodes of the sensors with positive voltages between 700 V and 1,000 V. A computer controlled, single ended, transformer coupled, gate drive circuit created the pulses (Fig. 3.8). A current limiting ballast resistor was used in series with the anode, and 100-Ω resistors were used in series with each cathode to measure current. The same circuitry powered Planar sensors. The pulses consumed between 168 μJ and 6 mJ each.

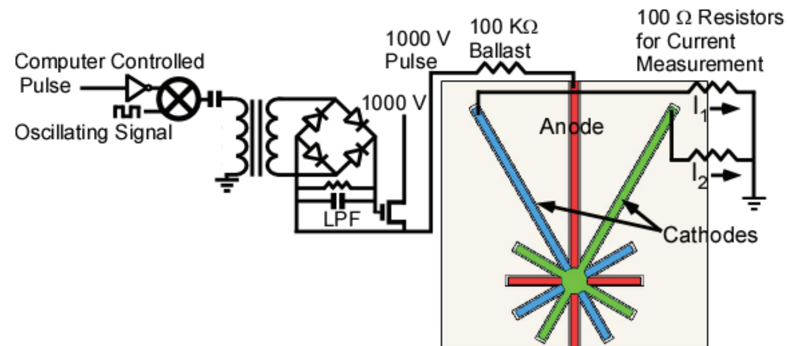

Figure 3.8: Pulse generating and readout circuitry used for sensor operation.

The applied voltage pulses resulted in current pulses through each cathode as shown in Fig. 3.9. The current pulses were approximately 40-100 ns in duration, with amplitudes of 1.3 mA to 2.85 A in the Bulk Foil sensors and 25 mA to 2 A in the Planar sensors, varying with temperature and pressure. The experimentally obtained pulses in both cathodes are shown in Fig. 3.5(b). They demonstrated damped trigonometric current oscillations.

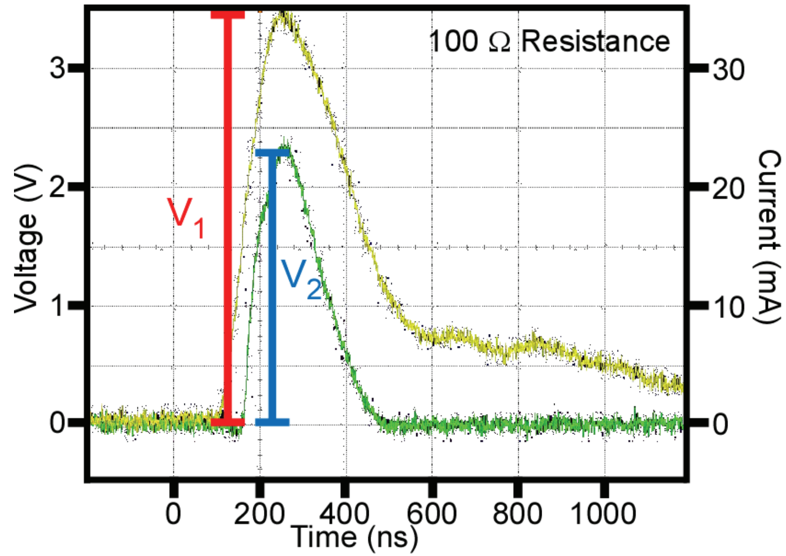

Figure 3.9: Oscilloscope trace of the voltage pulses used for pressure measurements. The voltage was measured across 100 Ω resistors and used to calculate the current, with V_1 as the voltage in cathode 1 and V_2 as the voltage in cathode 2.

The sum of the measured cathode current pulse peaks for a Bulk Foil device is presented in Fig. 3.10(a). At each temperature, this sum conforms to the equation:

$$I_{pk1} + I_{pk2} = C_1 \cdot \ln(p) - C_2 \qquad (3.5)$$

The terms C_1 and C_2, determined by a least-squares fit to the measured data in Fig. 3.10(a), are plotted in Fig. 3.10(b) as a function of temperature. At temperatures greater than 600ºC, terms C_1 and C_2 saturate, indicating the total cathode peak current becomes less dependent on temperature but remains dependent on pressure at higher operating temperatures. The pressure in equation 3.5 was measured with the external macroscale pressure transducer.

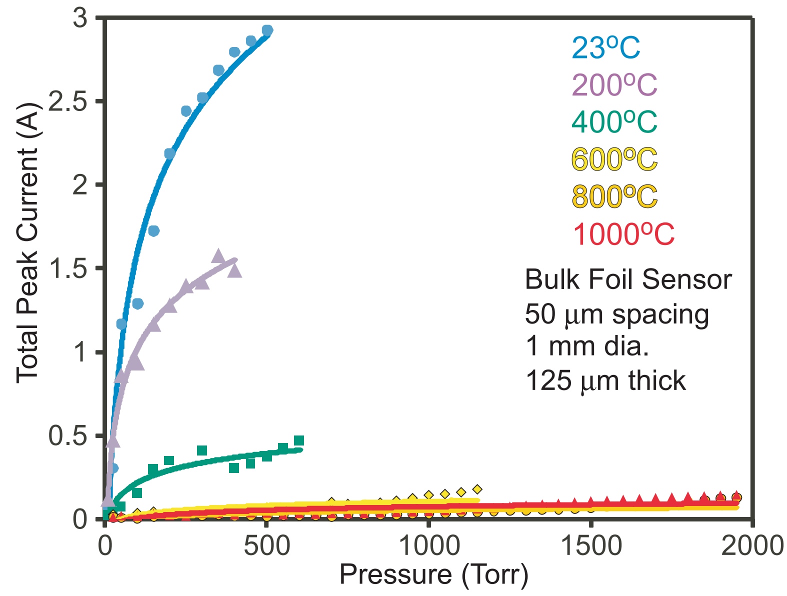

(a)

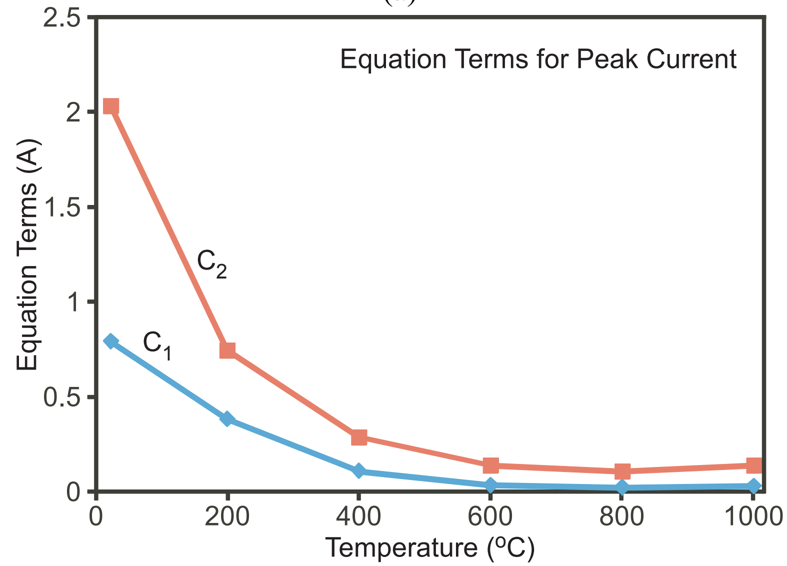

(b)

Figure 3.10: Measured current pulse peak values. (a) Sum of the pulse currents in two Bulk Foil cathodes as a function of pressure and temperature. The empirical curves for each temperature are indicated by the solid lines. (b) Temperature trend for equation terms C_1 and C_2 in the peak current equation.

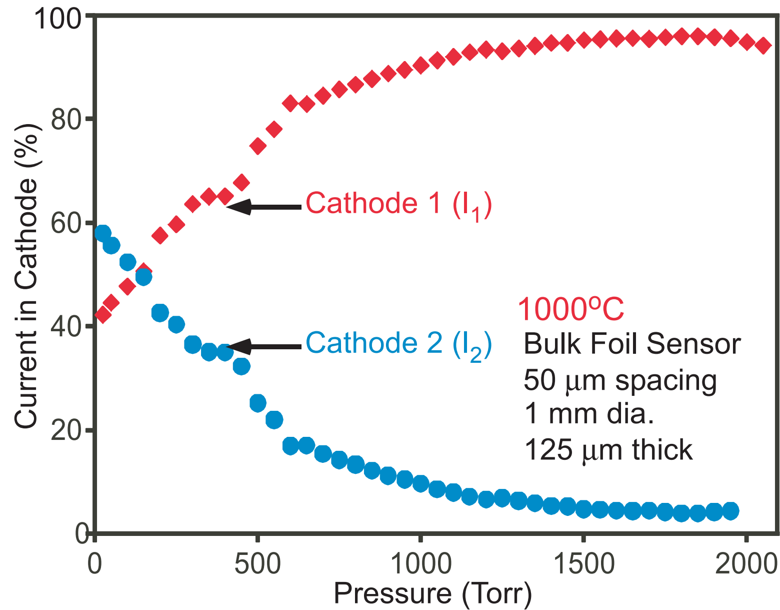

Figure 3.11: Percentage of total current in the cathodes at 1,000˚C in a Bulk Foil sensor with electrodes spaced 50 µm apart, 1 mm in diameter, and 125 µm thick.

The Bulk Foil sensors were tested in a nitrogen filled chamber with temperature and pressure control. Figure 3.11 shows fractional cathode currents, at 1,000˚C, for a sensor design with electrodes that were spaced 50 µm apart, 1 mm in diameter, and 125 µm thick. As noted, the output of the sensor is the differential peak current between two cathodes, expressed as a fraction of the total peak current. The typical output for this sensor is shown in Fig. 3.12(a). Figure 3.12(b) presents the typical output from a sensor design with electrodes spaced 100 µm apart, 1 mm in diameter, and 125 µm thick. The sensors demonstrate two regions of sensitivity (similar in some sense to touch-mode capacitive pressure sensors [Cho92]). At low pressures the response is highly linear, whereas at high pressures it conforms to equation 3.5. The transition between these two regions rises from about 100 Torr at room temperature to about 500 Torr at 1,000°C. The average sensitivities in the low pressure and high pressure operating regions of these sensors are shown in Fig. 3.13 as functions of temperature.

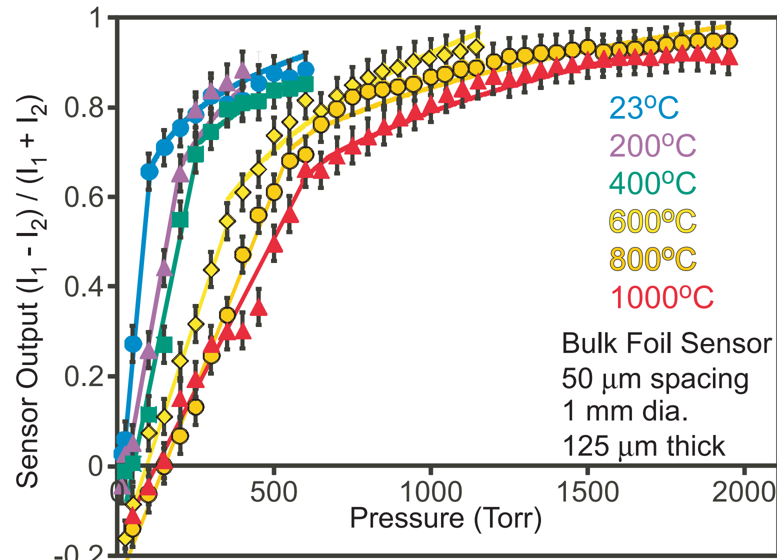

(a)

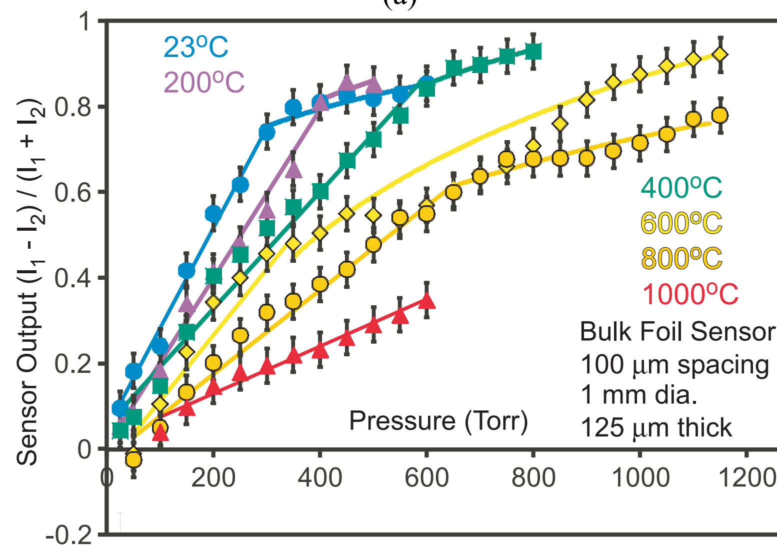

(b)

Figure 3.12: Differential current output determined from the percentage of total current in Bulk Foil sensors with electrodes (a) spaced 50 μm apart and (b) spaced 100 μm apart, 1 mm in diameter, and 125 μm thick. Each data point is the average of 100 measurements. The two empirical curves per temperature are indicated by the solid lines.

Sensitivity is measured in parts per million per Torr (ppm/Torr), in which the full-scale sensor output is viewed as a million "parts". The "parts per million" indicates the change in the percentage of the full scale sensor output (change in parts/one million parts), typically over a unit pressure for pressure sensitivity or over a unit temperature for temperature sensitivity. For these sensors, the sensitivity is measured per Torr. The

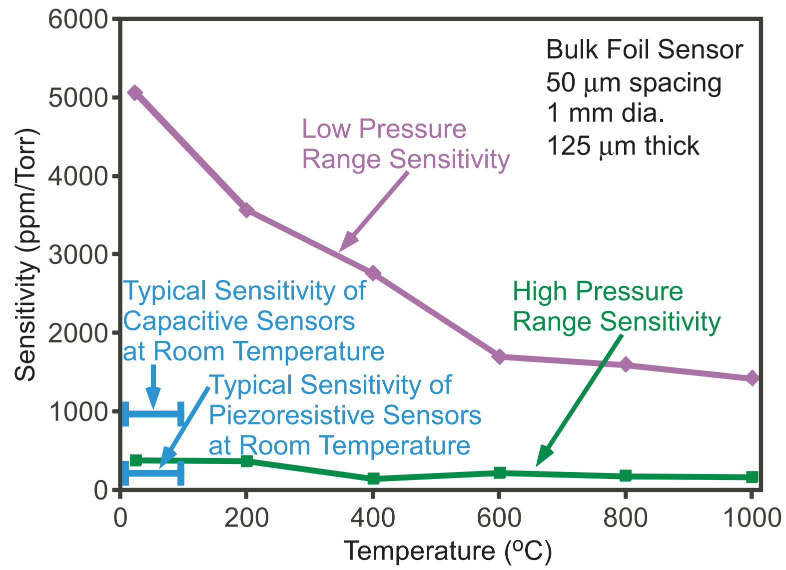

(a)

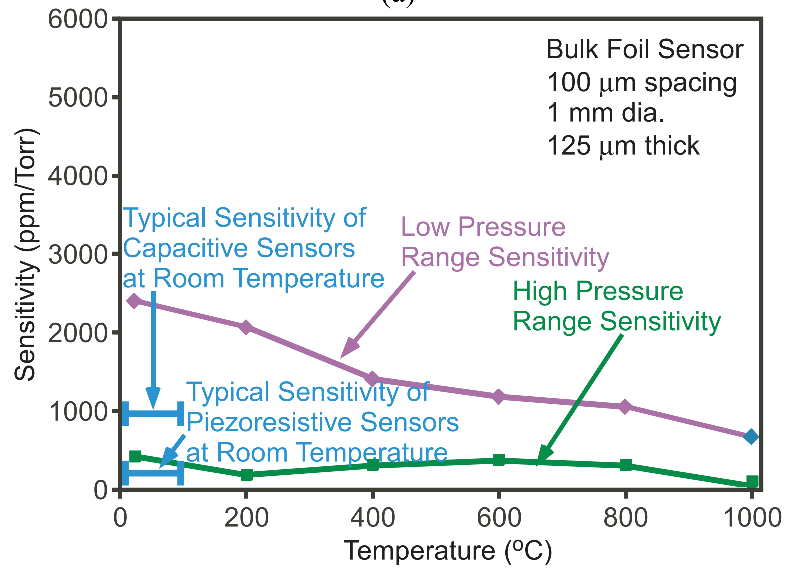

(b)

Figure 3.13: The average sensitivities in both the low and high pressure ranges for the Bulk Foil sensors in Fig. 3.12(a) and (b) as functions of temperature.

temperature coefficient of sensitivity is a measure of the change in sensor output as a function of temperature, and is measured in parts per million per kelvin. One sensor design typically demonstrated the maximum lower pressure sensitivity, 5,420 ppm/Torr, as well as the maximum higher pressure sensitivity, 500 ppm/Torr.

The use of three, or more, cathodes to simultaneously enhance both sensitivity and dynamic range (albeit at the cost of increasing lead count at the circuit interface) was explored. Devices with three or more cathodes were fabricated and the signal output of two cathodes was used. The signal generated from two cathodes of a Bulk Foil sensor that had three cathodes spaced 100 μm apart, 3 mm in diameter, and 50 μm thick, provided a relatively high sensitivity of 5,000 ppm/Torr. Unfortunately the sensor had a compromised dynamic range of only 300 Torr. Other design variations were also explored and the typical results are listed in Table 3.1. The minimum average temperature coefficient of sensitivity was -550 ppm/K.

Table 3.1: Typical performance of four different sensor designs with the highest performance in each category in bold.

Sensor Parameters	Max Low Pressure Sensitivity (ppm/Torr)	Max High Pressure Sensitivity (ppm/Torr)	Dynamic Range (Torr)	Temp. Coeff. of Sensitivity (ppm/K)
Planar W=300 μm G =50 μm	**9,800**	**1,400**	175	-1,412
Bulk D=1 mm W=125 μm G=50 μm	5,060	380	**2,000**	-650
Bulk D=1 mm W=125 μm G=100 μm	2,170	220	1,150	**-550**
Bulk D=2 mm W=125 μm G=100 μm	**5,420**	**500**	900	-925

The Planar sensors were tested in the context of a chemical sensing system, with an inert carrier gas (He) along with air and organic vapors (Chapter 4, Section 4.4).

Packaging these sensors with other devices and operating them concurrently demonstrated the ability of microdischarge-based sensors to function in systems, without disrupting the operation of other components. The helium, air, and organic vapors were introduced into the microscale package with the pressure set by a two-stage rotary vane roughing pump (Oerlikon Leybold Vacuum Trivac D 16B) and accompanying pressure controller (MKS® 600 Series). The pressure measured by the Planar pressure sensors was calibrated against an external macroscale pressure transducer (MKS® Baratron® Capacitance Manometer model #627B23TDC1B). Figure 3.14(a) illustrates the fractional cathode current and differential output of a Planar sensor packaged with other devices as described above, with three cathodes spaced 50 μm apart, 300 μm in width. In this geometry, the intermediate cathode was grounded. Typical sensitivity was 9,800 ppm/Torr in the lower pressures, from 30-100 Torr, and 1,400 ppm/Torr in the higher pressures, from 100-200 Torr. Figure 3.14(b) illustrates the output of a Planar sensor with five cathodes spaced 50 μm apart, 50 μm in width, which produced a uniform sensitivity of 2,000 ppm/Torr across both pressure regions from 25-275 Torr at 23˚C using cathodes 1 and 2. The remaining cathodes were grounded. The impact of Planar electrode geometries was also investigated. Planar sensors with five cathodes spaced 5 μm apart and 5 μm in width, and 10 μm apart and 10 μm in width, were examined but demonstrated low sensitivities, as did sensors with straight cathodes, as opposed to circular. This indicates radial symmetry of the cathodes around a central anode is a feature worth retaining.

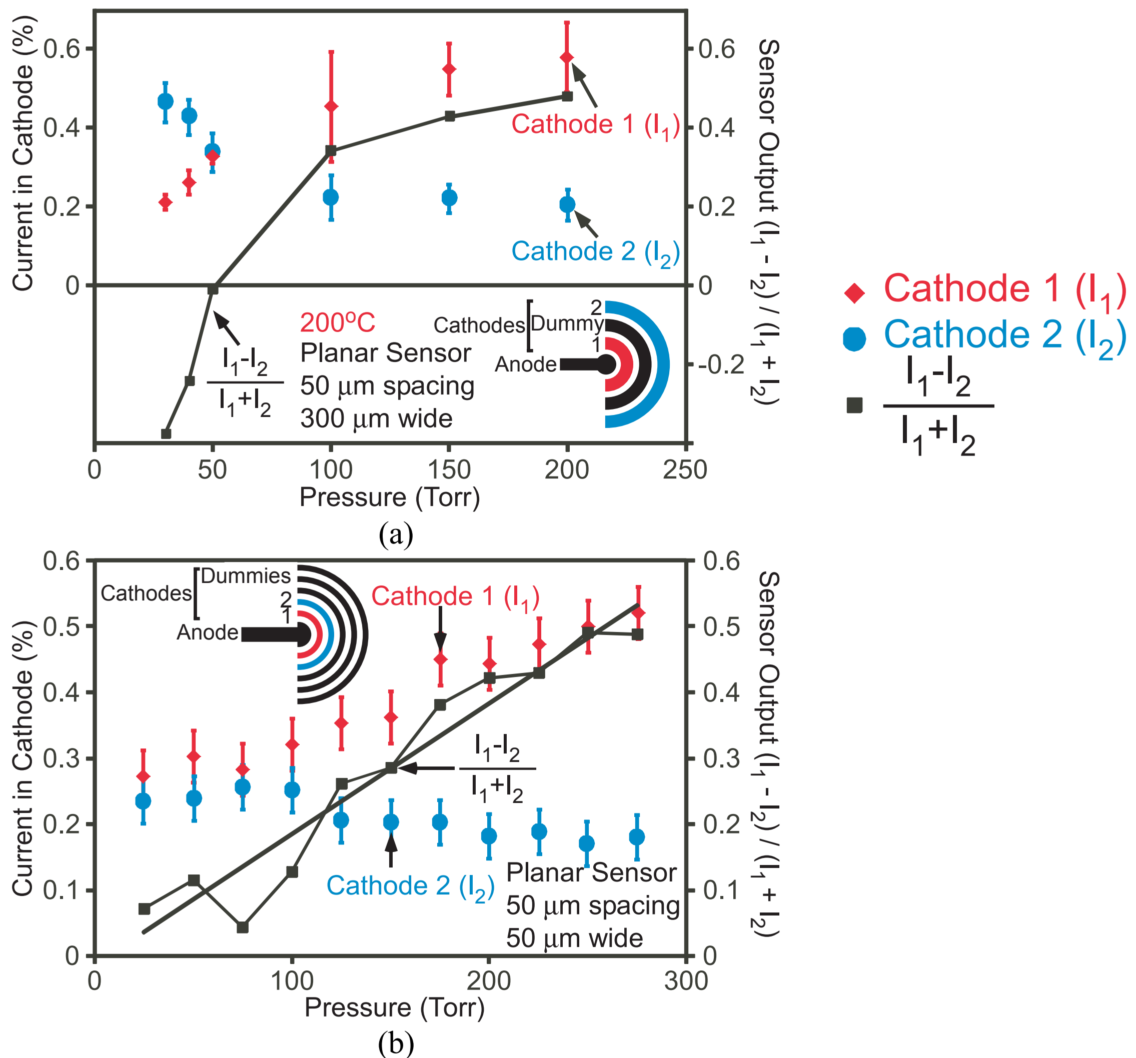

Figure 3.14: Percentage of total current and differential current output in Planar sensors with (a) electrodes spaced 50 µm apart, 300 µm in width and (b) electrodes spaced 50 µm apart, 50 µm in width. Each data point is the average of 100 measurements.

Sensitivity, dynamic range, and the temperature coefficient of sensitivity are metrics used to compare microdischarge-based pressure sensor designs to one another and other pressure sensors. The performance of four different sensor designs, both Planar and Bulk Foil, are shown in Table 3.1, with the highest performance in each category in bold. The data in the table represents typical operation of each sensor design.

3.5 DISCUSSION OF RESULTS

Several points concerning the sensor operation warrant a discussion, the temperature coefficients of sensitivity, the potential impact of electrode contamination, and the possibility of encapsulation.

The sensors demonstrate a negative temperature coefficient of sensitivity. For example, a sensor with electrodes spaced 50 μm apart, 1 mm in diameter, and 125 μm thick has a sensitivity in the low pressure region of 5,060 ppm/Torr at 23ºC and 1,420 ppm/Torr at 1,000ºC. There are a number of possible contributors to the temperature coefficient of sensitivity, ranging from changes in the nature of the microdischarge to structural effects such as minor variations in electrode separation caused by expansion mismatch with the substrate. For comparison, typical piezoresistive and capacitive pressure sensors have sensitivities of 100-1,000 ppm/Torr respectively, and temperature coefficients of sensitivity of ±1,000 ppm/K to ±5,000 ppm/K [Zha94, Hak06].

In nitrogen environments, coating of the electrode surfaces with contaminating thin films is not a primary concern, in these sensors. In the past, microdischarges have been used to, and can unintentionally, coat electrode surfaces in reactive environments [Sch05]. However, with discharges of sufficient energy, thin films are sputtered off the electrodes. This is demonstrated through the successful use of titanium electrodes, which form native titanium oxide layers in air. Radio frequency discharges are also utilized to remove coatings [Riz77].

In general, microdischarge-based pressure sensors should be calibrated for the gas environment in which they operate. To permit operation in variable environments that may additionally contain corrosive gases or even liquids, the pressure sensors can be

encapsulated within a sealed cavity with a flexible diaphragm. The sealed cavity could contain pure nitrogen, helium, or other gas in which the discharges would be created. The external fluidic pressure would be transferred to the encapsulated gas through the diaphragm, taking advantage of the high sensitivity of the pressure sensors.

CHAPTER 4

CHEMICAL SENSING MICROSYSTEM

This chapter discusses the exploratory use of the microscale-sputter-ion pump and microdischarge-based pressure sensor in a harsh environment microdischarge-based chemical sensing microsystem at temperatures of up to 200ºC. In particular, the ability of the micro-SIP to purify gas environments of contaminating gases is explored as it purifies spectra for an optical emission sensor. This system has three microdischarge-based devices in total: a pressure sensor, a gas purifier, and an optical emission sensor. The system operates by obtaining a gas sample while monitoring the pressure, purifying the sample using a micro-SIP, and determining the gases present in the sample using an optical emission sensor. The ability of the system to purify samples for carbon detection is discussed. Section 4.1 presents the need for harsh environment chemical sensors, a comparison of currently used harsh environment sensors, and a comparison of microdischarge-based optical emission sensors. Section 4.2 presents the need to remove contaminant gases such as nitrogen when performing spectral chemical sensing by illustrating the ability of nitrogen to preclude SF_6 detection. Section 4.3 presents the ability of micro-SIPs to purify gas environments from contaminating nitrogen and oxygen. Section 4.4 presents the system for gas phase chemical detection in harsh environments.

4.1 BACKGROUND

The detection of chemicals in harsh environments is important to numerous industries and researchers. In particular, the use of microscale harsh environment chemical sensors can potentially reduce the cost of drilling for petroleum exploration, field development, and long-term geological monitoring [Alb00]. During petroleum exploration and pumping, the flow of removed material is a combination of oil, water, and gases. Continuous down-hole analysis of gas during petroleum pumping is useful for the control of product quality, the detection of unwanted contaminants, and the optimization of product treatment downstream [Hun97]. Continuous chemical analysis is also useful during petroleum detection. The down-hole sensors for detection and monitoring must be able to withstand elevated temperatures and pressures. They also must be able to detect carbon, sulfur-containing gases, and contaminant gases such as H_2S and CO_2 [Col95, Hun97]. Other high temperature applications also require chemical sensing and monitoring. For example, automobile emission control requires monitoring of the levels of nitric oxides (NO_x) and hydrocarbons (C_xH_y). Two metrics of importance to high temperature, micromachined gas sensors are the temperature operating ranges and the number of chemicals detectable by the sensors. These metrics will be used to evaluate different sensors and sensor technologies.

Numerous miniature high temperature chemical sensors have been developed. Miniaturization of chemical sensors for portable applications often involves the utilization of new technologies as many macroscale technologies cannot be scaled using typical fabrication processes. Instead, many miniature sensors utilize the changing

properties of thin films in which target molecules are adsorbed on the surface of these films and cause some property of the thin films to change. The selectivity of the sensors is often tailored to the analyte(s) of interest by varying parameters including: dopants, grain sizes, catalysts, external filters, operating temperature, and many other factors [Wil01b].

There are three primary modes of operation of thin-film sensors. (1) Resistor type sensors (chemiresistors) which exhibit linear IV curves that reversibly change as a function of partial pressure of molecules. (2) Capacitor-type sensors based on metal/oxide/semiconductor (MOS) devices which show voltage-dependent CV curves. (3) Diode-type sensors which show partial-pressure-dependent non-linear IV and CV curves. In addition, field effect transistors utilizing chemical sensitive gates, chemFETs, acoustic wave technology including bulk and surface acoustic wave devices (BAW and SAW), and ion mobility sensors have been also used.

Chemiresistors in their simplest form consist of a selective layer whose conductivity is modulated by interaction with analyte(s). They are arguably the most commercially successful miniature gas sensor and have the advantages of compact size, simple fabrication, low cost, and simple measurement electronics [Wil01b, Jan03]. They are commonly used to monitor oxidizing and reducing gases such as O_2, H_2, CO, NO_2, and hydrocarbons [Gop96] and have a detection limit range from ppb's [Cai02] to a few hundred ppm [Dav05] depending on the coating used. Chemiresistors typically monitor one or several chemicals, but can be arranged in arrays to expand their analysis [Dom97]. Unfortunately, control of chemiresistors' surface properties can be challenging, especially when they are affected by usage conditions and temperature variations. In

addition, their sensitivity is highly dependent on the fabrication process and they can require hours to recover when operated at temperatures less than 200ºC. They are also hampered by signal-to-noise ratio limitations.

Several semi-conduction metal oxide (SMO) chemiresistors have been developed for use at high temperatures. Metal–oxide chemical sensors have been used in both the research and commercial communities because they can be fabricated at least as easily and with greater stability than other chemiresistive materials, such as polymers and organic films. Typical sensors use zirconium oxide, gallium oxide, or tungsten oxide while niobium oxide has also been utilized [Che08]. Vapors that can be sensed effectively include ammonia, hydrogen, hydrogen sulphide, ozone, propane, sulphur dioxide, hexane, carbon monoxide, various saturated and unsaturated hydrocarbons, and other reducing gases. A list of various semi-conduction metal oxide films used, vapors sensed, temperature ranges, and benefits of the various films is presented by Wilson [Wil01b]. The listed sensors use various metal-oxide films to detect between one and five vapors and operate at temperatures of 250-1,000ºC. For example, gallium oxide sensors have been fabricated which measure oxygen content from 600-1,000ºC [Fle91, Hoe01, Ogi01]. Other metal-oxide chemical sensors can measure NO and NO_2 [Hoe01, Miu03].

Metal insulator semiconductor (MIS) or metal oxide semiconductor (MOS) sensors measure capacitance changes with gas partial pressure. They are composed of a gas sensitive metal, typically platinum, deposited on an oxide adherent to a semiconductor. To operate at high temperatures, silicon carbide has been used instead of silicon, forming metal-insulator-silicon carbide (MISiC) structures. Species that have

been monitored with MISiCs at high temperatures include hydrogen, hydrocarbons, nitrogen oxides, and fluorine containing gases. Hydrogen and oxygen have been measured at 400ºC [Tob03] and 30 ppb of fluorine has been detected at 350ºC [Vas98]. These devices have been operated up to 600ºC for short periods of time but stable long-term operation is limited to a few days by measurand and temperature permanently induced modifications to the materials [Thi06].

Schottky-barrier sensors measure a shift to a lower bias voltage in the presence of certain gases. These devices originally used Pd:MOS structures, and later used metal/insulator/silicon carbide diodes with Pt Schottky contacts. Nitrides have been used as insulating layers for high temperature operation including gallium nitride, indium nitride, aluminum nitride, and boron nitride. They have been used to detect hydrogen and hydrogen containing gases at temperatures up to 600ºC as well as methane, ethylene, CO, NO, NO_2, butane, and propane [Kim01, Eic03]. However, extended operation at high temperatures is compromised due to junction breakdown and electromigration [Thi06].

ChemFETs measure the change in work function of a thin-film metal or polymer as a function of adsorbed vapor by using this thin film as a gate material in a field effect transistor. They have been shown to operate at temperatures as low as ambient using polymer films, but have previously been operated at temperatures of 200ºC [Cov04]. In general, ChemFETs are capable of higher signal-to-noise ratios than chemiresistors but are inherently more complex to fabricate and require more extensive control and measurement electronics. These characteristics increase their cost and limit the number of ChemFETs that can be placed inside a single device [Wil01b].

Surface acoustic wave sensors (SAW) measure the change in delay or resonant frequency of a surface acoustic wave launched on the surface of a piezoelectric material due to changes in the composition of the surrounding environment. They are one of the most sensitive micromachined high temperature sensors. Most commonly quartz, lithium niobate ($LiNbO_3$), and lithium tantalate ($LiTaO_3$) crystals are used as substrate materials. A device utilizing langasite (LGS) crystals is able to operate at 750ºC, a higher obtainable operating temperature than that of devices using common crystals, and can detect 1,000 ppm H_2 and 10 ppm C_2H_4 [Thi06]. Devices capable of detecting 10 gases have been developed [Fan99].

Ion mobility mass spectrometry (IMS) sensors separate and identify gas phase ions based on their different mobilities. Ions are carried between parallel plate electrodes by a flow of gas while RF and DC voltages cause the ions to follow trajectories perpendicular to the flow. The mobilities of the ions become field dependent in these conditions. An ion mobility spectrometer, capable of operating at atmospheric pressure, has been miniaturized and used to distinguish several gases [Mil01, Eic03a].

Devices which measure changes in electrochemical properties of a solution, such as ISFET's [Jan03], potentiometric sensors [Nam03] and ampereometric sensors [Mar05] have also been developed. These sensors have very low detection limits (in the ppb range) but show large variation, as it is difficult to construct miniature reference electrodes.

The microscale optical emission sensor presented in this chapter utilizes microdischarges between thin-film electrodes. Microdischarges are used in a variety of micro total analysis systems including microscale optical emission spectroscopy systems

for chemical sensing [Bro02, Fra03, Kar04]. These devices, based on microdischarge and arc emissions, operate by exciting gas species and observing the characteristic spectral output from the energy transitions [Bra68]. Similar devices developed by Caviton, Inc. have been shown to operate at 1,100ºC during metal detection tests [Cav07]. Since most atomic species produce emission lines, emission spectroscopy can be used to identify numerous species concurrently while providing specificity as each species has characteristic emission spectra. The detection is also rapid, requiring a few milliseconds. Devices utilizing microdischarges are well suited for high temperature operation as previously described in Chapter 3.

Various varieties of microfabricated sensors are compared in Fig. 4.1, showing the sensors' operating ranges and number of chemicals detectable by a single sensor of each type. All of the sensors demonstrate high sensitivity in harsh environments, but thin-film sensors focus on the detection of a single or several gases, as opposed to detecting a majority of the gases present. To counter this, arrays of sensors having different coatings are used instead of single sensors to expand the range and selectivity. The complexity of the sensor readout circuitry and the fabrication process determines the number of different devices on the array. It is assumed that although the sensors themselves are non-specific, the overall signature is specific [Gar99]. This solution is limited, as it is difficult to fabricate large arrays inexpensively. However, devices based on optical emission spectroscopy from microdischarges operate faster than thin-film devices and can detect a large number of specific chemicals concurrently, without the added complexity of having multiple devices. Figure 4.2(a) compares the sensitivity against the speed of detection for various types of chemical sensors and Fig. 4.2(b)

compares the selectivity against the number of detectable chemical species for gases and organic compounds.

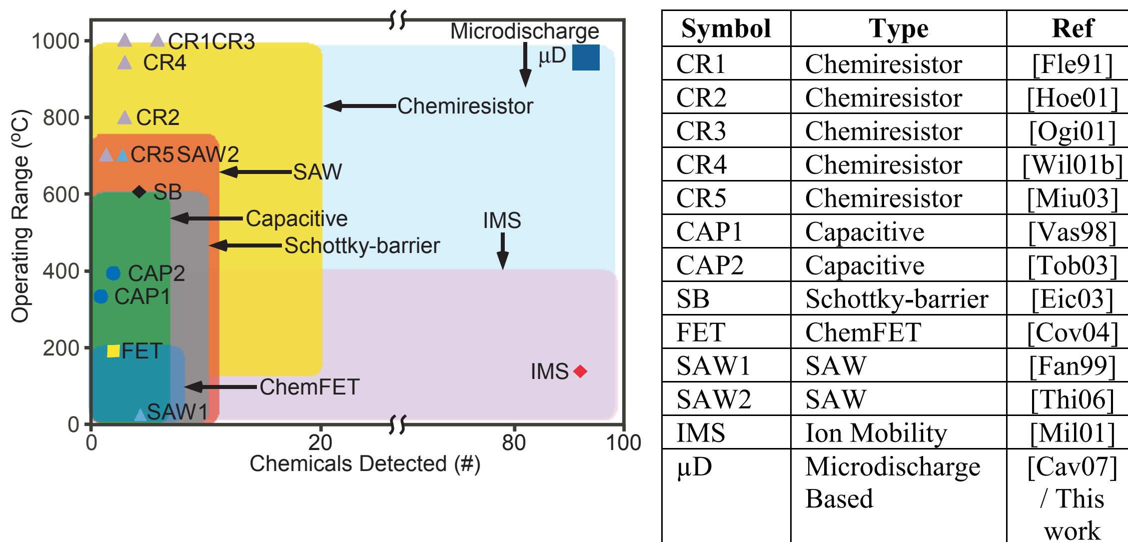

Symbol	Type	Ref
CR1	Chemiresistor	[Fle91]
CR2	Chemiresistor	[Hoe01]
CR3	Chemiresistor	[Ogi01]
CR4	Chemiresistor	[Wil01b]
CR5	Chemiresistor	[Miu03]
CAP1	Capacitive	[Vas98]
CAP2	Capacitive	[Tob03]
SB	Schottky-barrier	[Eic03]
FET	ChemFET	[Cov04]
SAW1	SAW	[Fan99]
SAW2	SAW	[Thi06]
IMS	Ion Mobility	[Mil01]
µD	Microdischarge Based	[Cav07] / This work

Figure 4.1: Plot of operating temperature range vs. number of detectable chemical species for various high temperature gas sensors. (See table for the list of abbreviations and references.)

Microdischarge-based sensors can also operate at both ambient and high temperatures, while some of the discussed thin-film sensors cannot operate at low ambient temperatures. In addition, most of the thin-film sensors have cross-sensitivities to many different chemicals, which make false positives problematic. Another issue with thin-film sensors is that the response, stability, and sensing properties of these films are highly dependent on the fabrication process [Thi06]. This results in short sensor lifetime or expensive calibration with numerous gases. Microdischarge-based optical emission sensors do not suffer from these issues. Additionally, utilizing pulsed discharges, they can operate for extended periods of time.

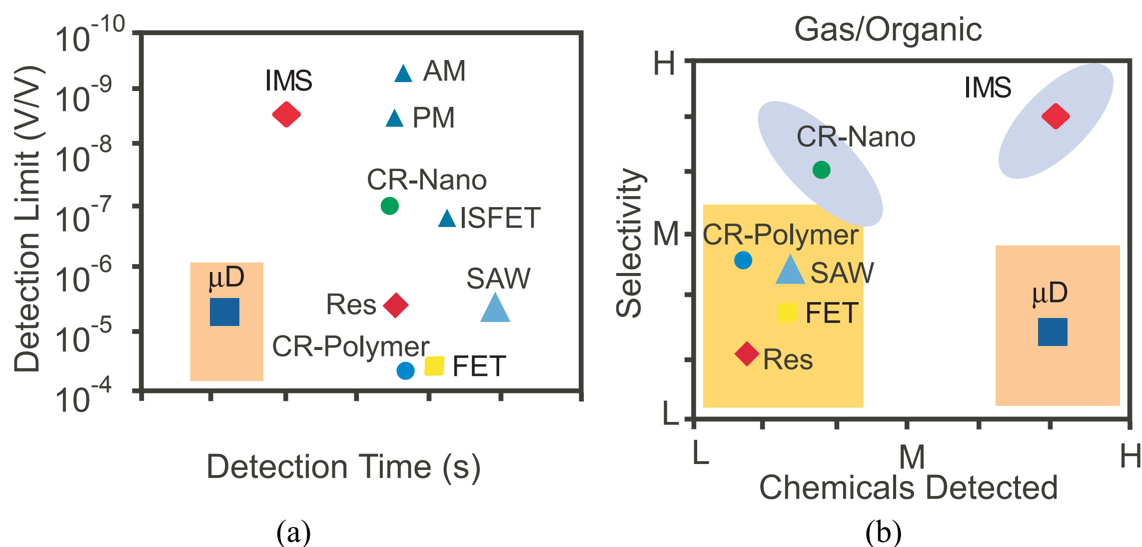

Symbol	Type	Ref
FET	ChemFET	[Dom97]
Res	Silicon Cantilevers	[Hie00]
CR-Nano	Chemiresistors coated with Au-Thiolate nanoclusters	[Cai02]
CR-Polymer	Chemiresistors coated with polymer	[Dav05]
AM	Ampereometric Sensors	[Mar05]
PM	Potentiometric Sensors	[Nam03]
IMS	Ion Mobility	[Mil01]
µD	Microdischarge Based	This work

Figure 4.2: (a) Plot of sensitivity vs. speed of detection for various kinds of chemical sensors (see table for the list of abbreviations and references). Each of the publications mentioned represent the best results of the various classes of devices. (b) Plot of selectivity vs. number of detectable chemical species for gases and organic compounds. L, M, and H represent a low, medium, and high number of chemicals [Mit08c].

Different varieties of microdischarge-based optical emission sensors have been developed. One of these sensors is a DC microdischarge-based sensor capable of detecting organic vapors at atmospheric pressure, with a helium carrier gas [Eij00]. This sensor is able to detect 3 ppm of methane. A low pressure dielectric barrier discharge sensor using diode laser atomic absorption spectrometry for detecting halogens in air has also been reported by Niemax's group [Mic01, Kun03]. It is able to detect 400 ppt of Cl and 2 ppb of F in helium while consuming 0.5-1 W of power, but the use of absorption spectrometry necessitates low operating pressures and a helium ambient. Furthermore,

capacitively coupled sensors have been developed which can operate at atmospheric pressure but require a helium carrier gas and 1.5 W of power [Gro92, Yos01]. A microwave-induced microdischarge sensor has also been developed, which can operate at atmospheric pressure and can detect chemical concentrations of 50 pg mL^{-1} [Bro02]. This sensor also operates in argon and helium ambient environments and consumes 20 W of power. Yet another microdischarge-based sensor is a miniature ICP sensor which can detect 45 ppb sulfur dioxide [Min03]. This device operates at low pressures (0.1-10 Torr), requires an argon environment, and uses 3 W of power. Although all of these devices are effective, some require operating pressures less than atmosphere or rely on RF and microwave generation. In general, they require 0.5-10 W of power, are designed for steady state operation, and have not been tested in high temperature environments.

A DC, microdischarge-based optical emission chemical sensor utilizing pulsed microdischarges and capable of operating at atmospheric pressure has been further developed in this work and was reported previously [Mit08a, Mit08b, Mit08c]. This sensor avoids the constraints of the previously described sensors as it does not require a reduced pressure for operation, and does not rely on RF and microwave generation. Additionally, this DC microdischarge-based sensor requires less power and has demonstrated high temperature operation. It is capable of detecting 50 ppm of carbon in acetone vapor and has simple, durable components, well suited for high temperature operation. The sensor consists of thin-film electrodes, between which microdischarges are created.

Several additional components are necessary to use this chemical sensor in harsh environments. Purification of a gas sample can become necessary as small amounts of

nitrogen dominate emission spectra with intense emission lines [Ark05]. For this purpose a microdischarge-based gas-purifier (that removes modest quantities of oxygen and nitrogen) is utilized. A high-temperature microdischarge-based pressure sensor (that minimizes packaging challenges presented by alternatives) is also included. (See Chapter 3.) These devices operate together in harsh environments to isolate a gas sample, selectively remove unwanted gas components, and detect the possible presence of a desired or contaminant gas. This harsh environment sensor differs from previously designed sensors as it is able to identify numerous gases concurrently time without being reconfigured.

4.2 Detrimental Effect of Contaminant Nitrogen in Spectral Chemical Sensing

4.2.1 Background

Spectral chemical sensing is limited by the ratio of emission line intensities to background emissions (relative sensitivity) as opposed to the absolute emission line intensities (absolute sensitivity). Unlike absolute sensitivity, the relative sensitivity cannot be increased by traditional methods like amplification or filtering. If the relative sensitivity is too low, weak emission lines produced by individual gases being examined will not be detected due to background spectra. This problem of low relative sensitivity in the presence of strong background spectra is illustrated by examining the ability of contaminant nitrogen to preclude the detection of other gas species in DC microdischarges. In particular, its ability to preclude the detection of SF_6 is examined.

DC microdischarges in SF_6 environments have previously been utilized to locally etch silicon, making the detection of SF_6, the identification of the species into which SF_6 decomposes, and the characteristics of the microplasmas of particular interest [Wil01a]. Optical emission spectroscopy is used to determine the extent to which SF_6 can be detected with background contamination, and the influence of pressure and applied power on SF_6 spectra. A detailed list of the previously recorded and theoretical emission lines produced by SF_6 dissociation in macroscale plasmas can be found in Appendix 4, as can the experimental set-up used to obtain microplasma spectra in SF_6 environments. A theoretical discussion of nitrogen's ability to mask SF_6 emission lines, due to their low relative sensitivity is also presented in this appendix. Several characteristics of SF_6 microplasmas are presented in Appendix 5.

4.2.2 Resulting Spectra in SF_6

Experiments were performed to determine if SF_6 emission lines could be detected in microplasmas with nitrogen contamination. The emission lines used to detect SF_6 have previously been theoretically and experimentally identified in macroscale SF_6 discharges. In summary, these emission lines include F I lines at 624.0 nm and 703.7 nm, S II lines at 532.1 nm and 545.4 nm, and an emission band comprised of continuously increasing emission line intensities between 420 nm and 500 nm, which terminates at 500 nm.

The spectra were produced by initiating microplasmas in a vacuum chamber within a controlled SF_6 environment. The microplasmas were created between pairs of planar copper electrodes with inter-electrode spacing of 500 μm, deposited on 500-μm-thick glass substrates. The examined discharges were characterized as microplasmas according to the description of Wilson *et al.* as they were self-contained glow discharges

confined over the cathodes [Wil03a]. These discharges were similar to the discharges previously used for *in-situ* silicon etching. However, the power densities of these microplasmas were higher than the power density used for etching due to the smaller electrode size. Wilson obtained power densities of 1-10 W/cm^2, while these microplasmas had power densities of 20-4,000 W/cm^2.

A two-stage rotary vane roughing pump (Oerlikon Leybold Vacuum Trivac D 16B), accompanying pressure controller (MKS® 600 Series), and external macroscale pressure transducer (MKS® Baratron® Capacitance Manometer model #627B23TDC1B) were used to set the pressure between 100 mTorr and 10 Torr. The flow rate of CP grade SF_6 gas (Airgas Inc.) into the chamber was controlled using MKS® Mass-Flo® Series Mass Flow Controllers (Model #'s 1479A13CR1BM and 1479A21CR1BM). SF_6 and air were introduced and pumped from the chamber at rates of 5.6-260 sccm, to obtain a constant gas composition and pressure. Power was supplied via a high-voltage power supply and a 100 kΩ ballast resistor was connected in series with the anode to limit current. The optical spectra produced were measured using an Ocean Optics USB2000™ spectrometer.

The spectra produced by microplasmas in SF_6 showed no indication of SF_6, or its dissociated by-products, and only displayed emission lines caused by contaminating nitrogen. The microplasma spectra in SF_6 were obtained in almost pure SF_6 environments, at total pressures between 100 mTorr and 10 Torr with currents between 500 μA and 4 mA. The spectra consisted of numerous closely spaced lines, as opposed to single lines as in atomic spectra, because the different energy levels in molecules have structures corresponding to many different vibrational and rotational levels. Figure 4.3(a)

shows a typical spectrum produced in SF_6, regardless of the pressure or gas flow rate. The spectrum contains no indication of fluorine, ionized sulfur, or an SF_6 emission band, and is dominated by N_2 and N_2^+ lines. The previously recorded molecular nitrogen emission lines at wavelengths of 316.0 nm, 337.1 nm, 357.7 nm, and 380.5 nm were all observed. Figure 4.3(b) shows the spectrum produced in SF_6 after the spectrum produced in air, before SF_6 introduction, has been subtracted out. This does not show any indication of SF_6 dissociation either. However, time evolution of the microplasmas from spectrum to spectrum could have affected this spectral subtraction.

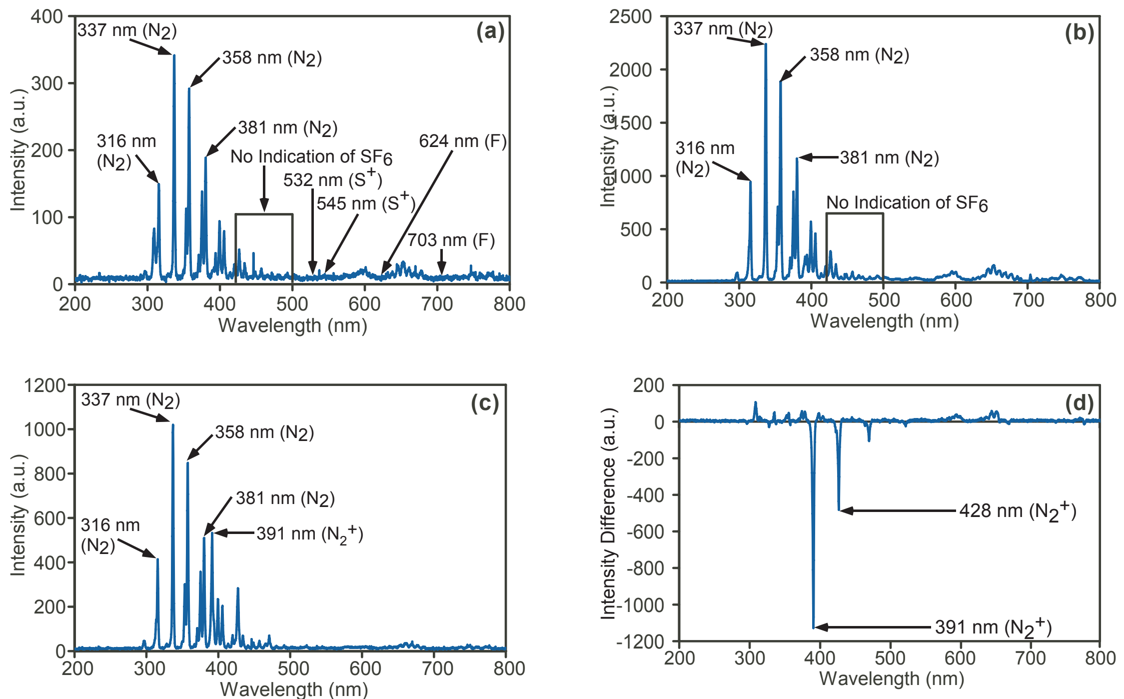

Figure 4.3: Microplasma emission spectra in air and SF_6 at 3 Torr. All figures use the same arbitrary unit scale for the intensity. (a) SF_6 environment with 800 V and 500 µA. (b) SF_6 environment with 1,000 V and 2.7 mA after the spectrum produced in air has been subtracted out. (c) Air environment with 500 V and 500 µA. (d) Average normalized difference between SF_6 and air emission spectra recorded between 400 mTorr and 10 Torr.

Figure 4.3(c) shows a reference spectrum recorded in an air environment with the same applied current and pressure used for the SF_6 spectrum in Fig. 4.3(a), for comparison. The spectra are almost identical except for the increase in N_2^+ emission line intensity as indicated by the previously mentioned 391.4 nm line. Figure 4.3(d) shows the average difference between 12 normalized spectra recorded in SF_6 and 12 in air at pressures from 400 mTorr to 10 Torr.

The spectra were all normalized to the strongest N_2 emission (337.1 nm) before the differences were calculated and averaged for each emission line. The N_2^+ emission line (391.4 nm) intensity in microplasmas was significantly reduced by a SF_6 environment relative to an air environment as indicated by the negative peak. A reduction of N_2^+ in an SF_6 environment is caused by the highly efficient charge transfer reaction [Arn04]:

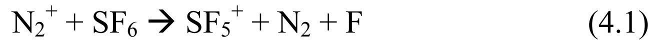

$$N_2^+ + SF_6 \rightarrow SF_5^+ + N_2 + F \qquad (4.1)$$

Given this reaction, it may be possible to use the N_2^+ emission line intensity to detect SF_6 in microplasmas. The SF_6 gas flow rate and pressure had no effect on the resulting spectra. Identically shaped titanium electrodes produce similar spectra to those obtained with copper electrodes.

Detailed views of the 400-510 nm regions of the spectra produced by microplasmas in air and SF_6 are shown in Fig. 4.4, where the molecular emission band has previously been observed. Even under magnified examination of these regions, there is little discernable difference between the spectra and no indication of a molecular band between 420 nm and 500 nm.

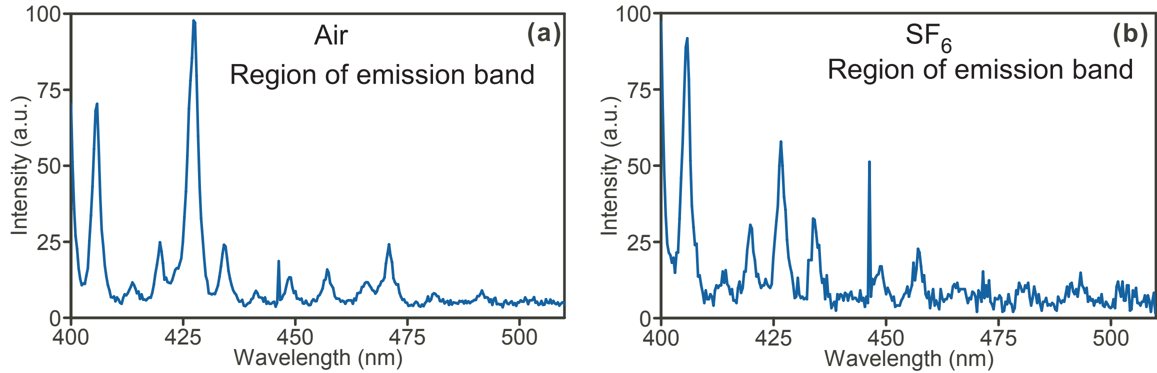

Figure 4.4: Emission spectra in (a) air and (b) SF_6 between 400 nm and 510 nm where the molecular emission band produced by SF_6 has been observed. Three consecutive measurements are averaged in each environment.

In macroscale discharges, the emission lines created by SF_6 in discharges are difficult to detect due to the low relative sensitivity of SF_6 compared to contaminating gas emission lines. Small amounts of nitrogen dominate SF_6 emission spectra at high and low pressures when both positive and negative high voltages are used to induce the discharges [Tei84, Tei85]. This low relative sensitivity is demonstrated by observing that in an environment of SF_6 + 470 ppm N_2, SF_6 and N_2 emission lines have equal intensities. In an environment of SF_6 + 1% N_2, SF_6 emission lines are approximately one-fourth as intense as N_2 emission lines and in an environment of SF_6 + 50% N_2, SF_6 emission lines are not detectable [Cas91]. The minimum excitation energy for N_2 is 8.399 eV [Sul01], which is slightly below the lowest level excitation energy of SF_6, the 1 $t_{1g} \rightarrow 6\ a_{1g}$ transition at 9.6 eV and 9.9 eV for triplet and singlet components respectively [Raj06]. The ionization energies of fluorine, SF_6, and N_2 range between 15.33 eV and 17.42 eV, which does not explain the differences in emission line intensity [Lid49, Hub79, Asg00]. The dissociation energy required to separate SF_6 into SF_5 and F is 9.6 eV, which is less than the ionization energy of N_2 and does not explain the line intensity difference [Raj06]. However, the difference in emission line intensity is explained by the relatively

small excitation cross section of SF_6 in comparison to nitrogen [Zen91]. Creating discharges with lower applied currents also increases the ability of nitrogen to dominate SF_6 emission lines, precluding SF_6 detection.

It is apparent that it is extremely difficult to detect SF_6 in microplasmas in the presence of contaminating nitrogen, which leads to low relative sensitivity. Whereas on the macroscale SF_6 can be detected with 1% nitrogen in the environment, this is not the case in microplasmas. This suggests that another issue has been encountered. One explanation is that the dielectric property of SF_6 is causing the power to be shunted to nitrogen in the discharge, which increases the amount of nitrogen excitation and decrease the amount of SF_6 excitation. Another explanation previously suggested is that the lower currents used in these microplasmas, 500 μA - 4 mA are limiting SF_6 detection. The inability to detect SF_6 in microplasmas demonstrates that accurate chemical sensing depends on the removal of contaminating nitrogen.

4.3 Using Micro-SIPs for Gas Purification

4.3.1 Concept, Operation, and Design of Gas Purifying Micro-SIPs

Given the detrimental effect nitrogen has on the detection of gases using spectral chemical sensing, as outlined in the previous section, microscale-sputter-ion pumps (micro-SIPs) which can remove nitrogen and oxygen provide a means of improving gas detection. If nitrogen and its background emission lines are removed from a sample, small concentrations of gases with weak emission lines can be detected and the relative sensitivity of the sensor is increased. The purification ability of micro-SIPs is a primary motivation for the development of the chemical sensing microsystem.

Micro-SIPs, as described in detail in Chapter 2, operate through the creation of DC microdischarges between two titanium thin-film electrodes. These microdischarges sputter the titanium cathodes of the micro-SIPs, bonding this titanium to gas molecules, and removing these molecules from the environment. Their ability to reduce pressure in sealed cavities has been discussed in Chapter 2 but their ability to purify gas environments has not. The sputtered titanium has been shown to react selectively with nitrogen and oxygen on the macroscale without interacting with helium, carbon, sulfur, and other gases of interest, making these devices ideal for removing air contamination [Den67].

The micro-SIPs used for gas purification in this application have circular anodes surrounded by large cathodes as shown schematically in Fig. 4.5 and are similar to the version 2 design previously described. The cathodes have areas of 1.52 mm^2 and discharge gaps of 50 μm. While the anode and cathode dimensions used for gas purification are identical to version 2 micro-SIPs, only three anode/cathode pairs are included and the entire device has an area of 25 mm^2. DC voltages of 1,000 V are applied to induce rapid purification, and a 2.5-MΩ ballast resistor is used. The micro-SIPs are fabricated as previously described using titanium as the electrode material as it has the ability to bond selectively with nitrogen and oxygen.

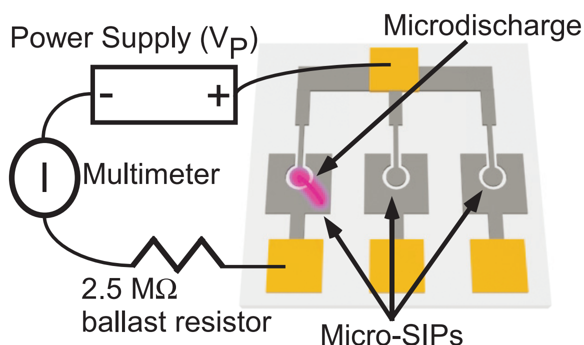

Figure 4.5: Gas-purifying micro-SIPs. A DC voltage is applied to selectively remove nitrogen and oxygen.

4.3.2 Results and Discussion

The gas purification provided by micro-SIPs was evaluated by examining the spectra produced by microdischarges over time in gas samples with known initial gas concentrations. A micro-SIP was operated in an environment containing 99.25% helium (99.995% pure) and 0.75% air to test the purification abilities at a pressure of 200 Torr. The micro-SIP was enclosed in a re-sealable glass package, 2.5 cm in diameter (4 cm^3). The gas concentration was set by MKS® Mass-Flo® Series Mass Flow Controllers (Model #'s 1479A13CR1BM and 1479A21CR1BM), accompanying pressure controller (MKS® 600 Series), and external macroscale pressure transducer (MKS® Baratron® Capacitance Manometer model #627B23TDC1B). The air initially in the package was removed by a two-stage rotary vane roughing pump (Oerlikon Leybold Vacuum Trivac D 16B). A needle valve was used to seal the re-sealable package while the micro-SIP operated.

Helium is the most commonly used carrier gas in gas chromatography, and was thus used as a carrier gas. The strongest nitrogen and oxygen emission line intensities were normalized to that of helium to account for variations in discharge intensity. A 56.5x reduction in nitrogen and a 16.2x reduction in oxygen were observed over five

hours as shown in Fig. 4.6. The final concentrations of the contaminant gases, based on the measured reduction in emission line intensities compared to the initial intensities, were 90 and 70 ppm, respectively. Figure 4.7 shows spectra produced before and after purification. The nitrogen and oxygen emission lines were almost completely removed, while a helium emission line remained, indicating that helium was not removed to a detectable extent. Nitrogen and oxygen produced strong background emission lines despite their relatively low concentrations in the first recorded spectrum (Fig. 4.7(a)), confirming the previous findings and demonstrating the advantage of removing these emission lines when detecting other gases.

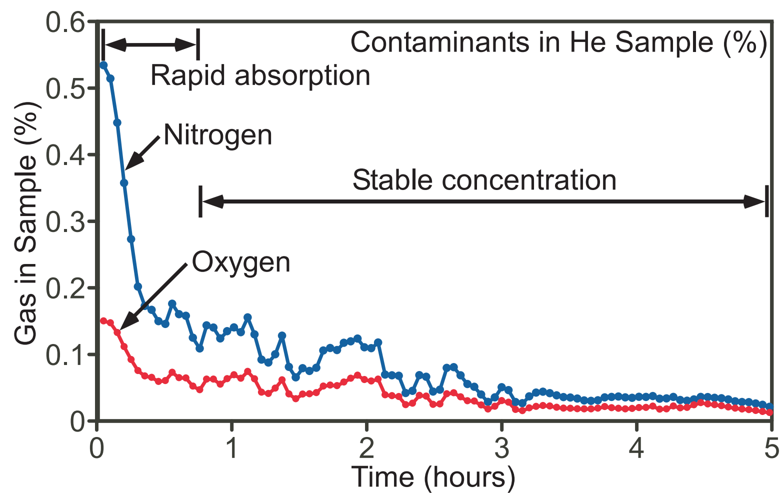

Figure 4.6: Percentage of contaminants (nitrogen and oxygen) in a helium sample during gas purification, showing the thorough removal of the unwanted gases.

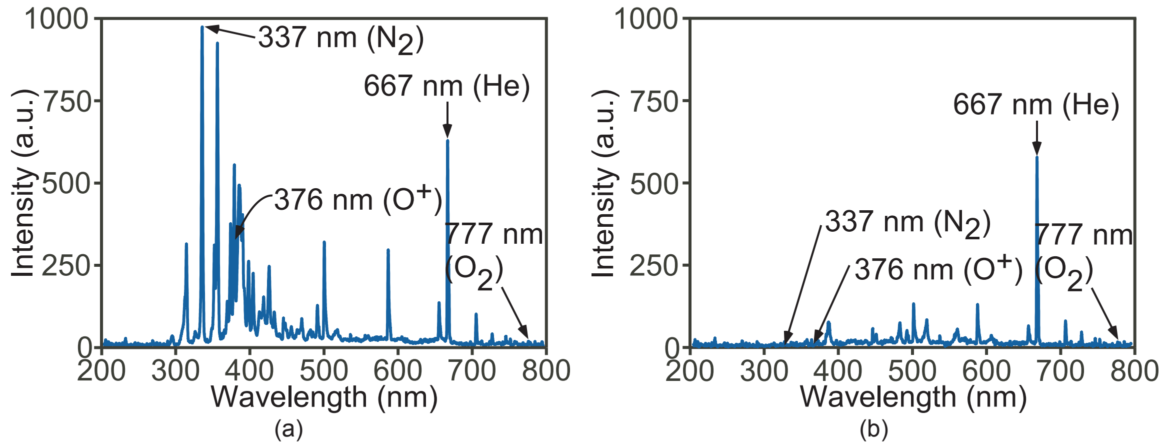

Figure 4.7: Spectra of the pump discharge in 99.25% helium with air contamination at 200 Torr (a) before purification and (b) after purification. Small amounts of nitrogen cause intense emission lines compared to helium at time = 0, demonstrating the necessity of nitrogen removal.

4.4 Harsh Environment Chemical Sensor

4.4.1 System Concept

An exploratory harsh environment chemical sensing microsystem has been developed to integrate and expand upon the operation of the described micro-SIP (Chapter 2 and Chapter 4, Section 4.3) and microdischarge-based pressure sensor (Chapter 3). Additionally, a microdischarge-based optical emission sensor is included to perform the sensing. The ability of the three microdischarge-based components to function at high temperatures makes them well suited to operate concurrently in a harsh environment system. These three devices are hermetically sealed inside a ceramic package with a quartz lid while micromachined valve(s) control the gas flow into and out of the package as shown in Fig. 4.8. The tubes connecting the microscale components to one another and to the external components have a 1 mm inner diameter, large enough to accommodate a high throughput if necessary.

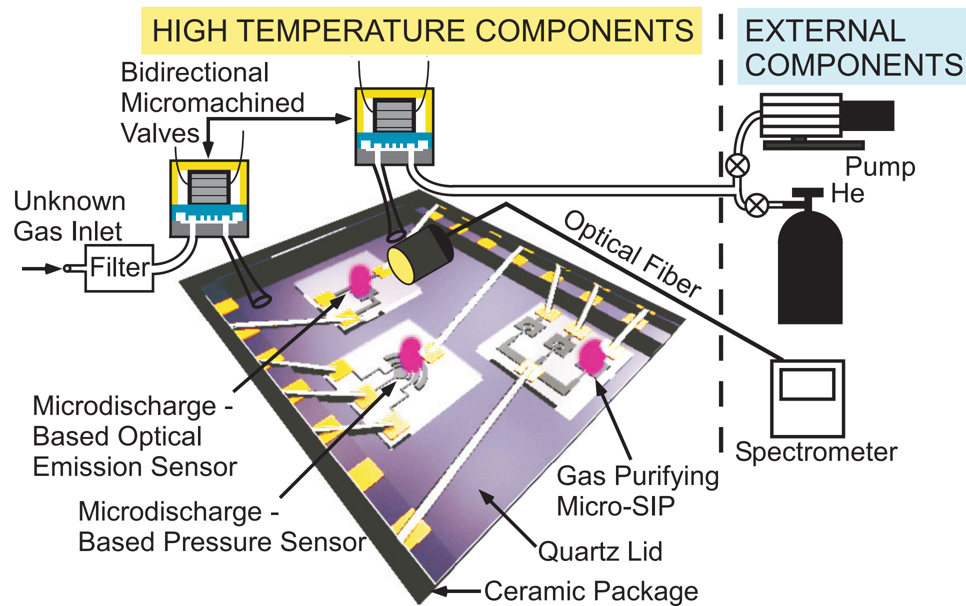

Figure 4.8: Schematic of the entire harsh environment chemical sensing system.

4.4.2 System Optical Emission Sensor

While the micro-SIP and pressure sensor have been previously described in Chapters 2 and 3 respectively, the optical emission chemical sensor and valves specific to this system have not been discussed. The optical emission chemical sensor (chemical detector) operates by creating pulsed microdischarges between thin-film anode/cathode pairs to fractionate and exciting gas species, shown schematically in Fig. 4.9(a). The spectra emitted from the microdischarges are characteristic of the energy transitions of the individual fractionated gases. This optical emission sensor is based on previously developed sensors which utilized a two electrode configuration and a three electrode flashFET configuration, for reduced power consumption, to detect chemicals at atmospheric pressure [Mit08a]. This sensor is able to detect carbon in acetone vapor at concentrations as low as 50 ppm. In addition, these microdischarge-based sensors have been used in a portable handheld gas detection system [Mit08b]. An optical fiber directly

opposite the microdischarges, outside the quartz lid, couples the emitted light to a spectrometer (Ocean Optics USB2000^{TM}). The recorded spectra are examined to determine the unknown gas composition based on the characteristic emission lines. Pulsed microdischarges have significant afterglow periods, lasting 7 ms, and integrating both the afterglow and initial discharge emissions for up to 10 ms in the spectrometer improves the ability to detect less dominant peaks [Mit08a]. This sensor is not designed for dusty or dirty environments, as contaminants short the sensor electrodes and block transmission through the quartz lid.

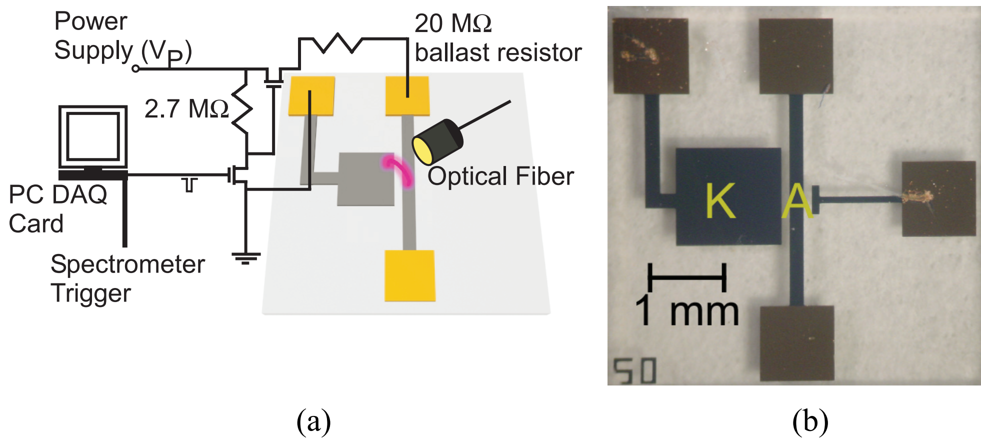

Figure 4.9: Microdischarge optical emission sensor (chemical detector) used to detect carbon and other vapors through recorded spectra. (a) Schematic. (b) Photograph.

The optical emission chemical sensors are of the three electrode flash-FET configuration, but are used in the traditional two electrode discharge mode of operation as shown in Fig. 4.9(b). As microdischarges have been shown to be confined over the cathode, relatively large cathodes, 1.82 mm^2, are used to produce a large glow region for improved optical emission detection. A 100-µm discharge gap separates the electrodes

and a voltage of 1,000 V is used to create the microdischarges. Computer-controlled pulses trigger the microdischarges and spectrometer. A 20-MΩ ballast resistor is used.

4.4.3 System Bidirectional Micromachined Valves

The bidirectional micromachined valves control the flow of gas into and out of the package and have separate inlets and outlets. They operate by depressing a bulk silicon micromachined plate against a Corning #7740 Pyrex glass substrate with inlet and outlet holes (Fig. 4.10). A commercially-available, multilayered piezoelectric PZT stack drives the silicon valve plate (Physik Instrumente, Germany, PL055), and has a footprint of 5 x 5 mm^2 with a height of 6 mm. The materials in the valves are selected so that the temperature expansion mismatches do not inhibit device operation over a wide range of temperatures. Macor™, a glass mica ceramic, is used as the primary packaging material. It can be easily machined with precision, and has a thermal expansion coefficient of 7.4 ppm/K. In addition, it has zero porosity, does not outgas in vacuum environments, and can be used with epoxy to provide a hermetic seal. The ceramic enclosure measures 1 x 1 x 1 cm^3, and has a 6 mm deep cavity, with 1 mm thick walls on all four sides. A thorough description and test results are in [Par08].

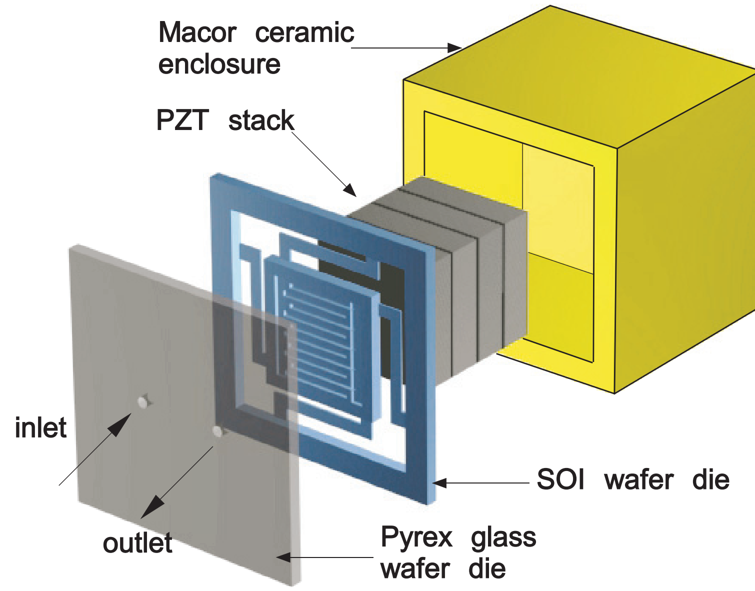

Figure 4.10: Microvalve concept: The valve consists of ceramic-PZT-Si-glass structure. A PZT stack actuator moves the silicon plate to open or close the valve. Micro-groove patterns are fabricated on the silicon plate to increase the flow area [Par08].

4.4.4 System Operation and Fabrication

The system utilizes bidirectional valves, a micro-SIP, a microdischarge-based pressure sensor, and an optical emission sensor to isolate, purify, and sense gas samples. One possible configuration for field use is shown in Fig. 4.8. Remote components, external to the harsh environments, include a two-stage rotary vane roughing pump (Oerlikon Leybold Vacuum Trivac D 16B), accompanying pressure controller (MKS® 600 Series), backfilling gas tank, and a spectrometer. In the proposed configuration, a sample is introduced into the empty package through one micromachined valve while a second connects the package to the external components for backfilling and pressure regulation. After a sample is introduced, the package is backfilled with an inert gas while the internal pressure sensor monitors the pressure in the package and the external pump controls it. When the desired pressure is reached, the package is isolated by closing the

valves. The gas-purifying micro-SIP is then operated while the chemical sensor is pulsed, recording spectra over time. The micro-SIP continues to operate until the relative sensitivity of unknown gas lines to background nitrogen lines is high enough for detection of the unknown gas, if present.

All three microdischarge-based devices were fabricated on a single wafer with two masks to simplify processing using the same process flow as the micro-SIPs in Chapter 2 and the pressure sensors in Chapter 3. A Ti film (1 μm thick) and an Au film (500 nm thick) were thermally evaporated onto #7740 Pyrex^{TM} glass wafers (500 μm thick) without removing the wafers from vacuum. The contact pads were patterned on the gold layer using photolithography and etched using Transene GE-8148 gold etchant, which does not etch titanium. The electrodes were then patterned in the titanium layer using photolithography. The final devices had footprints of 25 mm^2 each, with a combined active area of 10.5 mm^2. Solder and epoxy were used to connect the devices and seal them in 0.33 cm^3 ceramic packages as shown in Fig. 4.11.

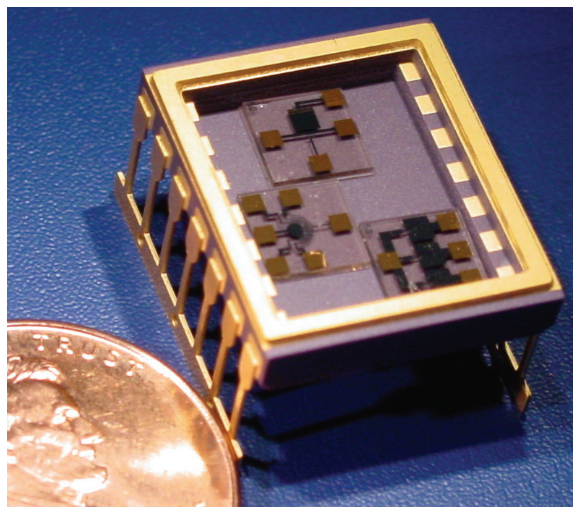

Figure 4.11: System before sealing in ceramic package next to a U.S. penny.

4.4.5 Results and Discussion

For the overall system, preliminary testing was performed at 200°C based on anticipated requirements [Sha06], although it can potentially operate at much higher temperatures. The setup for this testing utilized only one micromachined valve, through which both the sample and backfilling gas were introduced. Acetone vapor, 10,000 ppm, was introduced as a carbon source and helium was used to backfill the system to a final pressure of 200 Torr. The system was raised to 200°C and the optical emission sensor was operated every 20 seconds to determine gas concentrations based on emission line intensities. The sensor was operated for 50 ms and the emissions were integrated for 300 ms to capture the afterglow.

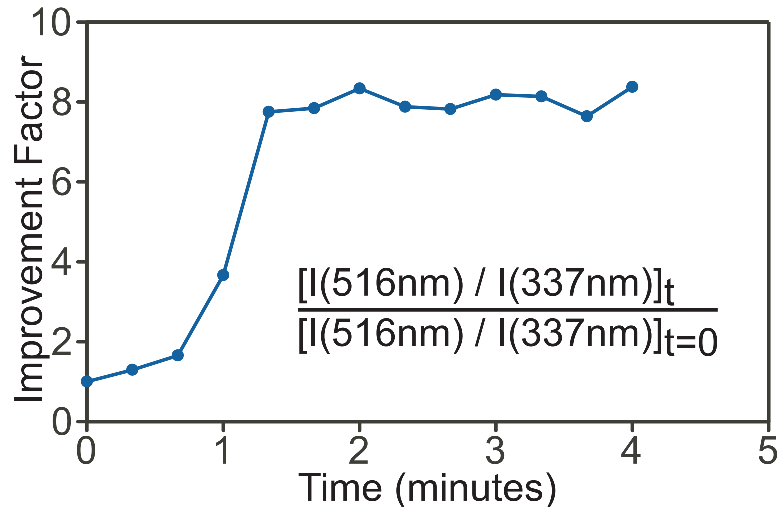

Figure 4.12: Ratio of carbon to nitrogen emission line intensity during gas purification at 200°C, based on their strongest emission lines.

The micro-SIP was operated and the strongest carbon emission line (516.4 nm) increased in intensity by 8x relative to strongest nitrogen emission line (337.1 nm) as shown in Fig. 4.12. This purification increased the ability to detect carbon with respect to

the contaminant gases by increasing the relative sensitivity. Figure 4.13 illustrates the recorded spectra before and after purification, indicating the increased emission line intensities of carbon and CN relative to the contaminant nitrogen.

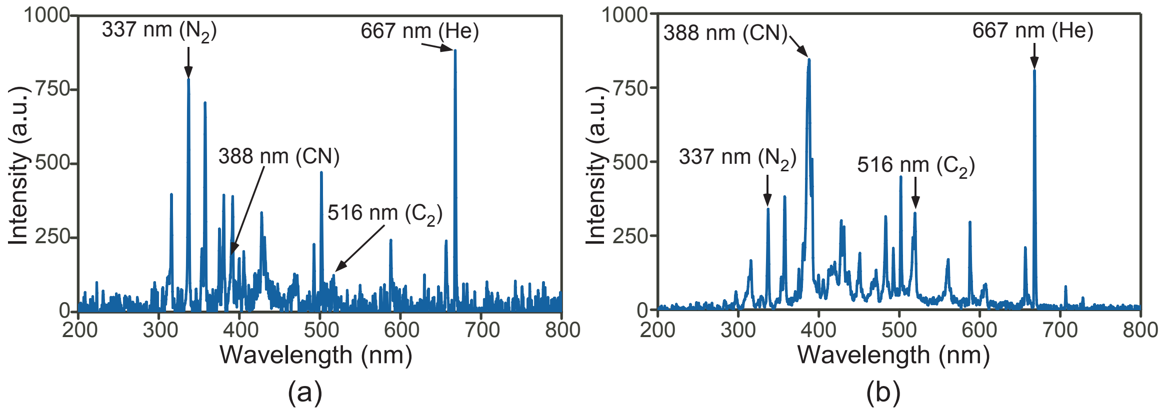

Figure 4.13: Spectra of acetone sample backfilled with helium during gas purification at 200°C. (a) Spectrum recorded before purification, showing strong nitrogen emissions and low C_2 emissions. (b) Spectrum recorded after purification, showing diminished nitrogen and increased CN and C_2 emissions.

CHAPTER 5

CONCLUSION

Microdischarge-based devices have been developed which control the pressure in sealed cavities, through sensing and actuation, at room temperature and at high temperatures. These devices have been combined with an optical emission sensor to create a harsh environment chemical detection microsystem.

5.1 Dissertation Summary

Chapter 2 outlined on-chip sputter-ion pumps and their use in the controlled reduction of pressure in large cavity packages. The devices utilized pulsed and DC microdischarges between thin-film titanium electrodes patterned on glass substrates. The micro-SIPs functioned in hermetically sealed cavities, without heating surrounding devices, and provided control over the amount of air and humidity removed from the inside of the cavity.

Micro-SIP pumping performance was characterized though experimental and modeling results. The influence of (1) the micro-SIP design, (2) the environment in which micro-SIPs were operated, (3) the mode of micro-SIP operation, and (4) microdischarge characteristics on micro-SIP pumping operation were investigated. These were explored through examining micro-SIP operation with varied discharge gap spacing

at varied pressures. The gas removal rates were found to depend on both the initial pressure and discharge gap spacing, and micro-SIPs with smaller discharge gaps operating at higher initial pressures removed air at the greatest rate. A theoretical model outlining the dependency of gas removal rates on microdischarge parameters was developed and was able match the experimentally obtained results. In an air environment, these devices reduced the pressure by 168 Torr in a 6.33 cm^3 cavity and 126 Torr in a 2.2 cm^3 cavity when starting at atmospheric pressure. Oxygen, nitrogen, and air pressures were reduced at rates of 11.5 Torr/h, 3.4 Torr/h, and 7.2 Torr/h, respectively, starting at 200 Torr. The pumps have been shown not to remove helium from the environment. Water vapor concentrating was reduced in a sealed package at a rate of 6% relative humidity per hour, starting with 61% relative humidity. Using pulsed discharges, 25 ms in duration, as opposed to DC discharges with same amount of energy, and enough time, micro-SIPs removed five times as much air. This indicated that shorter pulses were more energy efficient despite their slower removal rates. These data concerning the operation and characteristics of micro-SIPs suggest that they are promising for low-temperature pressure control of vacuum-sealed packages in microscale systems applications.

Chapter 3 outlined microdischarge-based pressure sensors, which operate by measuring the change, with pressure, in the spatial current distribution of pulsed DC microdischarges. These sensors are well-suited for high temperature operation because of the inherently high temperatures of the ions and electrons in the microdischarges. They provide an electrical readout, avoiding an intermediate transduction step, which can be convenient in some cases. The absence of a diaphragm, which is commonly used in

piezoresistive and capacitive pressure sensors, also provides natural tolerance for overpressure and consequently, mechanical robustness.

Two sensor versions were presented and demonstrated. The first type used three-dimensional arrays of horizontal bulk metal electrodes embedded in quartz substrates with electrode diameters of 1-2 mm and 50-100 μm inter-electrode spacing. These devices demonstrated they could operate over a range of at least 10-2,000 Torr, at temperatures as high as 1,000˚C, and it is expected these sensors could potentially operate at temperatures below room temperature and over larger dynamic pressure ranges. The maximum measured sensitivity was 5,420 ppm/Torr at the low end of the dynamic range and 500 ppm/Torr at the high end, while the temperature coefficient of sensitivity ranged from -925 ppm/K to -550 ppm/K. Sensors of the second type used planar electrodes, and had active areas as small as 0.13 mm^2, small enough to permit hybrid or monolithic integration with other components that constitute functional microsystems. These devices, when tested in a chemical sensing system flowing helium as a carrier gas, had a maximum sensitivity of 9,800 ppm/Torr, a dynamic range of 25-200 Torr, and a temperature coefficient of sensitivity of approximately -1,412 ppm/K. The sensitivity achieved compared favorably with conventional piezoresistive and capacitive pressure sensors of similar size.

Chapter 4 outlined a system for gas purification and gas phase chemical detection in harsh environments that integrated the micro-SIP and microdischarge-based pressure sensor. In particular, it described the need for removal of contaminant gases such as nitrogen when performing spectral chemical sensing. It then presented the ability of micro-SIPs to purify gas environments from contaminating nitrogen and oxygen,

achieving a 56.5x reduction in nitrogen concentration relative to helium. Finally, it described the chemical detection system which utilized three microdischarge-based devices: pressure sensor, gas purifier, and optical emission sensor. This system used the pressure sensor to measure the incoming sample and backfilling gas. The micro-SIP purified the microsystem environment of contaminating nitrogen and oxygen, increasing the strongest carbon emission by 8x relative to nitrogen. The system was used for carbon detection at temperatures of at least 200°C.

New microtransducers have been developed, providing advantageous options for microsystems and expanding the field of microdischarges to a larger range of sensing and actuating roles. The devices have expanded the field by providing alternatives which are small, simple to fabricate, and inexpensive. In addition, they provide electronic transduction and operate in both low and high temperature environments. These qualities are desirable in most microscale devices as demonstrated by the numerous potential uses. Additionally, the utility of microdischarges as a transduction method has been expanded. The developed devices have demonstrated that through simply measuring microdischarge characteristics, useful information such as pressure can be determined. The use of microdischarges will continue to expand, potentially simplifying currently complex microscale devices with simple electrode structures and ionized gas.

5.2 SUGGESTIONS FOR FUTURE WORK

5.2.1 Utilizing Micro-SIPs to Reach High Vacuum (10^{-6} Torr)

In the work presented in this thesis, micro-SIPs were operated at pressures between 30 Torr and 760 Torr. A logical progression is the development of micro-SIPs

capable of reducing the pressure to high vacuum levels (10^{-6} Torr) in microscale packages.

A micro-SIP capable of generating a high vacuum environment would have several advantages over other pumping technologies which have been proposed or previously utilized, outlined in Chapter 2. Microscale orbitron pumps have been proposed, but not developed, which would use external electron guns to introduce high energy electrons instead of utilizing magnetic fields. This would put orbitron pumps at a disadvantage compared to a micro-SIP, due to the power consuming electron emitters. Non-evaporable getters could be included in hermetically sealed environments to remove gases through oxide formation, hydride formation, and surface chemisorptions. However, NEGs typically require activation temperatures of 300ºC or higher, which can damage packaged devices while a micro-SIP would not substantially heat the surrounding environment as shown in Chapter 2. Additionally, a micro-SIP could set the vacuum level and pumping speed through user controlled electrical means. Microscale peristaltic pumps would be of limited use at low pressures, due to the long mean free path length, and a microscale turbomolecular pump would require a very high rotation rate, due to the small blade radius, to match the performance and rotation speed at the blade tip of the macroscale counterpart. A high vacuum micro-SIP would be advantageous as it would have no moving parts, increasing durability and reducing fabrication complexity.

The proposed micro-SIP for high vacuum generation would utilize thick titanium foil electrodes and a permanent magnet to create Penning discharges as shown in Fig. 5.1. The magnetic field would increase ionization, as in macroscale-SIPs, by causing the electrons emitted from the cathode to move in long helical trajectories which would

improve the chances of collision with gas molecules [Sch99, Wel03]. The field would be necessary as at these low pressures (p) and small discharge gaps (d), a very high breakdown voltage is required to induce ionization (without a magnetic field) as the mean free path length at 10^{-6} Torr is 51 m. Macroscale-SIPs utilize magnetic fields of 600-1,500 Gauss and the pumping rate is directly related to field strength [Rut99, Sch99].

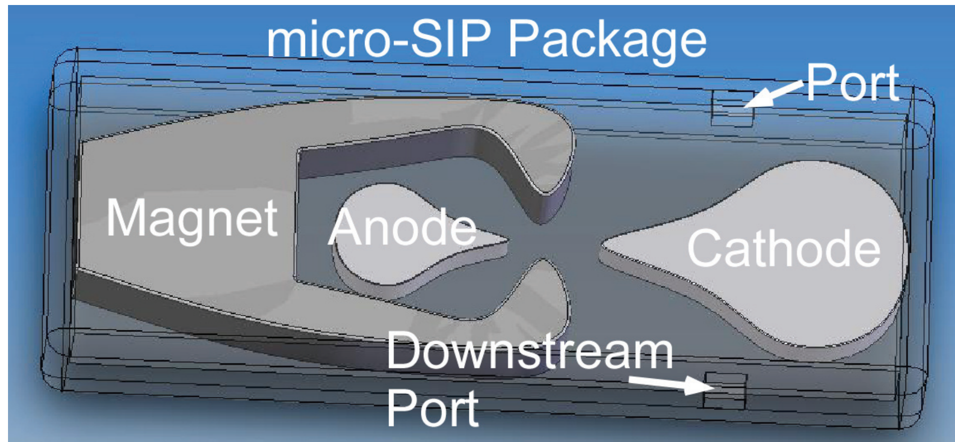

Figure 5.1: Schematic of a micro-SIP and accompanying magnet in a sealed package with outlet ports.

Miniaturized magnets have been used to enhance the parameters of DC microdischarges and have been shown to increase confinement, decrease sheath width, lower breakdown voltages, and increase current [Wil04, Ito08]. The current in magnetically enhanced microdischarges has been shown to increase with magnetic field strength, at a constant applied voltage, in a manner similar to macroscale discharges [Wen90]. Miniature magnets have also been used to increase the etch rate of silicon using a SF_6 microdischarge by 3x in localized areas and they have been integrated with a micro-machined Geiger counter to enhance the RF transmission from microdischarges initiated by incident beta particles [Eun08]. They have also been shown to increase electron magnetization at lower pressures [Ito08]. Previously, microscale magnets

creating magnetic fields of 3,000 Gauss were patterned and used [Fis01, Wil04]. For a micro-SIP, a niobium magnet should be considered in a magnetic flux circuit configuration (Fig. 5.1) to create the requisite magnetic field. The possible use of an electromagnet to assist the permanent magnet should also be considered.

The high vacuum micro-SIP could also be operated with little power using power-saving techniques for discharge initiation and energy control. A high impedance third electrode would be powered through a series inductor, facilitating discharge initiation with a relatively low voltage pulse between the anode and cathode; this would also allow the discharge current to be controlled through the anode, independently of the discharge initiation conditions [Mit08a, Mit08b]. Using this technique, the energy per discharge pulse has been reduced from 0.467 mJ to 2.5 μJ at 140 Torr, indicating its potential for micro-SIP energy reduction. A pulsed discharge-powering scheme should be used as it has been shown to increase power efficiency in Chapter 2. For example, bursts of pulses 10 ms in duration could be applied at a rate of 10 Hz, using 1 mJ per burst, consuming an average of 10 mW.

The electrode lifetime could be increased by using thick-film titanium electrodes patterned by micro-electro-discharge machining (μ-EDM) [Tak02, Tak04, Tak06, Ric08] or RIE [Aim04, Par07]. Electrodes 100-μm thick would provide extended lifetime over thin-film evaporated or sputtered electrodes, and could be used to create a cathode containing 5.66×10^{18} atoms. If this cathode is used, it would contain over six orders of magnitude more than the 3.26×10^{12} molecules of nitrogen and oxygen in a 1 mm^3 pump cavity at 100 mTorr, and three orders of magnitude more than the 1.63×10^{15} molecules present at 50 Torr. This titanium:gas molecule ratio would theoretically allow the pump

to be used for thousands of evacuations. Additionally, the use of pulse discharges would drastically increase device lifetime.

Several scientific and technical challenges would be presented in the development of this unique pumping mechanism. The electron response to the applied magnetic field must be understood to ensure the electrons are forced into spiral orbits, maximizing ionization. This could be accomplished through modeling. Additionally, a localized magnetic field of over 3,000 Gauss would be required from a microscale magnet. This could be addressed by increasing the localized field using appropriately shaped poles in the magnetic flux circuit. To prevent device contamination from sputtered titanium atoms, the micro-SIP could be situated in a separate cavity.

5.2.2 Harsh Environment Chemical Sensor Packaging

The developed harsh environment chemical sensor (Chapter 4, Section 4.4) was packaged in a DIP package for testing purposes, but a package which allows gas sampling in muddy, aqueous, or dusty environments would be advantageous for real-world use. A package with a permeable membrane, possibly constructed of GOR-TEX® fabric, could be developed to allow gas sampling. In addition, an optical fiber could be integrated with the package to secure the lens attached to the fiber optic cable. This would improve the consistency of the recorded spectra. A schematic of a potential packaging strategy is shown in Fig. 5.2.

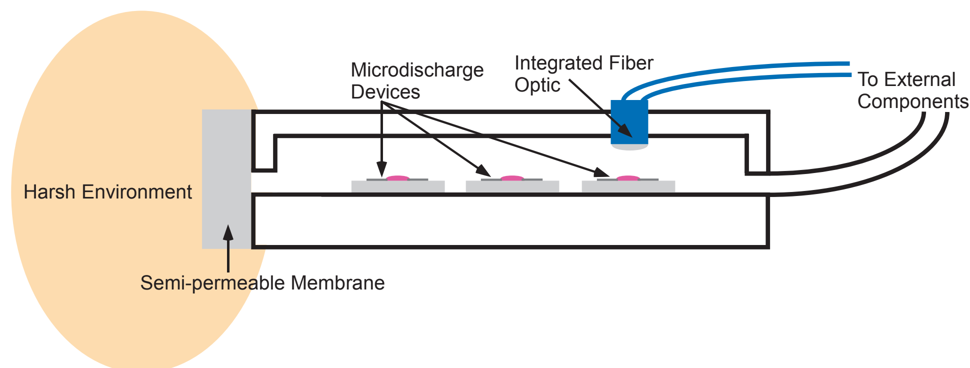

Figure 5.2: Schematic of harsh environment chemical sensor package with semi-permeable membrane and integrated fiber optic cable.

5.2.3 Selective Growth of Doped Nanowires Using Microdischarges

The current method of synthesizing doped SnO_2 nanowires for thin-film transistors (TFTs) does not allow selective growth in regions or patterns on a substrate without pre-growth patterning of the catalyst layer. Localized microdischarges may present a method of influencing growth through the local application of additional energy in the form of fast-moving ions and heat, as microdischarges have been shown to increase the gas temperature at the cathode by as much as 280˚C at 250 Torr [Boe05, Kus05]. This would allow for post-wafer-processing growth control and pattern generation. This method could also potentially be used to "write" nanowires by scanning a microdischarge. This has been initially explored and described in Appendix 6, however further investigation is required to determine the precise temperature at which nanowires are formed on the substrate. Holding the substrate slightly below this temperature would allow a slight temperature increase, caused by a microdischarge, to locally heat a region to a suitable temperature for growth.

APPENDICES

APPENDIX 1

CALCULATING MICRODISCHARGE PARAMETERS

The DC discharge parameters governing charged species and ionization in microdischarges can be calculated in both the discharge and the cathode sheath regions, as steady-state microdischarges operate similar to normal or abnormal glow discharges. In DC discharges, the electrons are drawn towards the anode, whereas the positive ions are drawn to the cathode forming a positively charged sheath around it. Upon cathode impact, the energetic ions eject high energy secondary electrons from the cathode, which sustains the microdischarge by ionizing additional neutral molecules and continuing the breakdown process. Current in the discharge is carried primarily by the faster moving electrons while current in the cathode sheath is composed of a combination of positive ions impacting the cathode from the microdischarge and secondary electrons ejected from the cathode upon ion impact. In microdischarges, the width of the sheath and the size of the microdischarge can be similar [Kus05]. A glow microdischarge created in a microdischarge-based pressure sensor is examined as are the formulas used for parameter calculations. The initial transient current pulses encountered during discharge initiation are not discussed in this Appendix. Additionally, the calculated parameters consider macroscale DC discharges, which typically underestimate the electric field strength in the

sheath region of microdischarges and do not consider the non-Maxwellian electron energy distribution function encountered in microdischarges.

A1.1 MICRODISCHARGE PARAMETERS IN A PRESSURE SENSOR

The electric field strength, ionization frequency, and other parameters are calculated for DC, glow microdischarges operating in steady-state, which are created and utilized by devices in this thesis. The microdischarge created between a parallel disk-shaped planar anode and a torus-shaped planar proximal cathode in a microdischarge-based pressure sensor is examined in detail. The electrodes in the sensor are composed of stainless steel and are spaced 50 μm apart, 125 μm thick, and 1 mm in diameter. An applied voltage of 1,000 V is considered with a maximum DC current of 300 μA. The electron temperature is assumed to be 3 eV (34,815 K) away from the cathode with an ion temperature of 0.03 eV (621 K) in a 23ºC (296 K) ambient environment, based on previous microdischarge models [Kus05]. The parameters are calculated over the actual sensor operating range, from 10-2,000 Torr and 23-1,000ºC in a nitrogen environment. The parameters describing the ions, electrons, ionization, and the electric field strength in the primary discharge are listed in Table A1.1. The microdischarge radius is measured along the axis parallel to the electrodes.

The ambient pressure and temperature affect all of the parameters as indicated by the calculated ranges. The effect on discharge size and electric field strength is examined. As the pressure increases, and as the temperature decreases, the discharges become exponentially more confined as shown in Fig. A1.1. However, as the discharge

radius is decreased, an increase in ionization is required and the electric field strength increases in response. The current is primarily limited by external ballast resistors.

Table A1.1: DC glow microdischarge operating parameters in a microdischarge-based pressure sensor, calculated over the range of 10-2,000 Torr and 23-1,000ºC.

Parameter	Symbol	Units	Value at 23ºC and 10 Torr	Range over Pressure Sensor Operation
Plasma Density	n_o	cm^{-3}	8.5×10^{13}	$8.5 \times 10^{13} – 1.1 \times 10^{15}$
Debye Length	λ_{De}	µm	1.4	0.39 – 1.4
Electron Temperature	T_e	eV	3	3.0 – 3.1
Electron Momentum Transfer Frequency	ν_{me}	Hz	5.0×10^{10}	$1.2 \times 10^{10} – 1.0 \times 10^{13}$
Electron Mobility	μ_e	$m^2/ V \cdot s$	3.5	0.018 – 15
Electron Velocity	v_e	m/s	1.2×10^6	1.2×10^6
Ion Temperature	T_i	eV	0.056	0.055 – 0.14
Ion-Neutral Interaction Frequency	ν_{mi}	Hz	1.2×10^8	$4.4 \times 10^7 – 2.4 \times 10^{10}$
Ion Mobility	μ_i	$m^2/ V \cdot s$	2.9×10^{-2}	$1.5 \times 10^{-4} – 7.9 \times 10^{-2}$
Ion Velocity	v_i	m/s	700	700 –1,100
Ion Diffusion Coefficient	D_i	m^2 / s	1.6×10^{-2}	$8.1 \times 10^{-6} – 1.1 \times 10^{-2}$
Ambipolar Diffusion Coefficient	D_a	m^2 / s	9.0×10^{-2}	4.5×10^{-4} – 0.26
Ionization Rate	ν_{iz}	Hz	4×10^7	$6.2 \times 10^6 – 8.0 \times 10^9$
Ion Diffusion Step Between Collisions	L_i	µm	3.7	0.018 – 16
Radius	R	µm	114	0.57 – 500
Electric Field Strength	E	V/cm	340	$6.4 – 6.8 \times 10^4$

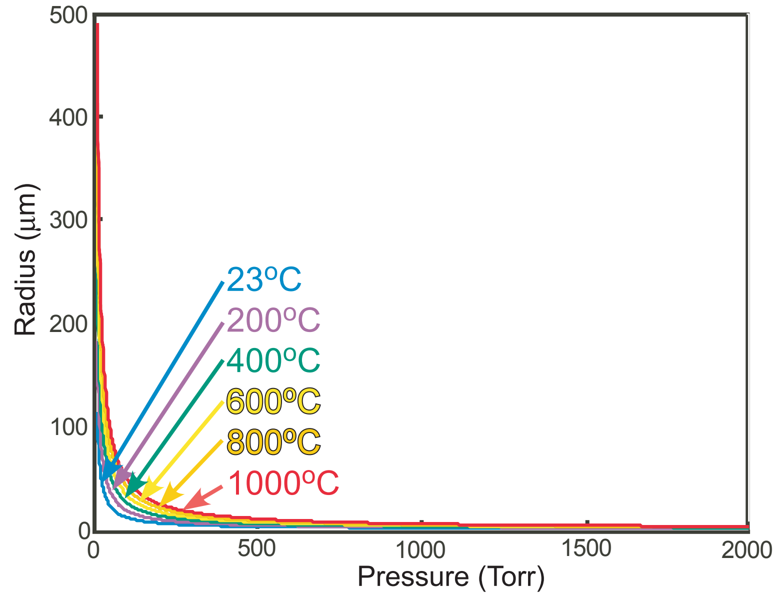

Figure A1.1: Radii of microdischarges as a function of pressure and temperature.

Outside of the sheath region, a microdischarge is considered quasineutral with an equal concentration of ions and electrons. Within the sheath region, ions are accelerated towards the cathode, less so in highly collisional sheaths, due to the high electric fields while electrons are repelled. These two factors cause both concentrations to decrease closer to the cathode. However as previously mentioned, the sheath region is positively charged due to a higher density of positive ions. A transition or presheath region exists, typically much wider than the sheath, in which a small electric field accelerates ions towards the cathode, imparting them with a velocity, u_s, at the sheath-presheath interface. At this interface, an equal concentration of electrons and ions, n_s, are considered present.

The sheath parameters including ion density, velocity, sheath width, maximum electric field strength, and current density are also calculated for microdischarges in the same sensor over the same operating range, listed in Table A1.2. At 23ºC and 10 Torr several parameters in the sheath and discharge can be compared. The ion density is slightly lower at the sheath-presheath boundary than in the discharge, 7.4×10^{13} cm^{-3} vs.

8.5×10^{13} cm^{-3}, due to the electric field attracting the ions and reducing the density in the presheath. This ion density outside the sheath at 10 Torr is comparable to the modeled density of 2×10^{13} cm^{-3} at 50 Torr in an argon microdischarge [Kus05]. The ion velocity is higher at the sheath-presheath boundary, 2,800 m/s vs. 700 m/s, due to higher electric field in the sheath causing ion acceleration. Additionally, the electric field strength at the cathode interface, in the sheath, is two orders of magnitude higher, 7.2×10^4 V/cm vs. 340 V/cm, although microdischarges traditionally have even higher field strengths in the sheath than this macroscale model predicts. As the pressure is increased, the sheath becomes more confined, increasing the electric field.

Table A1.2: DC sheath operating parameters in a microdischarge-based pressure sensor, calculated over the range of 10-2,000 Torr and 23-1,000ºC.

Parameter	Symbol	Units	Value at 23ºC and 10 Torr	Range over Pressure Sensor Operation
Density at Sheath Boundary	n_s	cm^{-3}	7.4×10^{13}	$9.4 \times 10^{12} – 8.4 \times 10^{13}$
Ion Velocity at Sheath Boundary	u_s	m/s	2,800	688 – 3,100
Sheath Width	s	µm	210	88 – 266
Sheath Electric Field Strength	E	V/cm	7.2×10^4	$5.6 \times 10^4 – 1.7 \times 10^5$
Current Density	J_o	A/cm^2	3.3×10^8	$1.0 \times 10^7 – 4.2 \times 10^8$

A1.2 BREAKDOWN VOLTAGE

Paschen's curve determines the microdischarge breakdown voltage between an anode and cathode. The breakdown voltage is a function of pressure (p) and electrode spacing (d). The breakdown voltage for a cathode, or for each cathode in a multi-cathode device, reaches a minimum at a certain value of pd. In a multi-cathode configuration, the

microdischarge will favor the proximal cathode at high pressures and the distal at low pressures. The pressure at which the breakdown voltage to a cathode is minimal is identified as p_{min} [Cob58]:

$$p_{min} = \left(\frac{1}{d_{min}} \right) \frac{2.718}{A} \ln \frac{1}{\gamma} \qquad \text{(A1.1)}$$

In a nitrogen ambient, A = 12 cm^{-1}Torr^{-1}, the secondary emission coefficient $\gamma = 0.02$ for nitrogen impinging on stainless steel, and d_{min} is the minimum anode/cathode spacing for the respective cathode.

A1.3 PRIMARY DISCHARGE

The parameters used to describe a DC microdischarge include the electron mobility, electric field strength, ambipolar diffusion coefficient, and discharge radius. Stable microdischarges, which remain in one location and demonstrate glow discharge characteristics, are created at high pressures without creating unstable arc discharges through the use of small discharge gaps between electrodes [Mit08b]. As the pressure is increased, microdischarges do change from normal glow discharges to abnormal glow discharges however, these discharge mechanisms are similar, and similar analysis can be applied for the different regions of operation [Cob58]. The area of the cathode covered by the discharges changes with pressure and temperature. The formulas are presented following the treatment in [Lie94]. The current density in a DC plasma can be expressed as:

$$J = en_0\mu_e E \, . \qquad \text{(A1.2)}$$

Integrating over the plasma density profile of a cylindrical discharge provides the discharge current as a function of the electric field strength:

$$I_{discharge} = 2\pi e n_0 \left(\frac{R^2}{\chi_{01}}\right) J_1\left(\chi_{01}\right) \mu_e E \,. \qquad \text{(A1.3)}$$

Here e is the absolute value of the charge of an electron, n_o is the plasma density, R is the radius of the discharge, χ_{01} is the first zero of the Bessel function, $J_1(\chi_{01})$ is the first order Bessel function evaluated at the zero of the zeroth order Bessel function, μ_e is the electron mobility, and E is the electric field strength. The plasma density is necessary to calculate the current in equation (A1.3) and is pressure dependent. This density is estimated based on the relationship between plasma density and pressure found to exist in an Ar microdischarge sustained with 2 mA over a pressure range similar to that encountered by the sensors [Kus05]. Additionally, fir_{01} is roughly 2.405 and $J_1(\chi_{01})$ is roughly 0.5202.

To determine the current, secondary parameters must be calculated. The electron mobility is:

$$\mu_e = \frac{e}{m_e \nu_{me}} , \qquad \text{(A1.4)}$$

where m_e is the electron mass and ν_{me} is the electron momentum transfer frequency.

The electron temperature, T_e is fairly constant in high pressure microdischarges for a given ambient temperature as most of the energy lost by electrons is in elastic collisions [Cob58]. However, T_e does decrease with increasing pressure to some extent. Assuming a Maxwellian electron velocity distribution, which is not always the case in microdischarges, and using a cross section for air of $\sigma_{air} = 0.8\ \sigma_{N2} + 0.2\ \sigma_{O2}$, the collision frequency coefficient for electrons at 3 eV is 1.44×10^{-7} cm^3/sec in air and 1.54×10^{-7}

cm^3/sec in nitrogen [Sli85]. This coefficient is used to calculate the electron momentum transfer frequency.

The electric field can be estimated by examining the power balance: the input power is equated to the power lost. Power is provided to a DC plasma through ohmic heating. For a cylindrical configuration, the ohmic power absorbed in a plasma is:

$$P_{abs} = 2\pi \int_0^R J \bullet E r dr \,. \tag{A1.5}$$

The power is lost in a DC plasma by particle loss, excitation, and ionization. This is a function of how much energy is required to ionize neutrals, and particle flux. This can be expressed by:

$$P_{loss} = 2\pi R \Gamma_r e \varepsilon_T \,, \tag{A1.6}$$

where Γ_r is the radial particle flux, and ε_T is the energy carried out per electron-ion pair created, which is strongly dependent on the electron temperature. This quantity is largely experimental, and for an electron temperature of 3 eV, is about 100 V [Lie94]. Equating the power absorbed and power lost and substituting the radial plasma density provides:

$$e n_0 \mu_e E^2 2\pi \int_0^R J_0(\beta r) r dr = 2\pi R (D_a \nu_{iz})^{1/2} n_0 J_1(\beta r) e \varepsilon_T \,, \tag{A1.7}$$

where ν_{iz} is the ionization rate which is a linear function of pressure, and $\beta = (\nu_{iz}/D_a)^{1/2}$. D_a is the ambipolar diffusion coefficient. Electron mobility is considered constant for a given pressure and temperature, and E has been taken out of the integral as it is assumed constant through the plasma. The plasma density falls out of the equation, and an expression for the electric field is:

$$E = \left(\frac{\nu_{iz} \varepsilon_T}{\mu_e} \right)^{1/2} . \tag{A1.8}$$

The mean free path lengths of the ions, λ_i is small compared to R at the pressures devices in this thesis operate. This allows the ionization rate to be substituted using the relationship:

$$\nu_{iz} = D_a \left(\frac{\chi_{01}}{R} \right)^2 . \quad \text{(A1.9)}$$

The electric field is then:

$$E = \frac{\chi_{01}}{R} \left(\frac{D_a \varepsilon_T}{\mu_e} \right)^{1/2} . \quad \text{(A1.10)}$$

As R is decreased, the loss of ions to recombination in the surrounding gas and walls increases, which requires an increase in the ionization process established by the electric field to maintain the necessary conductance. This requires the electric field strength to increase with decreasing discharge radius.

Given that the pressure ranges in which these devices are operated is sufficiently high, $\lambda_i \leq (T_i/T_e)R$, a diffusion equation with a constant coefficient D_a can be applied for a given pressure and temperature. T_i is the ion temperature. D_a is a function of ion and electron diffusion coefficients as well as their mobilities and is given by:

$$D_a = \frac{\mu_i D_e + \mu_e D_i}{\mu_i + \mu_e} . \quad \text{(A1.11)}$$

D_e and D_i are the electron and ion diffusion coefficients respectively while μ_e and μ_i are the electron and ion mobilities respectively. Since in processing type plasmas (weakly ionized discharges) $\mu_e >> \mu_i$ the ambipolar diffusion coefficient can be simplified and the Einstein relation can be used to re-express it as:

$$D_a \approx D_i \left(1 + \frac{T_e}{T_i} \right) . \quad \text{(A1.12)}$$

As the ambient temperature is increased, the electron and ion temperatures are increased. This affects the ion temperatures more significantly, as their temperatures are only slightly above that of the ambient gas. The electrons have very high temperatures, much higher than any of the ambient temperatures encountered, and are thus less affected. It is evident that in a typical processing plasma, the diffusion is limited by ion diffusion but is amplified by the ratio of electron to ion temperature.

The diffusion coefficient for ions is temperature dependent, and provided as:

$$D_i = \frac{eT_i}{m_i \nu_{mi}}, \tag{A1.13}$$

where m_i is the ion mass for nitrogen and ν_{mi} is the ion-neutral interaction frequency, which is highly gas species dependent:

$$\nu_{mi} = n\theta v_i, \tag{A1.14}$$

where n is the pressure and temperature-dependent gas particle density, v_i is the ion mean speed of relative motion (velocity), and Θ is the interaction cross section, which is approximately 5.2 x 10^{-19} m^2 for nitrogen. The ion-neutral interaction frequency causes the current to depend on both pressure and temperature. The ion mean speed of relative motion is:

$$v_i = \left(\frac{8eT_i}{\pi m_i}\right)^{\frac{1}{2}}. \tag{A1.15}$$

The radius of the discharge is also needed. It is based on the normalized average ion diffusion step between collisions, L_i, and the normalization pressure and temperature, p_0. As the distance of ion travel decreases, the discharge becomes more confined and

hence, has a smaller radius. $L_i(p_0)$ is used for diffusion step normalization. The radius is provided by:

$$R(p) = R_0\left(\frac{L_i(p)}{L_i(p_0)}\right), \tag{A1.16}$$

where

$$L_i(p) = \sqrt{\frac{D_i(p)}{\nu_{mi}(p)}}. \tag{A1.17}$$

R_0 is the radius of the discharge at p_0 (760 Torr and 23˚C), and is a free parameter.

A1.4 CATHODE SHEATH

Given the range of operating pressures of the DC microdischarge-based devices developed in this thesis, 10–2,000 Torr, the mean free path of the ions is less than the width of the sheath, $\lambda_i < s$, indicating collisional a sheath. In this case, the ion flow is impeded by collisional processes with neutrals, and the transport is mobility rather than inertia limited. This indicates the Child law parameters and sheath calculations for collisional as opposed to a collisionless sheaths apply. The following formulas are presented following the treatment in [Lie94]. The ion flux and current are constant throughout the width of a sheath:

$$I_{sheath_high_pressure} = \int_{area} en_s u_s , \tag{A1.18}$$

where the integral is over the partial electrode area covered by the sheath, n_s is the ion density, and u_s is the ion velocity, both at the sheath edge. The ion density at the edge of a high pressure, collisional sheath where the transport is diffusive, is:

$$n_s = n_0 \left[1 + \left(\frac{l u_B}{\pi D_a} \right)^2 \right]^{-1/2} . \quad \text{(A1.19)}$$

Here l is the discharge length and the Bohm velocity of the ions is:

$$u_B = (eT / m_i)^{1/2} . \quad \text{(A1.20)}$$

The ion velocity is not equal to the Bohm velocity for the highly collisional case and is:

$$u_s = \frac{u_B}{\left(1 + \pi \lambda_{De} / 2\lambda_i\right)^{1/2}} , \quad \text{(A1.21)}$$

where λ_{De} is the electron Debye length. The Debye length is calculated as:

$$\lambda_{De} = \left(\frac{\varepsilon_0 T_e}{e n_0} \right)^{\frac{1}{2}} , \quad \text{(A1.22)}$$

or in more practical units,

$$\lambda_{De}\left(cm\right) \approx 743 \sqrt{T_e / n_e} \quad \text{(A1.23)}$$

with T_e in volts and n_e (electron density) in cm^{-3}.

The electric field strength and sheath width are now calculated for a collisional sheath. If the current is continuous in the sheath:

$$n_i u_i = n_s u_s , \quad \text{(A1.24)}$$

where n_i and u_i are the density and velocity of ions in the sheath and n_s and u_s are the density and velocity of ions in at the sheath-presheath boundary. In high-pressure, high-voltage collisional sheaths, the ion velocity is constant as it is limited by a constant mobility and mean free path.

$$v_i = \mu_i E , \quad \text{(A1.25)}$$

where the ion mobility is given as:

$$\mu_i = \frac{e}{m_i \nu_{mi}}, \tag{A1.26}$$

where ν_{mi}, the ion-neutral interaction frequency, is constant. With the assumption of a constant mean free path, combining equations A1.24 and A1.25 provides:

$$n_i = \frac{n_s u_s}{\mu_i E}. \tag{A1.27}$$

Inserting the charge density into Gauss' law provides:

$$\frac{dE}{dx} = \frac{e n_s u_s}{\varepsilon_0 \left(\mu_i E\right)}. \tag{A1.28}$$

Integrating and solving for the electric field, E, by separation of variables provides:

$$E = \left(\frac{2 e n_s u_s}{\varepsilon_0 \mu_i}\right)^{\frac{1}{2}} x^{\frac{1}{2}}. \tag{A1.29}$$

Setting electric field to zero, which is an approximation, at the sheath-presheath boundary and integrating provides the potential in the sheath as:

$$\Phi = -\frac{2}{3}\left(\frac{2 e n_s u_s}{\varepsilon_0 \mu_i}\right)^{\frac{1}{2}} x^{\frac{3}{2}} \tag{A1.30}$$

Considering the voltage at the sheath-presheath interface to be zero, the current density as $J_0 = e n_s u_s$ (equation A1.18), the potential drop across the sheath, Φ, as $-V_0$, and the electrode position at the edge of the sheath to be $x = s$, the sheath width is given as:

$$s = \left(\frac{9}{8}\frac{\varepsilon_0 \mu_i V_0^{\,2}}{J}\right)^{1/3}. \tag{A1.31}$$

For a fixed current and voltage the sheath width scales weakly with mobility. The spacing dependence on current is due to the almost constant value of the ion velocity in this collisional case.

Considering the traditional Child law for the collisionless case, the sheath width is given as:

$$s = \frac{\sqrt{2}}{3} \lambda_D \left(\frac{2V_0}{T_e} \right)^{3/4} . \qquad \text{(A1.32)}$$

This sheath can be over 100 Debye lengths in width, indicating the average sheath in a processing type discharge can be about a centimeter.

A1.5 OTHER CURRENT GENERATING MECHANISMS

Calculations predict that thermionic and field emission currents are substantially lower than discharge currents, however localized hotspots or high field regions may make these currents substantial. Thermionic emission current is calculated using the Richardson-Dushman equation, listed in Appendix 3, equation A3.1. Operating a microdischarge-based pressure sensor with stainless steel electrodes at 1,000ºC produces a thermionic current density of 6.6 nA/cm^2, 52 pA, at the cathode. This is nine orders of magnitude less current than the discharge. However, the creation of localized hotspots can cause portions of the cathode to be heated to temperatures >> 1,000ºC, causing thermionic emission. Likewise microarcs utilizes these localized cathode spots and are sustained through thermionic emission.

The addition of electrons from field emission is considered, as these electrons contribute to the current density according to the Fowler-Nordheim equation (Appendix

3, equation A3.3). To obtain measurable changes in current density, the electric field strength needs to be on the order of 10^7 V/cm [Cob58]. COMSOL Multiphysics® predicts the maximum field strength in a microdischarge-based pressure sensor with 50 µm gaps to be 2.4 x 10^5 V/cm at 23ºC and 760 Torr (Fig. A1.2). The calculated maximum field strength in the sheath at 23ºC and 760 Torr, using the equations A1.29, is 1.1 x 10^5 V/cm, which is similar to the Multiphysics® model. Likewise, the electric field strength of a microdischarge near the cathode in a cylindrically symmetric metal-dielectric-metal stack is in excess of 8 x 10^4 V/cm [Kus05]. However, equation A1.29 is used to calculate the field strength in macroscale discharges, while microdischarges have exhibited higher than predicted field strengths in the sheath. With the given discharge gap spacing of the pressure sensor, the electric field across the entire gap would necessarily be higher than predicted by equation A1.29, indicating a higher field strength and the potential for field emission. Also, localized protrusions can increase the electric field strength, potentially inducing field emission.

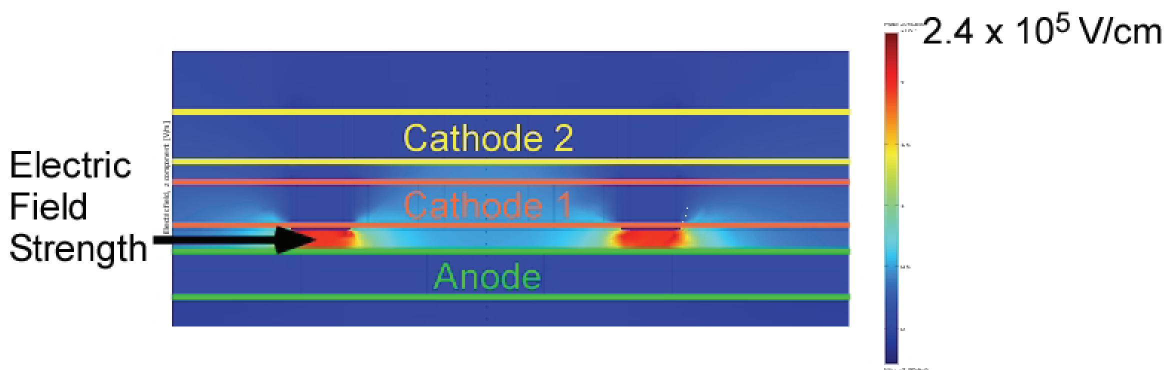

Figure A1.2: Predicted electric field strength in a microdischarge-based pressure sensor with 50-µm gaps and 125-µm-thick electrodes.

APPENDIX 2

X-RAY PHOTOELECTRON SPECTROSCOPY RESULTS

The atomic compositions of used and unused micro-SIP electrodes were examined by X-ray Photoelectron Spectroscopy. The examined micro-SIPs were of the version 2 design and had 150-μm discharge gaps. The used micro-SIP electrodes, which had been used to chemisorb air for one hour, had been operated at initial pressures of 200 Torr, 500 Torr, and 725 Torr while the unused micro-SIPs had never been packaged, and no voltage had been applied to any of the discharge gaps.

A2.1 MEASUREMENT DESCRIPTION

A Kratos Axis Ultra XPS was used for the measurements. For each specific electrode, a survey spectrum recording binding energies between 0 eV and 1,100 eV, as well as 20 eV narrow bandwidth spectra, were recorded. The narrow bandwidth spectra were centered at 532 eV for the oxygen 1s peak, 455 eV for the titanium 2p peak, and 399 eV for the nitrogen 1s peak. Pass energies of 160 eV and 20 eV were used for the survey and narrow spectra respectively. Two narrow spectra were recorded and averaged in each region to increase accuracy. An aluminum source was used to acquire spectra from the used electrodes while a magnesium source was used to acquire spectra from the unused electrodes.

After spectra were recorded, the compositions were determined using the CasaXPS© processing software package. The complete compositions of the samples were determined from the survey spectra while the narrow region spectra were used to determine the concentration of oxygen, titanium, and nitrogen relative to one another. The intensities of element induced peaks were measured by integrating the recorded counts and subtracting out the computed background counts around the peaks formed at particular binding energies. These peaks, which resulted from higher counts at specific binding energies, were used to characterize particular elements and the sample composition. The integrated intensity was adjusted for both relative sensitivity of the various photoelectron lines and the energy dependent instrument variations. A transmission correction factor was used to account for the variation in performance of the spectrometer as a function of kinetic energy for ejected electrons when measured using the different operating modes of the instrument. The recorded narrow spectra were calibrated so that the count peaks of interest were precisely aligned with the correct binding energies, while the wide survey spectra were not aligned to individual peaks. The count integration regions for peaks in the narrow spectra were adjusted to only encompass a single element induced peak for each particular element.

A2.2 ELECTRODE COMPOSITION RESULTS

Using this described method, the electrode compositions were determined. Figure A2.1 shows the complete average compositions of used anodes, used cathodes, and unused electrodes obtained from the survey spectra. At least three spectra produced from sampling anodes, cathodes, and unused electrodes were averaged to obtain the

composition measurements. Figure A2.2 shows the relative concentrations obtained from the narrow, focused, spectra of oxygen, titanium, and nitrogen.

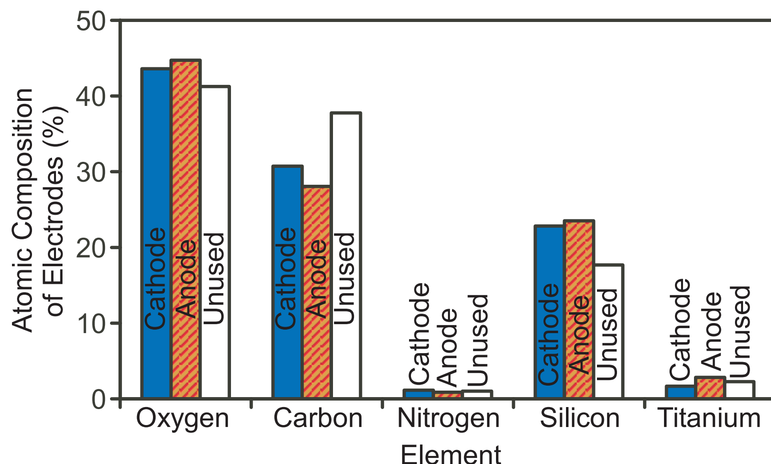

Figure A2.1: The atomic composition of used anodes, cathodes, and fresh unused titanium electrodes. These are the only five elements found in the electrode surfaces. Broad spectra are examined and at least three spectra are averaged for each data point.

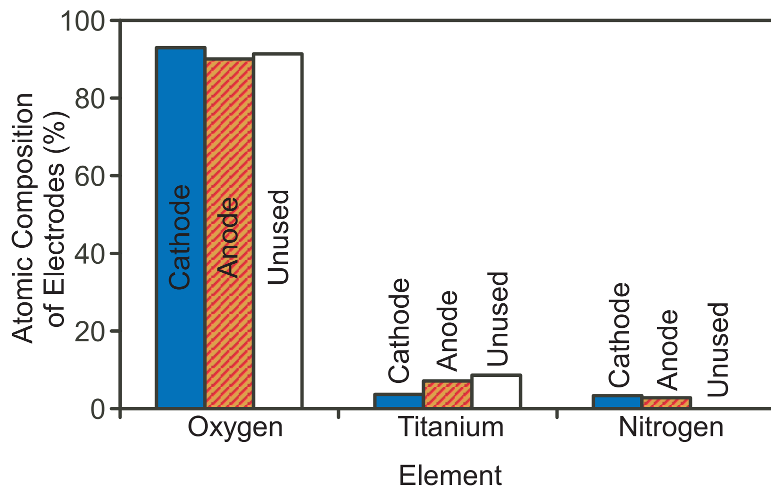

Figure A2.2: The distribution of oxygen, titanium and nitrogen based on the atomic composition of used anodes, cathodes, and fresh unused electrodes. Narrow, focused spectra are examined and at least three spectra are averaged for each data point. The figure only considers the concentration of these three elements in the sample.

The spectra had no discernable indication of nitrogen in the unused electrodes. Figures A2.3 and A2.4 show the percentage of titanium, nitrogen, and oxygen in both the

used cathodes and anodes, as a function of the initial environment pressure the micro-SIPs were operated in. However, there was no discernable relationship between the electrode composition and the initial pressure the micro-SIPs were operated at.

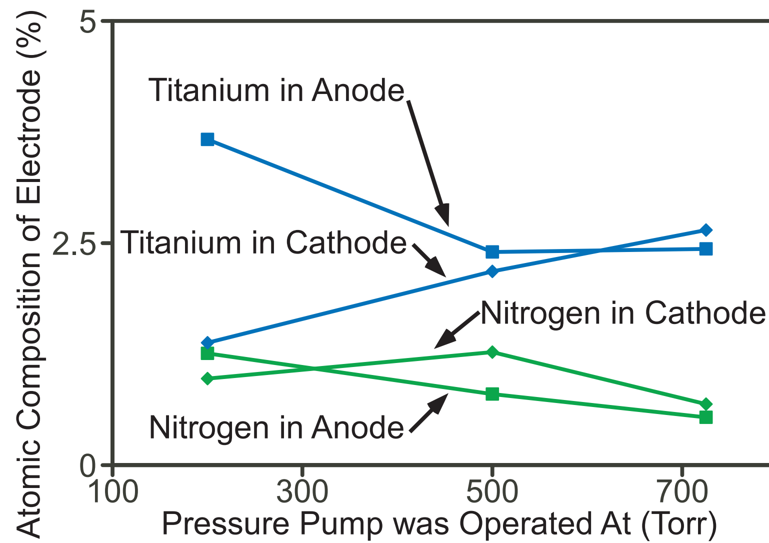

Figure A2.3: The atomic concentration of titanium and nitrogen in anodes and cathodes of micro-SIPs which had been operated at different initial pressures.

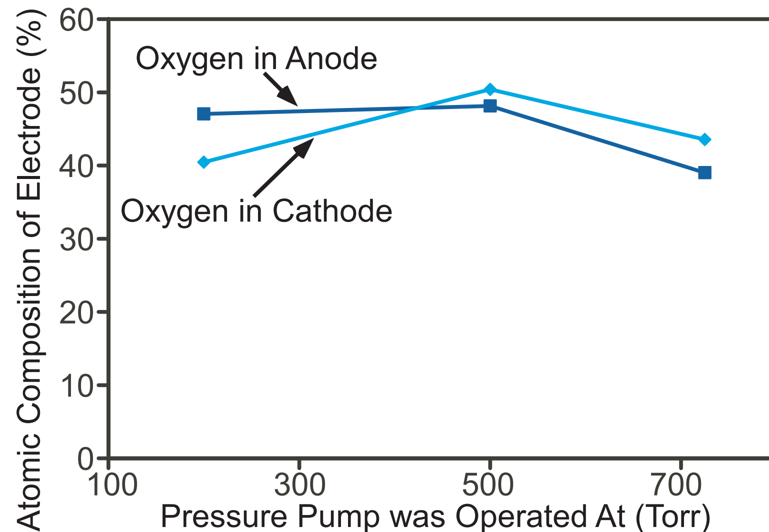

Figure A2.4: The atomic concentration of oxygen in anodes and cathodes of micro-SIPs which had been operated at different initial pressures.

Overall, the data collected and analyzed by the X-ray Photoelectron Spectroscopy method gave little information regarding micro-SIP operation as the anodes, cathodes, and unused electrodes had similar surface concentrations. These results were similar to the results obtained by Li *et al.* [Li07] in which XPS samples of titanium films used to chemisorb oxygen were examined. Li found that carbon and oxygen were present, and attributed the measured film surface compositions to the layer of reactive molecules that covered the titanium films when exposed to air. Given the similar surface concentrations of used and unused micro-SIPs, as well as titanium films measured by other researchers, it was apparent that exposing the surfaces to air was causing the titanium to oxidize after operation.

APPENDIX 3

CONSIDERATIONS FOR A MICROSCALE ION GAUGE

To determine if microscale ion gauges are a compelling alternative to microscale microdischarge-based pressure sensors, and to determine the limiting factors in their operation, macroscale ion gauges are examined and calculations for microscale gauge operation are performed. A summary of ion gauge operation is presented and the two primary types of ion gauges are discussed. The first is the “hot cathode” ion gauge, which uses a heated cathode to produce thermionic electrons. The second is the “cold cathode” ion gauge, which uses strong electric fields to cause field emission of electrons. The emission currents produced from microscale versions of these designs are examined. The pressure ranges over which ion gauges are operated is then considered.

A3.1 MACROSCALE ION GAUGES

Ion gauges typically measure vacuum levels between 10^{-3} Torr and 10^{-10} Torr by measuring the number created ions reaching an electrode. They use a triode structure, with a filament, a grid, and a collector. The filament is a cathode (≈ 30 V) which can be either of the “hot” or “cold” variety. The grid serves as an anode (≈ 150-210 V) while the collector is held at a negative voltage (≈ -30 V). Electrons are emitted from the cathode filament and move back and forth several times around the anode grid before

entering it, creating gas ions. The number of ions produced is proportional to the gas density multiplied by the electron current (≈ 10 mA). The ions are attracted to the collector, and the collector current is used to determine the pressure as it is based on the gas density and the resulting ionization. Ion gauges are difficult to calibrate as they depend on the gas environment in which they are used.

A3.2 HOT CATHODE IONIZATION GAUGES

Hot and cold cathode ion gauges are examined to determine which principle can potentially function with microscale dimensions. In hot cathode devices, the cathode is heated to decrease the work function of the cathode material. This leads to the thermionic emission of electrons, which are ejected with a lower applied potential (relative to the potential required without heating). The emitted current depends exponentially on the cathode temperature. A heater and gas triode are shown in the schematic in Fig. A3.1.

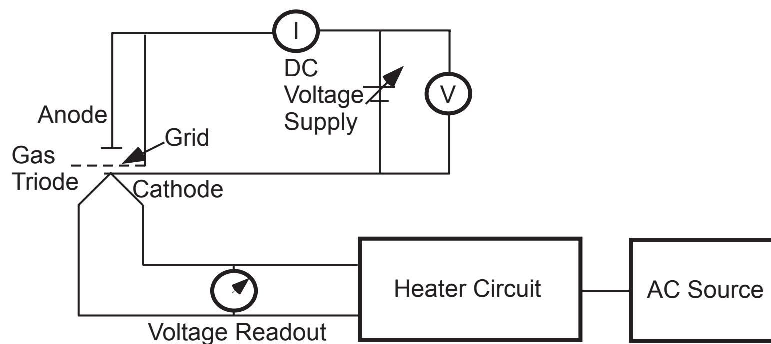

Figure A3.1: Schematic diagram of a thermionic cathode with heating circuit.

A3.3 COLD CATHODE IONIZATION GAUGES

Cold cathode ion gauges operate without applying heat to the cathode through the application of large potential differences between electrodes, which causes electron emission. There are two types of cold cathode ion gauges, the Penning gauge and the Inverted magnetron or Redhead gauge. They differ in the position of the anode with respect to the cathode and can use tapered electrodes and magnetic fields. Given that the cathodes are not heated, large potentials (≈ 4 kV) are used to extract field emission electrons from the cathode. Rare earth coatings are used in some devices to enhance electron emission.

A3.4 MICROSCALE HOT CATHODE ION GAUGES

The current produced by hot thermionic cathodes is limited by: 1) The heat of the cathode or 2) The space charge developed around the cathode. The influence of these two factors on a theoretical microscale ion gauge is examined to determine which factor is current limiting.

(1) The thermionic emission current density resulting from heating a cathode is described using the Dushman equation [Cob58]:

$$J = AT^2 e^{\frac{-\phi e}{kT}} \quad \text{where} \quad A = \frac{4\pi m k^2 e}{h^3}. \qquad \text{(A3.1)}$$

A is a universal constant, Φ is the thermionic work function, e is the electronic charge, k is Boltzmann's constant, and h is Planck's constant. The universal constant A is calculated as approximately 1.2×10^6 A/(m^{2}K^2), but is closer to 6×10^5 A/(m^{2}K^2), in practice and varies for different metals. This equation assumes the anode attracts all

emitted electrons. The current density, J, varies rapidly with the cathode temperature. Tungsten is examined as a sensor material and has a work function of ≈ 4.5 eV and a constant A of 7 x 10^5 A/(m^2K^2). On the macroscale to keep the work function around 2 eV, and the temperature at a reduced level, cathodes are coated with materials such as barium and calcium. Barium and strontium oxides are also used as cathode materials as they have a 1.3 eV work function. Figure A3.2 illustrates this best case scenario for current emission with a 1.3 eV work function, as well as the current emission using tungsten, as a function of temperature. Theoretically, higher current densities can be drawn from the cathode but the current density is limited to ≈2,000 A/(m^2K^2), and deteriorates the oxides quickly.

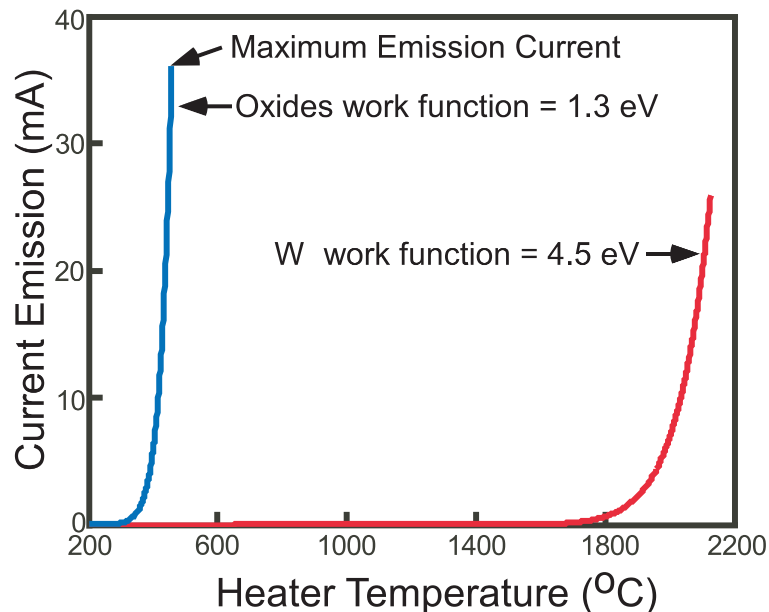

Figure A3.2: Emission current as a function of cathode temperature with two materials.

(2) The thermionic emission current density is also limited by the space charge induced electrostatic potential depression. As a space charge associated with an electron cloud develops at the cathode, the localized potential drops. If this space charge is strong

enough, it reverses the sign of the electric potential. This causes some of the electrons emitted from the cathode to be reflected back if they do not have enough energy to overcome the potential barrier. This regulation of electrons limits the emission current, and is described by the following equation for planar plate electrodes [Dav74]:

$$J = \frac{4V^{\frac{3}{2}}}{9kd^2} \text{ and } I = 2.33\times10^{-6}\frac{A}{d^2}V^{\frac{3}{2}} , \qquad \text{(A3.2)}$$

where V is the applied voltage, d is the distance between electrodes, and A is the effective electrode area. These equations are only valid if breakdown has not occurred and no background plasma exists. Figure A3.3 illustrates the maximum predicted space charge limited emission current in a microscale ion gauge, with a 35-µm gap, as a function of the potential difference between electrodes. As the discharge gap decreases, the emission current becomes decreasingly limited.

To determine if breakdown will occur, limiting the use of the ion gauge, the breakdown potential can be calculated. The breakdown potential is a function of the product of the pressure (p) and distance between electrodes (d). With a gap of 35 µm, tungsten electrodes, and an air environment with a pressure of 760 Torr, breakdown occurs with an applied voltage of 407 V. The breakdown potential decreases with decreasing discharge gap distance down to a minimum according to Paschen's curve. As the pd product is reduced beyond this minimum, the required voltage for breakdown increases as many emitted electrons do not collide with gas molecules as they travel between electrodes.

With an applied potential difference between 0 V and 407 V (potential differences not initiating breakdown) the limit on the emission current imposed by the space charge

region is higher than the current produced by the heaters as shown in Fig. A3.2. This indicates that in a microscale ion gauge, the temperature of the cathode is the limiting factor. Unfortunately, this indicates that operating ion gauges at different temperatures affects the emission current, as it is temperature dependent.

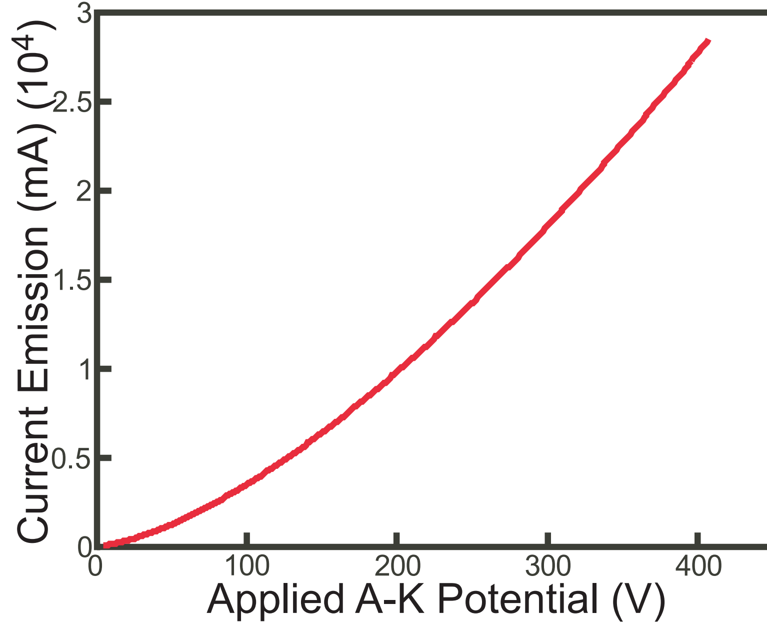

Figure A3.3: Emission current as a function of applied anode-cathode potential difference.

A3.5 MICROSCALE COLD CATHODE ION GAUGES

The emission current in cold cathode devices results from field emission, caused by high electric fields. The Fowler-Nordheim equation predicts the field-emission current density as:

$$J = \frac{4\sqrt{\mu\phi}}{\mu+\phi}\frac{e^3E}{8\pi h\phi}^2 \exp\left(-\frac{8\pi\sqrt{2m}\phi^{3/2}}{3heE}\right), \quad \text{(A3.3)}$$

where μ is the Fermi level, Φ is the work function of the material (4.1 eV for stainless steel), e is the charge of an electron, h is the Planck constant, and m is the electron mass,

and E is the electric field strength. This can also be written more simply for specific materials as [Cob58]:

$$J = K_1 E^2 \exp\left(-\frac{K_2}{E}\right), \quad \text{(A3.4)}$$

where K_1 and K_2 are variables dependent on the number of free electrons per unit volume. In macroscale devices, field strengths of ≈10^7 V/cm are required to produce measurable field currents [Bro01]. However, field emissions and field strengths of 10^5 V/cm are created with potentials as low as 1,000 V using fine pointed electrodes. Also, cathodes having electroplated materials can produce field emissions with field strengths of 10^6 V/cm [Cob58].

It does not appear that microscale cold cathode ion gauges can generate measurable field emission currents without initiating breakdown at pressures near atmospheric pressure. A microscale cold cathode ion gauge using a potential of 1,500 V with a 35-μm discharge gap, similar parameters to those used in Planar microdischarge-based pressure sensors, has an average field strength of 4.28 x 10^5 V/cm. A potential of 3,500 V is required to create an average electric field of 10^7 V/cm, but breakdown occurs at 407 V with discharge gaps of 35 μm at 760 Torr and at lower voltages at lower pressures. Microdischarges can have localized field strengths exceeding 5 x 10^7 V/cm in the sheath region. However, this indicates plasma is present, defeating the operation of ion gauges. Unless very strong localized fields near the cathode are created using pointed tips, this does not appear to be a viable emission mechanism.

A3.6 Operating Pressure Range

Overcoming the traditional operating rage of ion gauges presents the largest challenge to creating a microscale gauge which can operate in the same dynamic range, ≈10-2,000 Torr, as current microdischarge-based pressure sensors. Traditional ion gauges cannot operate if the ions recombine before reaching the anodes. If the mean-free path of the gas in which a gauge is operating in is smaller than the gauge's electrode spacing, the electrode current will saturate as the ions reach a constant drift velocity. This creates an upper pressure limit of 10^{-3} Torr for traditional hot and cold cathode gauges. In addition, at higher pressures, the reduction in the gas mean free path reduces the electron energy [Ede90]. However, Schulz and Phelps created a gauge for measuring pressure at almost 1 Torr by configuring the electric fields so the electrons travel in straight lines using parallel plate electrodes, a large collector, and by creating a sensor with a low sensitivity over a larger dynamic range [Sch57]. Other authors increased the maximum measurable pressure to 7.5 Torr [Kud81, Ede90]. Edelmann measured the change in drift velocity with pressure, when the mean-free path of a gas was less than the electrode spacing at higher pressures. To measure current in the traditional linear range in a microscale ion gauge, the mean-free path of the gas must remain greater than the electrode spacing. This indicates a sensor with a 35-µm gap functions up to 13.7 Torr in air. To operate up to 760 Torr, a gap of 112 nm is required. With a gap of 112 nm at 760 Torr, breakdown requires an applied potential of more than 2,000 V. This indicates that a microscale ion gauge could be developed with a discharge gap on the order of 100 nm as breakdown would not be initiated, given the large breakdown voltage.

A3.7 CONCLUSION

To measure pressure in the range of 10-2,000 Torr, there are several compelling reasons to use microscale microdischarge-based sensors as opposed to microscale ion gauges. To produce a linear output emission current over this pressure range, microscale ion gauges would require gaps on the order of tens of nanometers. Microscale ion gauges would additionally be more effective when utilizing hot cathodes, as the required potential for field emission in cold cathode sensors would initiate breakdown in many instances. If breakdown occurs, the devices would not function as ion gauges, but as microdischarge-based sensors. However, hot cathode ion gauges would be temperature dependent, requiring re-calibration at different temperatures. On the other hand, microdischarge-based sensors do not require nanometer scale discharge gaps or heated electrodes. In addition, they are not particularly sensitive to operating temperature. If an ion gauge is developed, a cathode material with a low work function should be utilized for higher emission currents at lower temperatures as should pointed electrodes.

APPENDIX 4

MICROPLASMA SF_6 EMISSION LINE DETECTION

To determine the effect nitrogen has on relative sensitivity in microplasma chemical sensing, the typical emission lines produced by SF_6 discharges must be identified and compared against recorded microplasma spectra. DC microplasmas in SF_6 environments with air contamination are examined due to their use in the localized etching of silicon. This section presents a detailed account of the previously recorded and theoretical emission lines produced by SF_6 dissociation in macroscale plasmas, the experimental set-up used to obtain microplasma spectra in SF_6 environments, and a theoretical discussion of nitrogen's ability to mask SF_6 emission lines, due to their low relative sensitivity.

A4.1 SF_6 EMISSION SPECTRUM CHARACTERIZATION

Plasmas in SF_6 environments are currently used to etch patterns on silicon wafers. They are used in relatively large electron cyclotron resonance (ECR) plasmas, and in microplasmas for localized etching [Wil01a]. This etching is performed by decomposing SF_6 though dissociative electron attachment, which produces SF_5^- ions and free fluorine atoms [d'Ag81, Arn04]. This etching typically takes place at pressures of 10-500 mTorr and with power densities of 10-500 mW/cm^2. SF_6 is also used as an insulating or

extinction gas in circuit breakers due to its high electronegativity [Air75, Vac85, Tan95, Har98].

On the macroscale, SF_6 characterization, discharge detection, and temperature measurements are all performed using optical spectroscopy [Air75, d'Ag81, Vac85, Cas91, Sug91, Zen91, Tan95, Har98, Sho98, Arn04]. The emission lines produced by macroscale discharges in SF_6 in the 200-800 nm range can be used for this detection of SF_6 in microscale discharges, in unknown gas environments.

Emission lines from F I and S II are used to indicate and measure the disassociation of SF_6. However, different emission lines are attributed to this dissociation. RF SF_6 glow discharges are shown to disassociate SF_6 into atomic fluorine with an emission line at 703.7 nm [d'Ag81, Sug91, Sho98]. This fluorine emission line is used to measure the annihilation rate of fluorine and the dissociation rate of SF_6. Another intense emitted fluorine emission line is observed in SF_6 arcs at atmospheric pressure at 624.0 nm [Air75, Tan95]. Both of these emission lines are confirmed as strong lines, resulting from neutral fluorine in discharges [Lid49, Har69]. Dissociating SF_6 through controlled electron bombardment produces spectra dominated by F I emission lines with the strongest lines occurring in a multiplet at 366.8 nm as well as at 685.6 nm, 690.2 nm, 739.8 nm, and 775.4 nm [Bla87a, Bla87b]. The absolute emission cross sections causing these emission lines are the largest in the SF_6 dissociation, larger than the emission cross section causing the line at 703.7 nm. Analyzing arc extinction using SF_6 in high current circuit breakers is traditionally performed by measuring the intensity of S II emission lines at 532.1 nm and 545.4 nm, and the intensities of these emission lines are used to determine temperature through the Boltzmann plotting [Air75,

Vac85, Tan95, Har98]. Strong S II emission lines are confirmed to exist at these wavelengths in discharges as well [Har69, Pet83].

The presence of SF_6 and its dissociation byproducts also produces a molecular emission band under DC and AC biases at currents of 10-40 μA in corona discharges. The emission band is comprised of continuously increasing emission intensities between 420 nm and 500 nm, which abruptly terminate at 500 nm [Cas91, Zen91]. This band exists under positive and negative DC voltages. A number of broad absorption maxima at 83.0 nm, 87.2 nm, 93.6 nm, and 105.4 nm are also attributed to the presence of SF_6 in plasmas [Her66]. Unfortunately, these wavelengths are shorter than our detectable limit.

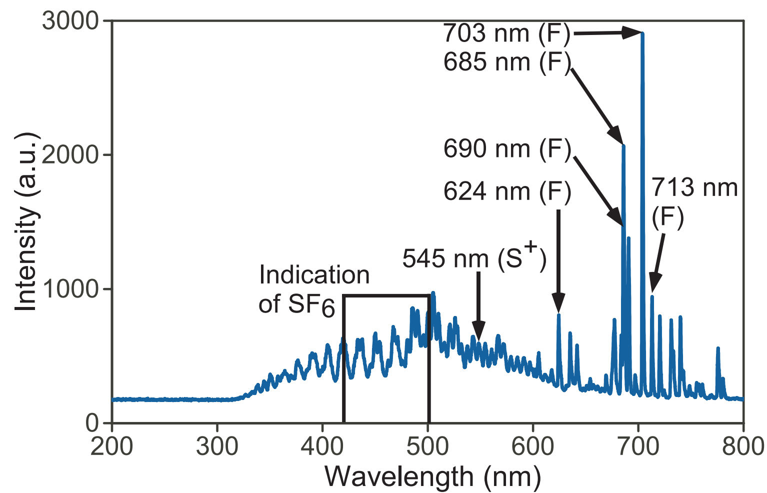

Figure A4.1: Emission spectrum of pure SF_6 produced in a RIE chamber. An excitation frequency of 13.56 MHz is used. Three consecutive measurements are averaged.

A reference spectrum displaying the emissions of an empty reactive ion etching chamber, with an applied RF frequency of 13.56 MHz, was taken through a quartz window and is shown in Fig. A4.1. The fluorine emission lines, ionized sulfur lines, and the molecular emission band previously described are present. This confirms that these

emission lines are caused by SF_6 and that the molecular emission band exists at pressures in the millitorr regime, as well as at 225 Torr as previously reported.

Nitrogen (N_2) and N_2^+ emission lines are observed in nitrogen and in SF_6 macroscale discharges with nitrogen introduced as an impurity. Strong observed N_2 emission lines occur at 316.0 nm, 337.1 nm, 357.7 nm, and 380.5 nm, while a strong N_2^+ emission line occurs at 391.4 nm [Cas91, Sug91, Zen91, Arn04] and 427.8 nm [Her50, Pea63].

Spectra similar to those produced by DC discharges in SF_6 in the macroscale domain are expected from microplasmas created in SF_6 in the microscale domain. The molecular emission band, neutral fluorine emission lines, and ionized sulfur emission lines which characterize SF_6 dissociation on the macroscale would serve as indications of the dissociation of SF_6 on the microscale, even in the presence of N_2 or N_2^+ impurities and resulting background emission lines.

A4.2 EXPERIMENTAL SETUP

The spectra were produced by initiating microplasmas in a vacuum chamber within a controlled SF_6 environment (Fig. A4.2). The microplasmas were created between pairs of planar copper electrodes with inter-electrode spacing of 500 μm, deposited on 500-μm-thick glass substrates. The anodes consisted of 2.5 mm x 100 μm leads with 50 μm x 250 μm electrodes on the end of the leads while the cathodes consisted of identical leads with 300 μm x 300 μm electrodes. The electrodes were composed of 15-μm-thick copper layers on top of 400-nm-thick titanium layers. To obtain spectra from discharges between titanium electrodes with identical designs, the

copper layers from the previously described electrodes were completely etched, exposing the titanium beneath.

A two-stage rotary vane roughing pump (Oerlikon Leybold Vacuum Trivac D 16B), accompanying pressure controller (MKS® 600 Series), and external macroscale pressure transducer (MKS® Baratron® Capacitance Manometer model #627B23TDC1B) were used to set the pressure between 100 mTorr and 10 Torr. The flow rate of CP grade SF_6 gas (Airgas Inc.) into the chamber was controlled using MKS® Mass-Flo® Series Mass Flow Controllers (Model #'s 1479A13CR1BM and 1479A21CR1BM). SF_6 and air were introduced and pumped from the chamber at rates of 5.6-260 sccm, to obtain a constant gas composition and pressure. Power was supplied via a high-voltage power supply and a 100 kΩ ballast resistor was connected in series with the anode to limit current. The setup was similar to that used for *in-situ* silicon etching, which contained similar concentrations of unwanted nitrogen.

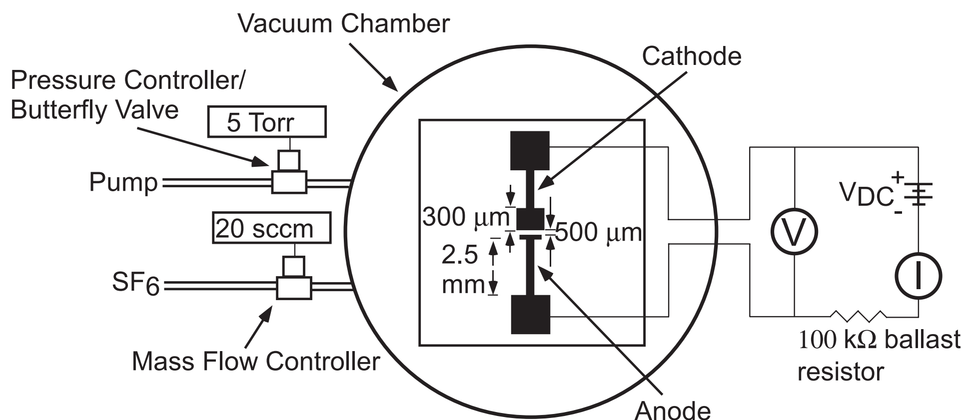

Figure A4.2: Schematic of electrodes and system set-up.

The optical spectra produced were measured using an Ocean Optics USB2000™ spectrometer. This spectrometer used a fixed grating and a linear CCD array detector

with a resolution of 0.37 nm. The observed emissions were integrated between 100 ms and 300 ms to observe weak emission lines without allowing the stronger emission lines to exceed the spectrometer's maximum detectable intensity. Three measurements were averaged for each recorded spectrum. The optical fiber attached to the spectrometer was fixed over the cathode glow region and the vacuum seal was not broken during the recording of compared spectra.

APPENDIX 5

SF_6 MICROPLASMA CHARACTERISTICS

Several discharge characteristics are noteworthy in SF_6 microplasmas created using the method described in Appendix 4. A higher breakdown voltage is encountered in SF_6 environments relative to air environments. This is due to the dielectric properties of SF_6. At a pressure of 5 Torr, 623 V and 75 μA are required in an SF_6 environment to initiate a microplasma while 434 V and 93 μA are required in air. In addition, more current flows through a microplasma in air. Applying 800 V to microplasmas at a pressure of 3 Torr results in a current of 2.2 mA in air, but only 500 μA in SF_6.

Increasing the power density of microplasmas in SF_6 increases the intensity of the emission lines. Figure A5.1 shows spectra produced in a SF_6 environment at 3 Torr. The less intense spectrum is produced by applying 800 V and 500 μA while the second spectrum is produced by applying 1,000 V and 3.8 mA. This ten-fold increase in applied power results in a 7.3 fold increase in the strongest N_2 emission line (337.1 nm). All line intensities increase by approximately the same factor. The increase in emission line intensity with increased power density is a direct result of increased ionization and can be used to measure characteristics such as electron density. It also expands microplasma, covering a larger cathode area.

Increasing the pressure of a SF_6 gaseous environment reduces the intensity of the spectral emissions. Figure A5.2 shows the spectra produced in SF_6 at 5 Torr and 10 Torr. Reducing the pressure from 10 Torr to 5 Torr causes the N_2 (337.1 nm), and all emission line intensities, to double. This is a result of the increasing mean free path length and resulting expansion of the microplasma as the pressure is reduced. As the pressure is increased, the glow becomes increasingly confined over the cathode.

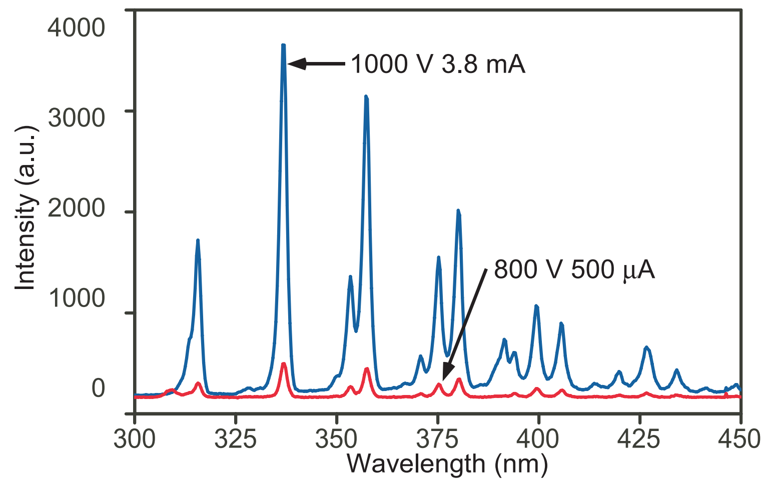

Figure A5.1: Emission spectra produced in SF_6 with different applied power. The stronger intensities are produced by applying 1,000 V and the weaker intensities are produced by applying 800 V.

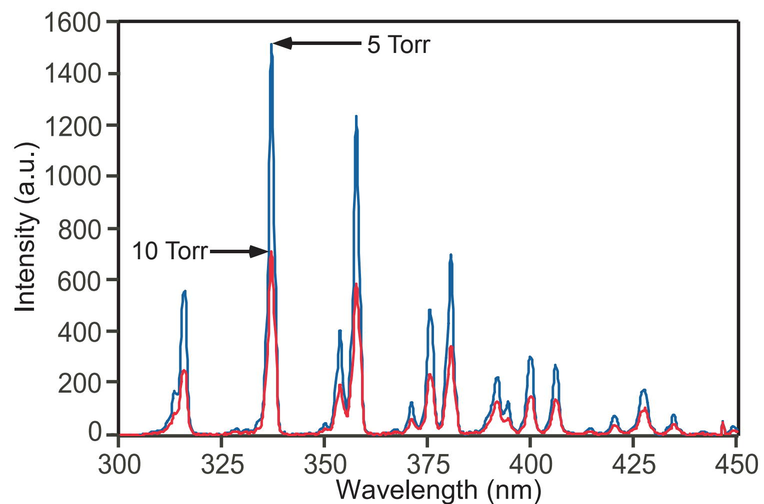

Figure A5.2: Emission spectra produced in SF_6 at different pressures. The stronger intensities are produced at 5 Torr and the weaker intensities are produced at 10 Torr.

APPENDIX 6

INVESTIGATION INTO THE GROWTH OF DOPED NANOWIRES USING MICRODISCHARGES

The current method of synthesizing doped SnO_2 nanowires for thin-film transistors (TFTs) does not allow selective growth in regions or patterns on a substrate without pre-growth patterning of the catalyst layer. Localized microdischarges may present a method of influencing growth through the local application of additional energy in the form of fast-moving ions and heat, as microplasmas have been shown to increase the gas temperature at the cathode by as much as 280˚C at 250 Torr [Kus05]. This would allow for post-wafer-processing growth control and pattern generation. This method could also potentially be used to "write" nanowires by scanning a microdischarge. The potential of this approach has been explored and will be described.

A6.1 INTRODUCTION

Nanowires are used in transparent TFTs as they show excellent optical transparency and high transistor performance in terms of transconductance, bias voltage range, and on/off ratio [Dat07]. The SnO_2 nanowire-based TFT approach offers a number of desirable properties such as low growth cost, high electron mobility, optical transparency, a low operation voltage, and may lead to large-scale applications of transparent electronics on diverse substrates. Nanowires are currently synthesized on a

substrate under conditions optimized to yield high-quality single-crystal materials, where the desired electronic and/or optoelectronic properties are defined by material composition, structure, and size. They are then transferred from the growth substrate to the device substrate and configured into a thin-film form. Conventional fabrication processes are used to in the final stages of the TFT device production.

The nanowire growth process involves the formation of compounds from gases and evaporated metals. In this instance, SnO_2 nanowires are formed from Au seed particles. Evaporated Sn and gaseous O_2 combine in the presence of the Au particles and solidify, forming SnO_2 nanowires. The Au particles continue to move on top of the growing SnO_2 nanowires, with liquid Sn remaining at the tip of the wires. As O_2 is added to the liquid Sn, the compound solidifies and increases the nanowire length.

Lightly doped nanowires are currently being produced by using a vapor transport synthesis and an *in-situ* doping process which shall be described. This process creates Sb-doped SnO_2 nanowires with resistivities as low as 4.1×10^{-4} Ω/cm, as well as Ta-doped SnO_2 nanowires [Dat07, Wan07]. Si substrates (100) are used for nanowire deposition. A catalyst-mediated vapor-liquid-solid (VLS) process, in which the Ta (or Sb) and Sn source materials are provided by a vapor transport method, is used to deposit the nanowires on the substrate. This VLS process involves creating high-purity (99.99%) powders containing the source materials (Sn:Ta = 95:5 in weight ratio) by mixing them thoroughly and loading them in an alumina boats. The Si growth substrates are sputter-deposited with a 5 nm Au film seed layer, serving as the catalyst in the VLS process, and are placed on top of the boat. The diameter of the Au particles determines the nanowire diameter. The boats are then loaded into an alumina reactor tube positioned inside a

horizontal tube furnace. During growth, the furnace is heated from room temperature to 900°C at a rate of 20°C/min under a flow of Ar gas (500 sccm) with an unknown trace amount of oxygen. The required growth time is 1 h at 900°C, followed by a cool down to room temperature at a rate of 5°C/min [Wan06, Dat07].

A6.2 SETUP

To examine the ability of microdischarges to influence nanowire growth, a system is used to create localized microdischarges during the VLS process on the surface of the seeded substrates. Si substrates with sputter-deposited 5 nm Au particles (5 / μm^2) are placed on a silicon nitride igniter (Igniters Direct™ Glo-stix™), which is capable of producing surface temperatures of 1,500ºC, for temperature control (Fig. A6.1). The igniter consists of a thin-film tungsten heater insulated in planar silicon nitride structure and heats an area 25 x 4.7 mm^2 to a constant temperature at a maximum rate of 100˚C/s. A quartz dielectric is placed between the Si and heater to prevent electrical contact. The Sn is contained in a crucible and heated, liquefying and evaporating it onto the adjacent substrate. K-type thermocouples are used to measure the temperature in the crucible and on the substrate. The pressure and gas composition ratio of He and O_2 is controlled by MKS® Mass-Flo® Series Mass Flow Controllers (Model #'s 1479A13CR1BM and 1479A21CR1BM) while the pressure is set by a two-stage rotary vane roughing pump (Oerlikon Leybold Vacuum Trivac D 16B), accompanying pressure controller (MKS® 600 Series), and external macroscale pressure transducer (MKS® Baratron® Capacitance Manometer model #627B23TDC1B). The microdischarge is created between a W anode and the Si/Au substrate, serving as the cathode. The substrate is used as the cathode, as it

is primarily heated in DC discharges due to the high energy ions which impinge upon it. A wire for electrical connectivity is soldered to the Si substrate and encased in ceramic epoxy, allowing conductivity even when the solder liquefies. An alternative set-up utilizes a Sn wire as the cathode electrode and the substrate as the anode, to directly sputter Sn onto the substrate. However, the low melting temperature of Sn causes the wire to melt at temperatures below the necessary substrate temperature, ≈850˚C.

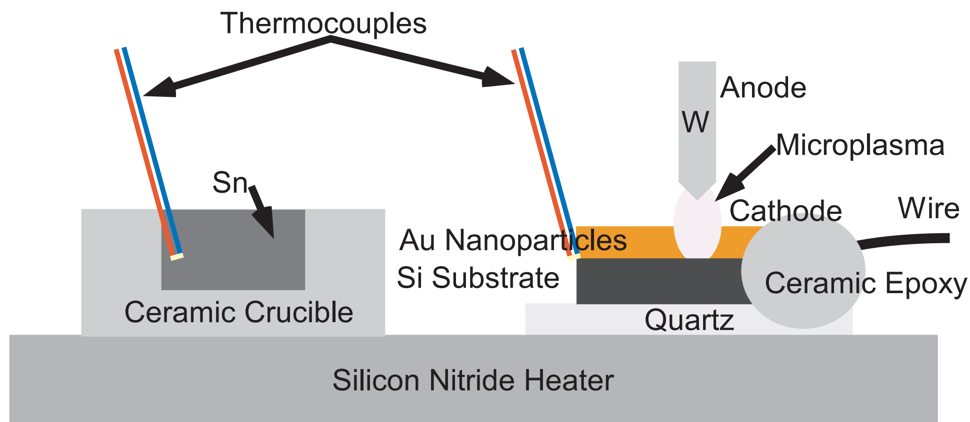

Figure A6.1: Layout with liquid tin in a ceramic crucible next to the substrate with a tungsten anode.

Numerous variables are considered, varied, and optimized when creating nanowires using this growth procedure. The substrate temperature needs to be controlled to prevent Sn from condensing. The Sn:O_2 ratio is also of importance, as an abundance of Sn results in condensed Sn on the substrate and an abundance of O_2 results of oxidation of the Sn liquid source. The O_2 density is controlled through the He:O_2 ratio, or N_2:O_2 ratio, depending on if helium or air is used as a filler gas in the previously described method. The amount of Sn is controlled through the Sn temperature, which effects evaporation and the amount of Sn deposited, and through the ambient pressure. The energy of the ions in the microdischarge and the confinement is controlled through

the applied power, discharge gap, and ambient pressure. The applied power is regulated through ballast resistors and the DC power supply. The procedural order in which O_2 is introduced, heat is applied to the crucible and substrates, and the microdischarge is initiated are also examined.

A6.3 RESULTS

Nanowires were grown using the described set-up and procedure. Certain process parameters resulted in nanowires over the entire substrate, while others resulted in localized regions of growth. A scanning electron microscope was used for imaging and Fig. A6.2 illustrates the nanowires which were approximately 50 nm in diameter, due to the 50 nm seed Au particles, and approximately 10 μm in length. Figure A6.3 illustrates a single nanowire and the initial Au seed at the tip. The entire substrate having regions with and without nanowire growth is shown in Fig. A6.4. An image of a region without growth is shown in Fig. A6.5, including the un-reacted Au particles.

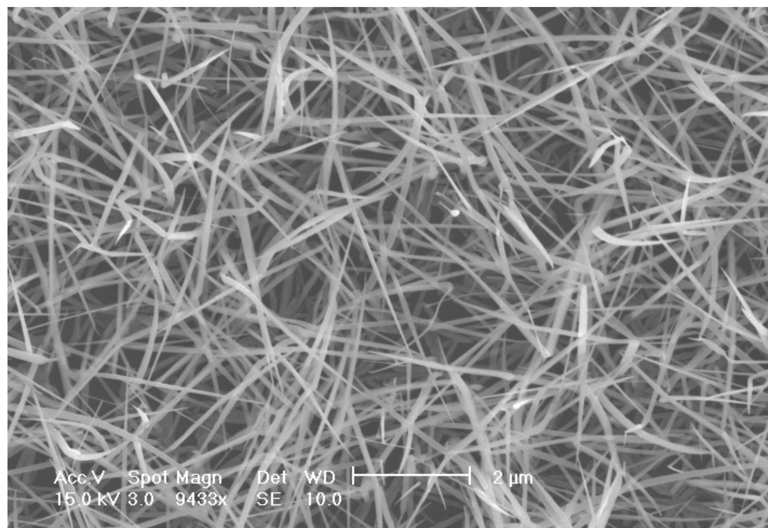

Figure A6.2: Nanowires, approximately 50 nm in diameter and 10 μm in length.

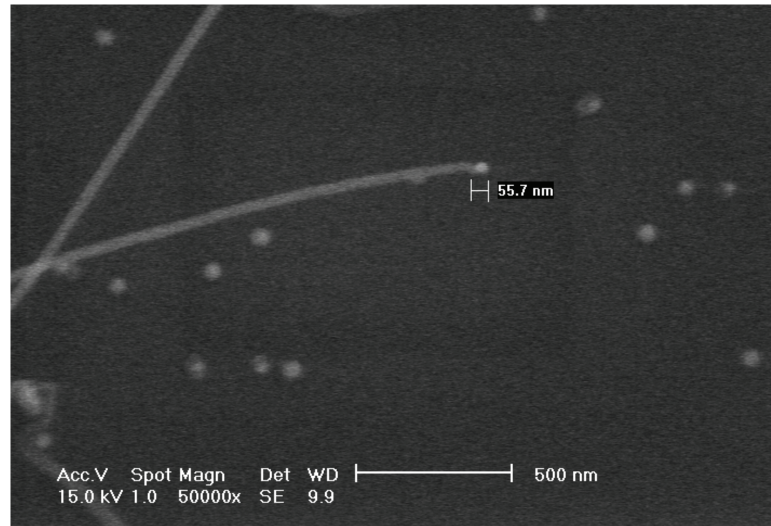

Figure A6.3: Gold particle at the tip of a nanowire, with additional particles in the background. The particle is measured as 55.7 nm in diameter.

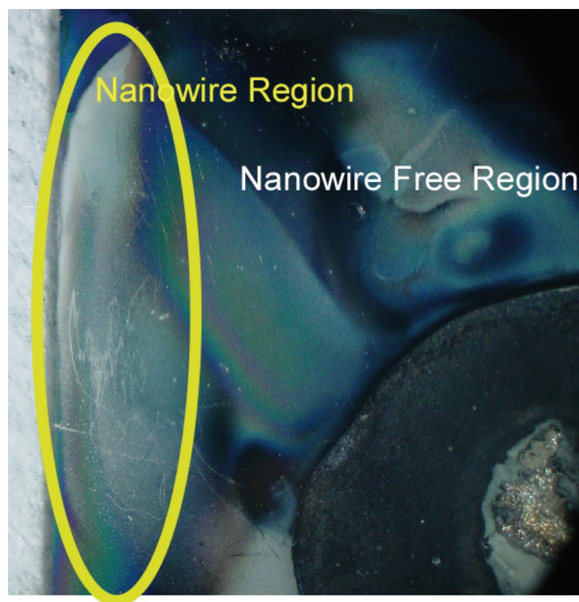

Figure A6.4: Silicon substrate showing regions with and without nanowire growth.

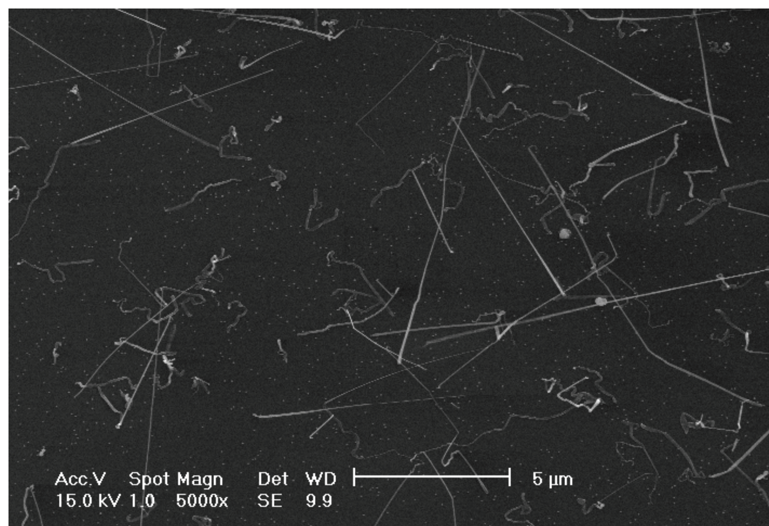

Figure A6.5: Region of low nanowire growth, demonstrating sparse nanowire formation.

The processing parameters were adjusted to determine optimal parameters for growth and the effect of each on the overall process. Table A6.1 outlines the ranges of examined parameters; the parameters used which resulted in nanowire formation, and the parameter set which produced the nanowires most consistently. These parameters were examined individually. The substrate temperature was required to exceed 830˚C to form nanowires. Below this, solid Sn or no nanowire formation was observed. The pressure determined the nanowire coverage of the substrate. At lower pressures, $\approx < 7$ Torr, the entire substrate was covered while at $\approx > 50$ Torr, only select regions were covered. This potentially is a result of heat gradients across the substrate at higher pressures. The O_2:He ratio was also of importance. With high O_2:He content, close to 1:1, nanowires were not formed as the Sn source was oxidized which limited evaporation. An environment of 5-10% O_2 was sufficient to produce nanowires. The temperature ramping time had little effect on the growth.

Table A6.1: Parameters varied to determine the optimum environment for nanowire growth.

Parameter	Range Tested	Range Producing Nanowires	Optimized
Substrate Temp (˚C)	380 – 900	830 – 900	830
Sn Temp (˚C)	150 – 800	715 – 780	780
Pressure (Torr)	5 – 100	7 – 50	50
O_2:He Ratio	1:19 – 1:1	1:19 – 1:4	1:9
O_2 Flow Rate (sccm)	5 – 100	5 – 20	10
Total Flow Rate (sccm)	100 – 200	100	100
Microdischarge Voltage (V)	500 – 2,000	500 – 1,000	500
Microplasma Current (mA)	0.27 – 6	0.27 – 6	5
Time at Max Temp (min)	10	10	10
Ramping Time (min)	1 – 10	1 – 6	1

The effect of localized microdischarges on nanowire growth was examined, but little correlation was found between the use of microdischarges and the produced nanowires. The microdischarges were confined to localized regions, 50 μm to 1 cm in diameter, which varied in size with pressure, the applied power, and the discharge gap between the substrate and the tungsten anode. Below 5 Torr, the microdischarges covered large regions of the substrate while above 50 Torr, the discharges exhibited arc-like characteristics. Using localized high-power discharges actually prevented nanowire growth in regions, as shown in Fig. A6.6.

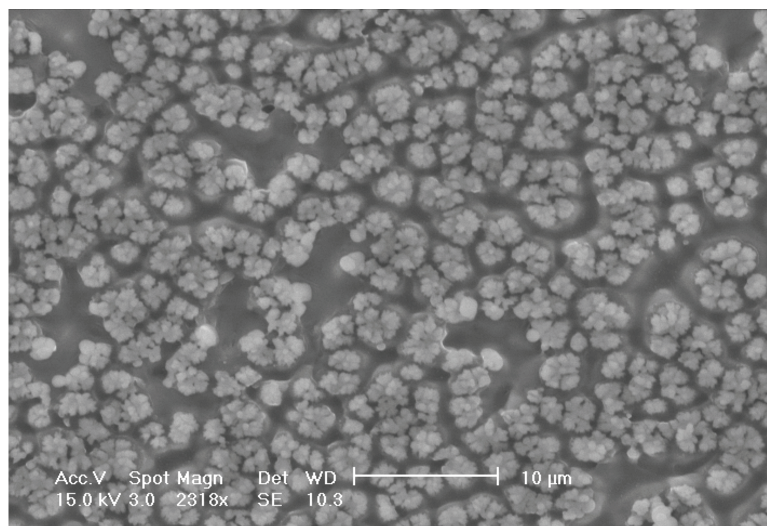

Figure A6.6: Resulting substrate exposed to a microdischarge with a high power density.

The substrate temperature appeared to be the most important parameter effecting nanowire growth. It was likely that nanowires selectively grew on the edges of the substrates and underneath the epoxy covering the substrate due to increased heating/heat conduction in these regions. Control substrates without epoxy were placed in the same environment, proximal to the epoxy covered substrates, and did not demonstrate nanowire formation while nanowires continued to form underneath the epoxy on the original substrate.

A6.4 CONCLUSIONS

Further investigation is required to determine the potential of localized microdischarges to assist nanowire growth. While DC microdischarges have been modeled and found to increase gas temperature at 250 Torr and 23˚C by 280˚C, with ions at 320˚C above ambient, the heating may be less pronounced at 5-50 Torr due to gas rarefaction or the high substrate temperature of 830˚C. If the precise temperature at which nanowires are formed on the substrate is determined, holding the substrate at this

temperature would allow a slight temperature increase caused by a microdischarge to locally heat a region to a suitable temperature for growth. This fabrication method does however suggest that nanowires can be selectively grown using locally heated regions.

BIBLIOGRAPHY

BIBLIOGRAPHY

[Abe02] D.C. Abeysinghe, S. Dasgupta, H.E. Jackson, and J.T. Boyd, "Novel MEMS pressure and temperature sensors fabricated on optical fibers," *Journal of Micromechanics and Microengineering*, 12(3), pp. 229-235, May 2002.

[Aim04] M. F. Aimi, M. P. Rao, N. C. MacDonald, A. S. Zuruzi, and D. P. Bothman, "High-aspect-ratio bulk micromachining of titanium," *Nature Materials*, 3(2), pp. 103-105, Feb. 2004.

[Air75] D.R. Airey, P.H. Richards, and J.D. Swift, "Time-resolved radial temperature profiles for 10kA SF_6 Arcs," *Journal of Physics D (Applied Physics)*, 8(16), pp. 1982-1993, Nov. 1975.

[Alb00] J.N. Albright and D.S. Dreesen, "Microhole technology lowers reservoir exploration, characterization costs," *Oil and Gas Journal*, 98(2) pp. 39-41, Jan. 2000.

[All03] D. M. Allen, "The state of the art of photochemical machining at the start of the twenty-first century," *Proceedings of the Institution of Mechanical Engineers Part B: Journal of Engineering Manufacturing*, 217(5), pp. 643-650, 2003.

[Ark05] V.I. Arkhipenko, A.A. Kirillov, L.V. Simonchik, and S.M. Zgirouski, "Influence of the nitrogen-helium mixture ration on parameters of a self-sustained normal dc atmospheric pressure glow discharge," *Plasma Sources Science and Technology*, 14(4), pp. 757-765, Nov. 2005.

[Arn04] T. Arnold, S. Grabovski, A. Schindler, and H.-E. Wagner, "Spatially resolved emission spectroscopic investigation of microwave-induced reactive low-power plasma jets," *Plasma Sources Science and Technology*, 13(2), pp. 309-314, May 2004.

[Asg00] M. Asgar Ali, K.K. Irikura, and Yong-Ki Kim, "Electron-impact total ionization cross section of $SF_x(x = 1\text{-}5)$," *International Journal of Mass Spectrometry*, 201(1-3), pp. 187-195, July 2000.

[Bar99] E. Barborini, P. Piseri, and P. Milani, "Pulsed microplasma source of high intensity supersonic carbon cluster beams," *Journal of Physics D (Applied Physics)*, 32(21), pp. L105-L109, Nov. 1999.

[Bec04] K.H. Becker, U. Kogelschatz, K.H. Schoenbach, and R.J. Barker, *Non-equilibrium Air Plasmas at Atmospheric Pressure. Chapter 6, DC and Low-frequency Air Plasma Sources* Bristol, U.K.: IOP Publishing, 2004.

[Ber87] S. Berg, H-O. Blom, T. Larsson, and C. Nender, "Modeling of reactive sputtering of compound materials," *Journal of Vacuum Science and Technology A (Vacuum, Surfaces, and Films)*, 5(2), pp. 202-207, March-April 1987.

[Ber88] S. Berg, T. Larsson, C. Nender, and H-O. Blom, "Predicting thin-film stoichiometry in reactive sputtering," *Journal of Applied Physics*, 63(3), pp. 887-891, Feb. 1988.

[Bes02] F.G. Bessoth, O.P. Naji, J. C. T. Eijkel, and A. Manz, "Towards an on-chip gas chromatograph: The development of a gas injector and a dc plasma emission detector," *Journal of Analytical Atomic Spectrometry*, 17(8), pp. 794-799, Aug. 2002.

[Bil67] D.G. Bills, "Electrostatic getter-ion-pump design," *Journal of Vacuum Science and Technology*, 4(4), pp. 149-155, July 1967.

[Bit66] D. L. Bitzer and H. G. Slottow, "The plasma display panel- a digitally addressable display with inherent memory," *Fall Joint Computer Conference*, San Francisco, CA, 1966, pp. 514-547.

[Bla87a] K.A. Blanks, A.E. Tabor, and K. Becker, "Absolute cross sections for fluorine 3*p* ->3*s* line emissions following single electron impact of NF_3, CF_4, and SF_4," *Journal of Chemical Physics*, 86(9), pp. 4871-4875, May 1987.

[Bla87b] K.A. Blanks and K. Becker, "Optical emissions in the wavelength region 2000-6000 A produced by electron impact dissociation of NF_3, CF_4, and SF_6," *Journal of Physics B (Atomic and Molecular Physics)*, 20(22), pp. 6157-6163, Nov. 1987.

[Boe05] J.P. Boeuf, L.C. Pitchford, and K.H. Schoenbach, "Predicted properties of microhollow cathode discharges in xenon," *Applied Physics Letters*, pp. 071501(1-3), 86(7), Feb. 2005.

[Bra68] R.S. Braman and A. Dynako "Direct current discharge spectral emission-type detector," *Analytical Chemistry*, 40(1), pp. 95-106, Jan. 1968.

[Bro01] I. Brodie, "The Fowler Nordheim equation revisited," *14th IEEE International Vacuum Microelectronics* Conference, Davis, California, Aug. 2001, pp. 69-70.

[Bro02] J.A.C. Broekaert, "The development of microplasmas for spectrochemical analysis," *Analytical and Bioanalytical* Chemistry, 374(2), pp. 182-187, 2002.

[Bou05] A. Bouzid, E.M. Bourim, M. Gabbay, and G. Fantozzi, "PZT phase diagram determination by measurement of elastic moduli," *Journal of the European Ceramic Society*, 25(13), pp. 3213-3221, Aug. 2005.

[Cai02] Q.–Y. Cai and E.T Zellers, "Dual-chemiresistor GC detector employing monolayer protected metal nanocluster interfaces," *Analytical Chemistry*, 74(14), pp. 3533-3539, July 2002.

[Cas91] A.M. Casanovas, J. Casanovas, V. Dubroca, F. Lagarde, and A. Belarbi, "Optical detection of corona discharges in SF_6, CF_4, and SO_2 under DC and 50-Hz AC voltages," *Journal of Applied Physics*, 70(3), pp. 1220-1226, Aug. 1991.

[Cav07] *Caviton, Inc. Microdischarge Technology*, http://www.caviton.com/technology.htm

[Che04] R. Chellini, "Pressure sensor for engine intake ports," *Diesel Progress International Edition*, 23(5), pp. 61, Sept./Oct. 2004.

[Che08] L. Chevallier, E. Di Bartolomeo, M. L. Grilli, and E. Traversa, "High temperature detection of CO/HCs gases by non-Nernstian planar sensors using Nb_2O_5 electrode," *Sensors and Actuators: B. Chemical*, 130(1), pp. 514-519, March 2008.

[Cho92] S.T. Cho, K. Najafi, C.E. Lowman, and K. D. Wise, "An ultrasensitive silicon pressure-based microflow sensor," *IEEE Transactions on Electron Devices*, 39(4), pp. 825-835, April 1992.

[Cho07] J. Choi, F. Iza, J. K. Lee, and C. Ryu, "Electron and ion kinetics in a DC microplasma at atmospheric pressure," *Transactions on Plasma Science*, 35(5), pp. 1274-1278, Oct. 2007.

[Cho08] J. Choi, K. Matsuo, H. Yoshida, T. Namihira, S. Katsuki, and H. Akiyama, "Characterization of a dc atmospheric pressure normal glow discharge," *Plasma Sources Science and Technology*, 14(4), pp. 700-711, Nov. 2005.

[Cob58] J.D. Cobine, *Gaseous Conductors Theory and Engineering Applications*, New York, New York: Dover Publications Inc., 1958.

[Col94] B.F. Coll and M. Chhowalla, "Modelization of reaction kinetics of nitrogen and titanium during TiN arc deposition," *Surface and Coating Technology*, 68-69, pp. 131-140, Dec. 1994.

[Col95] G.A. Cole, M.A Abu-Ali, E.L. Colling, H.I. Halpern, W.J. Carrigan, G.R. Savage, R.J. Scolaro, and S.H. Al-Sharidi, "Petroleum geochemistry of the Midyan and Jaizan basins of the Red Sea, Saudi Arabia," *Marine and Petroleum Geology,* 12(6) pp. 597-614, 1995.

[Cor07] *Corning Incorporated Pyrex® Brand 7740 Glass – Low Expansion Borosilicate Type 1 Glass*, http://www.corning.com/Lifesciences/technical_information/techDocs/descglasslabware.asp

[Cov04] J.A. Covington. J.W. Gardner, P.N. Bartlett, and C. –S. Toh, "Conductive polymer gate FET devices for vapour sensing," *IEE Proceedings: Circuits, Devices and Systems*, 151(4), pp. 326-334, Aug. 2004.

[d'Ag81] R. d'Agostino and D.L. Flamm, "Plasma etching of Si and SiO_2 in SF_6-O_2 mixtures," *Journal of Applied Physics*, 52(1), pp. 162-167, Jan. 1981.

[Dat07] E. N. Dattoli, Q. Wan, W. Guo, Y. Chen, X. Pan, and W. Lu, "Fully transparent thin-film transistor devices based on SnO_2 nanowires" *Nano Letters*, 7(8), pp. 2463-2469, May 2007.

[Dav74] R.C. Davidson, *Theory of Non-Neutral Plasmas*, Reading, Massachusetts: W.A. Benjamin, 1974.

[Dav05] C.E. Davis, C.K. Ho, R.C. Hughes, and M.L. Thomas, "Enhanced detection of m-xylene using a preconcentrator with a chemical sensor," *Sensors and Actuators B (Chemical)*, 104(2), pp. 207-216, Jan. 2005.

[Den67] D.R. Denison, "Performance of a new electrostatic getter-ion pump," *Journal of Vacuum Science and Technology*, 4(4), pp 156-162, July 1967.

[Dom97] K. Domansky, J. Li, and J. Janata, "Selective doping of chemically sensitive layers on a multisensing chip," *Journal of the Electrochemical Society*, 144(4), pp. 75-78, April 1997.

[Dou65] R.A. Douglas, J. Zabritski, and R.G. Herb, "Orbitron vacuum pump," *Review of Scientific Instruments*, 36(1), pp. 1-6, Jan. 1965.

[Ede90] C. Edelmann, "Measurement of high pressures in the vacuum range with the help of hot filament ionization gauges," *Vaccum*, 41(7-9), pp. 2006-2008, 1990.

[Ede03] J.G. Eden, S. –J. Park, N.P. Ostrom, S.T. McCain, C.J. Wagner, B.A. Vojak, J. Chen, C. Liu, P. von Allmen, F. Zenhausern, D.J. Sadler, C. Jensen, D.L. Wilcox, and J. J. Ewing, "Microplasma devices fabricated in silicon, ceramic, and metal/polymer structures: arrays, emitters and photodetectors," *Journal of Physics D (Applied Physics)*, 36(23), pp. 2869-2877, Dec. 2003.

[Ede05] J.G. Eden and S.-J. Park, " Microcavity plasma devices and arrays: A new realm of plasma physics and photonic applications," *Plasma Physics and Controlled Fusion*, 47(12), pp. B83-B92, Dec. 2005.

[Eic03] M. Eickhoff, J. Schalwig, G. Steinhoff, O. Weidemann, L. Gorgens, R. Neuberger, M. Hermann, B. Baur, G. Muller, O. Ambacher, and M. Stutzmann, "Electronics and sensors based on pyroelectric Al-GaN/GaN heterostructures: Part B: Sensor applications," *Physica Status Solidi C: Conferences*, 0(6) pp. 1908-1918, 2003.

[Eic03a] G.A. Eiceman, A. Tarassov, P.A. Funk, S.E. Hughs, E.G. Nazarov, and R.A. Miller, "Discrimination of combustion fuel sources using gas chromatography-planar field asymmetric-waveform ion mobility spectrometry," *Journal of Separation Science*, 26(6-7), pp. 585-593, May 2003.

[Eij00] J.C.T Eijkel, H. Stoeri, and A. Manz "An atmospheric pressure dc glow discharge on a microchip and its application as a molecular detector," *Journal of Analytical Atomic Spectrometry,* 15(3), pp. 297-300, March 2000.

[Erk95] A.I. Erko, L.A. Panchenko, S.A. Pikuz, A.R. Mingaleev, V.M. Romanova, T.A. Shelkovenko, A. Ya Faenov, B.A. Bryunetkin, T.A. Pikuz, and I. Y. Skobelev, "Microplasma object imaging spectroscopy by using zone plate surface structure on mica crystal," *Review of Scientific Instruments,* 66(2), pp. 1047-1049, Feb. 1995.

[Eun08] C.K. Eun, C. Wilson, and Y.B. Gianchandani, "A bulk silicon micromachined structure for gas microdischarge-based detection of beta-particles," *Journal for Micromechanics and Microengineering*, 18(9), pp. 095007 (10 pp.), Sep. 2008.

[Fan99] M. Fang, K. Vetelino, M. Rothery, J. Hines, and G.C. Frye, "Detection of organic chemicals by SAW sensor array," *Sensors and Actuators B (Chemical)*, 56(1), pp. 155-157, June 1999 .

[Far1839] M. Faraday, *Experimental Researches in Electricity, vol. I*, London, U.K.: Taylor and Francis, 1839.

[Far1844] M. Faraday, *Experimental Researches in Electricity, vol. II*, London, U.K.: Taylor and Francis, 1844.

[Far1855] M. Faraday, *Experimental Researches in Electricity, vol. III*, London, U.K.: Taylor and Francis, 1855.

[Fie04] R. Fielder, K. Stingson-Bagby, and M. Palmer, “State of the art in high-temperature fiber optic sensors,” *Proceedings of the SPIE - The International Society for Optical Engineering*, Philadelphia, PA, Dec. 2004, pp. 60-69.

[Fis01] K. Fischer, B. Chauduri, S. McNamara, H. Guckel, and Y.B. Gianchandani, “A latching, bistable optical fiber switch combining LIGA technology with micromachined permanent magnets,” *IEEE International Conference on Solid-State Sensors and Actuators (Transducers ’01),* Munich, Germany, June 2001, pp. 1340-3.

[Fle91] M. Fleischer and H. Meixner, “Gallium oxide thin films: A new material for high temperature oxygen sensors,” *Sensors and Actuators B (Chemical)*, B4(3-4), pp. 437-441, June 1991.

[Flo90] B. A. Flowers, R. A. Marsh, J. C. Haraf, and A. D. Lepage, U.S. Patent 4,926,335 (May 15, 1990).

[Foe06] R. Foest, M. Schmidt, and K. Becker, “Microplasmas, an emerging field of low-temperature plasma science and technology,” *International Journal of Mass Spectrometry*, 248(3), pp. 87-102, Feb. 2006.

[Fra03] J. Franzke, K. Kunze, M. Milcea, and K. Niemax, “Microplasmas for an-anlytical spectrometry,” *Journal of Analytical Atomic Spectrometry*, 18(7), pp. 802-807, July 2003.

[Fri06] S. Fricke, A. Friedberg, T. Ziemann, E. Rose, G. Muller, D. Telitschkin, S. Ziegenhagen, H. Seidel, and U. Schmidt, “High temperature (800°C) MEMS pressure sensor development including reusable packaging for rocket engine applications,” *Micro-Nano-Technology for Aerospace Applications, CANEUS2006*, Toulouse, France, Aug. – Sep. 2006, pp. 5p.

[Gar99] J. W. Gardner and P. N. Bartlett, *Electronic noses: principles and applications*, Oxford: Oxford University Press, 1999.

[Gib00] V.I. Gibalov and G.J. Pietsch, “The development of dielectric barrier discharges in gas gaps and on surfaces,” *Journal of Physics D (Applied Physics)*, 33(20) pp. 2618-2636, Oct. 2000.

[Gio89] E. Giorgi, B. Ferrario, and C. Boffito, “High-porosity coated getter,” *Journal of Vacuum Science and Technology A (Vacuum, Surfaces, and Films)*, 7(2), pp. 218-229, March-April 1989.

[Go06] D.B. Go, S.V. Garimella, and T.S. Fisher, "Numerical simulation of microscale ionic wind for local cooling enhancement," *Intersociety Conference on Thermal and Thermomechanical Phenomena and Emerging Technologies in Electronic System*, San Diego, CA, May – June 2006, pp. 45-53.

[Gop96] W. Gopel, "Ultimate limits in the miniaturization of chemical sensors," *Sensors and Actuators A (Physical)*, 56(1-2), pp. 83-102, Aug. 1996.

[Got99] J.R. Gottschalk, O. Shvydky, A.D. Compaan, C.E. Theodosiou, and W. Williamson Jr., "Time-resolved electrical and optical measurements in a plasma display panel," *Transactions on Plasma Science*, 27(3), pp. 772-777, June 1999.

[Gro92] R. Gross, B. Platzer, E. Leitner, A. Schalk, H. Sinabell, H. Zach, and G. Knapi, "Atomic emission gas chromatographic detection. Chemical and spectral interferences in the stabilized capacitive plasma (SCP)", *Spectrochimica Acta, Part B (Atomic Spectroscopy),* 47(1), pp. 95-106, Jan. 1992.

[Guc88] H. Guckel and D.W. Burns, U.S. Patent 4,744,863 (May 17, 1988).

[Gui03] Ph. Guillot, Ph. Belenguer, L. Therese, V. Lavoine, and H. Chollet, "Secondary electron emission coefficients of standard samples for GDOES," *Surface and Interface Analysis*, 35(7), pp. 590-592, July 2003.

[Guo08] S. Guo, H. Eriksen, K. Childress, A. Fink, and M. Hoffman, "High temperature high accuracy piezoresistive pressure sensor based on smart-cut SOI," *IEEE International Conference on Micro Electro Mechanical Systems (MEMS 08)*, Tucson, AZ, Jan. 2008, pp. 892-895.

[Hag56] H.D. Hagstrum, "Auger ejection of electrons from tungsten by noble gas ions," *Physical Review*, 104(2), pp. 317-318, Oct. 1956.

[Hak06] M. Gad-el-Hak, Ed., *The MEMS Handbook, Second Edition*., Boca Raton, FL: CRC Press, 2006.

[Hal91] H.J. Halama and Y. Guo, "Nonevaporable getter investigation at the National Synchrotron light source," *Journal of Vacuum Science and Technology A (Vacuum, Surfaces, and Films)*, 9 (3), pp. 2070-2073, May-June 1991.

[Har69] G. R. Harrison, *Massachusetts Institute of Technology Wavelength Tables*, Cambridge, MA, M.I.T. Press, 1969.

[Har98] K.T. Hartinger, L. Pierre, and C. Cahen, "Combination of emission spectroscopy and fast imagery to characterize high-voltage SF_6 circuit breakers, "*Journal of Physics D (Applied Physics)*, 31(19), pp. 2566-2576, Oct. 1998.

[Hen94] H. Henmi, S. Shoji, Y. Shoji, K. Yoshimi, and M. Esashi, “Vacuum packaging for microsensors by glass-silicon anodic bonding,” *Sensors and Actuators A (Physical)*, 43(1-3) pp. 243-248, May 1994.

[Her50] G. Herzberg, *Molecular Spectra and Molecular Structure I. Spectra of Diatomic Molecules 2d ed.*, New York, New York: D. Van Nostrand Company Inc., 1950.

[Her66] G. Herzberg, *Molecular Spectra and Molecular Structure III. Electronic Spectra and Electronic Structure of Polyatomic Molecules*, New York, New York: D. Van Nostrand Company, Inc., 1966.

[Hie00] A. Hierlemann, D. Lange, C. Hagleitner, N. Kerness, A. Koll, O. Brand, and H. Baltes, “Application-specific sensor systems based on CMOS chemical microsensors,” *Sensors and Actuators B (Chemical)*, 70(1-3), pp. 2-11, Nov. 2000.

[Hob00] J.P. Hobson and D.B. Salzman, “Review of pumping by thermal molecular pressure,” *Journal of Vacuum Science and Technology A (Vacuum, Surfaces, and Films)*, 18(4), 1758-1765, July 2000.

[Hoe01] U. Hoefer, J. Frank, and M. Fleischer, “High temperature Ga_2-O_3-gas sensors and SnO_2-gas sensors: a comparison,” *Sensors and Actuators B (Chemical)*, 78(1-3), pp. 6-11, Aug. 2001.

[Hol59] L. Holland, “Theory and design of getter-ion pumps,” *Journal of Scientific Instruments*, 36(3), pp. 105-116, March 1959.

[Hon08] Y.J. Hong, S. M. Lee, G. C. Kim, and J. K. Lee, “Modeling high-pressure microplasmas: comparison of fluid modeling and particle-in-cell Monte Carlo collision modeling,” *Plasma Processes and Polymers*, 5(6), pp. 583-592, Aug. 2008.

[Hop00] J.A. Hopwood, “A microfabricated inductively coupled plasma generator,” *Journal of Microelectromechanical Systems*, 9(3), pp. 309-313, Sep. 2000.

[Hua98] W.N. Huang, K.Y. Tong, and P.W. Chan, “A LED based on porous polycrystalline silicon,” *Materials and Devices for Silicon-Based Optoelectronics Symposium Mater Res. Soc.,* Boston, MA, Dec. 1997, pp. 163-168.

[Hub79] K.P. Huber and G. Herzberg, *Molecular Spectra and Molecular Structure IV. Constants of Diatomic Molecules*, New York, New York: Van Nostrand Reinhold Company, 1979.

[Hun97] A. Hunt, "Micro-sensor applications in petroleum drilling and completion," *IEE Colloquium on Microengineering and the Petrochemical Industry*, London, U.K., Jan. 1997, pp. 2/1-2/3.

[Ito08] T. Ito, K. Kobayashi, S. Hamaguchi, and M.A. Cappelli, "Magnetized microdischarge plasma generation at low pressure," *Thin Solid Films*, 516(19), pp. 6668-6672, Aug. 2008.

[Iza02] F. Iza and J. Hopwood, "Influence of operating frequency and coupling coefficient on the efficiency of microfabricated inductively coupled plasma sources," *Plasma Sources Science and Technology*, 11(3), pp. 229-235, Aug. 2002.

[Jan03] J. Janata, "Electrochemical microsensors," *Proceedings of the IEEE*, 91(6), pp. 864-869, June 2003.

[Jen02] G. Jenkins and A. Manz, "A miniaturized glow discharge applied for optical emission detection in aqueous analytes," J*ournal of Micromechanics and Microengineering*, 12(5), pp. N19-N22, Sep. 2002.

[Kar04] V. Karanassios, "Microplasmas for chemical analysis: analytical tools or research toys?," *Spectrochimica Acta, Part B (Atomic Spectroscopy)*, 59(7), pp. 909-928, July 2004.

[Kim90] L.C. Kimerling, "The influence of electronic excitation on the performance and reliability of semiconductor devices," *Reviews of Solid State Science*, 4(2-3), pp. 335-354, June-Sep. 1990.

[Kim95] Y. Kim and D.P. Neikirk, "Micromachined Fabry-Perot cavity pressure transducer," *Photonics Technology Letters*, 7(12), pp. 1471-1473, Dec. 1995.

[Kim01] C.K. Kim, J.H. Lee, S.M. Choi, I.H. Noh, H.R. Kim, N. I Cho, C. Hong, and G.E. Jang, "Pd- and Pt-SiC schottky diodes for detection of H_2 and CH_4 at high temperature," *Sensors and Actuators B (Chemical)*, B77(1-2), pp. 455-462, June 2001.

[Kon92] M. Konuma, *Film Deposition by Plasma Techniques*, New York, New York: Springer, 1992.

[Koo05] H. W.P. Koops, "Proposal of a miniature orbitron pump for MEMS applications," *Proceedings of the SPIE - The International Society for Optical Engineering*, Sevilla, Spain, May 2005, pp. 38-42.

[Koz96] F. Kozlowski, B. Huber, P. Steiner, and W. Lang, "Generating a microplasma with porous silicon," *Sensors and Actuators A (Physical)*, 53(1-3), pp. 284-287, May 1996.

[Kud81] J. Kudzia and W. Stowko, “A spherical high-pressure ion gauge,” *Vacuum*, 31(1), pp. 9-13, Jan. 1981.

[Kum93] S. Kumar and P.K. Ghosh, “Ion kinetic energy distribution in nitrogen d.c. discharge,” *International Journal of Mass Spectrometry and Ion Processes*, 127, pp. 105-109, Aug. 1993.

[Kun03] K. Kunze, M. Miclea, J. Franzke, and K. Niemax, “The dielectric barrier discharge as a detector for gas chromatography,” *Spectrochimica Acta, Part B(Atomic Spectroscopy)*, 58(8), pp. 1435-1443, Aug. 2003.

[Kur04] P. Kurunczi, N. Abramzon, M. Figus, and K. Becker, “Measurement of rotational temperatures in high-pressure microhollow cathode (MHC) and capillary plasma electrode (CPE) discharge,” *Acta Physica Slovaca*, 54(2), pp. 115-124, April 2004.

[Kus05] M.J. Kushner, “Modeling of microdischarge devices: plasma and gas dynamics,” *Journal of Physics D (Applied Physics)*, 38(11), pp. 1633-1643, June 2005.

[Lan29] L. Tonks and I. Langmuir, “Oscillations in ionized gases,” *Physical Review*, 33, pp. 195-210, Feb. 1929.

[Lea63] Lear Siegler Inc., "Development of experimental gas discharge display," Quarterly Progress Reports :#:2, 3, 4, 5, 6, and 7, Contract NOBSR-89201 Bu Ships, Aug. 1963-June 1965.

[Lew89] M.A. Lewis, D.A. Glocker, and J. Jorne, “Measurements of secondary electron emission in reactive sputtering of aluminum and titanium nitride,” *Journal of Vacuum Science and Technology A (Vacuum, Surfaces, and Films)*, 7(3), pp. 1019-1024, May-June 1989.

[Li05] C. Li and J. Hsieh, “Stability analysis of reactive sputtering process with variable sticking coefficients,” *Thin Solid Films*, 475(1-2), pp. 102-108, March 2005.

[Li07] C. Li, J. Huang, R. Lin, D. Lii, and C. Chen, “Performance characterization of nonevaporable porous Ti getter films,” *Journal of Vacuum Science and Technology A (Vacuum, Surfaces, and Films)*, 25 (5), pp. 1373-1380, 2007.

[Li07b] T. Li, Z. Wang, Q. Wang, X. Wei, B. Xu, W. Hao, F. Meng, and S. Dong, “High pressure and temperature sensing for the downhole applications,” *Proceedings of the SPIE - The International Society for Optical Engineering*, 6757, pp. 1-7, Sep. 2007.

[Lie94] M. A. Lieberman and A. J. Lichtenburg, *Principles of Plasma Discharges and Materials Processing*, New York, New York: John Wiley and Sons, 1994.

[Lid49] K. Liden, “The arc spectrum of fluorine,” *Arkiv for Fyski*, 1, pp. 229-265, 1949.

[Mad02] M. Madou, *Fundamentals of Microfabrication: The Science of Miniaturization, 2nd ed.*, Boca Raton, FL: CRC Press, 2002.

[Mar05] S.M. Martin, F.H. Gebara, B.J. Larivee, and R.B. Brown, “A CMOS-integrated microinstrument for trace detection of heavy metals,” *Journal of Solid State Circuits*, 40 (12), pp. 2777-2785, Dec. 2005.

[Mas05] N. Masoud, K. Martus, and K. Becker, “VUV emission from a cylindrical dielectric barrier discharge in Ar and in Ar/N_2 and Ar/air mixtures,” *Journal of Physics D (Applied Physics)*, 38(11), pp. 1674-1673, June 2005.

[Mat01] D.M. Mattox, “Reactive sputter deposition,” *Platting and Surface Finishing*, 88(1), pp. 74-77, Jan. 2001.

[Mat03] D. M. Mattox, *The Foundations of Vacuum Coating Technology*, Bracknell, U.K.: Noyes Publications, 2003.

[May56] F. B. Maynard, J. Carluccio, and W. G. Poelstra, "Grid switched gas tube for display presentation," *Electronics*, 29(8), pp. 154-156, Aug. 1956.

[Mcl60] N. McLoughlin, D. Reamer, and A. W. Turner, “The digitron: A cold-cathode character display tube," *Electronic Engineering*, 32, pp. 140-143, March 1960.

[McN05] S. McNamara and Y.B. Gianchandani, “On-chip vacuum generated by a micromachined knudsen pump,” *Journal of Microelectromechanical Systems,* 14(4), pp. 741-746, Aug. 2005.

[Mic01] M. Miclea, K. Kunze, G. Musa, J. Franzke, and K. Niemax, “Dielectric barrier discharge - a powerful microchip plasma for diode laser spectrometry,” *Spectrochimica Acta, Part B(Atomic Spectroscopy)*, 56(1), pp. 37-43, Jan. 2001.

[Mil01] R. A. Miller, E. G. Nazarov, G. A. Eiceman, and A. T. King, “A MEMS radio-frequency ion mobility spectrometer for chemical vapor detection*,” Sensors and Actuators A (Physical)*, 90(3), pp. 301–312, July 2001.

[Min03] O.B. Minayeya and J.A. Hopwood, “Microfabricated inductively coupled plasma-on-a-chip for molecular SO_2 detection: A comparison between global model and optical emission spectrometry," J*ournal of Analytical Atomic Spectrometry,* 18(8) pp. 856-863, Aug. 2003.

[Mit06a] B. Mitra, C.G. Wilson, L. Que, P. Selvaganapathy, and Y.B. Gianchandani, "Microfluidic discharge-based optical sources for detection of biochemicals," *Lab-on-a-Chip*, 6(1), pp. 60-65, Dec. 2006.

[Mit06b] J. Mitchell, G.R. Lahiji, and K. Najafi, "Long-term reliability, burn-in and analysis of outgassing in Au-Si Eutectic wafer-level vacuum packages," *Solid-State Sensors and Actuators Workshop (Hilton Head '06)*, Hilton Head Island, South Carolina, June 2006, pp. 376-379.

[Mit08a] B. Mitra and Y.B. Gianchandani, "The detection of chemical vapors in air using optical emission spectroscopy of pulsed microdischarges from two and three electrode microstructrues," *IEEE Sensors Journal*, 8(8), pp. 1445-1454, Aug. 2008.

[Mit08b] B. Mitra, B. Levey, and Y.B. Gianchandani, "Hybrid arc/glow microdischarges at atmospheric pressure and their use in portable systems for liquid and gas sensing," *IEEE Transactions on Electron Devices*, 36(4), pp. 1913-1924, Aug. 2008.

[Mit08c] B. Mitra, DC pulse-powered microdischarges on planar electrodes and their use in vapor and liquid phase chemical sensing in ambient air, *Ph.D. Thesis,* University of Michigan, Ann Arbor, 2008.

[Miu03] N. Miura, M. Nakatou, and S. Zhuiykov, "Impedancemetric gas sensor based on zirconia solid electrolyte and oxide sensing electrode for detecting total NO_x at high temperature," *Sensors and Actuators B (Chemical)*, 93(1-3), pp. 221-228, Aug. 2003.

[Moc91] R. Mock and H. Meixner, "A miniaturized high-temperature pressure sensor for the combustion chamber of a spark ignition engine," *Sensors and Actuators A (Physical)*, A25(1-3), pp. 103-106, Oct. 1990-Jan. 1991.

[Mos03] M. Moselhy, I. Petzenhauser, K. Frank, and K.H. Schenbach, "Excimer emission from microhollow cathode argon discharges," *Journal of Physics D (Applied Physics)*, 36(23), pp. 2922-2927, Dec. 2003.

[Nam03] H. Nam, G.S. Cha, T.D. Strong, J. Ha, J.H. Sim, R.W. Hower, S.M. Martin, and R.B. Brown, "Micropotentiometric sensors," *Proceedings of the IEEE*, 91(6), pp. 870-880, June 2003.

[Nan92] L. Nanai and I. Hevesi, "Time-resolved spectral investigations of laser light induced microplasma," *Spectrochimica Acta, Part A (Molecular Spectroscopy)*, 48(1), pp. 19-24, Jan. 1992.

[Ned98] A.A. Ned, R.S. Okojie, and A.D. Kurtz, " 6H-SiC pressure sensor operation at 600°C," *High Temperature Electronics Conference. HITEC*, Albuquerque, NM, June 1998, pp. 257-260.

[Ogi01] M. Ogita, K. Higo, Y. Nakanishi, and Y. Hatanaka, "Ga_2O_3 thin film for oxygen sensor at high temperature," *Applied Surface Science*, 175-176, pp. 721-725, May 2001.

[Ohr92] M. Ohring, *The Materials Science of Thin Films*, San Diego, CA: Academic Press Inc., 1992.

[Pea63] R.W.B. Pearse, *The Identification of Molecular Spectra*, *3d ed.,* London, U.K.: Chapman and Hall Ltd..

[Par00] S.-J. Park, C.J. Wagner, C.M. Herring, and J.G. Eden, "Flexible microdischarge arrays: Metal/polymer devices," *Applied Physics Letters*, 77(2), pp. 199-201, July 2000.

[Par07] E. R. Parker, M. P. Rao, K. L. Turner, C. D. Meinhart, and N. C. MacDonald, "Bulk micromachined titanium microneedles," *Journal of Microelectromechanical Systems*, 16(2), pp. 289-295, April 2007.

[Par08] J.M. Park, R.P. Taylor, A.T. Evans, T.R. Brosten, G.F. Nellis, S.A. Klein, J.R. Feller, L. Salerno, and Y.B. Gianchandani, "A piezoelectric microvalve for cryogenic applications," *Journal for Micromechanics and* Microengineering, 18(1), pp. 015023 (10 pp.), Jan. 2008.

[Pen00] C. Penache, A. Braeuning-Demian, L. Spielberger, and H. Schmidt-Boecking, "High pressure glow discharges based on MSE arrays," *IEEE International Conference on Plasma Science*, New Orleans, LA, June 2000, p. 111.

[Pen05] W. Peng, G.R. Pickrell, and A. Wang, "High-temperature fiber optic cubic-zirconia pressure sensor," *Optical Engineering*, 44(12), pp. 124402-1-124402-6, Dec. 2005.

[Pet93] S. Peter, R. Pintaske, G. Hecht, and F. Richter, "Ion energy distribution measurements in glow discharges," *Journal of Nuclear Materials*, 200(3), pp. 412-416, May 1993.

[Pet83] J.E. Pettersson, "The spectrum of singly ionized sulphur, SII," *Physica Scripta*, 28(3), pp. 421-434, Sep. 1983.

[Pie08] *Piezo Systems Inc. Piezoceramic Materials and Properties*, http://www.piezo.com/prodmaterialprop.html

[Pos00] O.B. Postel and M.A. Cappelli, "Vacuum ultraviolet emission and metastable state properties of DC microdischarges," *IEEE International Conference on Plasma Science*, Piscataway, NJ, June 2000, pp.127.

[Pul02] W. Pulliam, P. Russler, and R. Fielder, "High-temperature, high-bandwidth, fiber optic, MEMS pressure sensor technology for turbine engine component testing," *Proceedings of the SPIE - The International Society for Optical Engineering*, Newton, MA, Oct.- Nov. 2001, pp. 229-238.

[Qi01] B. Qi, G. Pickrell, P. Zhang, Y. Duan, W. Peng, J. Xu, Z. Huang, J. Deng, H. Xiao, Z. Wang, W. Huo, R. May, and A. Wang, "Fiber optic pressure and temperature sensors for oil down hole application," *Proceedings of the SPIE - The International Society for Optical Engineering,* Newton, MA, Oct.- Nov. 2001, pp. 182-190.

[Qia01] X. Qia and M.A. Fiddy, " Distributed optical fiber bragg grating sensor for simultaneously measurement of pressure and temperature in the oil and gas downhole," *Proceedings of the SPIE - The International Society for Optical Engineering*, Boston, MA, July-Aug. 2002, pp. 554-558.

[Que05] L. Que, C.G. Wilson, and Y.B. Gianchandani, "Microfluidic electrodischarge devices with integrated dispersion optics for spectral analysis of water impurities," *Journal of Microelectromechanical Systems*, 14(2), pp. 185-191, April 2005.

[Rah07] H. Rahanman, B. Lee, I. Petzenhauser, and K. Frank, "Switching characteristics of microplasmas in a planar electrode gap," *Applied Physics Letters*, 90(13) pp. 131505(1-3), March 2007.

[Rai97] Y.P. Raizer, *Gas Discharge Physics*, Berlin, Germany: Springer-Verlag, 1997.

[Raj06] G. G. Raju, *Gaseous Electronics*, Boca Raton, FL: CRC Press, 2006.

[Ran01] R. Ranjan, J.P. Allain, M.R. Hendricks, and D. N. Ruzic, "Absolute sputtering yield of Ti/TiN by Ar^+/N^+ at 400 – 800 eV," *Journal of Vacuum Science and Technology A (Vacuum, Surfaces, and Films)*, 19(3), pp. 1004-1007, May 2001.

[Rao92] K.P. Rao, "Effect of microstructure on the mechanical properties of microplasma arc welded austenitic stainless steels," *Praktische-*Metallographie, 29(2), pp. 101-108, Feb. 1992.

[Ric08] M.T. Richardson and Y.B. Gianchandani, "Achieving precision in high density batch mode micro-electro-discharge machining," *Journal of Micromechanics and Microengineering*, 18(1), pp. 015002-1-12, Jan. 2008.

[Riz77] A. Rizk and L. Holland, “Sputtering and chemical etching of carbon in a DC glow discharge,” *Vacuum*, 27(10-11), pp. 601-604, Oct.-Nov. 1977.

[Rob88a] R. T. Robiscoe and Z. Sui, “Circuit model of surface arcing,” *Journal of Applied Physics*, 64(9), pp. 4364-4374, Nov. 1988.

[Rob88b] R. T. Robiscoe, A. Kadish and W. B. Maier II, “A lumped circuit model for transient arc discharges,” *Journal of Applied Physics*, 64(9), pp. 4355-4363, Nov. 1988.

[Rut99] S.L. Rutherford, “Miniature sputter-ion pump design considerations,” *NASA/JPL Miniature Vacuum Pumps Workshop*, Mountain View, CA, July 1999.

[Sae08] *St707 Getter Alloy for Vacuum Thermal Insulation*, http://www.saesgetters.com/default.aspx?idpage=273.

[Sch57] G.J. Schulz and A.V. Phelps, “Ionization gauges for measuring pressures up to the millimeter range,” *Review of Scientific Instruments*, 28(12), pp. 1051-1054, Dec. 1957.

[Sch96] K.H. Schoenbach, R. Verhappen, T. Tessnow, P.F. Peterkin, and W. Byszewski, “Microhollow cathode discharges,” *Applied Physics Letters*, 68(1), pp. 13-15, Jan. 1996.

[Sch99] L. Schulz, “Sputter-ion pumps,” *CERN Accelerator School Vacuum Technology. Proceedings*, Snekersten, Denmark, May – June 1999, pp. 37-42.

[Sch05] C. Schrader, P. Sichler, L. Baars-Hibbe, N. Lucas, A. Schenk, S. Draeger, K.-H. Gericke, and S. Buttgenbach, “Micro-structured electrode arrays: plasma based sterilization and coating over a wide pressure range,” *Surface and Coating Technology*, 200(1-4), pp. 655-659, Oct. 2005.

[Sha06] Private Communications, Dr. Jagdish Shah, Principal Research Engineer, Schlumberger-Doll Research Center.

[Shi99] W. Shi, R.H. Stark, and K.H. Schoenbach, “Parallel operation of microhollow cathode discharges,” *Transactions on Plasma* Science, 27(1), pp. 16-17, Feb. 1999.

[Sho98] V. Shogun, A. Tyablikov, M. Abachev, V. Pashkov, W. Scharff, and T. Wallendorf, “An emission actinometric method for measuring plasmachemical reaction kinetic parameters with discharge power modulation by a series of short probing pulses,” *Surface and Coating Technology*, 98 (1-3), pp. 1406-1410, Jan. 1998.

[Sim93] J.B. Simeonsson and A.W. Miziolek, "Time-resolved emission studies of ArF-laser produced microplasmas," *Applied Optics*, 32(6), pp. 939-947, Feb. 1993.

[Sli85] S. Slinker and A.W. Ali, "Electron momentum transfer collision frequency in N_2, O_2, and air," *NRL Memorandum Report* 5614, 1985.

[Smi70] A.L. Smith and R. Breitwieser, "Richardson-Dushman equation monograph," *Journal of Applied Physics*, 41(1), pp. 436-437, Jan. 1970.

[Sob98] A. Sobel, "Television's bright new technology," *Scientific American*, 278(5), pp. 70-77, May 1988.

[Spa03] D.R. Sparks, S. Massoud-Ansari, and N. Najafi, "Chip-level vacuum packaging of micromachines using NanoGetters," *IEEE Transactions on Advanced Packaging*, 26(3), pp. 277-282, Aug. 2003.

[Sug91] S. Suganomata, T. Ishikawa, J. Tanaka, and H. Ozaki, "Asymmetrical emission profiles from low-frequency discharges in SF_6 and N_2 gases in a planar diode with a Si-wafer," *Japanese Journal of Applied Physics, Part 1 (Regular Papers and Short Notes)*, 30(1), pp. 180-181, Jan. 1991.

[Sta99] R.H. Stark and K. H. Schoenbach, "Direct current high-pressure glow discharges," *Journal of Applied Physics*, 85(4), pp. 2075-2080, Feb. 1999.

[Sta05] D. Staack, B. Farouk, A. Gutsol, and A. Fridman, "Characterization of a dc atmospheric pressure normal glow discharge," *Plasma Sources Science and Technology*, 14(4), pp. 700-711, Nov. 2005.

[Stu82] W.P. Stuart-Bruges, "Data acquisition for borehole evaluation," *Electronics and Power. Journal of the Institution of Electrical Engineers*, 28(11), pp. 763-766, Nov.-Dec. 1982.

[Sul01] J.P. Sullivan, J.P. Marler, S.J. Gilbert, S.J. Buckman, and C.M. Surko, "Excitation of electronic states of Ar, H_2, and N_2 by positron impact," *Physical Review Letters*, 87(7), pp. 073201(1-4), Aug. 2001.

[Tak02] K. Takahata and Y.B. Gianchandani, "Batch mode micro-electro-discharge machining," *Journal of Microelectromechanical Systems,* 11(2), pp. 102-110, April 2002.

[Tak04] K. Takahata and Y.B. Gianchandani, "A planar approach for manufacturing cardiac stents: Design, fabrication, and mechanical evaluation," *Journal of Microelectromechanical Systems,* 13(6), pp. 933-939, Dec. 2004.

[Tak06] K. Takahata and Y.B. Gianchandani, K.D. Wise, "Micromachined antenna stents and cuffs for monitoring intraluminal pressure and flow," *Journal of Microelectromechanical Systems,* 15(5), pp. 1289-1298, October 2006.

[Tan95] Y. Tanaka, Y. Yokomizu, T. Matsumura, and Y. Kito, "Transient behavior of axial temperature distribution in post-arc channel after current zero around nozzle throat in flat-type SF_6 gas-blast quenching chamber," *Journal of Physics D (Applied Physics)*, 28(10), pp. 2095, 1995.

[Tei84] T.H. Teich and R. Braunlich, "UV radiation from electron avalanches in SF_6 with small admixtures of nitrogen," *The Fourth International Symposium on Gaseous Dielectrics IV*, Knoxville, TN, April- May 1984, pp. 71-81.

[Tei85] T.H. Teich and R. Braunlich, "UV and other radiation from discharges in artificial air and its constituents," *International Conference on Gas Discharges and their Applications*, Oxford, U.K., Sep. 1985, pp. 441-444.

[Thi06] J.A. Thiele and M.P. da Cunha, "High temperature LGS SAW gas sensor," *Sensors and Actuators B (Chemical),* 113(2), pp. 816-822, Feb. 2006.

[Tob03] P. Tobias, B. Golding, and R.N. Ghosh, "Interface states in high temperature gas sensors based on silicon carbide," *IEEE Sensors Journal*, 3(5), pp. 543-547, Oct. 2003.

[Vac85] S. Vacquie, A. Gleizes, and H. Kafrouni, "Measurements of electron density in a SF_6 arc plasma," *Journal of Physics D (Applied Physics)*, 18(11), pp. 2193-2205, Nov. 1985.

[Var08] *Varian Inc., Vacuum Technologies, Ion Pumps,* http://www.varianinc.com/image/vimage/docs/products/ vacuum/pumps/ion/shared/ion-catalog.pdf

[Vas90] V.A. Vashchenko, B.S. Kerner, V.V. Osipov, and V.F. Sinkevich, "Excitation and evolution of microplasmas acting as spike autosolitons in silicon *p-i-n* structures," *Soviet Physics*-Semiconductors, 24(10), pp. 1065-1066, Oct. 1990.

[Vas98] A. Vasiliev, W. Moritz, V. Fillipov, L. Bartholomaeus, A. Terentjev, and T. Gabsugan, "High temperature semiconductor sensor for the detection of fluorine," *Sensors and Actuators B (Chemical)*, 49(1-2), pp. 133-138, June 1998.

[Ves05] A. Vesel, M. Mozetic, and A. Zalar, "AES investigation of anode deposits in magnetron-type sputter ion pump," *Applied Surface Science*, 246(1-3), pp. 126-131, June 2005.

[Von95] D. von der Linde and H. Schuler, "Observation of the dynamics of electron plasma oscillations in femtosecond laser produced plasmas," *Applied Physics Letters,* 66(7), pp. 807-808, Feb. 1995.

[Wal99] S.G. Walton, J.C. Tucek, R.L. Champion, and W. Yicheing, "Low energy, ion-induced electron and ion emission from stainless steel: The effect of oxygen coverage and the implications for discharge modeling," *Journal of Applied Physics*, 85(3), pp, 1832-1837, Feb. 1999.

[Wan05] Q. Wang, I. Koleva, V.M. Donnelly, and D.J. Ecounomou, "Spatially resolved diagnostics of an atmospheric pressure direct current helium microplasma," *Journal of Physics D (Applied Physics)*, 38(11), pp. 1690-1697, June 2005.

[Wan05b] X. Wang, B. Li, Z. Xiao, S. H. Lee, H. Roman, O.L. Russo, K.K. Chin, and K.R. Farmer, "An ultra-sensitive optical MEMS sensor for partial discharge detection," *Journal of Micromechanics and Microengineering*, 15(3), pp. 521-527, March 2005.

[Wan06] Q. Wan, E.N. Dattoli, W.Y. Fung, W. Guo, Y. Chen, X. Pan, and W. Lu, "High-performance transparent conduction oxide nanowires," *Nano Letters*, 6(12), pp. 2909-2915, Aug. 2006.

[Wan07] Q. Wan, E.N. Dattoli, and W. Lu, "Transparent metallic Sb-doped SnO_2 nanowires," *Applied Physics Letters*, 90(22), pp. 22107/1-3, May 2007.

[Wel01] K.M. Welch, *Capture Pumping Technology Second Fully Revised Edition*, New York, New York: Pergamon Press, 2001.

[Wel03] K.M. Welch, "Major advances in capture pumps in the last 50 years," *Journal of Vacuum Science and Technology A (Vacuum, Surfaces, and Films)*, 21(5), pp. S19-S24, Sep. 2003.

[Wen90] A.E. Wendt and M.A. Lieberman, "Spatial structure of a planar magnetron discharge," *Journal of Vacuum Science and Technology A (Vacuum, Surfaces, and Films)*, 8(2), pp. 902-907, March-April 1990.

[Wes68] G.F. Weston, *Cold Cathode Glow Discharge Tubes*, London, U.K.: IEEE Books Ltd., 1968.

[Wil99] J.Z. Wilcox, T. George, and J. Feldman, "Miniature ring-orbitron getter ion vacuum pumps," *NASA Tech Briefs*, 23(9), Sep. 1999.

[Wil01a] C.G. Wilson and Y.B. Gianchandani, "Silicon micromachining using in-situ DC microplasmas," *Journal of Microelectromechanical Systems*, 10(1), pp. 50-54, March 2001.

[Wil01b] D.M. Wilson, S. Hoyt, J. Janata, K. Booksh, and L. Obando, "Chemical sensors for portable, handheld field instruments," *IEEE Sensors Journal,* 1(4), pp. 256-274, Dec. 2001.

[Wil02] C.G. Wilson and Y.B. Gianchandani, "Spectral detection of metal contaminants in water using an on-chip microglow discharge," *IEEE Transactions on Electron Devices*, 49(12), pp. 2317-2322, Dec. 2002.

[Wil03a] C.G. Wilson, Y.B. Gianchandani, R.R. Arslanbekov, V. Kolobov, and A.E. Wendt, "Profiling and modeling of DC nitrogen microplasmas," *Journal of Applied Physics,* 94(5), pp. 2845-2851, Sep. 2003.

[Wil03b] C.G. Wilson. Microplasmas and microdischarges for manufacturing and sensing applications, *Ph.D. Thesis*, University of Wisconsin, Madison, 2003.

[Wil04] C.G. Wilson and Y.B. Gianchandani, "Miniaturized magnetic nitrogen DC microplasmas," *Transactions on Plasma Science,* 32(1), pp. 282-297, Feb. 2004.

[Wil07] C. G. Wilson and Y.B. Gianchandani, "Selective deposition of silicon at room temperature using DC microplasmas," *Transactions on Plasma Science*, 35(3), pp. 573-577, June 2007.

[Wil08] Private Communications, Dr. Jaroslava Wilcox, Research Engineer, NASA Jet Propulsion Laboratory.

[Wri07a] S.A. Wright and Y.B. Gianchandani, "A harsh environment, multi-plasma microsystem with pressure sensor, gas purifier, and chemical detector," *IEEE International Conference on Micro Electro Mechanical Systems (MEMS 07)*, Kobe, Japan, Jan. 2007, pp. 115-118.

[Wri07b] S.A. Wright and Y.B. Gianchandani, "Controlling pressure in microsystem packages by on-chip microdischarges between thin-film titanium electrodes," *Journal of Vacuum Science and Technology B*, 25(5), pp. 1711-1720, Sep. 2007.

[Wri08] S.A. Wright, and Y.B. Gianchandani, "Discharge-based pressure sensors for high temperature applications using three-dimensional and planar microstructures," *Journal of Microelectromechanical Systems*, in press.

[Wol91] R.A. Wolthuis, G.L. Mitchell, E. Saaski, J.C. Hartl, and M.A. Afromowitz, "Development of medical pressure and temperature sensors employing optical spectrum modulation," *IEEE Transactions on Biomedical Engineering*, 38(10), pp. 974-981, Oct. 1991.

[Yok05] K. Yokota, K. Nakamura, T. Kasuya, K. Mukai, and M. Ohnishi, "Deposition of titanium nitride films onto silicon by an ion beam assisted deposition method," *Thin Solid Films*, 473(2), pp. 340-345, Feb. 2005.

[Yos01] H. Yoshiki and Y. Horike, "Capacitvely coupled microplasma source on a chip at atmospheric pressure," *Japanese Journal of Applied Physics, Part 2 (Letters)*, 40(4A), pp. L350-L362, April 2001.

[Yos88] M. Yoshitake, K. Takiguchi, Y. Suzuki, and S. Ogawa, "Effects of oxygen pressure in reactive ion beam sputter depositions of zirconium oxides," *Journal of Vacuum Science and Technology A (Vacuum, Surfaces, and Films)* 6(4), pp. 2326-2332, July-Aug. 1988.

[Zen91] V. Zengin, S. Suzer, A. Gokmen, A. Rumeli, and M. Sezai Dincer, "Analysis of SF_6 discharge by optical spectroscopy," *Gaseous Dielectrics VI*, Knoxville, TN, Sep. 1990, pp. 595-599.

[Zha94] Y. Zhang and K. D. Wise, "Performance of nonplanar silicon diaphragms under large deflections," *Journal of Microelectromechanical Systems*, 3(2), pp. 59-68, June 1994.

[Zha02] Y. Zhao, Y. Liao, and S. Lai, "Simultaneous measurement of down-hole high pressure and temperature with a bulk-modulus and FBG sensor," *IEEE Photonics Technology Letters*, 14(11), pp. 1584-1586, Nov. 2002.

[Zhu98] S. Zhu, F. Wang, and W. Wu, "Simulations of reactive sputtering with constant voltage power supply," *Journal of Applied Physics*, 84(11), pp. 6399-6408, Dec. 1998.